

ACOUSTIC TRANSDUCTION – MATERIALS AND DEVICES

Period 1 January 1998 to 31 December 1998

Annual Report

VOLUME IV

**OFFICE OF NAVAL RESEARCH
Contract No: N00014-96-1-1173**

**APPROVED FOR PUBLIC RELEASE –
DISTRIBUTION UNLIMITED**

**Reproduction in whole or in part is permitted for any
purpose of the United States Government**

Kenji Uchino

PENNSTATE



**THE MATERIALS RESEARCH LABORATORY
UNIVERSITY PARK, PA**

**Reproduced From
Best Available Copy**

19990427 044

REPORT DOCUMENTATION PAGE

Form Approved
OMB No. 0704-0188

Public reporting burden for this collection of information is estimated to average 1 hour per response, including the time for reviewing instructions, searching existing data sources, gathering and maintaining the data needed, and completing and reviewing the collection of information. Send comments regarding this burden estimate or any other aspect of this collection of information, including suggestions for reducing this burden, to Washington Headquarters Services, Directorate for Information Operations and Reports, 1215 Jefferson Davis Highway, Suite 1204, Arlington, VA 22202-4302, and to the Office of Management and Budget, Paperwork Reduction Project (0704-0188), Washington, DC 20503.

1. AGENCY USE ONLY (Leave blank)		2. REPORT DATE 04/05/99	3. REPORT TYPE AND DATES COVERED ANNUAL REPORT 01/01/98-12/31/98	
4. TITLE AND SUBTITLE ACOUSTIC TRANSDUCTION -- MATERIALS AND DEVICES			5. FUNDING NUMBERS ONR CONTRACT NO: N00014-96-1-11173	
6. AUTHOR(S) KENJI UCHINO				
7. PERFORMING ORGANIZATION NAME(S) AND ADDRESS(ES) Materials Research Laboratory The Pennsylvania State University University Park PA 16802			8. PERFORMING ORGANIZATION REPORT NUMBER	
9. SPONSORING/MONITORING AGENCY NAME(S) AND ADDRESS(ES) Office of Naval Research ONR 321SS Ballston Centre Tower One 800 N Quincy Street Arlington VA 22217-5660			10. SPONSORING/MONITORING AGENCY REPORT NUMBER	
11. SUPPLEMENTARY NOTES				
12a. DISTRIBUTION / AVAILABILITY STATEMENT			12b. DISTRIBUTION CODE	
13. ABSTRACT (Maximum 200 words)				
14. SUBJECT TERMS			15. NUMBER OF PAGES	
			16. PRICE CODE	
17. SECURITY CLASSIFICATION OF REPORT	18. SECURITY CLASSIFICATION OF THIS PAGE	19. SECURITY CLASSIFICATION OF ABSTRACT	20. LIMITATION OF ABSTRACT	

ABSTRACT

This report documents work performed over the period 1 January 1998 to 31 December 1998 on a MURI under the Office of Naval Research Contract N00014-96-1-1173. The topic "Acoustic Transduction Materials and Devices" brings together groups in the Materials Research Laboratory (MRL), the Applied Research Laboratory (ARL), and the Center for Acoustics and Vibrations (CAV) at Penn State.

Research on the program is adequately represented in the 80 technical appendices.

Outstanding accomplishments include:

Exploration of several new relaxor ferroelectric perovskite solid solution with morphotropic phase boundaries. New evidence of the onset of nonlinearity in soft donor doped PZTs at surprisingly low (1V/cm) fields. Confirmation of the relaxor phase induced by electron irradiation in PVDF:TrFE copolymers, and a processing method which permits very high (4%) electrostrictive strain in the transverse direction, vital for the practical use in actuator systems. In composite transducer, "first fruits" of the cooperative program are cymbal arrays which form most effective acoustic projectors, and a new "dog bone" design which permits deeper submergence for the cymbal. Agile transducers, the 3-D acoustic intensity probe and high force high strain torsional and step and repeat systems continue to make excellent progress. In actuator studies true acoustic emission is proving to be an excellent tool in reliability studies and a new design of small-scale (mini) piezoelectric motor shows outstanding performance. Thick thin film studies and are now "gearing up" for the development of the mini tonpilz arrays. New combinations of ultrasonic and resonance methods appear to offer unique capability for complete characterization of ferroelectric piezoelectric materials.

The mode of presentation of the report emphasizes the outstanding progress made in published research. It is important to also document that the slower and more painstaking development of practical transducer systems in the cymbal and mini tonpilz arrays is progressing very favorably.

APPENDICES

VOLUME I

GENERAL SUMMARY PAPERS

1. Cross, L.E., "Recent Developments in Piezoelectric Ferroelectric Materials and Composites," Proceedings of the 4th European Conference on Smart Structures and Materials in Conjunction with the 2nd International Conference on Micromechanics, Intelligent Materials and Robotics, Harrogate, UK (6-8 July 1998).
2. Newnham R.E., "Functional Composites for Sensors and Actuators," Chapter in *The Era of Materials*, edited by S. Majumdar, R. Tressler, and E. Miller, 259-275, Pennsylvania Academy of Science (1998).
3. Uchino, K., "Piezoelectric Ultrasonic Motors: Overview," *Smart Mater. Struct.* **7**, 273-285 (1998).
4. Newnham, R.E., "Phase Transformations in Smart Materials," *Acta Cryst. A* **54**, 729-737 (1998).

2.0 MATERIALS STUDIES

2.1 Polycrystal Perovskite Ceramics

5. Liu, S.F., I.R. Abothu, S. Komarneni, P. Poosanaas, D.S. Paik, Y. Ito, and K. Uchino, "PLZT Ceramics from Conventional and Microwave Hydrothermal Powders," Proceedings in Asian Meeting on Ferroelectrics (AMF2), Singapore (December 8-11, 1998).
6. Abothu, I.R., P. Poosanaas, S. Komarneni, Y. Ito, and K. Uchino, "Nanocomposite Versus Monophasic Sol-Gel Processing of PLZT Ceramics," Proceedings in Asian Meeting on Ferroelectrics (AMF2), Singapore (December 8-11, 1998).
7. Kim, J.S., Y.H. Chen, and K. Uchino, "Dielectric and Piezoelectric Properties of Fe₂O₃-Doped 0.57PSN-0.43PT Ceramics," *J. Korean Phys. Soc.* **32** [2], S1248-1250 (1998).
8. Alberta, E.F. and A.S. Bhalla, "Electrical Property Diagram and Morphotropic Phase Boundary in the Pb(In_{1/2}Ta_{1/2})O₃-PbTiO₃ Solid Solution System," *Ferroelectric Letters* (1998). [accepted]
9. Meng, J.F., Z-Y. Cheng, B.K. Rai, R.S. Katiyar, E. Alberta, R. Guo, and A.S. Bhalla, "Photoluminescence in PbMg_{1/3}Nb_{2/3}O₃-PbIn_{1/2}Nb_{1/2}O₃ Systems," *J. Mater. Res.* **13** (7), 1861 (1998).
10. Alberta, E.F. and A.S. Bhalla, "Investigation of the Lead Indium Niobate-Lead Magnesium Niobate Solid Solution," *Materials Letters* (1998). [accepted]
11. Alberta, E.F., A.S. Bhalla, and T. Takenaka, "Large Hydrostatic Piezoelectric Constant and Temperature Dependence of the Piezoelectric Properties of Bi(NiTi)_{1/2}O₃:PbTiO₃ Ceramics," *Ferroelectrics Letters* (1998). [accepted]
12. Zhang, Q.M. and J. Zhao, "Electromechanical Properties of Lead Zirconate Titanate Piezoceramics Under the Influence of Mechanical Stress, *IEEE Trans. UFFFC* (accepted).
13. Kugel, V.D. and L.E. Cross, "Behavior of soft Piezoelectric Ceramics under High Sinusoidal Electric Fields," *J. Appl. Phys.* **84** (5), 2815-2830 (1998).

VOLUME II

2.0 MATERIALS STUDIES

2.1 *Polycrystal Perovskite Ceramics* (continued)

14. Du, X-H., Q.M. Wang, U. Belegundu, and K. Uchino, "Piezoelectric Property Enhancement in Polycrystalline Lead Zirconate Titanate by Changing Cutting Angle," J. Ceram. Soc. Jpn. (1999). [accepted]
15. Mueller, V. and Q.M. Zhang, "Nonlinearity and Scaling Behavior in Donor Doped Lead Zirconate Titanate Piezoceramic," Appl. Phys. Lett. **72**, 2692 (1998).
16. Uchino, K and H. Aburatani, "Field Induced Acoustic Emission in Ferroelectric Ceramics," Proc. IEEE Ultrasonic Symp., Sendai, Japan (October 1998). [in press]
17. Newnham, R.E. and S. Trolier-McKinstry, "Size Effects in Ferroics" Integrated Ferroelectrics **20**, 1-13, Gordon & Breach Science Publishers (March 1998).

2.2 *Relaxor Ferroelectric Single Crystal Systems*

18. Uchino, K., "High Electromechanical Coupling Piezoelectrics: Relaxor and Normal Ferroelectric Solid Solutions," Solid State Ionics **108**, 43-52 (1998).
19. Wada, S. S.E. Park, L.E. Cross, and T.R. Shrout, "Domain Configuration and Ferroelectric Related Properties of Relaxor Based Single Crystals," J. Korean Phys. Soc. **32**, S1290-S1293 (1998).
20. Belegundu, U., X. H. Du, and K. Uchino, "In-Situ Observation of Domain Orientation in $\text{Pb}(\text{Zn}_{1/3}\text{Nb}_{2/3})\text{O}_3\text{-PbTiO}_3$ Single Crystals," Proc. 5th Intl. Symp. Ferroic Domains and Mesoscopic Structures, University Park, PA (April 1998).
21. Du, X.H., J. Zheng, U. Belegundu, and K. Uchino, "Crystal Orientation Dependence of Piezoelectric Properties of Lead Zirconate Titanate Near the Morphotropic Phase Boundary," J. Appl. Phys. Ltrs. **72** (19), 2421-2423 (1998).
22. Rehrig, P.W., S.-E. Park, S. Trolier-McKinstry, G.L. Messing, B. Jones, and T.R. Shrout, "Piezoelectric Properties of Zirconium-Doped Barium Titanate Single Crystals Grown by Templated Grain Growth," submitted to J. Appl. Phys.
23. Du, X., Q.M. Wang, U. Belegundu, A. Bhalla, and K. Uchino, "Crystal Orientation Dependence of Piezoelectric Properties of Single Crystal Barium Titanate," Mat. Ltr. (1999) [accepted].
24. Guo, R., H.T. Evans, Jr., and A.S. Bhalla, "Crystal Structure Analysis and Polarization Mechanisms of Ferroelectric Tetragonal Tungsten Bronze Lead Barium Niobate," Ferroelectrics **206/207**, 123-132 (1998).

2.3 *New High Strain Polymer Materials*

25. Zhao, X., V. Bharti, Q.M. Zhang, T. Ramotowski, F. Tito, and R. Ting, "Electromechanical Properties of Electrostrictive P(VDF-TrFE) Copolymer," Appl. Phys. Ltrs. **73**, 2054 (1998).
26. Bharti, V., G. Shanthi, H. Xu, Q.M. Zhang, and K. Liang, "Evolution of Transitional Behavior and Structure of Electron Irradiated Poly(vinylidene fluoride-trifluoroethylene) Copolymer Films," Appl. Phys. Ltrs. [accepted].
27. Cheng, Z.-Y., V. Bharti, T.B. Xu, S. Wang, and Q.M. Zhang, "Transverse Strain Responses in Electrostrictive Poly (vinylidene fluoride-trifluoroethylene) Films and Development of a Dilatometer for the Measurement," J. Appl. Phys. [accepted]

VOLUME III

2.0 MATERIALS STUDIES

2.3 *New High Strain Polymer Materials* (continued)

28. Bharti, V., X.Z. Zhao, Q.M. Zhang, T. Ramotowaski, F. Tito, and R. Ting, "Ultrahigh Field Induced Strain and Polarized Response in Electron Irradiated Poly(vinylidene fluoride-trifluoroethylene) Copolymer," *Mat. Res. Innovat.* **2**, 57-63 (1998).
29. Su, J., P. Moses, and Q.M. Zhang, "A Bimorph Based Dilatometer for Field Induced Strain Measurement in Soft and Thin Free Standing Polymer Films," *Rev. Sci. Instruments* **69** (6), 2480 (1998).

3.0 TRANSDUCER STUDIES

3.1 *Composite Structures*

30. Hughes, W.J., "Transducers, Underwater Acoustic," *Encyclopedia of Applied Physics*, Vol. 22, 67 (1998).
31. Tressler, J.F., W.J. Hughes, W. Cao, K. Uchino, and R.E. Newnham, "Capped Ceramic Underwater Sound Projector."
32. Zhang, J., W.J. Hughes, A.C. Hladky-Hennion, and R.E. Newnham, "Concave Cymbal Transducers."
33. Wang, Q.M., X.-H. Du, B. Xu, and L.E. Cross, "Theoretical Analysis of the Sensor Effect of Cantilever Piezoelectric Benders," *J. Appl. Phys.* **85** (3), 1702-1712 (1998).
34. Fernandez, J.F., A. Dogan, J.T. Fielding, K. Uchino, and R.E. Newnham, "Tailoring the Performance of Ceramic-Metal Piezocomposite Actuators, 'Cymbals'," *Sensors and Actuator A65*, 228-237 (1998).
35. Wang, Q.M. and L.E. Cross, "A Piezoelectric Pseudoshear Multilayer Actuator," *Appl. Phys. Ltrs.* **72** (18), 2238 (1998).
36. Geng, X. and Q.M. Zhang, "Resonance Modes and Losses in 1-3 Composites for Ultrasonic Transducer Applications," *J. Appl. Phys.* **85** (3), 1342 (1999).

3.2 *Frequency Agile Transducers*

37. Hebert, C.A. and G. A. Lesieutre, "Flexural Piezoelectric Transducers with Frequency Agility Obtained Via Membrane Loads," *J. Intel. Mat. Sys. & Str.* (1998). [accepted].
38. Davis, C.L. and G.A. Lesieutre, "An Actively Tuned Solid State Vibration Absorber Using Capacitive Shunting of Piezoelectric Stiffness," *J. Sound & Vibration* (1998). [accepted]
39. Bernard, J., G.A. Lesieutre, and G.H. Koopmann, "Active Broadband Force Isolation using a Flexural Piezoelectric Inertial Actuator," *J. Sound & Vibration* (1999). [submitted]

VOLUME IV

3.0 TRANSDUCER STUDIES

3.3 3-D Acoustic Intensity Probes (continued)

40. Lauchle, G.C. and A.R. Jones, "Unsteady Lift Force on a Towed Sphere," J. Fluids and Structures **112** (1998).
41. Lauchle, G.C., A.R. Jones, J.J. Dreyer, and J. Wang, "Flow-Induced Lift Forces on a Towed Sphere," Proc. Of ASME Noise Control and Acoustics Division ASME 1998, NCA-28, 103-111 (1998).
42. Brungart, T.A. G.C. Lauchle, S. Deutsch, and E. Riggs, "Outer-Flow Effects on Turbulent Boundary Layer Wall Pressure Fluctuations," J. Acoust. Soc. Am. **105** (4) (April 1999).
43. Brungart, T.A., G.C. Lauchle, and R.K. Ramanujam, "Installation Effects of Fan Acoustic and Aerodynamic Performance," Noise Control Eng. J. **47** (January/February 1999).

4.0 ACTUATOR STUDIES

4.1 Materials : Designs : Reliability

44. Uchino, K., "New Trend in Ceramic Actuators," Proc. 6th Intl. Aerospace Symp. '98, Nagoya, Japan, p. S1-2, 1-10 (July 14-15, 1998).
45. Uchino, K., "Materials Issues in Design and Performance of Piezoelectric Actuators: An Overview," Acta. Mater. **46** (11), 3745-3753 (1998).
46. Yao, K., W. Zhu, K. Uchino, Z. Zhang, and L.C. Lim, "Design and Fabrication of a High Performance Multilayer Piezoelectric Actuator with Bending Deformation."
47. Aburatani, H. and K. Uchino, "Acoustic Emission in Damaged Ferroelectric Lead Zirconate Titanate Ceramics," Jpn. J. Appl. Phys. **37**, L553-L555 (1998).
48. Atherton, P.D. and K. Uchino, "New Developments in Piezo Motors and Mechanisms," Proc. 6th Intl. Conf. On New Actuators (Actuator 98) , Bremen, Germany, p. 164-169 (June 17-19, 1998).
49. Uchino, K. and B. Koc, "Compact Piezoelectric Ultrasonic Motors," 2nd Asian Meeting on Ferroelectrics (AMF-2), Singapore (December 7-11, 1998).
50. Koc, B., Y. Xu, and K. Uchino, "Ceramic/Metal Composite Piezoelectric Motors," IEEE Ultrasonic Symposium, Sendai, Japan (October 1998).
51. Koc, B., Y. Xu, and K. Uchino, "Roto-Linear Ultrasonic Motors," Proc. 6th Intl. Conf. On New Actuators (Actuator 98), Bremen, Germany, p. 349-352 (June 17-19, 1998).
52. Koc, B., A. Dogan, Y. Xu, R.E. Newnham, and K. Uchino, "An Ultrasonic Motor Using a Metal-Ceramic Composite Actuator Generating Torsional Displacement," Jpn. J. Appl. Phys. **37**, 5659-5662 (1998).

4.2 Photostrictive Actuators

53. Poosanaas, P. and K. Uchino, "Photostrictive Effect in Lanthanum-Modified Lead Zirconate Titanate Ceramics Near The Morphotropic Phase Boundary," J. Mat. Chem. & Phys. (October 1998). [submitted]
54. Uchino, K. and P. Poosanaas, "Photostriction in PLZT and Its Applications," Proc. CIMTEC '98, Florence, Italy (June 14-19, 1998).

VOLUME V

4.0 ACTUATOR STUDIES

4.3 *Torsional and High Force Actuators* (continued)

- 55. Glazounov, A.E., Q.M. Zhang, and C. Kim, "Torsional Actuator Based on Mechanically Amplified Shear Piezoelectric Response," *Sensors and Actuators* (1998). [submitted]
- 56. Frank, J., G.H. Koopmann, W. Chen, and G.A. Lesieutre, "Design and Performance of a High Force Piezoelectric Inchworm Motor."

5.0 MODELING and CHARACTERIZATION

5.1 *Finite Element and Other Methods*

- 57. Qi, W. and W. Cao, "Finite Element and Experimental Study of Composite and 1-D Array Transducers," *SPIE* **3341** (1998).
- 58. Wang, H., W. Jiang, and W. Cao, "Characterization of Lead Zirconate Titanate Piezoceramic Using High Frequency Ultrasonic Spectroscopy," *J. Appl. Phys.* (1998). [accepted]
- 59. Zhu, S.N., B. Jiang, and W. Cao, "Characterization of Piezoelectric Materials Using Ultrasonic and Resonant Techniques," *Proceedings of SPIE Imaging '98*, **3341**, 154-162 (1998).
- 60. Cao, W., "Virtual Design of Medical Transducers," *Proceedings of SPIE Imaging '98*, **3341**, 56-63 (1998).
- 61. Cao, W., "Elastic Property Characterization in Thin Samples of Sub-Wavelength in Thickness," *Ferroelectrics* **206/207**, 355-363 (1998).
- 62. Cao, W., S.N. Zhu, and B. Jiang, "Analysis of Shear Modes in A Piezoelectric Resonator," *J. Appl. Phys.* **83**, 4415-4420 (1998).

5.2 *Relaxor Ferroelectrics*

- 63. Giniewicz, J.R., A.S. Bhalla, and L.E. Cross, "Variable Structural Ordering in Lead Scandium Tantalate-Lead Titanate Materials," *Ferroelectrics* **211**, 281-297 (1998).
- 64. Pan, X., W.D. Kaplan, M. Rühle, and R.E. Newnham, "Quantitative Comparison of Transmission Electron Microscopy Techniques for the Study of Localized Ordering on a Nanoscale," *J. Am. Ceram. Soc.* **81** (3), 597-605 (1998).
- 65. Zhao, J., A.E. Glazounov, and Q.M. Zhang, "Change in Electromechanical Properties of 0.9PMN:0.1PT Relaxor Ferroelectric Induced by Uniaxial Compressive Stress Directed Perpendicular to the Electric Field," *Appl. Phys. Ltrs.* **74**, 436 (1999).
- 66. Zhao, J., V. Mueller, and Q.M. Zhang, "The Influence of the External Stress on the Electromechanical Response of Electrostrictive 0.9Pb(Mg_{1/3}Nb_{2/3})O₃-0.1PbTiO₃ in the dc Electrical Field Biased State," *J. Mat. Res.* **14**, 3 (1999).

VOLUME VI

5.0 MODELING and CHARACTERIZATION

5.3 *Thin and Thick Thin Films*

67. Maria, J.P., W. Hackenberger, and S. Trolier-McKinstry, "Phase Development and Electrical Property Analysis of Pulsed Laser Deposited $\text{Pb}(\text{Mg}_{1/3}\text{Nb}_{2/3})\text{O}_3\text{-PbTiO}_3$ (70/30) Epitaxial Films," *J. Appl. Phys.* **84** (9), 5147-5154 (1998).
68. Shepard, J.F., Jr., P.J. Moses, and S. Trolier-McKinstry, "The Wafer Flexure Technique for the Determination of the Transverse Piezoelectric Coefficient (d_{31}) of PZT Thin Films," *Sensors and Actuators A* **71**, 133-138 (1998).
69. Zavala, G. J.H. Fendler, and S. Trolier-McKinstry, "Stress Dependent Piezoelectric Properties of Ferroelectric Lead Zirconate Titanate Thin Films by Atomic Force Microscopy," *J. Korean Phys. Soc.* **32**, S1464-S467 (1998).
70. Wasa, K., Y. Haneda, T. Satoh, H. Adachi, I. Kanno, K. Setsune, D.G. Schlom, S. Trolier-McKinstry, C.-B. Eom, "Continuous Single Crystal PbTiO_3 Thin Films Epitaxially Grown on Miscal (001) SrTiO_3 ," *J. Korean Phys. Soc.* **32**, S1344-S1348 (1998).
71. Xu, B., Y. Ye, L.E. Cross, J.J. Bernstein, and R. Miller, "Dielectric Hysteresis from Transverse Electric Fields in Lead Zirconate Titanate Thin Films," *Appl. Phys. Ltrs.* (1998). [submitted]
72. Xu, B., N.G. Pai, Q.-M. Wang, and L.E. Cross, "Antiferroelectric Thin and Thick Films for High Strain Microactuators," *Integrated Ferroelectrics* **22**, 545-557 (1998).

5.4 *Domain Studies*

73. Erhart, J. and W. Cao, "Effective Material Properties in Twinned Ferroelectric Crystals," *J. Appl. Phys.* (1999). [submitted]
74. Belegundu, U., M. Pastor, X.H. Du, L.E. Cross, and K. Uchino, "Domain Formation in $0.90\text{Pb}(\text{Zn}_{1/3}\text{Nb}_{2/3})\text{O}_3\text{-}0.10\text{PbTiO}_3$ Single Crystals under Electric Field along [111] Direction," *IEEE '98*, Sendai, Japan (1998).
75. Zhu, S.N. and W. Cao, "Pyroelectric and Piezoelectric Imaging of Ferroelectric Domains in LiTaO_3 by Scanning Electron Microscopy," *Phys. Status Solidi* (1998). [submitted]
76. Hatch, D.M. and W. Cao, "Determination of Domain and Domain Wall Formation at Ferroic Transitions," *Ferroelectric* (1998). [submitted]
77. Mueller, V. and Q.M. Zhang, "Threshold of Irreversible Domain Wall Motion in Soft PZT-Piezoceramic. *Ferroelectrics* **206/207**, 113-122 (1998).
78. Aburatani, H., J.P. Witham, and K. Uchino, "A Fractal Analysis on Domain Related Electric Field Induced Acoustic Emission in Ferroelectric Ceramics," *Jpn. J. Appl. Phys.* **37**, 602-605 (1998).

5.5 Electrostriction

79. Newnham, R.E., V. Sundar, R. Yimnirun, J. Su, and Q.M. Zhang, "Electrostriction in Dielectric Materials," in *Advances in Dielectric Ceramic Materials*, eds. K. Nair and A. Bhalla. Ceramic Trans. **88**, 154-39 (1998).
80. Sundar, V., R. Yimnirun, B.G. Aitken, and R.E. Newnham, "Structure Property Relationships in the Electrostriction Response of Low Dielectric Permittivity Silicate Glasses," Mat. Res. Bull. **33**, 1307-1314 (1998).

APPENDIX 40



UNSTEADY LIFT FORCE ON A TOWED SPHERE

G. C. LAUCHLE

*Penn State University, Graduate Program in Acoustics and Applied Research Laboratory
P.O. Box 30, State College, PA 16804, U.S.A.*

AND

A. R. JONES

General Electric Co., Appliance Park, AP3-220, Louisville, KY 40225, U.S.A.

(Received 30 January 1998 and in revised form 24 August 1998)

An experimental effort to characterize the broadband flow-induced lift forces on a spherical body that is towed underwater is described. The body itself is the transducer which is comprised of a small geophone encased in a near-neutrally-buoyant sphere, 7.62 cm in diameter. The research described in this paper quantifies the flow-induced unsteady lift force signal as a function of the sphere diameter Reynolds number ($7620 < Re < 34290$) and the Strouhal number ($1.5 < St < 30$). It is found that the broadband flow-induced unsteady lift forces are proportional to the product of an area and the dynamic pressure of the flow, as expected. These data are compared to similar data measured previously on a finite-length, right-circular cylinder in cross flow. This comparison indicates that the cylindrical body creates more unsteady side force than does the spherical one, particularly at the lower end of the Strouhal number range.

© 1998 Academic Press

1. INTRODUCTION

VARIOUS NOISE SOURCES are known to affect the performance of drifting or moored hydrophones. In quiescent fluid, these sources include ambient background noise, electronic noise, and transducer suspension-induced noise. Because of ocean currents induced by tides, gravity, temperature gradients, or surface waves, many real-world situations result in a fluid that is not quiescent. Typical currents in the ocean have mean velocities ranging from 0.25 to 0.5 knots. It has been shown by Finger *et al.* (1979), McEachern (1980), and McEachern & Lauchle (1995) that this fluid flow can cause an additional flow-induced self-noise in the sensor that can dominate all the other sources combined. Flow-induced noise on hydrophones configured as bluff bodies depends strongly on the flow velocity, Reynolds number, sensor geometry, and Strouhal number. (Recall that the Reynolds number, $Re = UD/\nu$, where U is the mean flow velocity, D is body diameter, and ν is the kinematic viscosity of the fluid; the Strouhal number, $St = fD/U$, where f is the frequency in Hz.) In the absence of flow and other extraneous noise sources, the output from the hydrophone is the acoustic signal generated by a propagating wave of interest. However, when flow is present, hydrodynamic disturbances from large- and small-scale instabilities, vortex shedding, and turbulent velocity fluctuations can occur simultaneously on the surface of the hydrophone and in the near wake. These disturbances impart unsteady forces on the sensor itself, creating a flow-induced self-noise signal which contaminates or “masks” the desired acoustic signal.

Acoustic signals of interest in the ocean usually originate from a distance source; therefore, hydrophone directional sensitivity is oftentimes an important consideration in

undersea acoustic measurements. Pressure gradient and/or acoustic velocity hydrophones have a desirable directional axis of peak response (even at infrasonic and low frequencies). They can also be used in conjunction with a pressure sensor to infer intensity and propagation direction (Gabrielson *et al.* 1995a, b). Berliner & Lindberg (1995) have compiled a collection of papers reporting that acoustic velocity sensors are often used in lieu of omni-directional pressure hydrophones in many undersea applications. However, Finger *et al.* (1979), McEachern (1980), and Keller (1977) show that acoustic particle velocity (or pressure gradient) hydrophones exhibit a considerably higher sensitivity to flow effects than do pressure hydrophones. Keller (1977) quoted differences of approximately 50 dB at 10 Hz for a flow speed of 0.5 knots. These authors, in addition to Gabrielson *et al.* (1995b) and McEachern & Lauchle (1995), have shown that the flow-induced self-noise signal from an acoustic velocity sensor is directly related to the hydrodynamically induced body forces generated by the flow over the hydrophone. This, of course, is not unexpected because the sensors are inertial sensors. The measured unsteady velocity is related to the body acceleration by a frequency factor, and this relates to the unsteady force from Newton's second law of motion.

Most of the previously published work has considered the cylindrical-shaped hydrophone in cross flow, although Finger *et al.* (1979) indicated that there was little difference between the flow noise spectrum of a cylindrical pressure gradient hydrophone in cross flow and a spherical one. McEachern & Lauchle (1995) found that the cylinder aspect (length-to-diameter) ratio plays a key role in the flow-noise signal, as does the corner radius of the cylinder endcaps. The flow-induced fluctuating force levels decrease (to a degree) as these parameters are increased.

Based on this finding, and the apparent indifference noted by Finger *et al.* (1979) between a cylinder and a sphere, it is important to investigate more thoroughly the flow-induced forces generated by uniform flow over a sphere. Using typical water velocities of ocean currents ($0.25 \text{ kt} < U < 0.5 \text{ kt}$), and a range of sphere diameters considered in applications, the Reynolds number range of interest would be approximately $5000 < \text{Re} < 30\,000$ (here, $\nu = 10^{-6} \text{ m}^2/\text{s}$). The frequency range would be similar to that of the previous investigations ($10 \text{ Hz} < f < 100 \text{ Hz}$), which results in a Strouhal number range of 1.5–30. This range is considerably higher than the characteristic vortex shedding frequency range of a sphere. The unsteady force spectra are broadband in this range of Strouhal numbers.

The objective of the research presented in this paper is to characterize experimentally (and within the Reynolds and Strouhal number ranges noted above) the flow-induced unsteady side (lift) forces created on a spherical body configured as an acoustic particle velocity hydrophone operating underwater. The acquired spectral data are nondimensionalized and compared to similar nondimensional force spectral data obtained by McEachern & Lauchle (1995) for finite-length cylinders in cross flow. The fluid mechanics of a sphere depends in a rather complex way on the Reynolds number range also, so we will summarize those effects first.

2. FLUID FLOW REGIMES OF A SPHERE

The wake structure behind a sphere is more complex than that of a long cylinder. Extensive research has been conducted and vast amounts of experimental data have been accumulated. Of note, was the identification (Möller 1938; Taneda 1956; Achenbach 1974) of more than one characteristic vortex shedding frequency from a sphere. This has led to the definition of both high- and low-mode Strouhal numbers. Kim & Durbin (1988) identified these two modes as coexisting and due to the following.

(i) a vortex shedding associated with the large-scale instability in the wake. The shedding frequency of this mode, when nondimensionalized in the form of a Strouhal number is practically independent of Reynolds number. For $400 \leq Re \leq 10^5$, the Strouhal number for this mode is of order 0.2.

(ii) The second instability frequency is greater than the first, and is due to a small-scale instability associated with the separating shear layer. The Strouhal number for this mode increases logarithmically with Reynolds number, although it is indistinguishable from and equal to that of the lower mode for $Re \leq 800$. This small-scale instability frequency is sometimes difficult to detect at higher Reynolds numbers too ($Re \geq 15\,000$), because of masking by other broadband velocity fluctuations associated with the near wake.

The various flow regimes for a sphere, as summarized by Sakamoto & Haniu (1990) are as follows.

$Re < 5$. This is the region of Stokes flow which is completely driven by viscous forces. These forces are proportional to the product of the viscosity, velocity, and characteristic length (diameter).

$5 < Re < 300$. A wave-like laminar wake of very long period forms behind the sphere.

$300 < Re < 420$. A hairpin vortex begins to shed; a spectral peak shows up in the unsteady velocity spectrum.

$420 < Re < 480$. The shedding of the hairpin vortices becomes irregular. This is the early transition regime.

$480 < Re < 650$. The shedding mode is in a continuous state of randomness, or irregularity.

$650 < Re < 800$. The shedding pattern differs from that of lower Reynolds numbers due to a pulsation of the vortex sheet. Multiple frequencies are observed and the cores of the shed vortices begin to show signs of turbulence.

$800 < Re < 3\,000$. Some of the vortex tubes formed by the vortex sheet separating from the sphere surface enter into the vortex formation region, while others are shed in small vortex loops. The large-scale vortices move away from the sphere rotating at random about an axis parallel to the flow through the center of the sphere. The wake becomes turbulent at $Re \sim 2\,000$.

$3\,000 < Re < 6\,000$. This is another transition region where the measured low-mode shedding Strouhal numbers decrease rapidly with increasing Reynolds number. The power spectrum of the fluctuating wake velocity shows one characteristic peak plus considerable broadband energy on both sides of this peak. The vortex sheet is changing from laminar to turbulent in this regime.

$6\,000 < Re < 370\,000$. The separated vortex sheet is now completely turbulent. The vortices shed from the formation region become stabilized because the separated shear layer is no longer laminar, but turbulent. This stabilization causes the velocity fluctuation spectrum to lose some of the broadband nature observed in the previous region. The Strouhal frequency of regular shedding increases with Reynolds number and then approaches the constant value of 0.19 at $Re \sim 20\,000$.

In addition to these observations, Achenbach (1974) states that for Reynolds numbers between 6000 and 300 000 the vortex separation point rotates around the sphere. Taneda (1978) performed detailed flow visualization studies of the sphere wake in a Reynolds number range of 10^4 – 10^6 and found that the wake is not axisymmetric. He suggested, based on this and Achenbach's observations (rotating separation point), that a sphere subjected to uniform flow will have a completely random distribution of side forces.

For the frequencies, velocities, and length scales considered in the current study, the Reynolds number range falls within the range where random side (lift) forces are expected.

The Strouhal numbers are typically greater than 1.5, which are above the expected discrete vortex shedding ranges of the sphere. The data presented for the unsteady side forces are thus in a range of Strouhal numbers that has received very little attention in the past. The only other comparable data for this problem are presented by Willmarth & Enlow (1969). They determined unsteady sphere side forces and moments at Reynolds numbers greater than 4.8×10^5 , and for Strouhal numbers between approximately 10^{-4} and 0.2.

3. EXPERIMENTAL SETUP

3.1. THE SPHERICAL TEST MODEL

In accordance to the design recommendations presented by Gabrielson *et al.* (1995b), a GeoSpace Corp., GS20-DH7 geophone (velocity sensor) was encased in a neutrally buoyant spherical body so as to create a sensor capable of sensing weak underwater acoustic velocity fluctuations. The spherical acoustic velocity transducer, shown in Figure 1, is cast from a 3.5:1 by volume mixture of polystyrene micro balloons and epoxy resin, which resulted in a slightly negatively buoyant body. The slightly negative buoyancy was desired so that ballast weights could be avoided during testing that may adversely affect the flow-induced force measurements.

The spherical sensor was calibrated for force in water by mechanically exciting it with a shaker. Comparison of the geophone output voltage with that of a standard accelerometer securely mounted to the spherical surface provided a transfer function that, when corrected for the known sensitivity of the accelerometer and the mass of the hydrophone, yields a sensitivity function of the hydrophone in the units of V/N. The measured force sensitivity of the test hydrophone is 0 dB re 1 V/N at 65 Hz. The sensitivity varies with frequency, as expected, at -6 dB/octave. When the sphere is towed underwater, the measured geophone voltage autospectrum is divided by this force sensitivity function to yield the desired unsteady side force autospectrum.

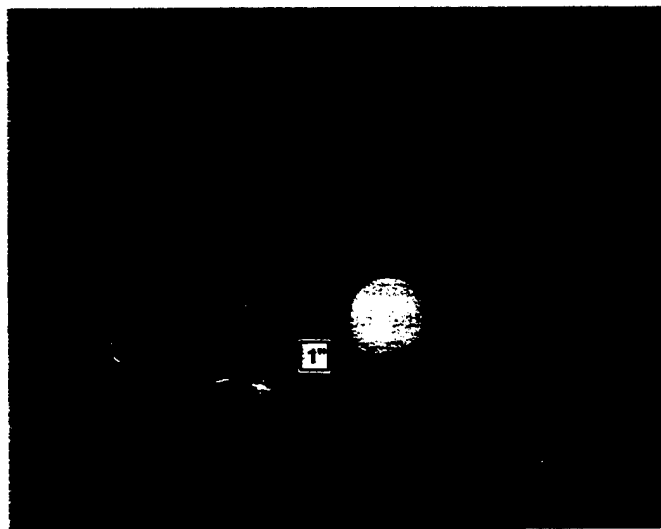


Figure 1. Photograph of the spherical velocity-sensitive sensor and test model. The long narrow rod on the bottom side was removed during testing. It was used only for the manufacturing process.

3.2. TOW TANK FACILITY

A long tow channel was developed specifically for the flow noise measurements performed in this study. Vibration isolation within the facility is critical because of the low-frequency range of interest, the low force levels being measured, and the extreme sensitivity of the acoustic velocity hydrophone to vibration. Therefore, much attention was given to the reduction of vibration from ambient noise sources and noise generated by the towing system itself. The tank, shown schematically in Figure 2 and photographically in Figure 3,

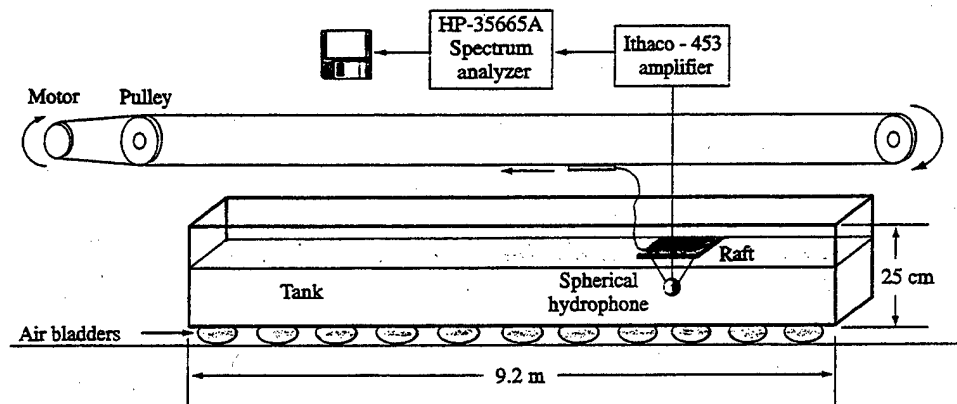


Figure 2. Schematic of the tow tank and data acquisition instrumentation.

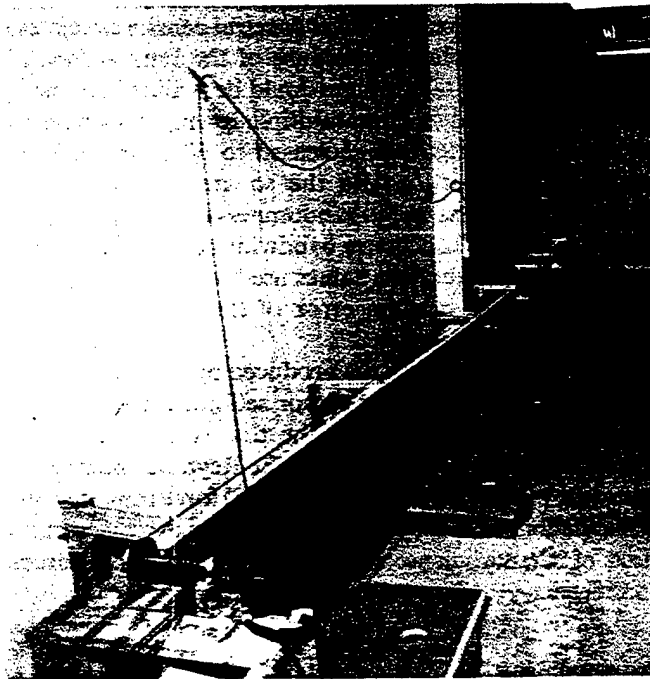


Figure 3. Photograph of the quiet tow tank facility showing its foundation of air-filled bladders and the monorail towing carriage.

sits on semi-inflated air bladders which rest on a concrete floor poured directly over bedrock in the basement of a laboratory building. This procedure effectively isolates the tank from seismic noise sources. A precision digitally controlled stepping motor drives a plastic coated cable the length of the tank. The cable is supported by a pulley mounted to the opposite wall. The motor has several stages of flexible shafts before being mechanically linked to the cable by two flexible driving belts. The only mechanical link from the tow cable to the tank is 3 mm diameter surgical rubber tubing, about 0.6 m in length, which extends from the cable to a smooth raft. A fin mounted on the back of the raft keeps it oriented properly. The sphere is suspended underneath the raft using 3X monofilament fishing line in a three-point suspension.

The geophone encased in the sphere is oriented normal to the flow direction so that side-to-side lift forces are sensed. Fluctuating drag forces are suppressed from the measurements because of the cosine directivity pattern of the geophone. We have elected not to measure the unsteady drag forces in this investigation because it is believed from this and other independent investigations that the side forces dominate the sensor self-noise signal. Support for this may be inferred from Taneda's (1978) observation of a random side-force field being produced by sphere wake nonaxisymmetry, and by Blake (1986) who states that the r.m.s. drag force of a cylinder is only 10% of the r.m.s. lift force. The side-to-side motion of the sphere at frequencies of 10 Hz or greater is extremely small, so blockage effects from the tank side walls were considered negligible. The width of the tank was four sphere diameters.

A small-diameter signal cable runs from the top of the sphere to the back of the raft. The signal cable is surrounded with nylon mesh to break up unwanted vortex shedding and instability frequencies associated with the cable itself. The signal cable continues from the raft to an overhead payout rig leading to an Ithaco (model 453) amplifier where the signal is amplified 50–70 dB before going to an HP-35665A FFT analyzer. A Hanning window was used in the analyzer which then provided power spectral density estimates in the 10–100 Hz frequency range with a 1 Hz resolution. Because of the limited time available for each towing run, no more than 20 spectral averages could be realized per run. Thus, to decrease the random error in the spectra, data from multiple towing runs were averaged together. The total number of ensembles was thus increased to 60 or more. The random error in spectrum level is inversely proportional to the square-root of the number of spectral averages, so the statistical variations due to randomness of the measured spectral levels is of order ± 0.6 dB. Because of the 1 Hz effective bandwidth of the spectral analysis, there is no bias error. The accuracy of the calibration values used to infer the unsteady forces is also of order ± 1 dB. Thus, the overall random error of the flow-induced forces presented is estimated to be of order ± 2 dB.

The flow over the spherical hydrophone is produced by towing it in a controlled manner in the long tow channel. The flow-induced sensor self-noise can be studied systematically with a constant diameter sensor by varying the tow velocity, and hence the Reynolds number. For tow speeds between 10 and 45 cm/s, the Reynolds number range is from 7620 to 34 290. The dependent variable is the fluctuating (lift) force imparted on the sphere by the unsteady velocity fluctuations caused by rectilinear motion in a quiescent and uniform body of liquid. The effects of inlet turbulence or the effects of non-fluid particles impacting the sphere are not considered.

3.3. SYSTEM BACKGROUND NOISE

Experiments were conducted to assure that the measured unsteady forces induced by facility background noise (ambient plus mechanical noise) were below those measured on

the sphere when exposed to flow. To reduce the ambient noise floor, all flow noise measurements were made after normal working hours when the ventilation system of the building was not in operation and other extraneous noise sources were at a minimum. The mechanical system noise is defined as the output noise of the submerged, but mechanically disconnected and stationary, spherical sensor while the tow cable is operated at the normal towing speeds. The ambient noise is defined as the submerged, stationary sensor output at zero tow cable speed. Spectra for each of these contaminating noises were determined at velocities from 10 to 45 cm/s, in increments of 2.5 cm/s. They were compared then to the flow-induced lift spectra. For the majority of the test velocities and frequencies considered, the signal-to-ambient or mechanical noise ratio was well above 10 dB, indicating that the system noise is not contaminating the flow-noise data; see Jones (1996) for additional details. At some lower towing speeds, however, it was observed that the broadband fluctuating lift flow-noise levels approached the levels of the background noise. To assure that the flow-noise data presented are not background-noise-limited, portions of the measured flow-noise spectra are omitted if the background noise level is within 6 dB or less of the measured flow noise level.

4. RESULTS

Figure 4 shows a family of flow-induced lift spectra measured in fresh, clean water at different towing speeds. These conditions correspond to $7620 < Re < 34\,290$. As noted in Section 3-3, portions of these individual spectra are necessarily omitted because of being within 6 dB of the background noise spectra corresponding to that particular towing speed. We note that a 6 dB or more signal-to-noise ratio is established for the entire frequency range at the higher Reynolds number conditions. The situation degrades—especially at the higher frequencies—as the tow speed is lowered below 20 cm/s.

4.1 DIMENSIONLESS FORM OF THE FLOW-INDUCED LIFT FORCE SPECTRA

Because the Reynolds number is greater than 6000 turbulence is present in the near wake of the sphere. It would be expected then, that the force levels would scale on the inertial forces of the flow (the high Reynolds numbers required for turbulent flow imply that the inertial

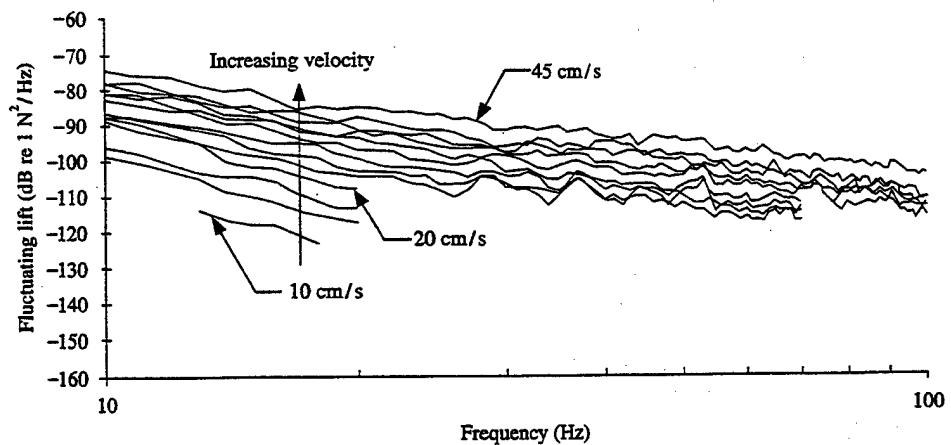


Figure 4. Autospectra of the fluctuating force sensed by the sphere in pure water for a range of flow velocities ($7620 < Re < 34\,290$).

forces dominate the viscous forces). We adopt the same scaling as first proposed for hydrophone flow-induced self-noise by McEachern (1993). Denoting the one-sided auto-spectrum of the force fluctuations by $G_F(f)$, the dimensionless form of the power spectral density function would be $G_F(f) (U/D)/(\rho U^2 A)^2$ which is expressed as a function of the Strouhal number $St = fD/U$. Here, ρ is the density of the liquid medium, A is the frontal area of the sphere exposed to flow, and St normalizes the frequency on the inertial time scale (D/U).

The spectra of Figure 4 are presented in the dimensionless inertial force spectrum format in Figure 5. The collapse of these spectra to the narrow band indicated suggests that the mechanism of flow-induced lift in this Reynolds and Strouhal number range is indeed the inertial forces created by the turbulent fluctuations in the separated vortex sheet. Such forces must also include those induced by the random rotation of the separation line and the resulting non-axisymmetry of the vortex structures downstream of separation. The Reynolds numbers shown here are below the boundary layer transition Reynolds number of a sphere ($\sim 300\,000$), so mechanisms due to transition or turbulent boundary layer pressure fluctuations are likely nonexistent.

Of particular interest are the flow-induced forces on a sphere compared to those of a cylinder in cross flow. Shown in Figure 5 are three straight lines representing the least mean-square fits of cylindrical sensor side force spectra (McEachern 1993) that were measured in a very quiet flooded quarry, and independently of the apparatus reported in this paper. The Reynolds number range for these experiments was 4000 to 18 000. The lower of the two spectra is for a cylinder having an aspect ratio of 1.0 and with rounded endcaps. The radius of the endcap corners is $R = 0.25D$, where D was 10.16 cm. This was the "quietest" cylinder geometry identified by McEachern. The middle trace of the three cylinder flow noise spectra was measured for a geometric configuration that most closely matches a sphere; the aspect ratio was 1.5 and the endcaps were hemispheres ($R = D/2$). The dimensionless force spectrum for this basically elongated sphere is seen to fall slightly below the current data due to a steeper spectral slope. The higher of the three cylinder flow noise spectra is for a right-circular cylinder in cross flow, i.e., the aspect ratio is 1.0, but there is no corner radius ($R = 0$). At the lower values of St , this cylindrical sensor generates more flow noise than the spherical sensor.

As one additional comparison of the subject experimental findings to an independently acquired data set, we refer to Figure 6. The dimensionless (lift) force spectra of the current

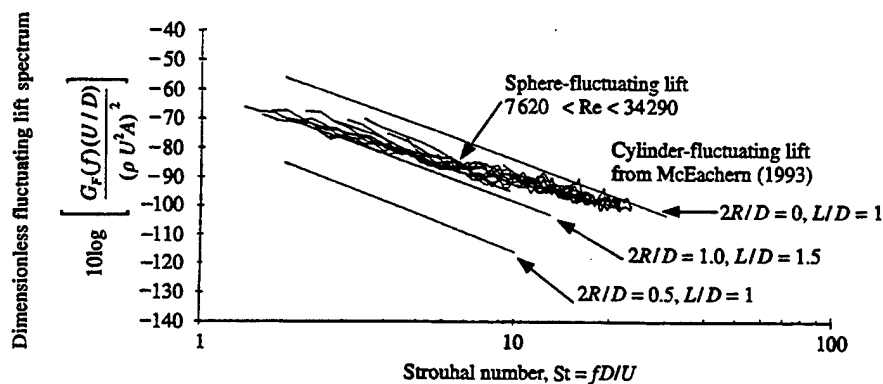


Figure 5. Autospectra of the fluctuating force normalized on the inertial force and time scales of the flow. Data are shown for the sphere ($7620 < Re < 34\,290$), and also for a series of cylinders tested previously by McEachern (1993) ($4000 < Re < 18\,000$).

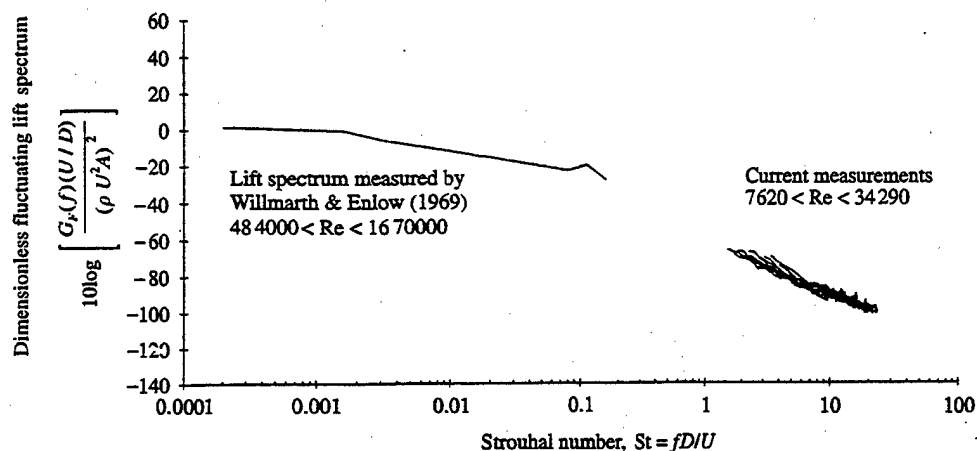


Figure 6. Autospectra of the fluctuating force measured on spheres normalized on the inertial force and time scales of the flow. Data are shown for the current investigation at $1.5 < St < 30$ along with those from the independent investigation of Willmarth & Enlow (1969) at $0.0002 < St < 2$.

investigation at high Strouhal numbers are compared to similarly normalized sphere lift spectra measured by Willmarth & Enlow (1969) at low Strouhal numbers. They performed these measurements on a spherical model operating in a wind tunnel at supercritical Reynolds numbers ($4.84 \times 10^5 \leq Re \leq 1.67 \times 10^6$). Their measured Strouhal number range was from approximately 2×10^{-4} to 0.2. Note that a narrow band of energy exists for $St \sim 0.15$ which is due to the lower vortex shedding mode discussed in Section 2.

5. CONCLUSIONS

An experimental investigation of the flow-induced fluctuating side-to-side lift force generated by a sphere set in uniform rectilinear motion has been described. A 7.62 cm diameter spherical sensor was tested in a specially designed low-noise tow tank that was filled with clean, fresh water. Empirical scaling laws, based on the classical unsteady lift coefficient, were used that allow the measured flow-induced fluctuating force frequency spectra to be collapsed to a reasonable single curve. In particular, for the Reynolds number range of $7620 < Re < 34290$, the unsteady forces were found to scale on the inertial forces created by turbulent flow near the sphere. The frequencies scale on the inertial time scale D/U under these conditions and, for $St > 1.5$, the spectra are broadband. Based on flow visualization, Taneda (1978) speculated that a sphere should generate a significant random lift force due to a non-axisymmetric wake that rotates randomly (Achenbach 1974) around the axis of mean flow. The results presented here support that claim, in that a broadband random lift coefficient is clearly measurable.

The nondimensional lift spectra measured for the sphere are similar to those measured in earlier investigations on a finite-length cylinder with various endcap geometries. The main difference between the two data sets is that the spectral levels roll off slightly faster for the cylinders as St increases. The right-circular cylinder in cross flow creates approximately 10 dB more spectral energy than does the sphere for $2 < St < 10$. An optimum cylinder endcap radius exists, and the side force spectral levels measured on a cylinder with this geometry are at least 20 dB lower than those of the sphere.

ACKNOWLEDGEMENTS

The work reported here has been supported by the Naval Air Warfare Center, Aircraft Division, Patuxent River, MD. and the Office of Naval Research, Code 321-SS. The authors are indebted to Drs James McEachern and Thomas Gabrielson for numerous fruitful discussions pertaining to this research.

REFERENCES

- ACHENBACH, E. 1974 Vortex shedding from spheres. *Journal of Fluid Mechanics* **62**, 209–221.
- BERLINER, M. J. & LINDBERG, J. F. (eds) 1995 *Acoustic Particle Velocity Sensors: Design, Performance, and Applications*, AIP Conference Proceedings 368, American Institute of Physics, Woodbury, NY, U.S.A. p. vii.
- BLAKE, W. K. 1986 *Mechanics of Flow-Induced Sound and Vibration*, Vol. 1, p. 240, Orlando: Academic Press.
- FINGER, R. A., ABBAGNARO, L. A. & BAUER, B. B. 1979 Measurement of low-velocity flow noise on pressure and pressure gradient hydrophones. *Journal of the Acoustical Society of America* **65**, 1407–1412.
- GABRIELSON, T. B., MCEACHERN, J. F. & LAUCHLE, G. C. 1995a Underwater acoustic intensity probe. United States Patent 5,392,258.
- GABRIELSON, T. B., GARDNER, D. L. & GARRETT, S. L. 1995b A simple neutrally buoyant sensor for direct measurement of particle velocity and intensity in water. *Journal of the Acoustical Society of America* **97**, 2227–2237.
- JONES, A. R. 1996 Flow-induced self noise on spherical and cylindrical sensors. M.S. Thesis, Graduate Program in Acoustics, Pennsylvania State University, University Park, PA, U.S.A.
- KELLER, B. D. 1977 Gradient hydrophone flow noise. *Journal of the Acoustical Society of America* **62**, 205–208.
- KIM, H. J. & DURBIN, P. A. 1988 Observations of the Frequencies in a sphere wake and of drag increase by acoustic excitation. *Physics of Fluids* **31**, 3260–3265.
- MCEACHERN, J. F. 1980 Experimental development of a compact flow shield. Institute of Electrical and Electronics Engineering Publication 80CH 1578-4 AES, 38–41.
- MCEACHERN, J. F. 1993 The effects of body geometry on the flow noise of cylinders in cross flow. Ph. D. Dissertation, Graduate Program in Acoustics, Pennsylvania State University, University Park, PA, U.S.A.
- MCEACHERN, J. F. & LAUCHLE, G. C. 1995 Flow-induced noise on a bluff body. *Journal of the Acoustical Society of America* **97**, 947–953.
- MÖLLER, W. 1938 Experimentelle untersuchung zur hydromechanik der kugel. *Physik Zeitschrift* **39**, 57–80.
- SAKAMOTO, H. & HANIU, H. 1990 A study on vortex shedding from spheres in uniform flow. *ASME Journal of Fluids Engineering* **112**, 386–392.
- TANEDA, S. 1956 Experimental investigation of the wake behind a sphere at low Reynolds numbers. *Journal of the Physical Society of Japan* **11**, 1104–1108.
- TANEDA, S. 1978 Visual observations of the flow past a sphere at Reynolds numbers between 10^4 and 10^6 . *Journal of Fluid Mechanics* **85**, 187–192.
- WILLMARTH, W. W. & ENLOW, R. L. 1969 Aerodynamic lift and moment fluctuations of a sphere. *Journal of Fluid Mechanics* **36**, 417–432.

APPENDIX 41



ASME International

The American Society of Mechanical Engineers
Three Park Avenue
New York, NY 10016-5990

Reprinted From
NCA-Vol. 25, Proceedings of the ASME Noise Control and
Acoustics Division

Editors: M. C. Hastings, S. M. Grace, A. D. Pierce, M. L. Pollack,
R. C. Marboe, T. M. Farabee, W. Keith, N. G. Humbad, V. Dayal,
M. K. Vaidya, E. Ayorinde, and S. F. Wu
Book No. G01089 - 1998

FLOW-INDUCED LIFT FORCES ON A TOWED SPHERE

Gerald C. Lauchle
Andrew R. Jones
James J. Dreyer
Jack Wang

Penn State University
Applied Research Laboratory and Graduate Program in Acoustics
P. O. Box 30, State College, PA 16804

ABSTRACT

An experimental and computational effort to characterize the broadband flow-induced forces on a spherical body that is towed underwater is described. The body itself is the transducer which is comprised of a small geophone encased in a near-neutrally-buoyant sphere, 7.62 cm in diameter. The research described in this paper quantifies the flow-induced unsteady lift force signal as a function of the sphere diameter Reynolds number ($215 < Re < 34,290$) and the Strouhal number ($1.5 < St < 30$). It is found that the broadband flow-induced force spectral levels may be separated into two regimes characterized by: 1) unsteady laminar flow in which the forces are proportional to the product of viscosity, mean shear, and area; and 2) turbulent flow in which the unsteady lift forces are proportional to the product of an area and the dynamic pressure of the flow. The low-Reynolds number data were acquired by towing the sphere in various mixtures of glycerine and water. The high Reynolds number lift force spectra, obtained in pure water, are compared to similar data measured previously on a finite-length, right-circular cylinder in cross flow. This comparison indicates that the cylindrical body creates more unsteady side force than does the spherical one, particularly at the lower end of the Strouhal number range. This is also the range of Reynolds number ($Re < 3,000$) where a simulation of the unsteady laminar flow-induced forces, based on a numerical solution of the Reynolds-averaged Navier-Stokes equations, could be performed. The sphere was held fixed in these simulations, and the resulting forces are thus due to the unsteady flow of fluid around the body itself, with no influence due to free-stream turbulence or tow cable. The computational spectra are found to agree remarkably well with those measured.

INTRODUCTION

Various noise sources are known to affect the performance of drifting or moored hydrophones. In quiescent fluid, these sources include ambient background noise, electronic noise, and transducer suspension-induced noise. Because of ocean currents induced by tides, gravity, temperature gradients, or surface waves, many real-world situations result in a fluid that is not quiescent. Typical currents in the ocean have mean velocities ranging from 0.25 to 0.5 knots. It has been shown by Finger, et al (1979), McEachern (1980), and McEachern and Lauchle (1995) that this fluid flow can cause an additional flow-induced self noise in the sensor that can dominate all the other sources combined. Flow-induced noise on hydrophones configured as bluff bodies depends strongly on the flow velocity, Reynolds number, sensor geometry, and Strouhal number. (Recall that the Reynolds number, $Re = UD/\nu$, where U is the mean flow velocity, D is body diameter, and ν is the kinematic viscosity of the fluid; the Strouhal number, $St = fD/U$, where f is the frequency in Hz). In the absence of flow and other extraneous noise sources, the output from the hydrophone is the acoustic signal generated by a propagating wave of interest. However, when flow is present, hydrodynamic disturbances from large and small-scale instabilities, vortex shedding, and turbulent velocity fluctuations can occur simultaneously on the surface of the hydrophone and in the near wake. These disturbances impart unsteady pressures on the sensor itself creating a flow-induced self noise signal which contaminates or "masks" the desired acoustic signal.

Acoustic signals of interest in the ocean usually originate from a distance source; therefore, hydrophone directional sensitivity is oftentimes an important consideration in undersea

acoustic measurements. Pressure gradient and/or acoustic velocity hydrophones have a desirable directional axis of peak response (even at infrasonic and low frequencies). They can also be used in conjunction with a pressure sensor to infer intensity and propagation direction (Gabrielson, et al 1995 a,b). Berliner and Lindberg (1995) have compiled a collection of papers that indicate that acoustic velocity sensors are often used in lieu of omnidirectional pressure hydrophones in many undersea applications. However, Finger, et al (1979), McEachern (1980), and Keller (1977) show that acoustic particle velocity (or pressure gradient) hydrophones exhibit a considerably higher sensitivity to flow effects than do pressure hydrophones. Keller (1977) quoted differences of approximately 50 dB at 10 Hz for a flow speed of 0.5 knots. These authors, in addition to Gabrielson, et al (1995b) and McEachern and Lauchle (1995), have shown that the flow-induced self noise signal from an acoustic velocity sensor is directly related to the hydrodynamically-induced body forces generated by the flow over the hydrophone. Such forces are the result of the surface integrated dynamic wall pressure fluctuations. Noting also that the measured unsteady velocity is related to the body acceleration by a frequency factor, the unsteady force is inferred from Newton's second law of motion.

The majority of the previously published work has considered the cylindrical-shaped hydrophone in cross flow, although Finger, et al (1979) indicated that there was little difference between the flow noise spectrum of a cylindrical pressure gradient hydrophone in cross flow and a spherical one. McEachern and Lauchle (1995) found that the cylinder aspect (length-to-diameter) ratio plays a key role in the flow noise signal, as does the corner radius of the cylinder endcaps. The flow-induced fluctuating force levels decrease (to a degree) as these parameters are increased.

Based on this finding, and the apparent indifference noted by Finger, et al (1979) between a cylinder and a sphere, it is important to investigate more thoroughly the flow-induced forces generated by uniform flow over a sphere. Using typical water velocities of ocean currents ($0.25 \text{ kt} < U < 0.5 \text{ kt}$), and a range of sphere diameters considered in applications ($0.13 \text{ cm} < D < 13 \text{ cm}$), the Reynolds number range of interest would be approximately $200 < Re < 30,000$ (here, $v = 10^{-6} \text{ m}^2/\text{s}$). The frequency range would be similar to that of the previous investigations ($10 \text{ Hz} < f < 100 \text{ Hz}$), which results in a Strouhal number range of 1.5 to 30. This range is considerably higher than the characteristic vortex shedding frequency range of a sphere. The unsteady force spectra are broadband in this range of Strouhal numbers.

The objective of the research presented in this paper is to characterize both experimentally and computationally the flow-induced unsteady forces created on spherical bodies configured as acoustic particle velocity sensors. We present a systematic experimental investigation of the unsteady side forces (lift) generated by the flow over such bodies within the Reynolds

number, velocity, and Strouhal number ranges noted above. The experiments are designed such that a single spherical sensor of 7.62 cm diameter is used throughout. The Reynolds number is varied at constant velocity and constant sphere diameter by changing the viscosity of the water. This is done by adding glycerine to the water. We wish to identify the ways in which the unsteady flow-induced force spectra scale with the independent variables. Such scaling depends on the Reynolds number range which determines the laminar or turbulent nature of the surface and wake flow. A CFD simulation for the unsteady flow over a sphere at Reynolds numbers of 1000 and 3000 is also incorporated to help verify the scaling relations identified.

The wake structure behind a sphere is more complex than that of a long cylinder. Extensive research has been conducted and vast amounts of experimental data have been accumulated. Of note, was the first identification by Möller (1938) of more than one characteristic vortex shedding frequency from a sphere. This has led to the definition of both high and low-mode Strouhal numbers. Kim and Durbin (1988) identified these two modes as coexisting and due to: 1) a vortex shedding associated with the large-scale instability in the wake. The shedding frequency of this mode, when non-dimensionalized in the form of a Strouhal number is practically independent of Reynolds number. For $400 \leq Re \leq 10^5$, the Strouhal number for this mode is of order 0.2. 2) The second instability frequency is greater than the first, and is due to a small-scale instability associated with the separating shear layer. The Strouhal number for this mode increases with Reynolds number, although it is indistinguishable from and equal to that of the lower mode for $Re \leq 800$. This small-scale instability frequency is sometimes difficult to detect at higher Reynolds numbers too ($Re \geq 15,000$), because of masking by other broadband velocity fluctuations associated with the near wake. The various flow regimes for a sphere are nicely summarized by Sakamoto and Haniu (1990). For the frequencies, velocities, and length scales considered in the current study, the Strouhal numbers are typically greater than 1.5, i.e., they are well above the expected vortex shedding ranges for the sphere. The data and computations presented for the unsteady lifting forces are thus in a range of Strouhal numbers that has received very little attention in the past.

EXPERIMENTS

Following Gabrielson, et al (1995b), a GeoSpace Corp., GS20-DH7 geophone (velocity sensor) was encased in a neutrally buoyant spherical body as to create a sensor capable of sensing weak underwater acoustic velocity fluctuations. Our spherical acoustic velocity transducer is cast from a 3.5:1 by volume mixture of polystyrene micro balloons and epoxy resin which resulted in a slightly negatively buoyant body. The slightly negative buoyancy was desired so that ballast weights could be avoided during testing that may adversely affect the flow-induced force measurements.

The spherical sensor, being an inertial sensor, was calibrated for force, in water, by exciting it with a shaker. Comparison of the geophone output voltage with that of a standard accelerometer securely mounted to the spherical surface provided a transfer function that when corrected for the known sensitivity of the accelerometer and the mass of the hydrophone yields a sensitivity function of the hydrophone. The measured force sensitivity of the test hydrophone is 0 dB re 1 volt/N at 65 Hz, and the sensitivity varies with frequency, as expected, at -6 dB/octave. The sensitivity measurements were repeated in glycerol mixtures in anticipation of changes in sensitivity due to changes in sensor buoyancy. The changes observed were less than 1 dB which is in agreement with what one would predict from the formula presented by Gabrielson, et al (1995b).

Tow Tank Facility

A long tow channel was developed specifically for the measurements performed in this study. Vibration isolation within the facility is critical because of the low-frequency range of interest, the low force levels being measured, and the extreme sensitivity of the acoustic velocity hydrophone to vibration. Therefore, much attention was given to the reduction of vibration from ambient noise sources and noise generated by the towing system itself. The tank, shown schematically in Fig. 1, sits on semi-inflated air bladders which rest on a concrete floor poured directly over bedrock in the basement of a laboratory building. This procedure effectively isolates the tank from seismic noise sources. A precision digitally-controlled stepping motor drives a plastic coated cable the length of the tank. The cable is supported by a pulley mounted to the opposite wall. The motor has several stages of flexible shafts before being mechanically linked to the cable by two flexible driving belts. The only mechanical link from the tow cable to the tank is 3 mm diameter surgical rubber tubing, about 0.6 m in length, which extends from the cable to a smooth raft. A fin mounted on the back of the raft keeps it oriented properly.

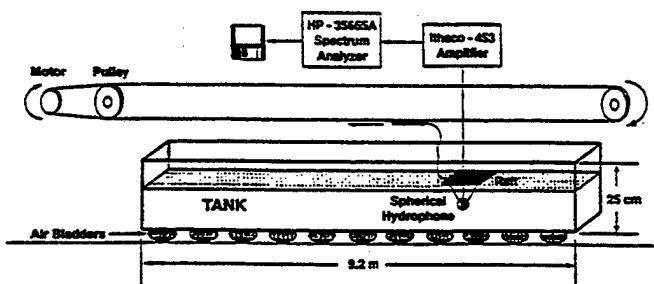


Figure 1. Schematic of the tow tank and data acquisition instrumentation.

The sphere is suspended underneath the raft using 3X monofilament fishing line in a three-point suspension. The geophone encased in the sphere is oriented normal to the flow direction so that side-to-side lift forces are sensed. Fluctuating drag forces are suppressed from the measurements because of the cosine directivity pattern of the geophone. We have elected not to measure the unsteady drag forces in this investigation because it is well known that the rms drag force of cylinders and spheres is of order 10% of the rms side force, e.g., Blake (1986). The computations we show here also support this decision. The side-to-side motion of the sphere at frequencies of 10 Hz or greater is extremely small, so blockage effects from the tank side walls was considered negligible. The width of the tank was four sphere diameters.

A small diameter signal cable runs from the top of the sphere to the back of the raft. The signal cable is surrounded with nylon mesh to break up unwanted vortex shedding and instability frequencies associated with the cable itself. The signal cable continues from the raft to an overhead payout rig leading to an Ithaco (model 453) amplifier where the signal is amplified 50 to 70 dB before going to an HP-35665A FFT analyzer. A Hanning window was used in the analyzer which then provided power spectral density estimates in the 10 to 100 Hz frequency range with a 1 Hz resolution. Because of the limited time available for each towing run, no more than 20 spectral averages could be realized per run. Thus, to decrease the random error in the spectra, data from multiple towing runs were averaged together. The total number of ensembles was thus increased to 60 or more. The random error in spectrum level is inversely proportional to the square-root of the number of spectral averages, so the statistical variations due to randomness of the measured spectral levels is of order ± 0.6 dB. Because of the 1 Hz effective bandwidth of the spectral analyses, there is no bias error. The accuracy of the calibration values used to infer the unsteady forces is also of order ± 1 dB. Thus, the overall random error of the presented flow-induced forces is estimated to be of order ± 2 dB.

Procedures

The flow over the sphere is produced by towing it in a controlled manner in the long tow channel. The physics of the flow-induced forces can be studied systematically with a constant diameter sphere, and through varying the flow velocity and Reynolds number independently. In pure water, the Reynolds number for constant diameter is varied by changing the flow velocity. The Reynolds number for constant diameter and constant velocity is then varied by changing the viscosity of the working fluid. This is accomplished by using glycerol as the working fluid. The towing velocities range from 10 to 45 cm/s. The kinematic viscosity of the working fluid is varied from 1.01×10^{-6} m²/s for pure water to 3.54×10^{-5} m²/s for 76.5% glycerol. The specific gravity of the fluid changes from 1.0 to 1.2

over this range. The percentages of glycerine selected for testing are chosen for a continuous, overlapping Reynolds number range.

This procedure allows for a large range of Reynolds numbers to be achieved with a constant diameter sphere operating over a relatively small range of speeds. The dependent variable is the fluctuating (lift) force imparted on the sphere (due to the surface integrated unsteady wall pressure fluctuations) caused by rectilinear motion in a quiescent and uniform body of liquid.

Experiments were conducted to assure that the measured unsteady forces induced by facility background noise (ambient plus mechanical noise) were below those measured on the sphere when exposed to flow. To reduce the ambient noise floor, all flow noise measurements were made after normal working hours when the ventilation system of the building was not in operation and other extraneous noise sources were at a minimum. For the majority of the test conditions, the system background noise did not contaminate the flow-induced force data acquired. However, at some of the lower towing speeds and for the higher concentrations of glycerol corresponding to low-Reynolds number flow conditions, it was observed that the broadband fluctuating lift levels rapidly approached the levels of the background noise. This may be due to the fact that the sphere simply does not produce much fluctuating force at low Reynolds numbers where the predominant flow structures are laminar. To assure that the fluctuating force data presented are not background noise limited, portions of the measured force spectra are omitted if the background spectral level is within 6 dB or less of the measured level under towed conditions.

RESULTS

Figure 2 shows a family of flow-induced lift spectra measured in pure water at different speeds correspond to $7,620 < Re < 34,290$. We note that a 6 dB or more signal-to-noise ratio is established for the entire frequency range at the higher Reynolds number conditions. The situation degrades - especially at the higher frequencies - as the tow speed is lowered below 20 cm/s.

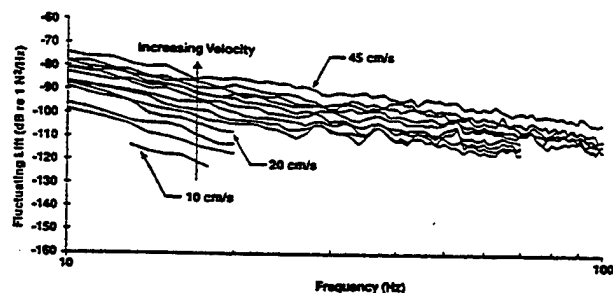


Figure 2. Autospectra of the fluctuating lift force sensed by the sphere in pure water for a range of tow (flow) velocities corresponding to $7,620 < Re < 34,290$.

A similar set of force spectral data is given in Fig. 3 for $2,421 < Re < 7,263$, which was obtained by towing the sphere in 38% glycerol. The general trend observed by Jones (1996) for other concentrations of glycerol is that as the percentage of glycerine increases, the higher the tow velocity has to be in order to have an acceptable signal-to-noise ratio. This is consistent with the notion that the Reynolds number has to be above some critical value before any flow-induced force is detected. That Reynolds number, based on the current data, appears to be of order 3,000 (note the gap between the 10 cm/s spectrum of Fig. 3 and the 15 cm/s spectrum which corresponds to $Re = 3,631$). This is above the transition Reynolds number ($Re \sim 2,000$) where the vortex cores in the wake of the sphere first become turbulent, and it is within the lower range of Reynolds numbers where the vortex sheet being shed from the sphere is transitioning to turbulent flow. The force fluctuations detected below this Reynolds number are extremely weak and are apparently due to unsteady laminar flow mechanisms.

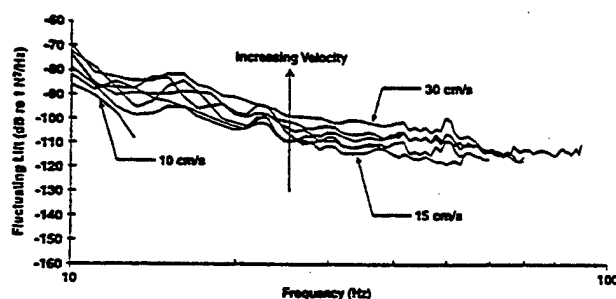


Figure 3. Autospectra of the fluctuating force sensed by the sphere in 38% glycerol for a range of flow velocities corresponding to $2,421 < Re < 7,263$.

Dimensionless Form of the Flow Noise Spectra at High Reynolds Numbers

With turbulence present in the near wake of the sphere, it would be expected that the force levels would scale on the inertial forces of the flow (the high Reynolds numbers required for turbulent flow imply that the inertial forces dominate the viscous forces). We adopt the same scaling as first proposed for hydrophone flow-induced self noise by McEachern (1993). Denoting the one-sided autospectrum of the force fluctuations by $G_F(f)$, the dimensionless form of the power spectral density function would be $G_F(f)/(U/D)(\rho U^2 A)^2$ which is expressed as a function of the Strouhal number $St = fD/U$. Here, ρ is the density of the liquid medium, A is the frontal area of the sphere (or cylinder, in the case of McEachern's results) exposed to flow, and St normalizes the frequency on the inertial time scale (D/U).

The spectra of Fig. 2 are presented in the dimensionless inertial force spectrum format in Fig. 4. The collapse of these

spectra to the narrow band indicated suggests that the mechanism of flow-induced lift in this Reynolds number and Strouhal number range is indeed the inertial forces created by the turbulent near wake along with the turbulent vortex sheet that exists downstream of the separated shear layer on the spherical surface.

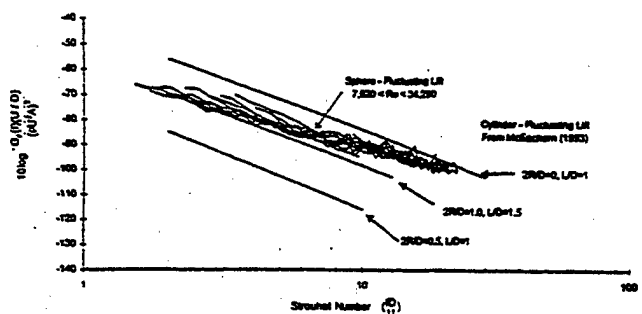


Figure 4. Autospectra of the fluctuating force normalized on the inertial force and time scales of the flow. Data are shown for the sphere ($7,620 < Re < 34,290$), and for a series of cylinders tested previously by McEachern (1993) ($4,000 < Re < 18,000$).

Of particular interest is the flow-induced forces on a sphere compared to those of a cylinder in cross flow. Shown on Fig. 4 are three straight lines representing the least mean-square fits of the normalized cylindrical sensor side force spectra (McEachern 1993) that were measured in a very quiet flooded quarry, and independently of the apparatus reported in this paper. The Reynolds number range for these experiments was 4,000 to 18,000, and the cylinder diameter was the same as that of the sphere used here (7.62 cm). The lower of the two spectra is for a cylinder having an aspect ratio of 1.0 and with rounded endcaps. The radius of the endcap corners is $R = 0.25D$, where D was 10.16 cm. This was the "quietest" cylinder geometry identified by McEachern. The middle trace of the three cylinder flow noise spectra was measured for a geometric configuration that most closely matches a sphere; the aspect ratio was 1.5 and the endcaps were hemispheres ($R = D/2$). The dimensionless force spectrum for this basically elongated sphere is seen to fall slightly below the current data due to a steeper spectral slope. The higher of the three cylinder flow noise spectra is for a right-circular cylinder in cross flow, i.e., the aspect ratio is 1.0, but there is no corner radius ($R = 0$). At the lower values of St , this cylindrical shape generates more fluctuating force than the sphere.

We realize that comparing non-dimensional force spectra measured on bluff bodies of different geometry may lead to misinterpretation because of changes in frontal area and perhaps even alterations in the characteristic length scale used to non-dimensionalize the frequency. We have cautiously performed this

comparison here because the frontal areas of all cylinders considered are practically identical to the frontal area of the sphere. The test velocities were nearly the same, and the cylinder and sphere diameters were identical. Current research deals with the development of rigorous theoretical models for these force spectra, and one of the issues to be addressed in this work is the validity of the chosen scaling parameters used here.

Dimensionless Form of the Flow Noise Spectra at Low Reynolds Numbers

It is stressed that the measurement of a fluctuating flow-induced force level independent of facility and environmental background noise at Reynolds numbers less than 2,000 was very difficult. However, a limited set of spectral data were acquired in the higher concentrations of glycerol that appear not to be background noise limited. They were found not, however, to depend on the inertial forces and time scales defined in the previous section. The variation of the low Reynolds number forces on flow velocity was very weak, approximately dependent on the first power of U . The spectral roll-off with increasing frequency was noted to be smaller also. We know that viscous forces are dominant at low Reynolds numbers and that they are determined by the product of the viscous shear stress and the surface area over which they act. The viscous stress is the product of the viscosity, μ and to the rate of change of speed with distance. Consider the distance involved here as D , and the area as D^2 . Then,

$$\text{Viscous Force} = \mu(U/D)D^2 = \mu UD \quad (1)$$

For shear layer flows, the viscous length scale is ν/u_τ , where u_τ is the shear velocity. It follows that,

$$\text{Viscous Time Scale} = (\nu/u_\tau)/u_\tau = \nu/u_\tau^2 \quad (2)$$

A suggested dimensionless form of the unsteady force spectrum measured under very low Reynolds number conditions is thus $G_f(f) \{U^2/\nu\}/(\mu UD)^2$ which is expressed as a function of $f\nu/U^2$. We note that the shear velocity is proportional to free-stream velocity, so we use U rather than u_τ .

Figure 5 shows the available force spectra measured at very low Reynolds numbers, non-dimensionalized according to the viscous force and time scales defined here. The straight lines that pass through the actual spectra are a least mean-square fit of the measured spectra at the particular glycerol concentration noted on the figure. It is interesting, if not perplexing, that we even measure an unsteady flow-induced force at these Reynolds numbers. Even though turbulence is absent, there can still be dynamic forces created because of unsteady laminar flow. The

collapse of the data of Fig. 5 is not as good as it is for higher Reynolds numbers (Fig. 4), but it is reasonable enough to suspect that some type of unsteady laminar flow instabilities indeed exist.

The scatter in the spectra of Fig. 5 is likely due to random intermittency of the flow, or even to non-stationarity. If experimental data measured at Reynolds numbers between 4,217 and 7,620 were included in either Fig. 4 or Fig. 5, the collapse would be very poor, see Jones (1996) for details. Thus there is an intermediate Reynolds number range where neither of the scaling relationships work very well. The experimental conditions of Fig. 5 are at a low enough Reynolds number, where the gross features of the flow field can be simulated using CFD methods as described in the next section.

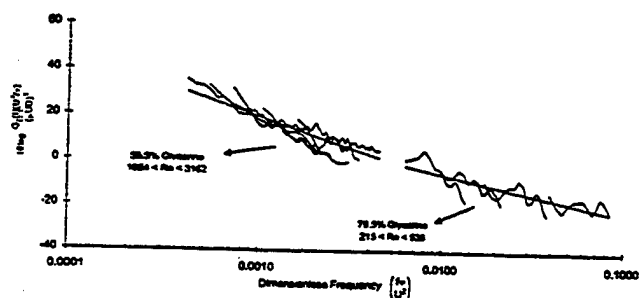


Figure 5. Autospectra of the fluctuating force measured on the sphere at low Reynolds numbers ($215 < Re < 3,162$). They are normalized on the viscous force and time scales of the flow.

NUMERICAL SIMULATIONS

Two calculations were carried out for this work; both involved flow about a sphere at conditions that were considered to be in the laminar flow regime. As such, no model of turbulent mixing was utilized in either of the calculations. Additionally, in both cases, the spheres were held rigidly in place and the flow field was permitted to develop from specified upstream far-field conditions. These two facts are important to keep in mind because the computer code that was utilized, and is described briefly below and in detail in the references, has both high (turbulent) Reynolds number capability as well as a feature for trajectory prediction of untethered bodies. Neither of these options were exercised here.

The computer code used for the numerical prediction of the flow field is called the Unsteady Computation of Field Equations (UNCLE). It has been under development over the last ten years or so, primarily at the Engineering Research Center at Mississippi State University. In this paper, the solution algorithm in UNCLE will not be discussed in detail. For a detailed description, see Zierke, et al. (1997).

The numerical solution begins with the governing

equations. For unsteady (and perhaps turbulent) flow in water about a moving body, the appropriate governing equations are the incompressible, Reynolds-averaged Navier-Stokes equations written in time-dependent, curvilinear coordinates, e.g., Taylor (1991). To facilitate numerical solution, the equations are cast in artificial compressibility form and the thin-layer approximation is made for the viscous terms.

The equations are discretized in space using standard cell-centered finite-volume differencing. The advective fluxes are handled with the approximate Riemann solver approach and higher-order accuracy is provided by a MUSCL-type formulation (Whitfield and Taylor, 1994). In both cases presented in this work, third-order upwind-biased differencing is used for these fluxes. The discrete equations are marched in time using the Discrete Newton Relaxation (DNR) approach of Vanden and Whitfield (1995). This is essentially a Newton-Raphson iteration where the Jacobian matrices are estimated by discrete differencing. The linear system that results at each Newton iteration is solved approximately by a series of symmetric block Gauss-Seidel iterations. In this work, both cases use one Newton iteration, with five symmetric Gauss-Seidel sweeps, per time step.

To facilitate the handling of complex geometries, or, as in this case, to minimize memory requirements, the code can be run on multiple block grids. Updates at block interfaces are handled explicitly. Both cases presented in this work utilized the same 8 block grid.

For completeness, though they are not exercised here, it should be mentioned that UNCLE has an algebraic eddy viscosity model for turbulent mixing based on the Baldwin and Lomax (1978) method, an unsteady multigrid capability for convergence acceleration (Sheng, et al., 1995), and a six-degree-of-freedom coupling for body trajectory prediction (Dreyer, et al., 1997).

Computational Results

Calculations were carried out for a sphere operating at Reynolds numbers of 1054 and 3162. The computational grid utilized for both sphere calculations possessed an O-O topology with singular lines at the poles (positive and negative z axes). The sphere diameter was taken to be 1.0 and the grid's outer surface was spherical with a diameter of 10. The grid was divided into 8 equal-sized blocks. The total number of grid points was 291,720. Wall-normal spacing at the sphere surface was 0.0025 diameters. Solution on this grid using UNCLE required approximately 115 Mbytes of RAM for Real*8 precision.

The time step for the calculation was chosen so that unsteady forces at a dimensional frequency of 196 Hz could be resolved (the experiments were for 1-100 Hz). This translated to a nondimensional time step of $\delta t = 0.01$. Each time step requires about 72 s of CPU time on an IBM RS6000 Model 3AT workstation.

Both calculations were carried out for a duration corresponding to a nondimensional time interval of $t=100$ units.

This corresponds physically to the time required for the sphere to travel 100 diameters. A complete calculation, beginning to end, requires approximately 200 CPU hours on the 3AT. It is noted that an examination of the L_2 norms of the Navier Stokes residuals in UNCLE indicated that the solutions are polluted by initial transients up until approximately $t = 30$. The unsteady force solutions are considered reliable only after this time.

The unsteady forces and moments acting on the sphere were calculated by simply integrating the wall pressure and wall shear stresses over the surface of the sphere at each time step following Jonnalagadda (1996). Figure 6 shows the time trace of the three principle force coefficients computed for $Re = 3162$. Here, F_x is the streamwise drag force normalized on the dynamic head of the flow and D^2 . Force coefficients F_y and F_z are for the side (lift) forces. The presence of the initial transients is clear in this figure for $t \leq 30$. It is also clear that the fluctuating drag force is substantially less than the fluctuating side forces. This is one reason the fluctuating drag was not considered in the experimental study.

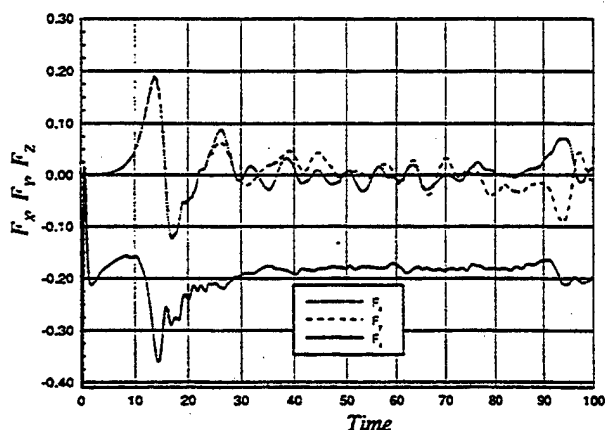


Figure 6. Computational results for the unsteady sphere forces in the x (streamwise), y and z (transverse) directions. Numerical transients exist for $t < 30$.

Figures 7 and 8 show the computed global flow field around the sphere at $Re = 3162$ and $t = 70$. Figure 7 indicates the relative magnitude of the static pressure at an instant of time near the sphere surface and in its wake. As expected the highest static pressure is at the forward stagnation point and the lowest is in the base region of the wake. Figure 8 shows a more detailed view of this pressure field along with vectors that indicate the direction and magnitude of the local velocity. As pointed out by Taneda (1977) and others, a vortex sheet separates from the sphere's surface and then rolls up to form a pair of streamwise vortices in the wake. This behavior is evident from the results of Fig. 8.

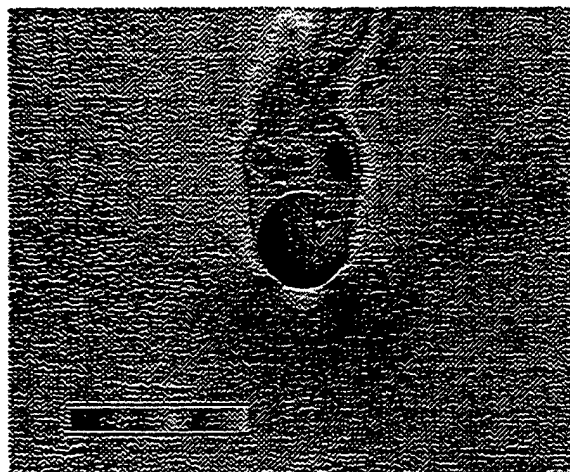


Figure 7. Instantaneous static pressure pattern for sphere at $t = 70$ and $Re = 3162$.

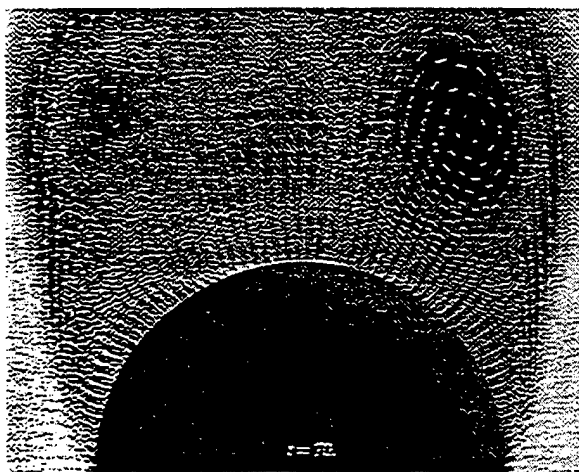


Figure 8. Same as Fig. 7, but with flow velocity vectors superimposed.

Frequency Domain Calculations

The time domain force data were processed further in the frequency domain. The initial, transient portions of the data were not used in the spectral computations. A Fast Fourier Transform (FFT) algorithm in MATLAB (Krauss, 1994) was used for the power spectrum estimations. At least a 1024-point FFT was needed to resolve the vortex shedding frequency at the Strouhal number of 0.2. A 2048-point FFT was thus used in this program. For consistency with the experimental results, the power spectrum estimations were normalized by the square of the FFT size, which is what is used by the HP analyzer of the experimental program (Hewlett Packard Co., 1993). We note that the MATLAB power spectral density function is normalized by only the FFT size.

The spectra generated from the F_y computational results are normalized using the viscous force and time scales of Eq. (1) and (2). This scaling has been chosen because the computational Reynolds numbers are low, and it is desired to compare the computations with experimental spectra measured at consistent values of these Reynolds numbers ($Re = 3165$ and 1055). Figure 9 shows the experimental results of Fig. 5 compared to the CFD results for these two Reynolds numbers. The spectral characteristics of the computations and the experiments are quite similar indicating that the measured high-frequency, low-Reynolds number fluctuating side force on the sphere is probably real. Direct and large-eddy simulations similar to these were performed by Tomboulides, et al. (1993) for $25 \leq Re \leq 1000$. At $Re = 1000$, their results compare favorably with what is presented here.

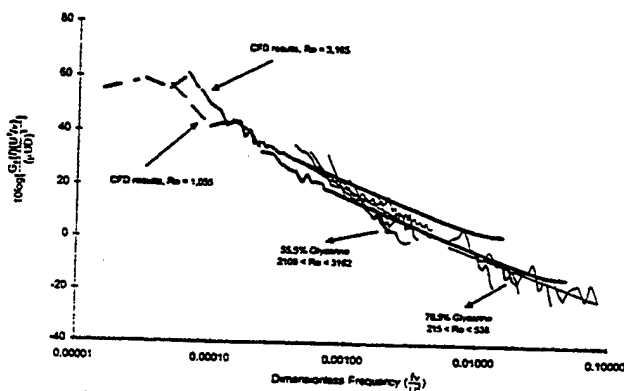


Figure 9. Same as Fig. 5, but with CFD predicted results superimposed for comparison.

CONCLUSIONS

An investigation of the flow-induced fluctuating lift force generated by a sphere in rectilinear motion has been described. A 7.62 cm diameter spherical sensor was tested in a specially designed low noise tow tank. Both pure water and various concentrations of glycerol were utilized in these experiments in order to cover a wide range of Reynolds numbers. Empirical scaling laws were suggested that permit the measured flow-induced fluctuating force frequency spectra to be collapsed to a reasonable single curve. Two different scaling regimes were identified depending on the Reynolds number range of the measurement.

Under high-Reynolds number conditions ($Re \geq 7,620$), the unsteady forces were found to scale on the inertial forces created by turbulent flow on and near the sphere. The frequencies scale on U/D under these conditions. At Reynolds numbers less than about 2,000 there appears to be a weak unsteadiness created by the sphere flow field, and the magnitude of the induced lift scales on μUD , a viscous force. The spectral frequencies in this

range scale on the viscous time scale, U^2/ν . The origin of these detected flow-induced forces was not quantified, but they are believed to be due to unsteady laminar flow. At Reynolds numbers between these two ranges, no reasonable scaling relation could be identified. A computational fluid dynamics simulation for this lower Reynolds number range was also performed. The unsteady lift spectra predicted in the simulation, when scaled like the experimental spectra, agree with the experimental results.

The high Reynolds number non-dimensional lift spectra measured for the sphere are similar to those measured in earlier investigations on a finite-length cylinder with various endcap geometries. The main difference between the two data sets is that the spectral levels roll off slightly faster for the cylinders as St increases. The right-circular cylinder in cross flow creates approximately 10 dB more spectral energy than does the sphere for $2 < St < 10$. An optimum cylinder endcap radius exists, and the side force spectral levels measured on a cylinder with this geometry are at least 20 dB lower than those of the sphere.

ACKNOWLEDGMENTS

The work reported here has been supported by the Naval Air Warfare Center, Aircraft Division, Patuxent River, MD and the Office of Naval Research, Code 321-SS.

REFERENCES

- Baldwin, B. S. and Lomax, H., 1978, "Thin-Layer Approximation and Algebraic Model for Separated Turbulent Flows," AIAA-78-257, Proceedings, 16th Aerospace Sciences Meeting, Huntsville, AL.
- Berliner, M. J. and Lindberg, J. F. eds., 1995, "Acoustic Particle Velocity Sensors: Design, Performance, and Applications," AIP Conference Proceedings 368, American Institute of Physics, Woodbury, NY, p. vii.
- Blake, W. K., 1986, "Mechanics of Flow-Induced Sound and Vibration," Vol. 1, Academic Press, Orlando, p.240.
- Dreyer, J. I., Taylor, L. K., Zierke, W. C., Davoudzadeh, F., 1997, "A First-Principle Approach to the Numerical Prediction of the Maneuvering Characteristics of Submerged Bodies," ASME Fluids Engineering Division Summer Meeting, Vancouver, British Columbia, Canada.
- Finger, R. A., Abbagnaro, L. A., and Bauer, B. B., 1979, "Measurement of Low-Velocity Flow Noise on Pressure and Pressure Gradient Hydrophones," Journal of the Acoustical Society of America, Vol. 65, pp. 1407-1412.
- Gabrielson, T. B., McEachern, J. F., and Lauchle, G. C., 1995a, "Underwater Acoustic Intensity Probe," United States Patent 5,392,258.
- Gabrielson, T. B., Gardner, D. L., and Garrett, S. L., 1995b, "A Simple Neutrally Buoyant Sensor for Direct Measurement of Particle Velocity and Intensity in Water," Journal of the Acoustical Society of America, Vol. 97, pp. 2227-2237.

Hewlett Packard Co., Englewood, CO, 1993, "HP 35665A Dynamic Signal Analyzer Operator's Reference," pp. 4-153 and 4-210.

Jonnalagadda, R., 1996, "Reynolds Averaged Navier-Stokes Computation of Forces and Moments for Appended SUBOFF Configurations at Incidence," M.S. Thesis, Mississippi State University, MS.

Jones, A. R., 1996, "Flow-Induced Self Noise on Spherical and Cylindrical Sensors," M.S. Thesis, Graduate Program in Acoustics, Pennsylvania State University, University Park, PA.

Keller, B. D., 1977, "Gradient Hydrophone Flow Noise," *Journal of the Acoustical Society of America*, Vol. 62, pp. 205-208.

Kim, H. J. and Durbin, P. A., 1988, "Observations of the Frequencies in a Sphere Wake and of Drag Increase by Acoustic Excitation," *Physics of Fluids*, Vol. 31, pp. 3260-3265.

Krauss, T. P., et al., 1994, "MATLAB, Signal Processing Toolbox User's Guide," The Math Works Inc., Natick, MA, pp. 1-63 - 1-71.

Kraichnan, R. H., 1956, "Pressure Fluctuations in Turbulent Flow Over a Flat Plate," *Journal of the Acoustical Society of America*, Vol. 28, pp. 378-390.

McEachern, J. F., 1980, "Experimental Development of a Compact Flow Shield," IEEE Publication 80CH 1578-4 AES, pp. 38-41.

McEachern, J. F., 1993, "The Effects of Body Geometry on the Flow Noise of Cylinders in Cross Flow," Ph. D. Dissertation, Graduate Program in Acoustics, Pennsylvania State University, University Park, PA.

McEachern, J. F. and Lauchle, G. C., 1995, "Flow-Induced Noise on a Bluff Body," *Journal of the Acoustical Society of America*, Vol. 97, pp. 947-953.

Möller, W., 1938, "Experimentelle untersuchung zur hydromechanik der kugel," *Phys. Zeitschrift*, Vol. 39, pp. 57-80.

Sakamoto, H. and Haniu, H., 1990, "A Study on Vortex Shedding from Spheres in Uniform Flow," *Transactions of the ASME Journal of Fluids Engineering*, Vol. 112, pp. 386-392.

Sheng, C., Taylor, L. K., and Whitfield, D. L., 1995, "A Multigrid Algorithm for Unsteady Incompressible Euler and Navier-Stokes Flow Computations," Sixth International Symposium on Computational Fluid Dynamics, Lake Tahoe, Nevada.

Taneda, S., 1977, "Visual Observations of the Flow Past a Sphere at Reynolds Numbers Between 10^4 and 10^6 ," *Journal of Fluid Mechanics*, Vol. 85, pp. 187-192.

Taylor, L. K., 1991, "Unsteady Three-Dimensional Incompressible Algorithm Based on Artificial Compressibility," Ph.D. Dissertation, Mississippi State University, MS.

Tomboulides, A. G., Orszag, S. A., and Karniadakis, 1993, "Direct and Large-Eddy Simulation of Axisymmetric Wakes," AIAA-93-0546, Proceedings, 31st Aerospace Sciences Meeting and Exhibit, Reno, NV.

Vanden, K. J. and Whitfield, D. L., 1995, "Direct and Iterative Algorithms for the Three-Dimensional Euler Equations," *American Institute of Aeronautics and Astronautics Journal*, Vol. 33, pp. 851-858.

Whitfield, D. L. and Taylor, L. K., 1994, "Numerical Solution of the Two-Dimensional Time-Dependent Incompressible Euler Equations," MSSU-EIRS-ERC-93-14, Mississippi State University, MS.

Zierke, W. C., ed., 1997, "A Physics-Based Means of Computing the Flow Around a Maneuvering Underwater Vehicle," Applied Research Laboratory, Penn State University Technical Report TR 97-002.

APPENDIX 42

Outer-flow effects on turbulent boundary layer wall pressure fluctuations

Timothy A. Brungart, Gerald C. Lauchle,^{a)} Steven Deutsch, and Eric T. Riggs
*Applied Research Laboratory, The Pennsylvania State University, P.O. Box 30, State College,
Pennsylvania 16804-0030*

(Received 12 November 1997; revised 4 November 1998; accepted 16 January 1999)

The outer-flow contribution to the pressure fluctuations occurring at the wall beneath a turbulent boundary layer was studied experimentally. A moving wall wind-tunnel facility was developed for the work. A flat test plate was suspended at various heights over the movable tunnel wall such that interacting and noninteracting turbulent boundary layers were developed in the resultant channel. Mean and fluctuating velocity components were measured for cases with and without wall motion. Pressure fluctuations were measured, with pinhole microphones on the surface of the test plate forming the upper-channel boundary, at corresponding test conditions. The data show that the wall-pressure fluctuations are relatively insensitive to the details of the outer flow, even over the range of frequencies dominated by outer-flow turbulence structures. © 1999 Acoustical Society of America. [S0001-4966(99)02904-5]

PACS numbers: 43.28.Ra, 43.30.Nb, 43.50.Nm [LCS]

INTRODUCTION

Wall-pressure fluctuations induced by turbulent flow have been studied extensively over the past four decades both theoretically¹⁻⁶ and experimentally.⁷⁻¹² Theoretical work has focused on understanding how turbulent velocity fluctuations induce wall-pressure fluctuations. Experimental efforts have focused on obtaining spectral measurements of the wall-pressure field free from background noise and transducer spatial resolution limitations. The work has been motivated by the need to reduce noise levels in engineering applications ranging from sonar systems to automobiles to aircraft.

In spite of the vast quantity of work performed to date, significant issues still remain. Keith *et al.*¹³ note that for the data sets they examined, pipe flow wall-pressure spectra, $G_T(\omega)$, exhibit lower levels than comparable external flows when scaled on outer-flow variables: $[G_T(\omega)/\rho^2 \delta^* U_e^3]$ vs $(\omega \delta^*/U_e)$. Here, ρ is the fluid density, δ^* is the boundary layer displacement thickness, and U_e is the free-stream velocity. They support this observation with speculation that spectra measured in a developing flow should exhibit some of the characteristics of both internal and external flows. Here, internal refers to those flows that are completely dominated by viscous effects such as fully developed pipe and channel flows. External refers to boundary layer flows where viscous effects are confined to a region very near a bounding surface. Studies of developing channel flow^{13,14} show that, over the range $0.1 < \omega \delta^*/U_e < 0.3$, as the flow develops, the spectra decrease from the levels of the external flows to the levels of the internal pipe flows. Others^{11,13} point out that the physical features of the outer flow for the internal and external flow cases are distinctly different and that these differences may account for the differences observed in the wall-pressure fluctuations. Measurements of the wall-pressure

fluctuations on the fuselage of a sailplane,¹⁵ and in a wind tunnel,¹⁶ indicate the spectral levels to be well correlated with velocity fluctuations at a distance of 2.6δ above the wall, where δ is the boundary layer thickness. These velocity fluctuations result from the large-scale irrotational motion above the boundary layer and are absent in internal flows.

In order to provide additional insight into the contribution of the outer flow to the wall-pressure fluctuations, experiments were conducted where the outer flow of an equilibrium turbulent boundary layer was systematically modified and the effects on the wall-pressure fluctuation statistics were examined. An equilibrium boundary layer was developed in a channel. It was modified by (1) varying the height of the upper channel wall, and (2) moving the lower boundary at the same speed and direction as that of the mean flow.

I. EXPERIMENTAL APPARATUS AND MEASUREMENT TECHNIQUES

A. Moving wall wind tunnel

A moving wall wind-tunnel facility¹⁷ was used for this investigation, and is shown schematically in Fig. 1. A muffler is soft coupled to the blower inlet and the outlet air passes through a rubber bellows to an acoustically treated labyrinth inside the blower box. The flow is diffused in the wind tunnel over a distance of 0.819 m to a square settling section measuring 1.473 m on a side. The diffuser consists of four screened sections increasing monotonically in area with streamwise distance. The settling section cross-sectional area is constant, has a length of 0.619 m, and is lined with seven fine screens designed to reduce both free-stream velocity nonuniformities and turbulence levels. Downstream from the settling section is a 64:1, 1.16-m long contraction nozzle which discharges into a 0.294-m diameter, semicylindrical test section.

The moving wall wind tunnel was placed inside the

^{a)}Also with the Graduate Program in Acoustics.

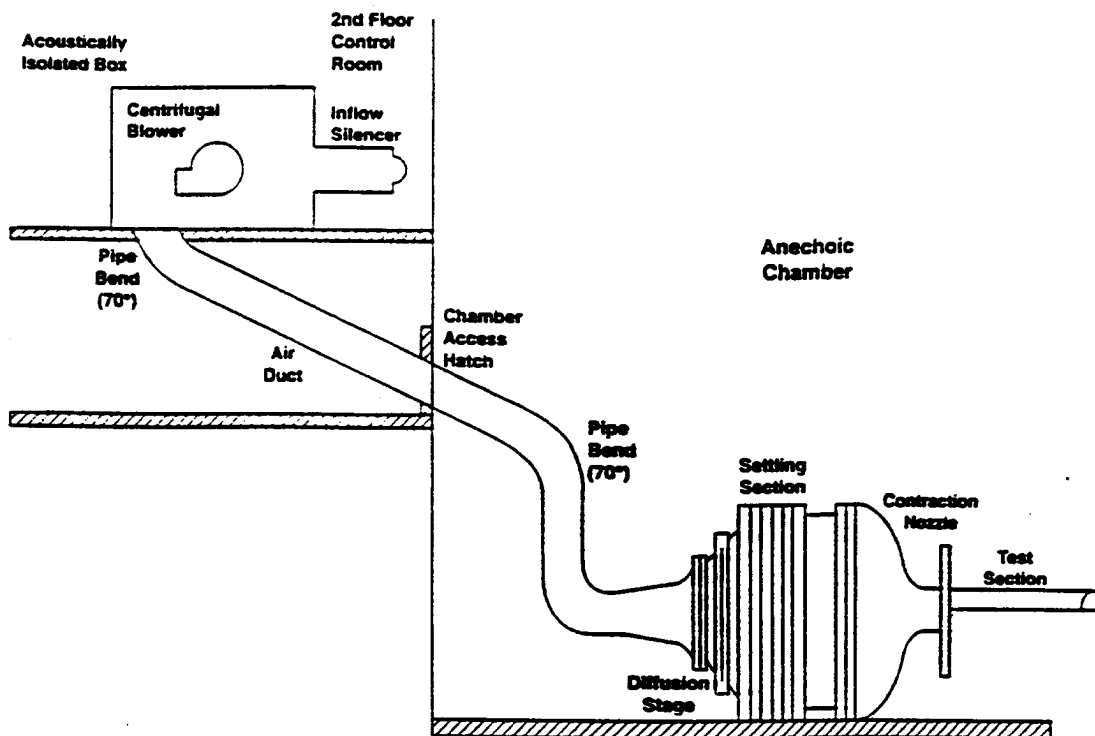


FIG. 1. Schematic of the moving-wall wind-tunnel facility.

ARL Penn State flow-through anechoic chamber^{18,19} in order to isolate the tunnel from airborne noise. This chamber meets the requirements of both ISO 3745 and IEC 268 from 90 Hz to 12.5 kHz. Sound-pressure measurements can be made to ISO tolerances within 1.0 to 4.0 m of a source at frequencies as low as 70 Hz. The moving air generated by the wind tunnel passes through a permeable wall of the chamber with no measurable (above ambient) noise.

The moving wall wind-tunnel test section is shown schematically in Fig. 2. Slots are cut into the Plexiglas dome to

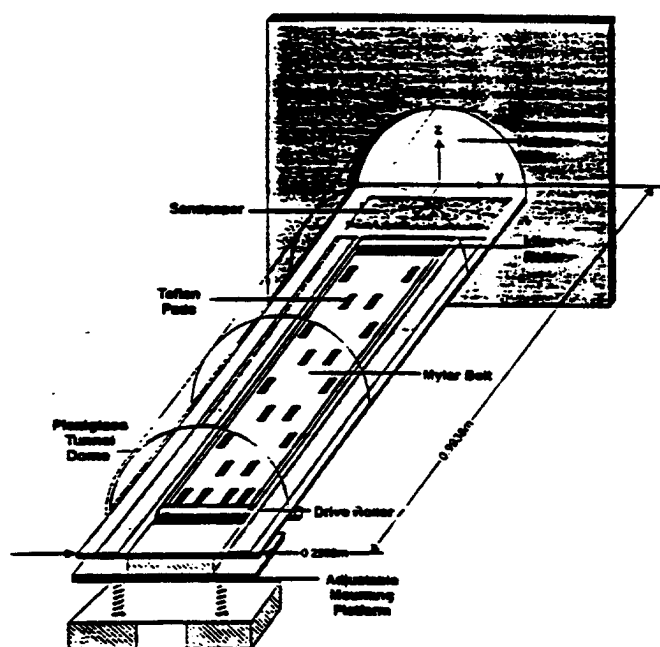


FIG. 2. Schematic of the moving-wall wind-tunnel test section.

permit measurement probe access inside the test section. The moving-wall assembly is vibration isolated from the test section. The moving wall is powered by an electric motor that is located in an acoustically isolated enclosure placed adjacent to the wind-tunnel test section. The motor drives the moving wall at a maximum speed of 18.3 m/s. The wall is a 0.019-cm thick Mylar belt which slides over Teflon pads. The drive roller is connected to the motor shaft with a flexible coupling. A fully developed turbulent boundary layer profile is generated only a few centimeters downstream from the entrance to the test section by lining the joint section with 36-grit sandpaper. This surface roughness trips the laminar boundary layer to a turbulent one.

The flat test plate is shown in Fig. 3. It is designed to span and fit tightly against the moving-wall test section at three heights above the moving surface. The leading edge was designed²⁰ to be resistant to flow separation due to small flow misalignments. The plate leading edge is positioned at the same axial location as the exit of the wind-tunnel contraction nozzle. Its leading edge is roughened with sandpaper to trip the boundary layer from laminar to turbulent.

Microphone measurement cavities are milled into the test plate in which small-diameter pinholes are used to connect the microphone cavity to the flow surface. This procedure helps to minimize spatial averaging effects on the plate turbulent boundary layer wall-pressure fluctuation measurements. The microphone is placed inside the cavity with its protective grid attached. The Helmholtz resonance frequency is estimated²¹ to be 5.6 kHz. Figure 4 shows the pinhole microphone response to white-noise excitation in a plane wave tube. A peak in the response occurs near the predicted resonance frequency. The other peaks are acoustic resonances of the tube.

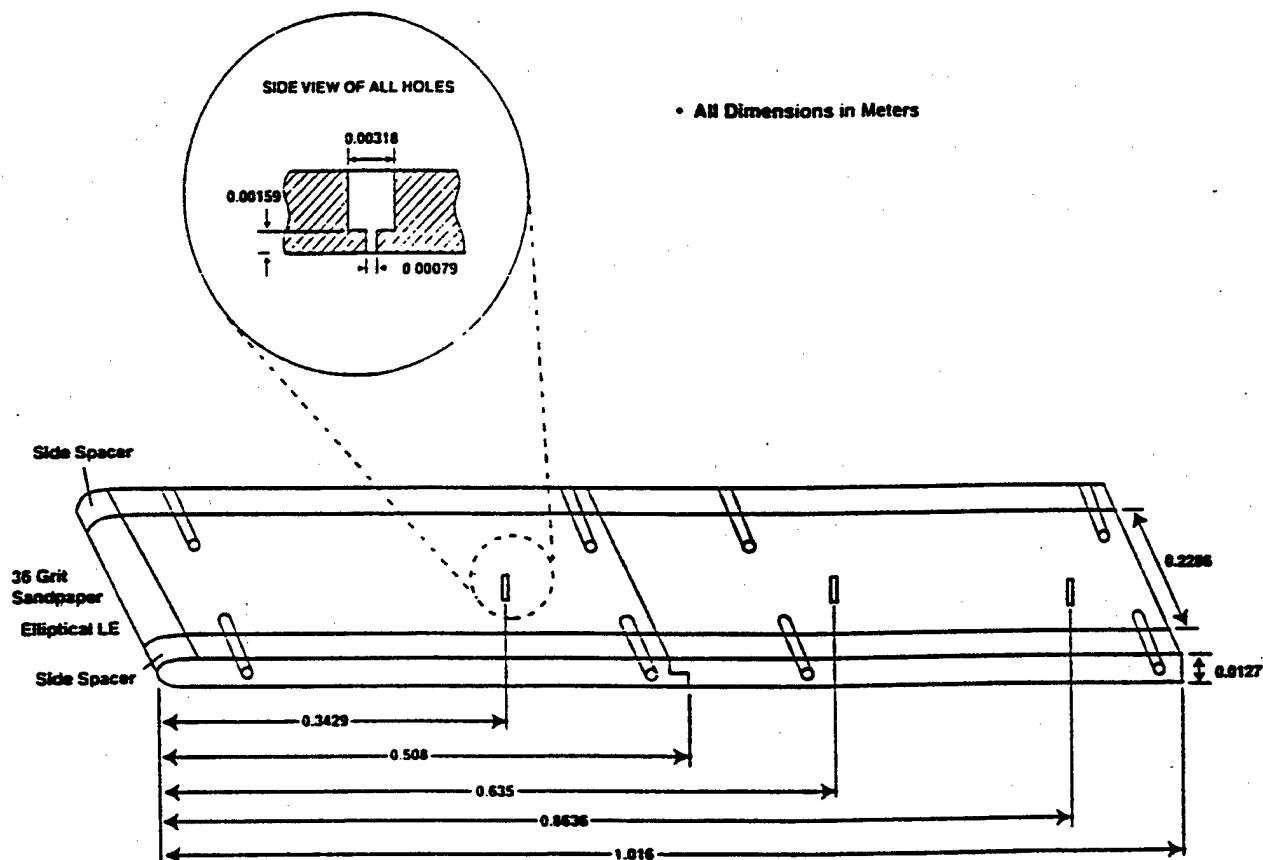


FIG. 3. Schematic of the test plate with pertinent dimensions.

B. Velocity measurements

For steady-state velocity measurements outside of the boundary layer, Pitot-static probes are used. For boundary layer velocity measurements, a flattened total head probe is used. A differential pressure transducer is used in conjunction with an integrating voltmeter to measure the pressures. The maximum uncertainty in the velocity measurements is estimated as $\pm 0.94\%$, $\pm 0.46\%$, and $\pm 0.24\%$ at flow speeds of 10.7, 15.3, and 21.4 m/s respectively.

A two-channel, TSI IFA 300 anemometer is used for measuring both mean and fluctuating velocities. Velocity statistics are calculated with TSI's THERMALPRO software. The hot-wire probes are aligned with the flow field and positioned with a traversing apparatus. A single-component TSI

model 1218E standard probe and a TSI model 1241 end flow "X" probe are used. Hot-wire data are sampled at a frequency of 10 kHz with a low-pass antialiasing filter set at 5 kHz. Data are acquired for a period of 6.55 s providing 64 000 points at each measurement location. A typical outflow time scale is approximately 0.0013 s, so data are acquired over a period of 5000 time scales. A hot-wire overheat ratio of approximately 1.7 is used. The single-wire probes are calibrated *in situ* over a range of velocities while the X-wire probes are calibrated over a range of velocities and yaw angles in a special probe-calibration facility. Sensor yaw corrections are applied to the X-wire probes following the analysis of Lekakis *et al.*²² The velocity calibrations are repeated prior to every measurement.

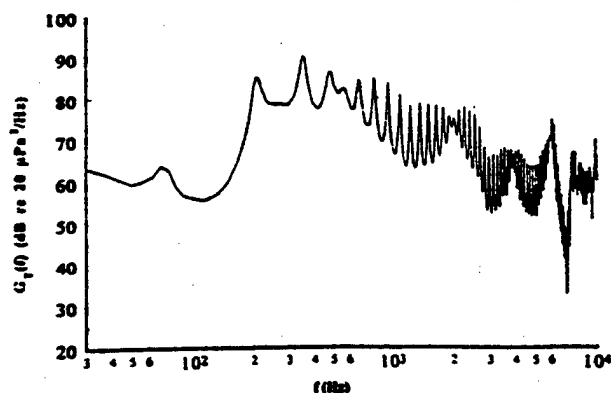


FIG. 4. Pinhole microphone response to white-noise excitation in a plane wave tube.

C. Wall-pressure fluctuation measurements

The turbulent boundary layer wall-pressure fluctuations are measured with a Brüel and Kjaer (B&K) model 4138, 0.318-cm diameter condenser microphone placed in the seating hole of interest with a connecting preamplifier supported from above through the tunnel dome. The microphone signals are high-pass filtered above 20 Hz, amplified 10 to 20 dB, and processed with an FFT analyzer. Microphone calibrations were performed at the beginning of every test.

The turbulent boundary layer wall-pressure fluctuation signals are low-pass filtered at 10 kHz and sampled at 25.6 kHz with a record length of 4096 points. This provides an effective spectral bin width of 6.25 Hz. Typically, 512 and 256 averages are taken for each stationary and moving wall

condition, respectively, and a Hanning window function is used for all measurements. The normalized random error for a measured autospectrum, $\hat{G}_T(f)$, is given by²³ $\varepsilon_r[\hat{G}_T(f)] = (1/\sqrt{n_d})$ where n_d is the number of spectral averages. This gives values of 0.044 and 0.063 for 512 and 256 averages and corresponds to spectral estimates, with 95%-confidence intervals, of $\pm 8.8\%$ and $\pm 12.5\%$, respectively. Because the analysis bandwidth was not changed during the experiments, there are no bias errors.

II. RESULTS

A. Noninteracting boundary layers

This section presents the results of the flat plate flow and wall-pressure field evaluation where the plate and moving wall were separated by 5.40 cm, which is 2.4 plate boundary layer thicknesses based on measurements at $X=0.883$ m and a 15.3 m/s test velocity. This distance was sufficient to prevent the plate and Mylar belt shear layers from coalescing over the length of the moving-wall test section. The potential core of the exit wall jet is separated by the plate and Mylar belt shear layers throughout most of the test section length; thus, this flow will be referred to as external.

The streamwise variation in the free-stream velocity between the stationary belt forming the bottom test section wall and the flat plate at a reference speed of 16.9 m/s was found to be less than $\pm 1\%$. Operating the belt at the free-stream velocity tends to increase the free-stream velocity by approximately 1% at all measurement locations.

1. Wall boundary layers

The mean-velocity profiles on upper and lower walls were measured over the center 25% span with the belt held stationary, and found to be similar in the spanwise direction at all axial locations. All data shown were taken upstream from where three-dimensional corner disturbances contaminate the 2-D flowfield. Purtell *et al.*²⁴ state that examination of the boundary layer wake region is important not only to describe the boundary layer, but also in determining the state of development of the flow. All wall boundary layer mean-velocity profiles, measured at numerous streamwise (i.e., X) locations and free-stream speeds, were found to collapse on outer-flow variables (i.e., Z/δ^* vs U/U_e). The collapse of the data indicates that the boundary layer is fully developed at these conditions. See Brungart¹⁷ for additional details.

The friction velocity, u_* , and pressure-gradient parameter, Π , are determined by a least-squared error fit of the boundary layer velocity data to the law-of-the-wall and Coles²⁵ wake function. A typical measured and predicted test plate boundary layer velocity profile, expressed in inner-flow variables (i.e., U/u_* vs Zu_*/ν) is shown in Fig. 5. These results agree well and are typical of those obtained with the Mylar wall boundary layer as well. The measured Π value of 0.58 is consistent with the range of 0.5 to 0.6 identified by Coles²⁵ for a zero-pressure gradient flow. The data show further that, at the measurement location farthest downstream, $X=0.883$ m, the opposing boundary layers are still separated by 1.27 cm at a free-stream speed of 15.2 m/s.

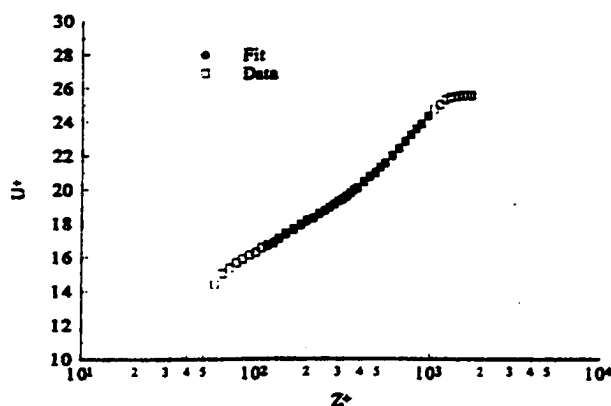


FIG. 5. Typical flat test plate boundary layer velocity profile expressed in inner-flow variables, wall stationary, $X=0.883$ m, $U_e=24.6$ m/s, $u_* = 0.96$ m/s, $\Pi=0.58$.

Typical streamwise (i.e., u') and wall-normal (i.e., v') turbulent rms velocity fluctuation profiles for the two opposing walls, scaled on outer-flow variables, are shown in Fig. 6, and found to be in good agreement with data from Klebanoff.²⁶ The boundary layer displacement thickness, δ^* , used for nondimensionalization, is determined from integration of the measured mean-velocity profiles. The deviations above $Z/\delta^*=9$ are due to interaction effects with the Mylar wall boundary layer. The current turbulence stress data (not shown) are in good agreement with Klebanoff's²⁶ reported profile at values of Z/δ greater than 0.3. At values of Z/δ less than 0.3, the current data drop below Klebanoff's data and decrease as the wall is approached. This can be attributed to X-wire probe resolution limitations in the current experiments. The length scales in Klebanoff's flow were much larger than in the current experiments and probe resolution problems were not as severe.

Figure 7 compares the mean-velocity profile in the channel with and without wall motion. Positive Z is towards the moving wall. For the cases reported here, the wall is moving at a speed equal to the free-stream speed. Figure 7 shows that the boundary layer mean-velocity profile over the test plate is unmodified by the motion of the belt; however, the Mylar wall boundary layer mean-velocity profile becomes fuller with wall motion. The effect of wall motion on the streamwise turbulent rms velocity fluctuation component is shown

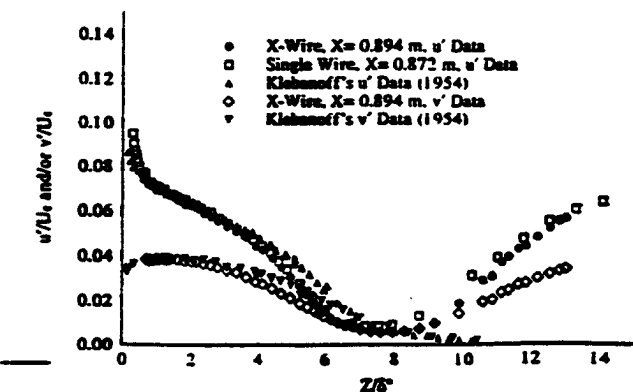


FIG. 6. Flat test plate boundary layer streamwise and wall-normal turbulence component rms velocity fluctuation profiles scaled with outer-flow variables and compared with data from Klebanoff (Ref. 26), $h_{ch}=5.40$ cm.

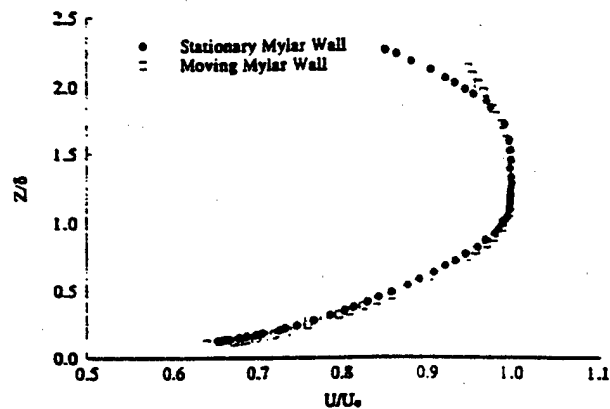


FIG. 7. Effect of wall motion on the flat test plate boundary layer velocity profile. $X=0.894$ m. $U_e=15.4$ m/s. $h_{ch}=5.40$ cm.

in Fig. 8. The data show that the only effect of the wall motion is to suppress the velocity fluctuations in the Mylar belt boundary layer. Similar results¹⁷ were obtained for the v' and Reynolds stress profiles, $\rho u'v'$. In this case of non-interacting boundary layers, wall motion reduces the magnitude of the production term in the turbulence kinetic energy budget, thereby suppressing the turbulent velocity fluctuations in the moving-wall layer only.

2. Wall-pressure fluctuations

Typical spectra of the plate turbulent boundary layer wall-pressure fluctuations are shown in Fig. 9. The spectra were measured at $X=0.864$ m ($X/\delta=42.1$ at 10.6 m/s) at a number of free-stream speeds. The narrow bands of higher energy in the spectra at approximately 175 Hz at 13.8 m/s and 225 Hz at 17.1 m/s are aerodynamic noise associated with the test plate and are not present in an empty tunnel. Finite coherence values between two pinhole microphones separated by 0.229 m in the test plate confirmed the acoustic nature of this narrow-band energy. With this microphone separation, the turbulent boundary layer wall-pressure fluctuations are incoherent while acoustical signals are coherent within an acoustic wavelength.

The distinct "breakpoint" in the two highest speed spectra at approximately 6 to 7 kHz in Fig. 9, although

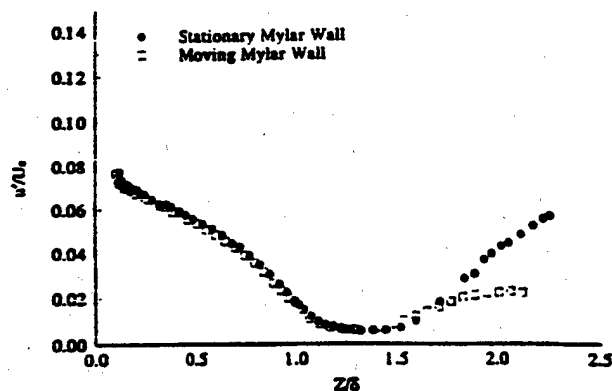


FIG. 8. Effect of wall motion on the flat test plate boundary layer stream-wise turbulence component rms velocity fluctuation profile. $X=0.894$ m. $U_e=15.4$ m/s. $h_{ch}=5.40$ cm.

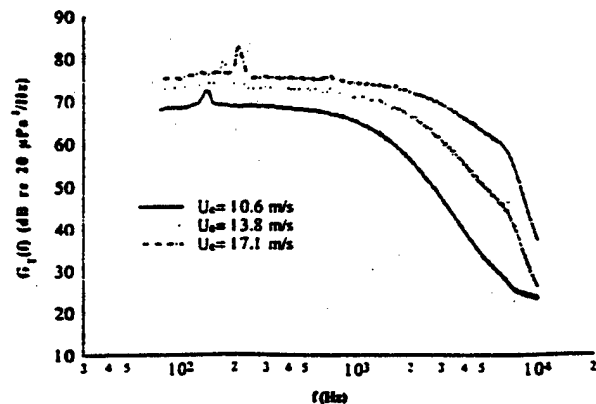


FIG. 9. Typical flat test plate boundary layer pressure fluctuation spectra. wall stationary, $X=0.864$ m. $h_{ch}=5.40$ cm.

higher than the 5.6 kHz determined from the acoustic data of Fig. 4, are due to the Helmholtz resonance excitation of the pinhole cavity/microphone system. Panton and Miller²⁷ studied excitation of flush-mounted Helmholtz resonators by turbulent boundary layer flow. They found that the boundary layer-induced Helmholtz frequency was, in general, slightly different from that produced by acoustic excitation because of the interaction of the turbulence with the acoustical (i.e., lumped air mass) motion in the orifice.

The steep, higher-frequency drop-off in the two higher-speed spectra in Fig. 9 is likely due to: (1) the Helmholtz resonance of the microphone/cavity system, and (2) spatial averaging of the wall-pressure fluctuations. In order to obtain a true point measurement of the turbulent boundary layer wall-pressure fluctuations, free from the effects of spatial averaging, the transducer diameter, $d_{transducer}$, must be of the same size or smaller than the smallest-length scale which characterizes the flow. The smallest-length scales present in a boundary layer, which give rise to measurable high-frequency pressure fluctuations, occur near the wall where the dynamics of the flow are influenced significantly by the effects of viscosity. A characteristic velocity fluctuation in this region is given by the friction velocity, u_τ , and the viscous length scale²⁸ is ν/u_τ , where ν is the kinematic viscosity. Therefore, $d^+ = (d_{transducer} u_\tau / \nu)$ must be $O(1)$ in order to resolve the high-frequency turbulent boundary layer wall-pressure fluctuations free from the effects of spatial averaging. Values of d^+ for the current measurements, at the location farthest downstream, range from 23.6 at 10.6 m/s to 45.1 at 13.8 m/s. The effect of spatial averaging is to reduce the microphone's sensitivity to high-wave number and high-frequency turbulence structures. According to analysis, based on the methods of Corcos,²⁹ the 10.6, 13.8, and 17.1 m/s spectra of Fig. 9 are attenuated by 3 dB at frequencies of 2830, 3600, and 4600 Hz, respectively, due to the effects of spatial averaging.

The moving wall introduces additional, unwanted tonal noise into the wind tunnel at frequencies below approximately 3 kHz. Comparison of pressure spectra measured with the wall moving and with and without air flow showed that a reasonable broadband signal-to-noise ratio exists in this frequency range. These comparisons also showed that at frequencies above approximately 3 kHz, the broadband noise

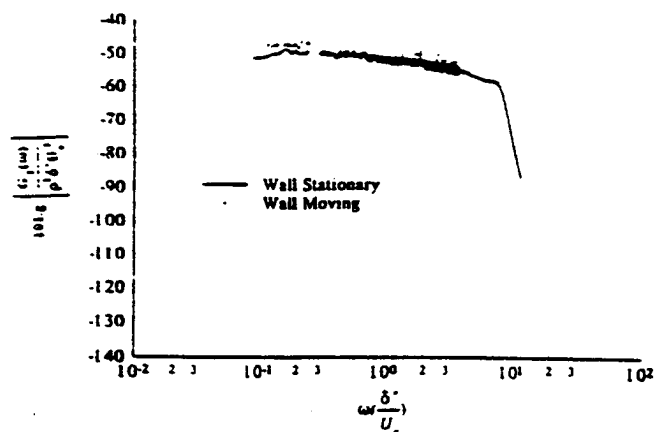


FIG. 10. Effect of wall motion on the flat test plate boundary layer pressure fluctuation spectrum. $X=0.864$ m. $U_c=18.3$ m/s. $h_{ch}=5.40$ cm.

associated with the belt sliding over the Teflon pads dominates the turbulent boundary layer wall-pressure fluctuation signal. Coherence measurements between the signals from the pinhole microphone and a frame-mounted accelerometer showed conclusively that the tones present in the spectrum of turbulent boundary layer wall-pressure fluctuations, when the belt is running, are a result of the vibration of the moving-wall apparatus.

A procedure¹⁷ for removing the vibration-induced tonal signal from the wall-pressure fluctuation signal utilizes the measured coherence between the signal from the microphone and the signal from the accelerometer mounted on the frame of the moving-wall apparatus. Frequency ranges of high coherence ($\gamma^2 \geq 0.1$) were basically edited out of the pinhole microphone spectral data.

The effect of adjacent wall motion on the measured fixed-wall turbulent boundary layer wall-pressure fluctuations is shown in Fig. 10. These data, scaled on outer-flow variables, indicate that the wall motion has little if any effect on the measured wall-pressure fluctuations at this value of $h_{ch}/\delta=2.75$, where h_{ch} denotes the channel height.

B. Developing flow results

This section presents the results of the flat plate flow and dynamic wall-pressure field evaluation for cases with and without wall motion where the test plate and Mylar wall boundary layers are interacting. The degree of the interaction is dependent on the axial location of interest and the distance separating the test plate from the Mylar wall. The plate/wall separation was reduced from $h_{ch}/\delta=2.6$ used in Sec. A to $h_{ch}/\delta=1.5$ and 0.7 for the current situation.

1. Boundary layer evaluation

The streamwise variation in the maximum core velocity measured between the stationary belt forming the bottom test-section wall and the plate mounted above it was evaluated by Pitot-static probe measurements. The measurements show that the flow decelerates somewhat through the channel. This effect is due, of course, to the coalescence of the opposing shear layers.

Test plate boundary layer mean-velocity profiles measured at $X=0.318$ m, for $10.8 \text{ m/s} \leq U_c \leq 18.3 \text{ m/s}$, and for

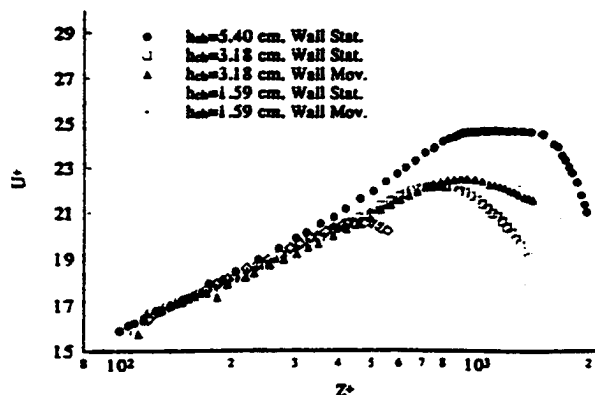


FIG. 11. Flat test plate boundary layer velocity profiles plotted in inner-flow variables for three channel heights. $X=0.894$ m. $U_{cmax}=15.4$ m/s.

the values of h_{ch}/δ noted above, were found to collapse well when normalized with outer-flow variables. This indicates that the boundary layer is fully developed. The impending downstream convergence of the shear layers was evident from the small spatial extent of uniform flow for the channel height of 1.5δ . The shear layers coalesce at $X=0.318$ m when $h_{ch}/\delta=0.7$. When normalized on inner-flow variables, the developing flow boundary layer mean-velocity profiles at this location are in excellent agreement with the logarithmic law-of-the-wall and Coles'²⁵ wake function. The measurements show that for $h_{ch}=2.6 \delta$ and 1.5δ , the turbulent boundary layers are identical, fully developed, zero-pressure gradient, and under equilibrium conditions. The narrowest channel boundary layer, however, appears to be thinner and exhibits increased turbulence intensities relative to the larger plate/wall separations. This suggests that the interaction between the plate and Mylar wall shear layers has begun to modify the boundary layer flow upstream of the measurement location.

External and developing mean flow-velocity profiles measured farther downstream for both stationary and moving-wall conditions are shown in Fig. 11. The profiles are normalized with the test plate inner-flow variables and collapse well for $Z^+ < 200$. For $Z^+ > 200$, the values of U^+ for the largest channel height are greater than those of the developing flow cases. This indicates the formation of a well-defined outer flow.²⁵ The data for the narrower plate/wall separations follow the logarithmic law-of-the-wall (i.e., $\Pi=0$) up to values of Z^+ near the channel centerline where the velocity reaches its maximum. This behavior is consistent with that of a fully developed turbulent channel flow as well as pipe-flow data.³⁰

The rms value of the u' turbulence component, normalized by the local mean-flow velocity, U_{local} , is shown in Fig. 12. The wall-normal turbulence component and the turbulence stress profiles follow similar trends. The indicated behavior suggests that h_{ch} is not an appropriate scaling parameter for the external flow case. This makes physical sense because the plate boundary layer is unaffected by the presence of the Mylar wall spaced at $h_{ch}=2.6 \delta$.

Figure 13 shows that the rms values of the u' turbulence levels normalized by U_{cmax} and expressed as a function of

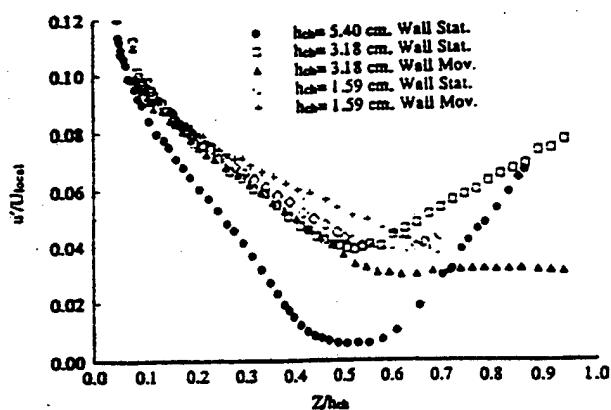


FIG. 12. Flat test plate boundary layer streamwise turbulence component rms velocity fluctuation profiles normalized with the local mean velocity and channel height, $X=0.894$ m, $U_{el,max}=15.4$ m/s.

Z/δ result in a slightly better collapse of the data than the normalization of Fig. 12. Here, $U_{el,max}$ is the maximum mean velocity measured in the channel. The wall-normal turbulence component and the Reynolds stress data behave in a like manner. The plate external boundary layer can be viewed as having been modified by the presence of the Mylar wall boundary layer at values of Z greater than 0.7δ . Identical outer-flow length scales characterize the plate boundary layer for $Z < 0.7\delta$ in both the wider channels but not the narrow channel. This is reasonable, since the interaction between the plate and Mylar wall shear layers must be strongest for the narrow channel where the flow is most fully developed as a channel flow. The outer-flow length scale associated with the narrow channel must be smaller than that associated with the larger channels.

Figures 12 and 13 show that the rms turbulence fluctuations near the test plate ($Z \sim 0$) scale differently, depending on the channel width. This behavior indicates two flow types: one exhibiting the characteristics of an external turbulent boundary layer, and the other, a turbulent channel flow. The data for $h_{ch}/\delta = 1.4$ exhibits characteristics of each.

The effect of wall motion on the mean velocity is dependent on h_{ch} . For $h_{ch}/\delta = 1.4$, moving the wall at the free-

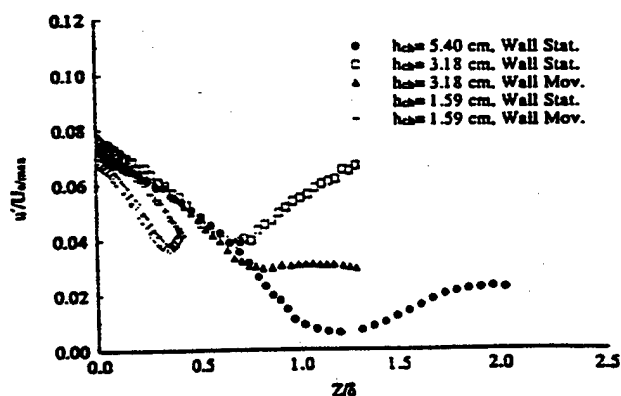


FIG. 13. Flat test plate boundary layer streamwise turbulence component rms velocity fluctuations normalized with the channel maximum velocity and expressed as a function of height above the surface, $X=0.894$ m, $U_{el,max}=15.4$ m/s.

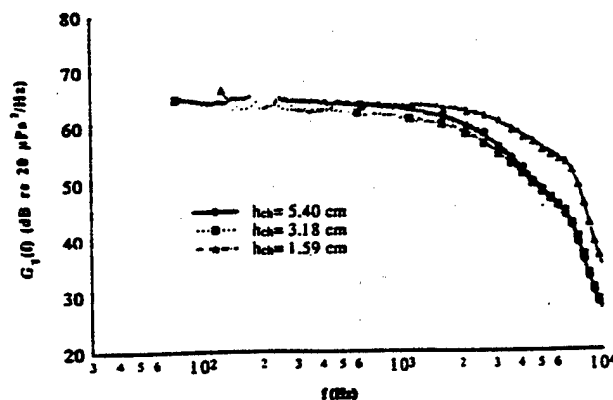


FIG. 14. Comparison of flat test plate boundary layer wall-pressure fluctuation spectra for three channel heights, wall stationary, $X=0.864$ m, $U_{el,max}=15.3$ m/s.

stream speed increases U_b , the semichannel bulk or average velocity, approximately 2%. For the case of $h_{ch}/\delta = 0.7$, U_b is increased 8%. The data show that the percent increase in u_r due to wall motion is identical to the corresponding increase in U_b . For $h_{ch}/\delta = 1.4$, the effect of wall motion is limited to $Z/h_{ch} > 0.5$. Here, $u'/U_{el,max}$ and $v'/U_{el,max}$ are reduced by more than a factor of two (2) to near-constant values of 0.03 and 0.02, respectively. Similar trends are noted for the Reynolds stresses. The situation for $h_{ch}/\delta = 0.7$ is somewhat different because the changes occur closer to the wall.¹⁷

2. Wall-pressure fluctuations

Wall-pressure fluctuation power spectra measured under stationary wall conditions are shown in Fig. 14 for the three plate/wall separations examined. The large and intermediate channel-separation spectra are almost identical. The plate-pressure fluctuations measured in the narrow channel situation exhibit increased high-frequency energy relative to the other separations. At low frequencies (up to 1200 Hz), the spectral levels of all separations considered are within 1 dB of each other.

Figure 15 compares wall-pressure fluctuation power spectra measured with and without wall motion for $h_{ch}/\delta = 1.4$. Clearly, wall motion has no significant effect on the stationary wall-point pressure spectrum. Figure 16 shows the

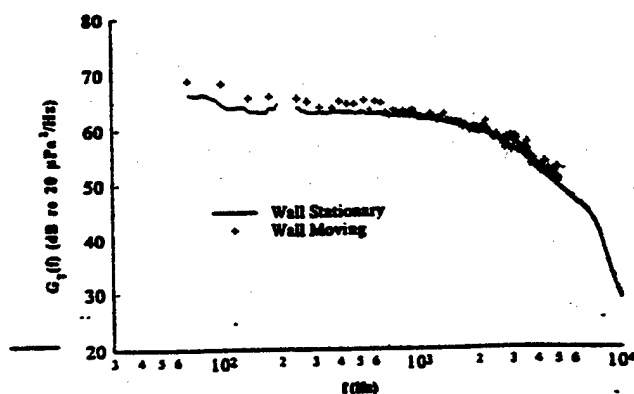


FIG. 15. Effect of wall motion on flat test plate boundary layer wall-pressure fluctuation spectra, $X=0.864$ m, $U_{el,max}=15.9$ m/s, $h_{ch}=3.18$ cm.

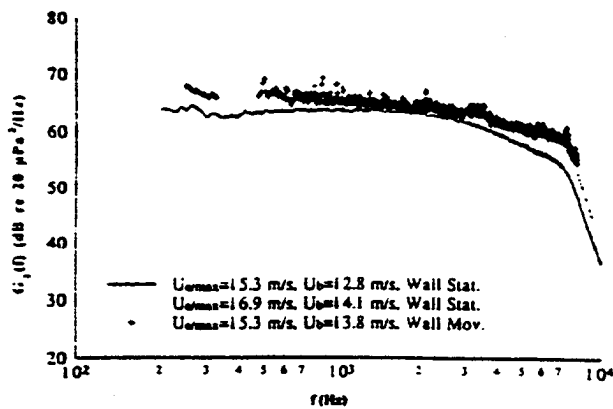


FIG. 16. Effect of wall motion on flat test plate boundary layer wall-pressure fluctuation spectra: comparison of spectra measured with approximately equivalent bulk velocity values. $X=0.864$ m. $h_{ch}=1.59$ cm.

effect of wall motion when the channel separation is decreased to 0.7δ . We note that $U_{e,max}$ is the moving-wall speed. The fixed wall-point wall-pressure spectrum under moving-wall conditions is higher in level than the corresponding stationary wall spectrum. However, it is the same as the stationary wall-pressure spectrum measured at a nearly equivalent value of U_b .

III. DISCUSSION

The current external flow turbulent boundary layer wall-pressure fluctuation measurements, nondimensionalized with outer-flow variables, are favorably compared to similar data measured by Farabee¹¹ in Fig. 17. Farabee's data were acquired with a pinhole microphone on the test-section wall of a low-noise wind tunnel with $U_e=15.5$ m/s, $\delta^*=0.450$ cm, and $d^+=33$. The flow conditions for the subject data are $U_e=15.3$ m/s, $\delta^*=0.338$ cm, and $d^+=32.7$.

Keith *et al.*¹³ speculate that in developing flows, turbulent boundary layer wall-pressure spectra might display characteristics of both internal and external flows due to the existence of a free stream and the proximity of boundary layers on opposite and adjacent walls. In their¹³ comparison of pressure spectra from numerous experimental investigations, developing channel flow measurements¹⁴ in which the spectrum level decreases from the levels of external flows to the levels of internal pipe flows over the frequency range $0.1 < \omega \delta^*/U_e < 0.3$ support their argument. The channel height for these¹⁴ measurements was 6δ , and the span-wise width was 16δ . The data shown in Fig. 17 are for 2.75δ and 15δ , respectively, yet the current measurements are almost identical to Farabee's¹¹ "external" flow measurements (i.e., test-section height and width both equal to 21.9δ). This indicates that over the range of frequencies presented, the shear layers on adjacent and opposite tunnel walls have negligible effect on the measured turbulent boundary layer wall-pressure fluctuations.

Figure 18 shows an additional comparison of the current data at $U_e=10.6$ m/s, $\delta^*=0.366$ cm, and $d^+=23.7$, with those of Schewe¹⁰ at $U_e=6.3$ m/s, $\delta^*=0.460$ cm, and $d^+=19$. The two data sets are in excellent agreement and again

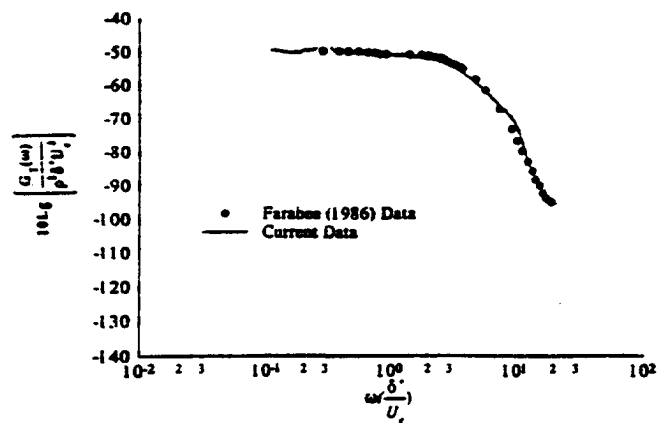


FIG. 17. Comparison of flat test plate boundary layer pressure spectrum with data from Farabee (Ref. 11), wall stationary, $X=0.864$ m, $U_e=15.4$ m/s, $h_{ch}=5.40$ cm.

show that the effect of the opposite and adjacent shear layers on the measured turbulent boundary layer wall-pressure fluctuations is negligible.

The moving wall-pressure spectral results for $h_{ch}=2.6 \delta$ (shown in Fig. 10) are consistent with the stationary-wall results. The velocity measurements, Figs. 7 and 8, showed that the wall motion influences only the belt boundary layer and has no effect on the plate turbulent boundary layer. The stationary wall data shows that boundary layers on opposite and adjacent tunnel walls have no effect on the wall-pressure fluctuations. Therefore, wall motion would not be expected to modify the wall-pressure fluctuations measured on the flat plate, and Fig. 10 shows this to be the case.

Farabee and Casarella¹⁶ identify four regions in the turbulent boundary layer as dominating the wall-pressure fluctuations over four specific frequency ranges. The low-frequency range, defined by $\omega \delta^*/u_\tau \leq 5$, is dominated by sources associated with the large-scale structures induced by the unsteady potential flow observed above the boundary layer. Due to facility noise contamination, these sources could not be measured. A mid-frequency range is presumed dominated by structures in the outer region of the boundary layer (i.e., $5 \leq \omega \delta^*/u_\tau \leq 100$). It thus extends from the lowest frequencies measured to 528 Hz for the Fig. 14 external-flow

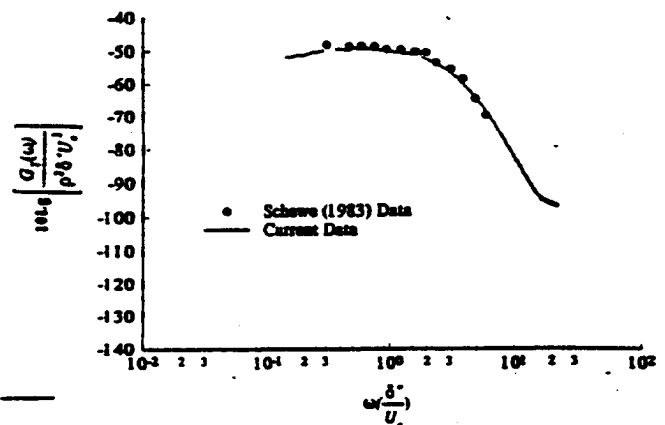


FIG. 18. Comparison of flat test plate boundary layer pressure spectrum with data from Schewe (Ref. 10), wall stationary, $X=0.864$ m, $U_e=10.6$ m/s, $h_{ch}=5.40$ cm.

spectrum. Flow structures in the boundary layer log region supposedly dominate the Fig. 14 spectrum from 528 to 1223 Hz. Higher frequencies arise from turbulent structures closer to the wall, in the boundary layer buffer region.

The plate flow modifications due to reducing h_{ch} from 2.6δ to 1.4δ occur exclusively in the outer portion of the external flow boundary layer, above $Z/\delta \approx 0.7$, where the velocity statistics are modified substantially. The spectra of Fig. 14 are almost identical except for a 1-dB difference over the lower range of frequencies measured. It appears that the flow modifications were insufficient to effect any significant change on the wall-pressure fluctuations.

The intermediate channel height stationary-wall results discussed above are consistent with the moving-wall data. The velocity data showed that wall motion tended to increase U_b by roughly 2%. For Z values where the flow was modified, the turbulence intensity levels fall roughly midway between the stationary wall results for $h_{ch} = 2.6 \delta$ and 1.4δ . Therefore, the effect of wall motion on the pressure fluctuations measured for $h_{ch}/\delta = 1.4$, at a given velocity, is expected to be negligible, as Fig. 15 supports.

Compared to the external boundary layer, the 0.7δ channel-velocity statistics have been modified even more than those in the 1.4δ channel, yet Fig. 14 shows that only at frequencies above 1200 Hz have the wall-pressure fluctuations been modified by more than 1 dB from the external-flow spectrum. These results demonstrate an insensitivity of the wall-pressure spectrum to the outer-flow structures that supposedly dominate the mid-range of frequencies.¹⁶

For the case of wall motion in the 0.7δ channel, U_b is not only increased by 8%, but the flow characteristics are changed from approximately that of a fully developed channel flow to that of a moving-wall channel flow. The turbulence data and mathematical analysis in Brungart¹⁷ indicate that the turbulence quantities for the stationary and moving-wall cases converge as the plate is approached and scale reasonably well on the local velocity. Figure 16 shows that the moving-wall spectrum is higher in level than the corresponding stationary-wall spectrum and is the same as the stationary wall-pressure spectrum measured at the value of the average velocity, U_b . The pressure fluctuations are essentially independent of the details of the outer flow.

The insensitivity of the currently discussed wall-pressure fluctuations to the specifics of the outer flow is further demonstrated in Fig. 19, which shows the nondimensionalized spectra, compared with a similar spectrum measured by Lauchle and Daniels¹² in fully developed pipe flow, and to an external turbulent boundary layer spectrum measured by Schewe.¹⁰ The outer flows under which these three spectra were measured are distinctly different, yet the wall-pressure spectra are almost identical. Spectra measured at the same momentum-thickness Reynolds number have the same ratio of inner-to-outer flow time and amplitude scales. They can, therefore, be compared across the entire frequency range when nondimensionalized with either inner- or outer-flow variables. The momentum-thickness Reynolds number of the Fig. 19 data range from 1120 to 1800.

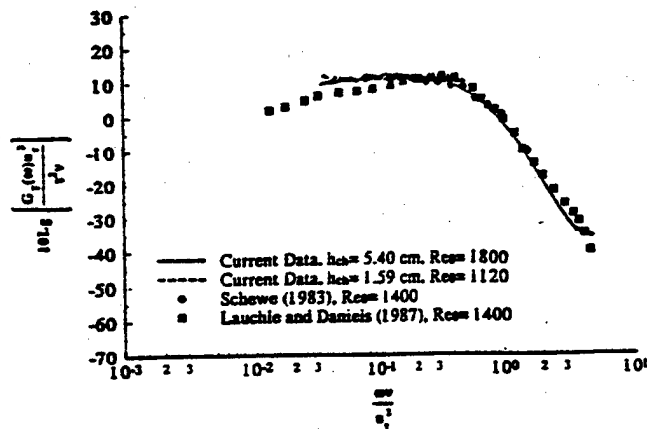


FIG. 19. Comparison of turbulent boundary layer wall-pressure fluctuation spectra normalized with inner-flow variables and measured in different facilities, or under different outer-flow conditions, but all at comparable values of Re_τ .

IV. SUMMARY

To better understand the outer-flow contribution to the pressure fluctuations occurring at the wall beneath a turbulent boundary layer, we have modified the outer flow of a flat plate boundary layer and compared the velocity and pressure fluctuation statistics with those of the unmodified outer-flow case. The modification was performed by setting one wall of a channel into streamwise motion. The height of the test plate above the moving (or stationary) wall was varied such that interacting and noninteracting turbulent boundary layers were included in the test matrix. The moving tunnel wall is effective in modifying the channel mean velocity, turbulence levels, Reynolds stresses, and, depending on the channel height, the wall-pressure fluctuations. This work has also demonstrated the relative insensitivity of the wall-pressure fluctuations to the details of the outer flow, even at those frequencies that are considered to be influenced by outer-flow turbulence structures.

ACKNOWLEDGMENTS

This work was conducted at the Applied Research Laboratory of the Pennsylvania State University through a grant from Ford Motor Co. This support, including that of Dr. Gary S. Strumolo, the project monitor at Ford, is gratefully acknowledged.

¹R. H. Kraichnan, "Pressure Fluctuations in Turbulent Flow Over a Flat Plate," *J. Acoust. Soc. Am.* **28**, 378-390 (1956).

²G. M. Lilley and T. H. Hodgson, "On Surface Pressure Fluctuations in Turbulent Boundary Layers," AGARD Report No. 276, April 1960.

³R. L. Panton and J. H. Lindeberger, "Wall Pressure Spectra Calculations for Equilibrium Boundary Layers," *J. Fluid Mech.* **65**, 261-287 (1974).

⁴W. C. Meecham and M. T. Tavis, "Theoretical Pressure Correlation Functions in Turbulent Boundary Layers," *Phys. Fluids* **23**, 1119-1131 (1980).

⁵D. M. Chase, "Modeling the Wavevector-Frequency Spectrum of Turbulent Boundary Layer Wall Pressure," *J. Sound Vib.* **70**, No. 1, 29-67 (1980).

⁶D. M. Chase, "The Character of the Turbulent Wall Pressure Spectrum at Subconvective Wavenumbers and a Suggested Comprehensive Model," *J. Sound Vib.* **112**, 125-147 (1987).

⁷W. W. Willmarth and C. E. Wooldridge, "Measurements of the Fluctua-

- ing Pressure at the Wall Beneath a Thick Turbulent Boundary Layer," *J. Fluid Mech.* 14, 187-210 (1962).
- ⁸M. K. Bull, "Wall-Pressure Fluctuations Associated with Subsonic Turbulent Boundary Layer Flow," *J. Fluid Mech.* 28, 719-754 (1967).
- ⁹W. K. Blake, "Turbulent Boundary Layer Wall Pressure Fluctuations on Smooth and Rough Walls," *J. Fluid Mech.* 44, 637-660 (1970).
- ¹⁰G. Schewe, "On the Structure and Resolution of Wall-Pressure Fluctuations Associated with Turbulent Boundary-Layer Flow," *J. Fluid Mech.* 134, 311-328 (1983).
- ¹¹T. M. Farabee, "An Experimental Investigation of Wall Pressure Fluctuations Beneath Non-Equilibrium Turbulent Flows," David W. Taylor Naval Ship Research and Development Center Report No. DTNSRDC-86/047 (1986).
- ¹²G. C. Lauchle and M. A. Daniels, "Wall Pressure Fluctuations in Turbulent Pipe Flow," *Phys. Fluids* 30, 3019-3024 (1987).
- ¹³W. L. Keith, D. A. Hurdiss, and B. M. Abraham, "A Comparison of Turbulent Boundary Layer Wall Pressure Spectra," *J. Fluids Eng.* 114, 338-347 (Sept. 1992).
- ¹⁴W. L. Keith and J. C. Bennett, "Low Frequency Measurements of the Wall Shear Stress and Wall Pressure in a Turbulent Boundary Layer," *AIAA J.* 29, No. 4, 526-530 (1991).
- ¹⁵R. L. Panton, A. L. Goldman, R. L. Lowery, and M. M. Reischman, "Low-Frequency Pressure Fluctuations in Axisymmetric Turbulent Boundary Layers," *J. Fluid Mech.* 97, Part 2, 299-319 (1980).
- ¹⁶T. M. Farabee and M. J. Casarella, "Structural Features of Wall Pressure Fluctuations Beneath Turbulent Boundary Layers," *Phys. Fluids A* 3, No. 10, 2410-2420 (1991).
- ¹⁷T. A. Brungart, "Boundary Condition Effects on Turbulent Boundary Layer Wall Pressure Fluctuations," Ph.D. thesis, Penn State University, 1997.
- ¹⁸J. H. Proulx and R. C. Marboe, "ARL Penn State Flow-Through Anechoic Chamber," ARL Penn State Technical Memorandum 89-65, 22 February 1990.
- ¹⁹R. C. Marboe, G. C. Lauchle, and W. A. Kargus IV, "Quiet Wall Jet Facility for Basic Aero/Hydroacoustics Research," NCA-Vol. 10, *Hydroacoustics Facilities, Instrumentation and Experimental Techniques*, ASME, 1991.
- ²⁰M. R. Davis, "Design of Flat Plate Leading Edges to Avoid Flow Separation," *AIAA J.* 18, No. 5, 598-600 (1980).
- ²¹L. E. Kinsler, A. R. Frey, A. B. Coppens, and J. V. Sanders, *Fundamentals of Acoustics*, 3rd ed. (Wiley, New York, 1982), p. 227.
- ²²I. C. Lekakis, R. J. Adrian, and B. G. Jones, "Measurement of Velocity Vectors with Orthogonal and Non-orthogonal Triple-Sensor Probes," *Exp. Fluids* 7, 228-240 (1989).
- ²³J. S. Bendat and A. G. Piersol, *Random Data: Analysis and Measurement Procedures*, 2nd ed. (Wiley, New York, 1986).
- ²⁴L. R. Puntell, P. S. Klebanoff, and F. T. Buckley, "Turbulent Boundary Layers at Low Reynolds Numbers," *Phys. Fluids* 24, 802-811 (1981).
- ²⁵D. E. Coles, "The Law of the Wake in the Turbulent Boundary Layer," *J. Fluid Mech.* 1, 191-226 (1956).
- ²⁶P. S. Klebanoff, "Characteristics of Turbulence in a Boundary Layer with Zero Pressure Gradient," NACA Technical Note 3178 (1954).
- ²⁷R. L. Panton and J. M. Miller, "Excitation of a Helmholtz Resonator by a Turbulent Boundary Layer," *J. Acoust. Soc. Am.* 58, 800-806 (1975).
- ²⁸H. Tennekes and J. L. Lumley, *A First Course in Turbulence* (MIT Press, Cambridge, MA, 1972).
- ²⁹G. M. Corcos, "Resolution of Pressure in Turbulence," *J. Acoust. Soc. Am.* 35, 192-199 (1963).
- ³⁰E. R. Lindgren, "Experimental Study on Turbulent Pipe Flows of Distilled Water," Oklahoma State Univ., Civil Eng. Dept., Report 1 AD621071 (1965).

APPENDIX 43

Installation effects on fan acoustic and aerodynamic performance

Timothy A. Brungart,^{a)} Gerald C. Lauchle,^{b)} and Ryan K. Ramanujam^{a)}

(Received 1998 February 23, revised 1999 January 19; accepted 1999 January 28)

Sound power measurements were performed on an upright vacuum cleaner in order to identify predominant noise generating mechanisms and to recommend corrective noise control modifications that would cause no increase in production costs. These modifications were then implemented and their effectiveness quantified. In general, the noise radiated by the vacuum cleaner is dominated by aerodynamic sources. Aerodynamic interactions occur between the electric motor cooling fan and nearby motor mounting fixtures resulting in intense tones at blade rate and harmonic frequencies. These tones are reduced by as much as 25 dB in level, to the broadband sound power level of the unit, by eliminating certain flow obstructions, and mounting the motor in an alternative fashion. Motor cooling performance is also dramatically improved by the new mounting arrangement resulting in a 26 °C reduction in steady-state operating temperature. © 1999 Institute of Noise Control Engineering. [S0736-2501(99)00101-0]

Primary subject classification: Primary subject classification: 12.4.4; Secondary subject classification: 21.6.5

1. INTRODUCTION

A vacuum cleaner is an air-moving device that can generate excessive noise levels due to many separate but often times interacting, noise generating mechanisms. Induction motors can be annoying acoustically because of brush arcing, rotor-stator interactions, tones created by cooling fans, bearings, and rotor imbalance. The vacuum working fan can create noise by numerous mechanisms including inflow distortions and turbulence, impeller-cutoff interactions, impeller-particle interactions, impeller-volute interactions, and stalled impeller blades due to excessive aerodynamic loading. As a system, the fan and motor can couple with supporting structures to cause mechanical and flow-induced vibrations of the housing which, in some instances, radiates acoustic energy.

It is desirable to incorporate noise and flow control measures into certain present and future vacuum cleaner designs. The purpose of this work is to identify the most dominant noise generating features of an upright vacuum cleaner and to demonstrate such noise control measures. The corrections to be demonstrated, however, are restricted to those that would result in no degradation of performance and no increase in production costs.

2. SOUND POWER MEASUREMENT SETUP AND PROCEDURES

The noise emitted from the vacuum cleaner of interest, as well as the effect of the noise control modifications performed, is quantified in terms of sound power. Sound power is the amount of acoustic energy per unit time radiated by a source (in watts). In general, sound pressure measurements for a source such as a vacuum cleaner are dependent on microphone location relative to the vacuum cleaner. Thus, it is not accurate to quantify the noise emit-

ted from such a source, or the effect of noise control modifications, in terms of sound pressure alone.

Sound power is defined by:

$$W = \int_S I \cdot n dS, \quad (1)$$

where W is the radiated sound power, I [W/m^2] is the acoustic intensity, and S [m^2] is the measurement surface area enclosing the source. The integral in Eq. (1) may be approximated as the summation of many intensity measurements over small areas, S_n :

$$W \approx \sum_{n=1}^N I_n S_n. \quad (2)$$

The normal component of the intensity vector I_n is assumed to be constant over S_n , and N is the total number of measurement surfaces. Theoretically, the shape of the measurement surface is arbitrary. In practice, however, it is usually chosen as a parallelepiped or a hemisphere. If the measurement location is beyond the near field of the source and the acoustical environment is anechoic, the magnitude of the intensity vector is related to the sound pressure by:

$$|I| = \frac{\langle p^2 \rangle}{\rho c}, \quad (3)$$

where $\langle p^2 \rangle$ is the mean-squared acoustic pressure and ρc is the characteristic acoustic impedance of air. Typically, the distance from the source must be at least 3/4 of the longest wavelength of sound of interest for the relationship given in Eq. (3) to be valid.

ISO standard 7779¹ provides explicit guidelines for the determination of sound power from sound pressure measurements. In accordance with ISO 7779, the sound power radiated from the vacuum cleaner was measured in the ARL Penn State Flow-Through Anechoic Chamber. This chamber, shown schematically in Fig. 1, is described in more detail elsewhere.^{2,3}

For testing, the upright vacuum cleaner was positioned on a small piece of low nap carpet located on the concrete

^{a)} Applied Research Laboratory, Penn State University, P. O. Box 30, State College, PA 16804 U.S.A.

^{b)} Graduate Program in Acoustics and Applied Research Laboratory, Penn State University, P.O. Box 30, State College, PA 16804, U.S.A.

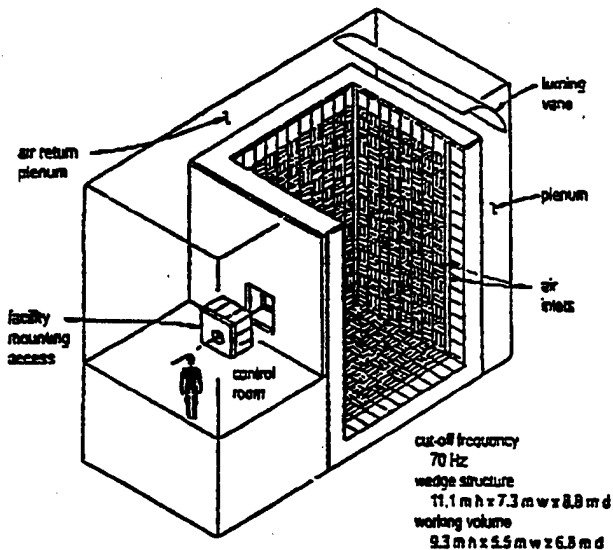


Fig. 1 - Schematic of the ARL Penn State Flow-Through Anechoic Chamber.

floor of the chamber; thus, the acoustical environment was hemianechoic. Seventeen (17) point sound pressure measurements were performed at the locations shown in Fig. 2. The rectangular control surface over which the sound pressure measurements were performed has dimensions of 2.413 m long by 1.727 m high by 2.337 m wide. These dimensions were chosen based upon the dimensions of the vacuum cleaner and the relationship between source dimensions and measurement positions specified in ISO 7779. The radiated sound power level (L_w) is computed from

$$L_w = 10 \log \left(\frac{1}{N} \sum_{n=1}^N 10^{0.1 L_{p,n}} \right) + 10 \log \left(\frac{S}{S_0} \right) \quad (4)$$

where $L_{p,n}$ is the sound pressure level (in decibels re 2×10^{-5} Pa) measured at location n , S is the rectangular control surface area, and S_0 is the reference area of 1 m^2 .

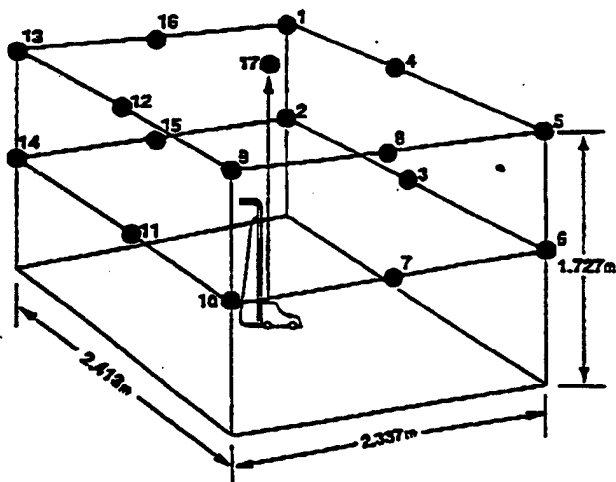


Fig. 2 - Sound pressure level measurement locations for the determination of sound power.

Equation (4) is valid only for quantities measured in the SI system of units.

The sound pressure data were acquired with a Spectral Dynamics SD 380 multi-channel fast Fourier transform (FFT) processor, a 12.5 mm Brüel and Kjær (B&K) type 4181 microphone and matching preamplifier, and a B&K type 2807 power supply. The microphone calibration was verified periodically with a B&K type 4220 pistonphone. Software developed in-house was used to process the sound pressure data.

3. ACOUSTIC CHARACTERIZATION OF THE BASELINE UNIT

In practice, a vacuum cleaner operates under a variety of flow conditions ranging from free delivery to stall. Free-delivery conditions are achieved by allowing the flow to pass into the vacuum working fan with no flow resistance at the inlet nozzle. Stalled conditions are achieved by blocking the flow of air to the working fan. When the unit is locked, a mechanical flap blocks the airflow from the floor resulting in stalled flow conditions. Since upright vacuum cleaners are most often turned on while in their locked upright position, noise control efforts focused on the radiated noise at stalled flow conditions.

Figure 3 shows the sound power level of the baseline unit in its locked upright position. This spectrum is compared to the sound power level of the same unit operating without a vacuum working fan (VWF) but with the electric motor operating in its standard configuration at its standard rpm. In general, the blade passage tone of the electric motor cooling fan (1×EMCF BR) is by far the most prominent component of the sound power of this unit. The data show clearly that the electric motor causes the 4200-Hz 1×EMCF BR tone and second harmonic. The 1×EMCF BR tone is also the most annoying component of the radiated sound not only because of its large amplitude but because of its proximity in frequency to the peak of human auditory response. Other, less significant tones (from an annoyance standpoint), which appear in the spectra include the motor shaft rate fundamental (1×SR) and third harmonic (3×SR), the vacuum working fan blade passage tone

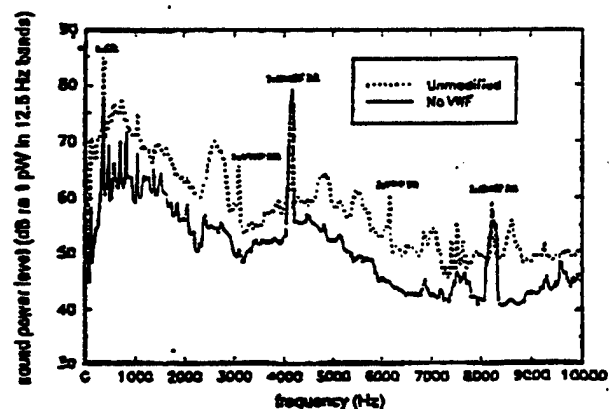


Fig. 3 - The contribution of the electric motor to the sound power of the vacuum cleaner at stalled flow conditions.

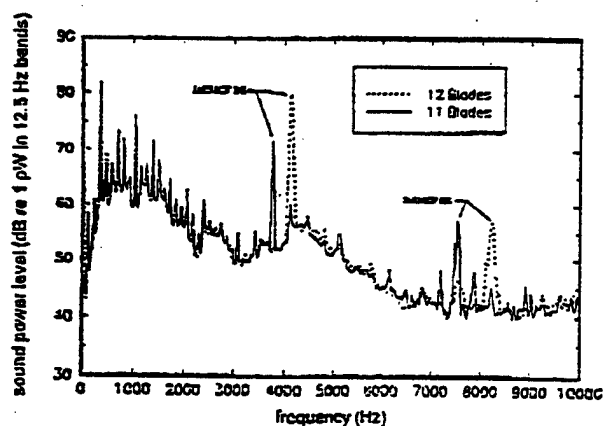


Fig. 4 – The effect of replacing the 12-blade electric motor cooling fan with an 11-blade fan on the sound power of the vacuum cleaner in the absence of the vacuum working fan.

(1×VWF BR), and the second harmonic of the electric motor cooling fan blade passage tone (2×EMCF BR).

Figure 3 shows that the vacuum working fan is responsible for an increase in the 1×SR tone level of approximately 7 dB over that generated by the electric motor alone, and of course, is responsible for its blade passing tone and second harmonic. The increase in 1×SR noise level with the vacuum working fan installed is attributed to mechanical imbalance of the vacuum working fan. In general, the vacuum working fan/airflow at stall increases the broadband noise level approximately 6 to 8 dB over the broadband noise radiated by the electric motor alone. In the 2400- to 2900-Hz region, however, running the vacuum working fan results in an approximate 15 dB increase in sound power level over that generated by the electric motor alone. Free-delivery conditions result in an approximate 5 dB increase in sound power level from 500 to 2500 Hz relative to stalled flow conditions. At other frequencies, the levels measured under free-delivery and stalled flow conditions vary by less than 1 to 2 dB.

4. NOISE CONTROL MODIFICATIONS PERFORMED

Since the electric motor cooling fan is responsible for the most prominent and annoying tone emitted from this particular vacuum cleaner, efforts focused on ways to reduce this component. Inspection of the manner in which the electric motor is mounted to the vacuum working fan casing revealed that the electric motor cooling fan operates almost in contact with six gussets situated directly beneath the fan, two posts located just outside the fan disk, and two notches in the shroud located just above the fan. The interaction of the 12-blade electric motor cooling fan with this even number of disturbances in such close proximity is responsible for the extremely high level of the 1×EMCF BR tone. This suggests that a fan with an odd number of blades may reduce the tone by reducing the in-phase interactions between the blades and the flow obstructions.⁴

The effect on the sound power level of replacing the 12-blade electric motor cooling fan with an 11-blade ver-

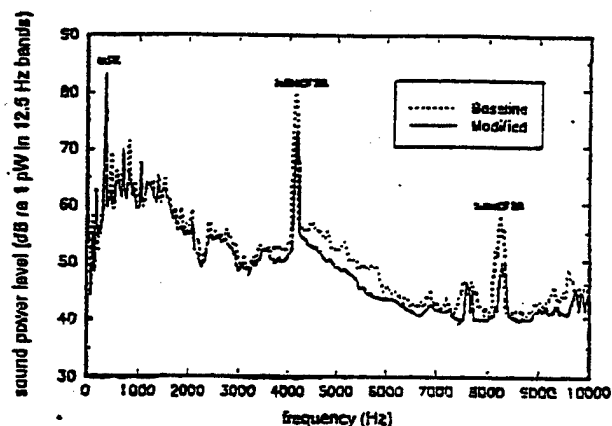


Fig. 5 – The effect of removing the gussets situated directly beneath the 12-blade electric motor cooling fan on the sound power of the electric motor.

sion is shown in Fig. 4. These data were acquired with the unit operating with the vacuum working fan removed and the electric motor operating at its standard rpm. The data show that the 1×BR tone of the 11-blade electric motor cooling fan is some 9 dB lower than the 1×BR tone level of the 12-blade electric motor cooling fan. The level of the second harmonic of each tone is identical.

Figure 5 shows that removal of the gussets results in a 5-dB reduction in the 1×EMCF BR sound power tone level, and an 8-dB reduction in the second-harmonic for the 12-blade fan. Identical reductions were achieved when the 11-blade electric motor cooling fan was used. A 5-dB increase in sound power level at the 1×SR frequency is apparent between the baseline and modified configurations. The changes in the level of the shaft rate tone are likely due to shaft chatter caused by interchanging electric motor cooling fans. Considering the 20 000 RPM rotation rate of the shaft, it is not surprising that replacing a factory balanced motor/fan assembly with a different fan would tend to increase shaft chatter and, in turn, the tone radiated at the 1×SR frequency. Because the noise radiated at 1×SR is predominantly vibration induced, either precision balancing of the electric motor shaft/cooling fan/vacuum working fan arrangement or appropriate alteration of the motor support structure is expected to reduce this tone. Fortunately, this tone occurs in the range of frequencies where human hearing is less sensitive than at the higher frequencies where the 1×EMCF BR tone occurs.

Removal of the remaining motor fan flow obstructions that were molded into the vacuum fan volute results in the virtual elimination of the electric motor cooling fan blade rate tones. Figure 6 compares the sound power levels generated by the modified electric motor arrangement operating with the 12-blade cooling fan to the baseline motor configuration. The data were taken with the vacuum working fan removed from the vacuum cleaner but with the electric motor operating at its standard location and rpm. The 12-blade 1×EMCF BR tone level is reduced an additional 20 dB by removing the two posts located just outside the fan disk and by filling in the shroud notches located in the volute just above the fan. The 2×EMCF BR tone is also eliminated. Similar results were achieved for the 11-blade

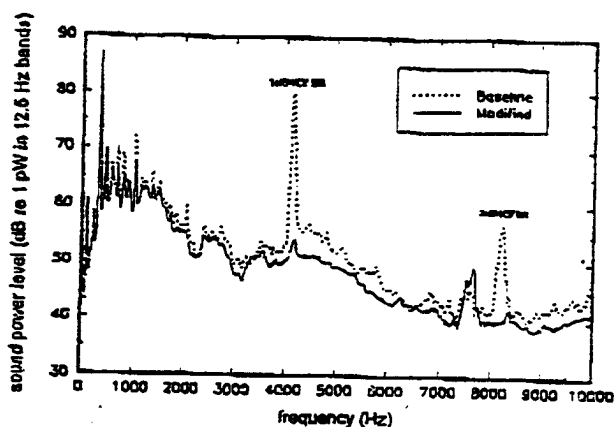


Fig. 6 - Comparison of the sound power of the modified electric motor with a 12-blade cooling fan to the sound power of the baseline motor configuration.

cooling fan, where the blade rate and harmonic tone levels were reduced to the broadband sound power level. The modified, quiet electric motor mounting arrangement is compared photographically to the baseline motor mounting arrangement in Fig. 7.

5. FAN AERODYNAMIC PERFORMANCE

Since the function of the electric motor cooling fan is to cool the electric motor, its aerodynamic effectiveness is best quantified in terms of motor temperature. The baseline electric motor mounting arrangement tends to obstruct the radial discharge of air from the electric motor cooling fan due to the presence of the motor mounting posts and gussets. Removing the posts and gussets should not only reduce the noise radiated by the electric motor cooling fan, but should improve its aerodynamic performance as well.

Motor temperatures were measured by attaching OMEGA Type J Iron-Constantan thermocouples directly to the mounting assemblies at identical locations and orientations. The thermocouple wires were fed through the vacuum cleaner body and attached to an analog temperature display. The baseline and modified motors were started simultaneously with the motors initially at room temperature

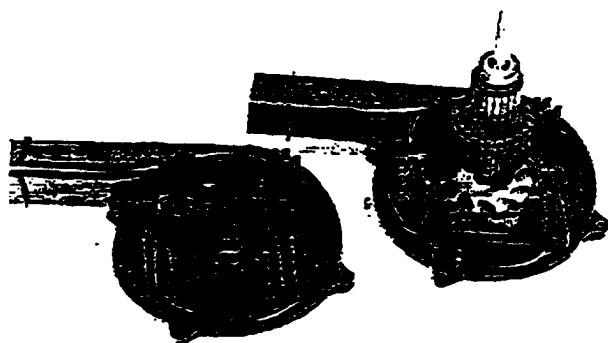


Fig. 7 - Photographs of the modified, quiet electric motor mounting arrangement (right) and the baseline electric motor mounting arrangement (left).

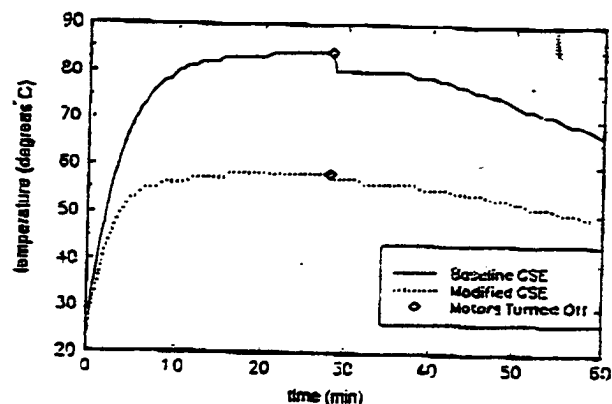


Fig. 8 - Comparison of the operating temperature measured on both the baseline and modified electric motors.

(23 °C); the temperature of each was recorded at 30-s intervals. The motors were turned off momentarily after a period of 28 min due to the appearance of a temperature ceiling, above which the temperature of the motors did not increase after several minutes. The test continued for another 30 min. The results are shown in Fig. 8. The modified motor operates at a temperature some 26 °C cooler than the baseline motor, thus, the overall aerodynamic performance of the modified unit was improved.

6. CONCLUSIONS

The acoustic diagnostics performed showed that the most prominent tone radiated by the subject vacuum cleaner is generated by an interaction between the electric motor cooling fan and surrounding gussets and posts. These same gussets and posts also served to block the radial discharge of air from the fan and inhibit cooling performance. The intense and annoying 1×EMCF BR tone was completely eliminated, and the fan aerodynamic performance was improved, resulting in a 26 °C reduction in motor operating temperature, by removing the fixtures surrounding the cooling fan and mounting the motor in an alternate fashion. With the exception of the shaft-rate and vacuum working fan-related tones, the noise radiated by the modified vacuum cleaner is generally broadband. The shaft-rate tones are controllable by appropriate balancing of the electric motor/shaft assembly. Reduction of the 1×VWF BR tone and its harmonics could be achieved by enlarging the volute casing. This is expected to reduce the level of the vacuum working fan tones by increasing the cutoff clearance. It may also reduce the vacuum working fan-generated broadband noise due to reduced flow velocities inside the scroll casing. The noise reduction effectiveness of such a modification has been demonstrated⁵ with no apparent change in fan efficiency. It was not attempted here because of the manufacturing costs associated with the implementation of a new design vacuum working fan volute.

Additional noise control measures, beyond the minimization of line component levels, must address the broadband sound radiated by the vacuum working fan. Minor and inexpensive modifications, however, are unlikely to be effective. This is because, in a system such as the subject

vacuum cleaner, the quality of the flow through the system and the noise generated by its fan are coupled. Regions of high shear and high pressure loss necessitate that a fan run faster to overcome these losses and to achieve a given mass flow rate. Thus, a more efficient flow path in conjunction with a fan designed for improved acoustical performance is likely to be necessary for improved acoustical performance beyond that demonstrated here.

7. ACKNOWLEDGMENT

This work was sponsored by the Royal Appliance Mfg. Co.; their support is gratefully acknowledged.

8. REFERENCES

- ¹*Acoustics-Measurements of Airborne Noise Emitted by Computer or Business Equipment*, International Standard ISO 7779:1988 (International Organization for Standardization, Geneva, Switzerland, 1988).
- ²R. C. Marboe, G. C. Lauchle, and W. A. Kargus IV, "Quiet wall jet facility for basic aero/hydroacoustics research," in *Hydroacoustic Facilities, Instrumentation, and Experimental Techniques*, edited by T. M. Parabec and R. E. A. Arndt (American Society of Mechanical Engineers, New York, 1991), NCA-Vol. 10, pp. 69-73.
- ³J. H. Prom and R. C. Marboe, "ARL Penn State Flow-Through Anechoic Chamber," ARL Penn State Technical Memorandum No. 89-65 (22 February 1990).
- ⁴K. B. Washburn and G. C. Lauchle, "Inlet flow conditions and tonal sound radiation from a subsonic fan," *Noise Control Eng. J.* 31, 101-110 (1988).
- ⁵W. Leidel, "Einfluß von Zungenabstand und Zungenradius auf Kennlinie und Geräusch eines Radialventilators," Forschungsbericht DLR-FB 69-16, Deutsche Forschungsanstalt für Luft- und Raumfahrt, Köln/Porz, Germany (1969).

ACTUATOR STUDIES

**Materials : Designs :
Reliability**



NEW TREND IN CERAMIC ACTUATORS

Kenji Uchino

International Center for Actuators and Transducers
Materials Research Laboratory, The Pennsylvania State University
University Park, PA 16802, USA

ABSTRACT

During the past few years, piezoelectric and electrostrictive ceramic materials have become key components in smart actuator/sensor systems for use as precision positioners, miniature ultrasonic motors and adaptive mechanical dampers. In particular, multilayer structures have been intensively investigated in order to improve their reliability and to expand their applications. Recent developments in USA, Japan and Europe will be compared.

INTRODUCTION

Piezoelectric actuators are forming a new field midway between electronic and structural ceramics [1-4]. Application fields are classified into three categories: positioners, motors and vibration suppressors. The manufacturing precision of optical instruments such as lasers and cameras, and the positioning accuracy for fabricating semiconductor chips, which are adjusted using solid-state actuators, is of the order of $0.1 \mu\text{m}$. Regarding conventional electromagnetic motors, tiny motors smaller than 1 cm^3 are often required in office or factory automation equipment, and are rather difficult to produce with sufficient energy efficiency. Ultrasonic motors whose efficiency is insensitive to size are superior in the mini-motor area. Vibration suppression in space structures and military vehicles using piezoelectric actuators is also a promising technology.

Multilayer structures are mainly used for practical applications, because of their low drive voltage, high energy density, quick response and long lifetime [5,6]. Figure 1 illustrates multilayer, multimorph and multilayer-moonie structures, which will be covered in this article. Recent investigations have focused on the improvement of reliability and durability in multilayer actuators.

This article reviews the investigations of device structures, reliability issues, and recent applications of multilayer actuators, comparing the developments in USA, Japan and Europe.

MULTILAYER STRUCTURES

Two preparation processes are possible for multilayer ceramic devices: one is a cut-and-bond method and the other is a tape-casting method. The tape-casting method requires expensive fabrication facilities and sophisticated techniques, but is suitable for the mass-production of thousands of pieces per month. Tape-casting also provides thin dielectric layers, leading to low drive voltages of 40 - 100 V [7,8].

A multilayer actuator with interdigital internal electrodes has been developed by Tokin [9,10]. In contrast to the conventional electrode configuration in Fig. 1, line electrodes are printed on piezoelectric ceramic green sheets, and are stacked in such a way that alternating electrode lines are displaced by one-half pitch (see Fig. 2). This actuator generates motions at right angles to the stacking direction using the longitudinal piezoelectric effect. Long ceramic actuators up to 74 mm in length are manufactured.

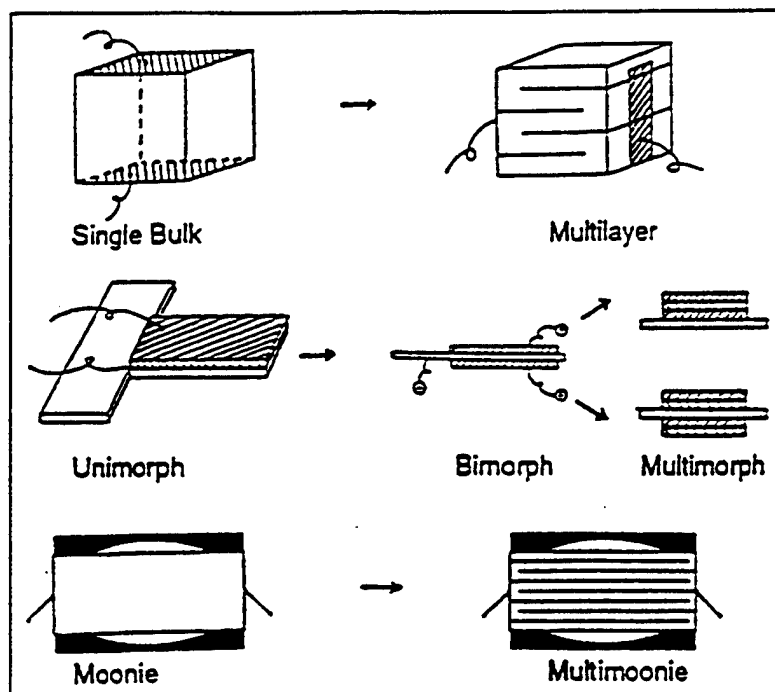


Fig.1 Examples of multilayer, multimorph and multilayer-moonie structures.

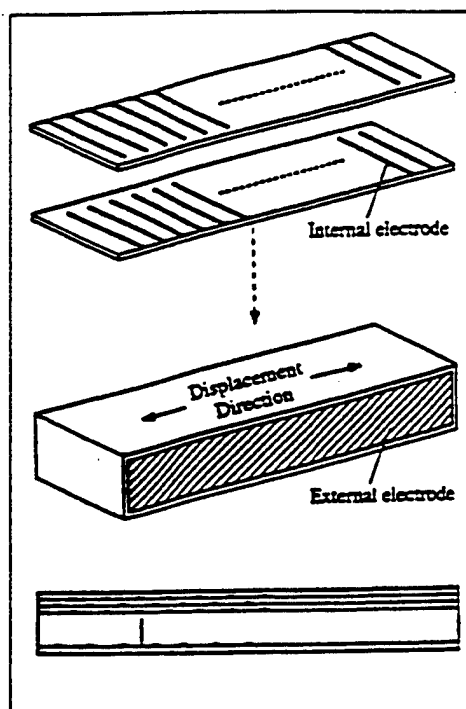


Fig.2 Structure of an internal interdigital electrode actuator.

A three-dimensional positioning actuator with a stacked structure has been proposed by PI Ceramic (Fig.3), in which shear strain is utilized to generate x and y displacements [11].

Composite actuator structures called "moonies" and "cymbals" have been developed at Penn State University to provide characteristics intermediate between the multilayer and bimorph actuators. These transducers exhibit an order of magnitude larger displacement than the multilayer, and much larger generative force with quicker response than the bimorph [12,13]. The device consists of a thin multilayer piezoelectric element and two metal plates with narrow moon-shaped cavities bonded together as shown in Fig. 1. A moonie $5 \times 5 \times 2.5 \text{ mm}^3$ in size can generate a $20\mu\text{m}$ displacement under 60V, eight times as large as the displacement of a multilayer of the same size [14]. This new compact actuator has been used to make a miniaturized laser beam scanner [14]. Moonie/cymbal characteristics have been investigated for various constituent materials and sizes [15,16].

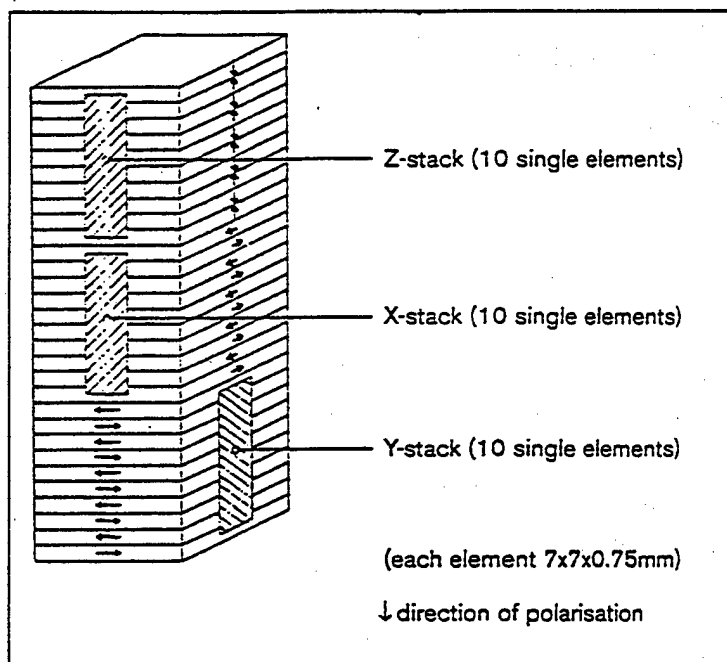


Fig.3 3-D controllable multilayer piezoelectric actuator.

RELIABILITY OF MULTILAYER ACTUATORS

As the application fields expand, the reliability and durability issues of multilayer actuators become increasingly important. The reliability of ceramic actuators depends on a number of complex factors, which can be divided into three major categories: reliability of the ceramic itself, reliability of the device design, and drive technique.

Compositional changes of actuator ceramics and the effect of doping are primary issues used in stabilizing the temperature and stress dependence of the induced strains. A multilayer piezo-actuator for use at high temperatures (150°C) has been developed by Hitachi Metal, using Sb_2O_3 doped $(\text{Pb,Sr})(\text{Zr,Ti})\text{O}_3$ ceramics [17]. Systematic data on uniaxial stress dependence of piezoelectric characteristics have been collected on various Navy PZT materials [18]. Grain size and porosity control of the ceramics are also important in controlling the reproducibility of

actuators [19]. Aging phenomena, especially the degradation of strain response, are, in general, strongly dependent on the applied electric field as well as on temperature, humidity and mechanical bias stress [20].

The device design strongly affects its durability and lifetime. Silver electrode metal tends to migrate into the piezoceramic under a high electric field in high humidity. Silver:palladium alloys suppress this behavior effectively. Resistive coatings of the device should also be taken into account [21]. To overcome electrode delamination, improved adhesion can be realized by using a mesh-type electrode or an electrode material with mixed metal and ceramic (the matrix composition!) powders. Pure ceramic electrode materials have also been developed using semiconductive perovskite oxides (barium titanate-based PTCR ceramics) [22]. The lifetime characteristics of a multilayer actuator with applied DC or unipolar AC voltage at various temperatures [23,24] and at various humidities [25] were investigated by Nagata et al. The relationship between the logarithm of the lifetime and the reciprocal of absolute temperature showed linear characteristics similar to Arrhenius type. Nevertheless, the degradation mechanism remains a critical problem.

In multilayer actuators, reduction of the tensile stress concentration around the internal electrode edge of the conventional interdigital configuration is the central problem. Regarding the destruction mechanism of multilayer ceramic actuators, systematic data collection and analysis have led to considerable progress [26-33]. Two typical crack patterns are generated in a conventional interdigital multilayer device: one is a Y-shaped crack located on the edge of an internal electrode, and the other is a vertical crack located in a layer adjacent to the top or bottom inactive layer, connecting a pair of internal electrode.

To overcome this crack problem, three electrode configurations have been proposed as illustrated in Fig. 4: plate-through, interdigital and slit, and interdigital and float electrode types. The "float electrode" type is an especially promising design which can be fabricated using almost the same process as the conventional multilayer actuator, and lead to much longer lifetimes [34]. An empirical rule "the thinner the layer, the tougher the device" [27,28] is also very intriguing, and will be more theoretically investigated in the near future.

Failure detection or lifetime prediction methods are expected to remarkably increase the reliability of multilayer actuators. Acoustic emission and surface potential monitoring are promising methods [35]. Penn State has developed a modified multilayer actuator containing a strain gauge as an internal electrode [36]. This internal strain gauge electrode can detect the crack initiation sensitively and monitor the field-induced strain [37].

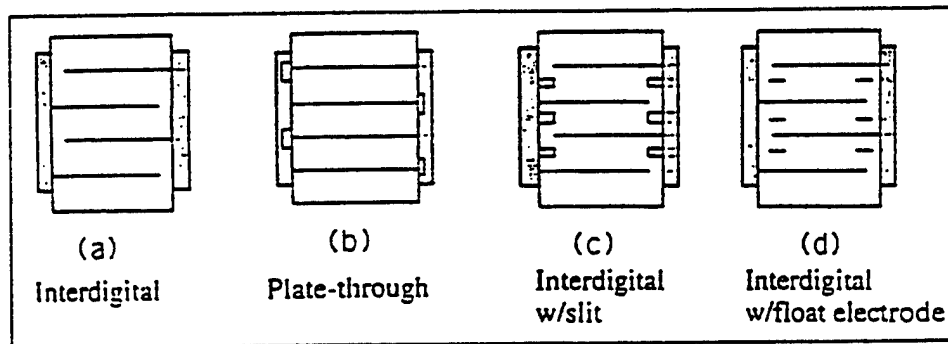


Fig.4 Various internal electrode configurations in multilayer actuators.
(a) Interdigital, (b) Plate-through, (c) Slit-insert, and (d) Float electrode.



Regarding drive techniques for ceramic actuators, pulse drive and AC drive require special attention; the vibration overshoot associated with a sharp-rise step/pulse voltage causes a large tensile force, leading to delamination of the multi-stacked structure, while long-term application of AC voltage generates considerable heat. A special pulse drive technique using a mechanical bias stress are required in the first case, and heat generation can be suppressed by changing the device design. An analytical approach to the heat generation mechanism in multilayer actuators has been reported, indicating the importance of larger surface area [38]. Heat generation in piezoelectric ceramics is mainly attributed to the P-E hysteresis loss under large electric field drive [39,40]. For ultrasonic motors, antiresonance drive is preferable to resonance drive because of higher efficiency and lower heat generation for the same vibration level [41].

APPLICATIONS OF CERAMIC ACTUATORS

Table I compares a variety of ceramic actuator developments in the USA, Japan and Europe. Additional details will be described in this section.

Table I Ceramic actuator developments in the USA, Japan and Europe.

	US	Japan	Europe
TARGET	Military-oriented products	Mass-consumer products	Laboratory equipment
CATEGORY	Vibration suppressor	Mini-motor Positioner	Mini-motor Positioner Vibration suppressor
APPLICATION FIELD	Space structure Military vehicle	Office equipment Cameras Precision machines Automobiles	Lab stage-stepper Airplanes Automobiles Hydraulic systems
ACTUATOR SIZE	Up-sizing (30 cm)	Down-sizing (1 cm)	Intermediate size (10 cm)
MAJOR MANUFACTURER	AVX/Kyocera Morgan Matroc Itek Opt. Systems Burleigh AlliedSignal	Tokin Corp. NEC Hitachi Metal Mitsui-Sekka Canon Seiko Instruments	Philips Siemens Hoechst Ceram Tec. Ferroperm Physik Instrumente

USA

The principal target is military-oriented applications such as vibration suppression in space structures and military vehicles. Substantial up-sizing of the actuators is required for these purposes.

A typical example is found in the aircraft wing proposed by NASA [42]. A piezoelectric actuator was installed near the support of the wing, allowing immediate suppression of unwanted mechanical vibrations. Several papers have been reported on damper and noise cancellation applications [43,44].

Passive dampers constitute another important application of piezoelectrics, where mechanical noise vibration is radically suppressed by the converted electric energy dissipation through Joule heat when a suitable resistance, equal to an impedance of the piezoelectric element $1/\omega C$, is connected to the piezo-element [45].

A widely-publicized application took place with the repair of the Hubble telescope launched by the Space Shuttle. Multilayer PMN electrostrictive actuators corrected the image by adjusting the phase of the incident light wave (Fig.5) [46]. PMN electrostrictors provided superior adjustment of the telescope image because of negligible strain hysteresis.

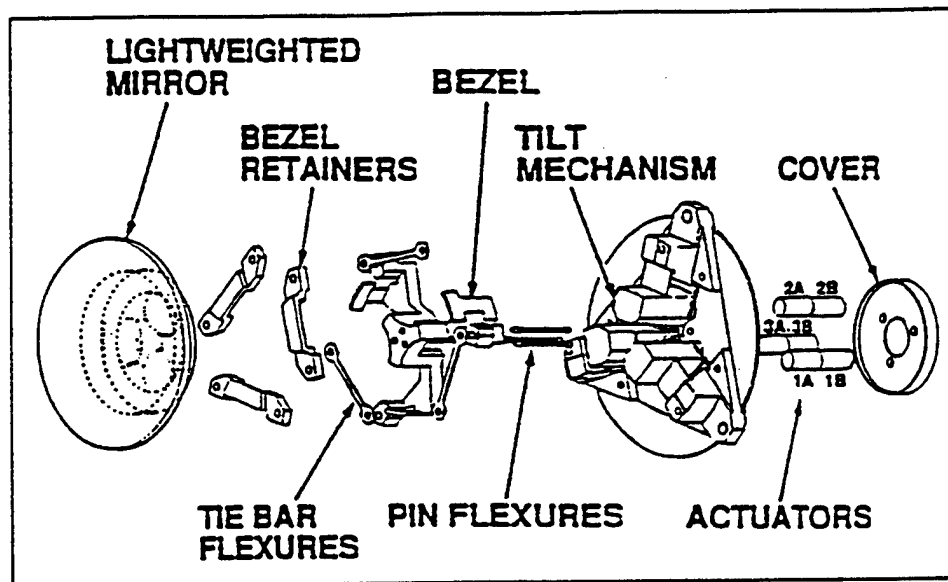


Fig.5 Articulating fold mirror using PMN multilayer actuators.

JAPAN

Japanese industries seek to develop mass-consumer products, especially mini-motors and micro positioners, aiming at applications such as office equipment and cameras/video cameras. Tiny actuators smaller than 1cm^3 are the main focus in these products.

A dot matrix printer was the first widely-commercialized product using multilayer ceramic actuators [47]. Each character formed by such a printer was composed of a 24×24 dot matrix in which a printing ribbon was impacted by a multiwire array. The printing element was composed of a multilayer piezoelectric device with a sophisticated hinge lever magnification mechanism. The magnification by a factor of 30 resulted in an amplified displacement of 0.5 mm and an energy transfer efficiency greater than 50%. A modified impact printer head has been developed by Tokin, using new interdigital internal electrode type actuators, which have lowered production cost [48]. A color ink-jet printer has also been commercialized by Seiko Epson, using multilayer piezo-actuators [49].

Automotive applications by Toyota Motor have been accelerated recently. Multilayer actuators have been introduced to an electronically controlled suspension [50] and a pilot injection system for diesel engines [51].

Efforts have been made to develop high-power ultrasonic vibrators as replacements for conventional electromagnetic motors. The ultrasonic motor is characterized by "low speed and high torque," which is contrasted with the "high speed and low torque" of the electromagnetic

motors. After the invention of π -shaped linear motors [52], various modifications have been reported [53,54]. The Mitsui Petrochemical model is of particular interest because the motor body is composed of only one component prepared by a cofiring method as illustrated in Fig. 6 [54]. A maximum speed of 200 mm/s and a maximum thrust of 60 gf were reported for this motor.

Camera motors utilize a traveling elastic wave induced by a thin piezoelectric ring. A ring-type slider in contact with the "rippled" surface of the elastic body bonded onto the piezoelectric can be driven in both directions by exchanging the sine and cosine voltage inputs. Another advantage is its thin design, making it suitable for installation in cameras as an automatic focusing device. Nearly 80 % of the exchange lenses in Canon's "EOS" camera series have been replaced by ultrasonic motor mechanisms [55].

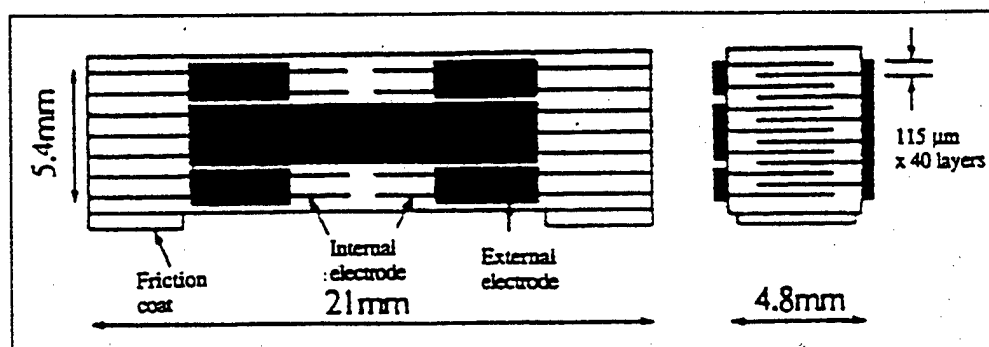


Fig.6 Monolithic multilayer piezoelectric linear motor.

Intriguing research programs are underway in Japan on the vibration damping of earthquakes, using piezoelectric actuators [56,57]. Active damping of a multilayer piezo-actuator was tested using an actual size H-type steel girder, and was verified to be effective during earthquakes.

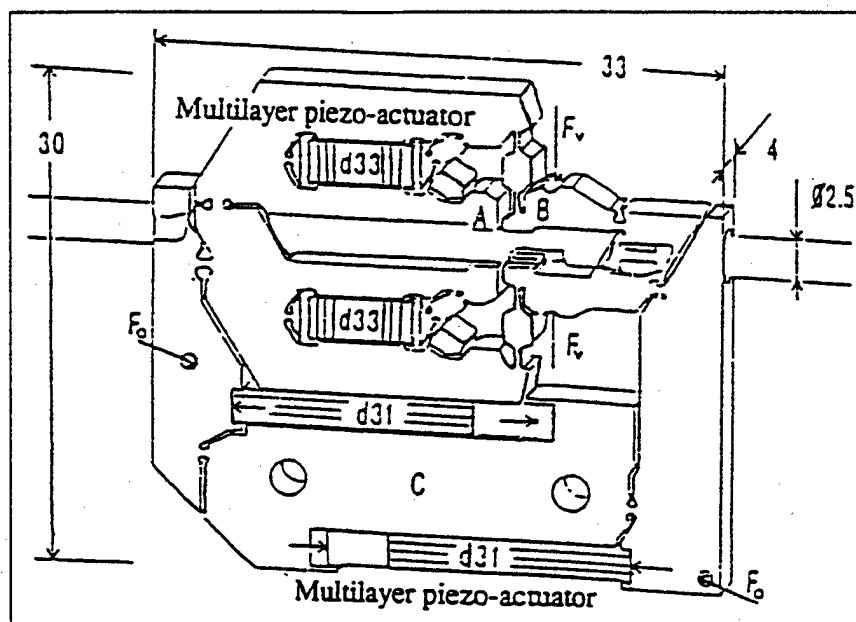


Fig.7 An inchworm using multilayer piezoelectric actuators.

EUROPE

Ceramic actuator development has begun relatively recently in Europe with a wide range of research topics. A current focus of several major manufacturers is on laboratory equipment products such as laboratory stages and steppers with rather sophisticated structures.

Figure 7 shows a walking piezo motor with 4 multilayer actuators by Philips [58]. Two short actuators function as claspers while the longer two provide a proceeding distance in an inchworm mechanism. Physik Instrumente has developed more complicated two-leg type walkers [59].

CONCLUSIONS

Twenty years have passed since the intensive development of piezoelectric actuators began in Japan, then spread worldwide. Presently, the focus has been shifted to practical device applications. This article has reviewed several reliability issues of the multilayer ceramic actuators as well as new actuator structures, and compared the developments of recent applications among USA, Japan and Europe.

The markets in USA are chiefly limited to military and defense applications, and it is difficult to estimate the amount of sales. The current Navy needs include smart submarine skins, hydrophone actuators, and prop noise cancellation. Smart aircraft skins are an Air Force objective, while Army requires helicopter rotor twisting, aeroservoelastic control and cabin noise/seat vibration cancellation.

Meanwhile in Japan, piezoelectric shutters (Minolta Camera) and automatic focusing mechanisms in cameras (Canon), dot-matrix printers (NEC) and part-feeders (Sanki) are now commercialized and mass-produced by tens of thousands of pieces per month. During the commercialization, new designs and drive-control techniques of the ceramic actuators have been mainly developed over the past few years. A number of patent disclosures have been generated by NEC, TOTO Corporation, Matsushita Electric, Brother Industry, Toyota Motors, Tokin, Hitachi Metal and Toshiba.

If we estimate the annual sales in 2001 (neglecting the current economic recession in Japan), ceramic actuator units, camera-related devices and ultrasonic motors are expected to reach \$500 million, \$300 million and \$150 million, respectively. Regarding the final actuator-related products, \$10 billion is a realistic goal [55].

Future research trends can be divided in two ways: up-sizing in space structures and down-sizing in office equipment. Further down-sizing will also be required in medical diagnostic applications such as blood test kits and surgical catheters.

Key words for the future of multilayer ceramic actuators are "miniaturization" and "hybridization." Layers thinner than 10 μm , corresponding to current multilayer capacitor technology, will also be introduced in actuator devices replacing the present 100 μm sheets. Piezoelectric thin films compatible with silicon technology are a focus in micro-electromechanical systems. Ultrasonic rotary motors as small as 2 mm in diameter [60] and two-dimensional micro-optical-scanner [61], both of which were fabricated on a silicon membrane are good examples.

Non-uniform configurations or hetero-structures of different materials, layer thickness, or electrode patterns will be adopted for practical devices. Functionally gradient piezoelectric actuators now being prototyped indicate a new trend [62].

REFERENCES

1. Uchino K: Piezoelectric Actuators/Ultrasonic Motors. Kluwer Academic Pub., MA 1996.
2. Uchino K: Ceramic Actuators: Principles and Applications. MRS Bull. 1993, 18: 42 - 48.
3. Uchino K: Materials Update: Advances in Ceramic Actuator Materials. Mater. Lett. 1995, 22: 1 - 4.
4. Uchino K: New Piezoelectric Devices for Smart Actuator/Sensor Systems. Proc. 4th Int'l Conf. Electronic Ceramics & Appl. 1994, 179 -191.
5. Yoshikawa S, Shrout T: Multilayer Piezoelectric Actuators -- Structures and Reliability. AIAA/ASME/ASCE/AHS/ASC Struct. Struct. Dyn. Mater. Conf. 1993, 34: 3581-3586.

6. Uchino K: Manufacturing Technology of Multilayered Transducers. Proc. Amer. Ceram. Soc., Manufacture of Ceramic Components 1995, 81-93.
7. Dibbern U: Piezoelectric Actuators in Multilayer Technique. Proc. 4th Int'l Conf. New Actuators (Actuator '94), Germany 1995, 114 - 118.
8. Takada S, Inoue Y, Oya K, Inagawa M: 100 V DC Driving Type Multilayer Piezoelectric Actuator. NEC Giho 1994, 47: 98 -102.
9. Ohashi J, Fuda Y, Ohno T: Multilayer Piezoelectric Ceramic Actuator with Interdigital Internal Electrodes. Jpn. J. Appl. Phys. 1993, 32: 2412 - 2414.
10. Ohashi J, Fuda Y, Ohno T: Multilayer Piezoelectric Ceramic Actuator with Interdigital Internal Electrodes. Tokin Tech. Rev. 1993, 19: 55 - 60.
11. Bauer A, Moller F: Piezo Actuator Special Design. Proc. 4th Int'l Conf. New Actuators (Actuator '94), Germany 1995, 128 - 132.
12. Sugawara Y, Onitsuka K, Yoshikawa S, Xu QC, Newnham RE, Uchino K: Metal-Ceramic Composite Actuators. J. Amer. Ceram. Soc. 1992, 75: 996 - 998.
13. Onitsuka K, Dogan A, Tressler JF, Xu QC, Yoshikawa S, Newnham RE: Metal-Ceramic Composite Transducer, The "Moonie". J. Intelligent Mater. Systems and Struct. 1995, 6: 447 - 455.
14. Goto H, Imanaka K, Uchino K: Piezoelectric Actuators for Light Beam Scanners. Ultrasonic Techno 1992, 5: 48 -51.
15. Tressler JF, Xu QC, Yoshikawa S, Uchino K, Newnham RE: Composite Flextensional Transducers for Sensing and Actuating. Ferroelectrics 1994, 156 (Proc. 8th Int'l Mtg. Ferroelectricity): 67 - 72.
16. Dogan A, Fernandez JF, Uchino K, Newnham RE: New Piezoelectric Composite Actuator Designs for Displacement Amplification. Proc. 4th Euro Ceramics 1994, 5: 127 - 132.
17. Watanabe J, Sometsugu T, Watanabe Y, Johmura S, Kurihara K, Kazama Y: Multilayer Piezoelectric Ceramic Actuator for High Temperature Use. Hitachi Metal Giho 1993, 9: 59 - 64.
18. Zhang QM, Zhao JZ, Uchino K, Zheng JH: Change of the Weak Field Properties of $\text{Pb}(\text{Zr,Ti})\text{O}_3$ Piezoceramics with Compressive Uniaxial Stresses and Its Links to the Effect of Dopants on the Stability of the Polarizations in the Materials. J. Mater. Res. 1996, [in press].
19. Okada N, Ishikawa K, Murakami K, Nomura T, Ogino M: Improving Hysteresis of Piezoelectric PZT Actuator. Bull. Shizuoka Univ. Electron. Sci. Grad. School 1993, 14: 7 -13.
20. Sakai T, Ishikiriya M, Terai Y, Shimazaki R: Improvement in the Durability of PZT Ceramics for an Actuator. Toyota Tech. Rev. 1992, 42: 52 -59.
21. Takada S: Quality Improvement of Multilayer Piezoelectric Actuator. NEC Giho 1992, 45: 109 -113.
22. Abe K, Uchino K, Nomura Late S: Barium Titanate-Based Actuator with Ceramic Internal Electrodes. Ferroelectrics 1986, 68: 215 - 223.
23. Nagata K, Kinoshita S: Life Time of Multilayer Ceramic Actuator at High Temperature. J. Powder and Metallurgy 1994, 41: 975 - 979.
24. Nagata K, Kinoshita S: Relationship between Lifetime of Multilayer Ceramic Actuator and Temperature. Jpn. J. Appl. Phys. 1995, 34: 5266 -5269.
25. Nagata K, Kinoshita S: Effect of Humidity on Life Time of Multilayer Ceramic Actuator. J. Powder and Metallurgy 1995, 42: 623 - 627.
26. Furuta A, Uchino K: Dynamic Observation of Crack Propagation in Piezoelectric Multilayer Actuators. J. Amer. Ceram. Soc. 1993, 76: 1615 - 1617.
27. Aburatani H, Harada S, Uchino K, Furuta A, Fuda Y: Destruction Mechanisms in Ceramic Multilayer Actuators. Jpn. J. Appl. Phys. 1994, 33: 3091 - 3094.
28. Furuta A, Uchino K: Destruction Mechanism of Multilayer Ceramic Actuators: Case of Antiferroelectrics. Ferroelectrics 1994, 160: 277 - 285.
29. Wang H, Singh RN: Electric Field Effects on the Crack Propagation in a Electro-strictive PMN-PT Ceramic. Ferroelectrics 1995, 168: 281 - 291.
30. Cao HC, Evans AG: Electric-Field-Induced Fatigue Crack Growth in Piezoelectrics. J. Amer. Ceram. Soc. 1994, 77: 1783 - 1786.
31. Schneider GA, Rostek A, Zickgraf B, Aldinger F: Crack Growth in Ferroelectric Ceramics under Mechanical and Electrical Loading. Proc. 4th Int'l Conf. Electronic Ceram. and Appl., Germany, 1994, 1211 - 1216.
32. Suo Z: Models for Breakdown Resistant Dielectric and Ferroelectric Ceramics. J. Mech. Phys. Solids 1993, 41: 1155 - 1176.
33. Hao TH, Gong X, Suo Z: Fracture Mechanics for the Design of Ceramic Multilayer Actuators. J. Mech. Phys. Solids 1996, [in press].
34. Aburatani H, Uchino K, Furuta A and Fuda Y: Destruction Mechanism and Destruction Detection Technique for Multilayer Ceramic Actuators. Proc. 9th Int'l Symp. Appl. Ferroelectrics 1995, 750 - 752.

35. Uchino K, Aburatani H: Destruction Detection Techniques for Safety Piezoelectric Actuator Systems. Proc. 2nd Int'l conf. Intelligent Materials 1994, 1248 - 1256.
36. Sano M, Ohya K, Hamada K, Inoue Y, Kajino Y: Multilayer Piezoelectric Actuator with Strain Gauge. NEC Giho 1993, 46 (10): 100 - 103.
37. Aburatani H, Uchino K: Stress and Fatigue Estimation in Multilayer Ceramic Actuators Using an Internal Strain Gauge. Abstract Annual Mtg. & Expo. Amer. Ceram. Soc., Int'l Symp. Solid-State Sensors and Actuators 1996, SXIX-37-96: 191.
38. Zheng JH, Takahashi S, Yoshikawa S, Uchino K: Heat Generation in Multilayer Piezoelectric Actuators. J. Amer. Ceram. Soc. 1996, [in press].
39. Hirose S, Takahashi S, Uchino K, Aoyagi M, Tomikawa Y: Measuring Methods for High-Power Characteristics of Piezoelectric Materials. Proc. Mater. Res. Soc., '94 Fall Mtg. 1995, 360: 15 - 20.
40. Takahashi S, Sakaki Y, Hirose S, Uchino K: Stability of $\text{PbZrO}_3\text{-PbTiO}_3\text{-Pb}(\text{Mn}_{1/3}\text{Sb}_{2/3})\text{O}_3$ Piezoelectric Ceramics under Vibration-Level Change. Jpn. J. Appl. Phys. 1995, 34: 5328 - 5331.
41. Hirose S, Aoyagi M, Tomikawa Y, Takahashi S, Uchino K: High-Power Characteristics at Antiresonance Frequency of Piezoelectric Transducers. Proc. Ultrasonic Int'l 1995, 1 - 4.
42. Heeg J: Analytical and Experimental Investigation of Flutter Suppression by Piezoelectric Actuation. NASA Tech. Pap., NASA-TP-3241 1993, 47.
43. Mather GP, Tran BN: Aircraft Cabin Noise Reduction Tests Using Active Structural Acoustic Control. Pap. Amer. Inst. Aeronaut Astronaut 1993, AIAA-93-4437: 7.
44. Agrawal BN, Bang H: Active Vibration Control of Flexible Space Structures by Using Piezoelectric Sensors and Actuators. Amer. Soc. Mech. Eng. Des. Eng. Div. 1993, 61:169 - 179.
45. Uchino K, Ishii T: Mechanical Damper Using Piezoelectric ceramics. J. Jpn. Ceram. Soc. 1988, 96: 863 - 867.
46. Wada B: Summary of Precision Actuators for Space Application. JPL Document D-10659, 1993.
47. Yano T, Fukui I, Sato E, Inui O, Miyazaki Y: Impact Dot-Matrix Printer Head Using Multilayer Piezoelectric Actuators. Proc. Electr. & Commun. Soc. (Spring) 1984, 1: 156.
48. Ono Y, Fuda Y: Multilayer Piezoelectric Ceramic Actuator with Interdigital Internal Electrodes for Impact Dot-Matrix Printers. Proc. Symp. on Electro-Magnetic Related Dynamics 1994, 6th: 135 - 138.
49. Yonekubo S: Color Inkjet Printer by Multi-Layer Piezoelectric Actuator. J. Electron. Photo Soc. 1995, 34: 226 - 228.
50. Fukami A, Yano M, Tokuda H, Ohki M, Kizu R: Development of Piezo-electric Actuators and Sensors for Electronically Controlled Suspension. Int. J. Veh. Des. 1994, 15: 348 - 357.
51. Abe S, Igashira T, Sakakibara Y, Kobayashi F: Development of Pilot Injection System Equipped with Piezoelectric Actuator for Diesel Engine. JSAE Rev. (Soc. Automot. Eng. Jpn.) 1994, 15: 201 - 208.
52. Tohda M, Ichikawa S, Uchino K, Kato K: Ultrasonic Linear Motor Using a Multilayered Piezoelectric Actuator. Ferroelectrics (Proc. ECAPD-1/ISAF '88) 1989, 93: 287 - 294.
53. Funakubo T, Tsubata T, Taniguchi Y, Kumei K, Fujumura T, Abe C: Ultrasonic Linear Motor Using Multilayer Piezoelectric Actuators. Jpn. J. Appl. Phys. 1995, 34: 2756 - 2759.
54. Saigoh H, Kawasaki M, Maruko N, Kanayama K: Multilayer Piezoelectric Motor Using the First Longitudinal and the Second Bending Vibrations. Jpn. J. Appl. Phys. 1995, 34: 2760 - 2764.
55. Uchino K: Piezoelectric Actuators/Ultrasonic Motors - Their Developments and Markets. Proc. 9th Int'l Symp. Appl. Ferroelectrics 1995, 319 - 324.
56. Shimoda H, Ohmata J, Okamoto F: Seismic Response Control of a Piping System by a Semiactive Damper with Piezoelectric Actuators. J. Precision Engr. Jpn. 1992, 58: 2111 - 2117.
57. Fujita T: Can Piezoelectric Actuators Control Vibrations of Buildings? New Ceramics 1994, 7 (12): 52 - 55.
58. Koster MP: A Walking Piezo Motor. Proc. 4th Int'l Conf. New Actuators, Germany 1994, 144 - 148.
59. Gross R: A High Resolution Piezo Walk Drive. Proc. 4th Int'l Conf. New Actuators, Germany 1994, 190 - 192.
60. Flynn AM, Tavrow LS, Bart SF, Brooks RA, Ehrlich DJ, Udayakumar KR, Cross LE: Piezoelectric Micromotors for Microrobots. IEEE J. Microelectromechanical Systems 1992, 1: 44 - 51.
61. Goto H: Miniature 2D Optical Scanner and Its Application to an Optical Sensor. J. Opt. Tech. Contact 1994, 32: 322 - 330.
62. Kim HS, Choi SC, Lee JK, Jung HJ: Fabrication and Piezoelectric Strain Characteristics of PLZT Functionally Gradient Piezoelectric Actuator by Doctor Blade Process. J. Korean Ceram. Soc. 1992, 29: 695 - 704.

APPENDIX 45



MATERIALS ISSUES IN DESIGN AND PERFORMANCE OF PIEZOELECTRIC ACTUATORS: AN OVERVIEW

K. UCHENO

International Center for Actuators and Transducers, Materials Research Laboratory, The Pennsylvania State University, University Park, PA 16802, U.S.A.

(Received 4 April 1997; accepted 9 March 1998)

Abstract—The performance of ceramic actuators is dependent on complex factors, which are divided into three major categories: the properties of the ceramic itself, and coupled issues with the device design and drive technique. These important issues are reviewed from these viewpoints. Optimization of ceramic actuator composition and doping is necessary to enhance the induced strains and to stabilize temperature and external stress dependence. The device design affects considerably its durability and lifetime. Failure detection or “health” monitoring methods of ceramic actuators will increase the reliability remarkably. Regarding drive techniques, pulse drive and a.c. drive require special attention; the vibration overshoot after applying a sharp-rise step/pulse voltage to the actuator causes a large tensile force and a long-term application of a.c. voltage generates considerable heat. © 1998 Acta Metallurgica Inc.

1. INTRODUCTION

The application area of ceramic actuators has become remarkably broad [1,2]. New actuator materials such as phase change materials, semiconductive piezoelectric monomorphs, and photostrictors have also been proposed, which seem to be very promising. There still remain, however, problems in reliability that need to be addressed before these devices can become general-purpose commercialized products. The performance of ceramic actuators is dependent on complex factors, which are divided into three major categories: the properties of the ceramic itself, and the coupled issues of the device design and drive technique. This paper reviews these important issues from these viewpoints.

2. MATERIALS IMPROVEMENTS

The reproducibility of the strain characteristics depends strongly on grain size, porosity, and impurity content. Increasing the grain size enhances the magnitude of the field-induced strain, but degrades the fracture toughness and increases the hysteresis [3]. The grain size should be optimized for each application. Hence, fine powders made from wet chemical processes such as coprecipitation and sol-gel will be required.

Porosity does not affect the strain behavior significantly. Figure 1 shows the tip deflection of a unimorph made from a $\text{Pb}(\text{Mg}_{1/3}\text{Nb}_{2/3})\text{O}_3$ -based material plotted as a function of sample porosity [4]. The deflection did not show variation below 8% porosity.

The impurity, donor- or acceptor-type, provides remarkable changes in strain. Figure 2 shows

dopant effects on the field-induced strain in $(\text{Pb}_{0.73}\text{Ba}_{0.27})(\text{Zr}_{0.75}\text{Ti}_{0.25})\text{O}_3$ [5]. Since donor doping provides “soft” characteristics, the sample exhibits larger strains and less hysteresis when driven under a high electric field (1 kV/mm). On the contrary, the acceptor doping provides “hard” characteristics, leading to a very small hysteretic loss and a large mechanical quality factor when driven under a small a.c. electric field (i.e. ultrasonic motor applications!).

Figure 3 shows the temperature rise vs vibration velocity for undoped, Nb-doped, and Fe-doped $\text{Pb}(\text{Zr,Ti})\text{O}_3$ samples. The suppression of heat generation is remarkable in the Fe-doped (acceptor-doped) ceramic [6].

The temperature dependence of the strain characteristics must be stabilized using either composite or solid solution techniques [7]. The recent new trends are found in developing high temperature actuators for engine surroundings and cryogenic actuators for laboratory equipment and space structures.

Ceramic actuators are recommended to be used under bias compressive stress, because the ceramic is, in general, relatively weak under externally applied tensile stress. Figure 4 shows the compressive uniaxial stress dependence of the weak-field piezoelectric constants d in various PZT ceramics. Note the significant enhancement in the d values for hard piezoelectric ceramics [8]. Systematic studies on the stress dependence of induced strains are eagerly awaited, including the composition dependence of mechanical strength.

Although the aging effect is very important, not many investigations have been done so far. The aging effect arises from two factors: depoling and

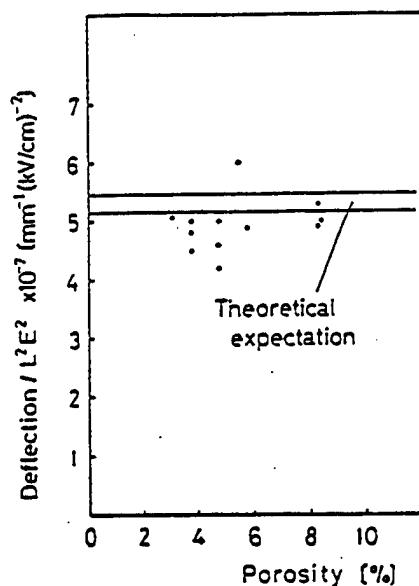


Fig. 1. Tip deflection of a PMN unimorph plotted as a function of the sample porosity.

destruction. Creep and zero-point drift of the displacement are caused by the depoling of the ceramic. Another serious degradation of the strain is produced by a very high electric field under an elevated temperature, humidity, and mechanical stress. Change in lifetime of a multilayer piezoelectric actuator with temperature and d.c. bias voltage has been reported by Nagata [9]. The lifetime $t_{d.c.}$ under d.c. bias field E obeys an empirical rule:

$$t_{d.c.} = AE^{-n} \exp(W_{d.c.}/kT) \quad (1)$$

where n is about 3 and $W_{d.c.}$ is an activation energy ranging from 0.99 to 1.04 eV.

3. NOVEL CERAMIC ACTUATOR MATERIALS

Novel functions of materials are sometimes realized by superimposing two different effects. Newly discovered materials, shape memory ceramics, monomorphs, and photostrictors, use sophisticated coupled effects of piezoelectricity with another phenomenon. The shape memory function arises from a phase transition, while the monomorph and the photostriction are associated with a semiconductor contact effect and a bulk photovoltaic effect, respectively. These "very smart" multifunctional actuator materials will be utilized for future promising devices.

3.1. Shape memory ceramics

Concerning the phase-change-related strains, polarization induction by switching from a macroscopically nonpolar state into a polar state, as in switching from an antiferroelectric to a ferroelectric state, has been proposed. Different from a shape memory alloy, the strain control is achieved electrically in the antiferroelectric ceramic, leading to much faster response and lower drive power than in the thermally-driven alloy. After the first report by Berlincourt *et al.* [10], lead zirconate based ceramics

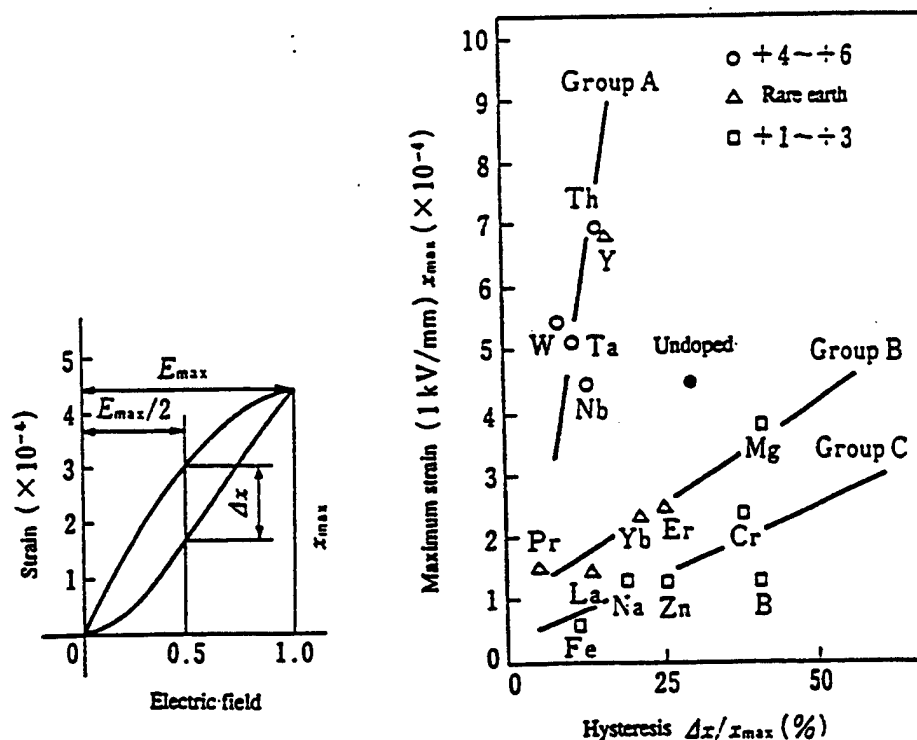


Fig. 2. Dopant effect on the field induced strain in $(\text{Pb}_{0.73}\text{Ba}_{0.27})(\text{Zr}_{0.75}\text{Ti}_{0.25})\text{O}_3$.

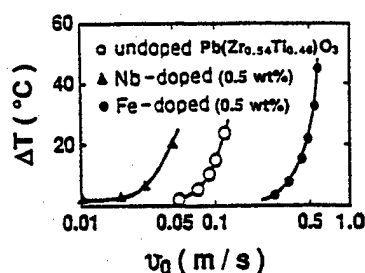


Fig. 3. Temperature rise vs effective vibration velocity for PZT samples doped with Nb or Fe.

were investigated intensively for their field-induced strain characteristics, and a shape memory effect was discovered [11, 12].

Figure 5 shows the field-induced strain curves taken for the lead zirconate stannate based system $[\text{Pb}_{0.99}\text{Nb}_{0.02}((\text{Zr}_x\text{Sn}_{1-x})_1 - y\text{Ti}_y)_{0.98}\text{O}_3]$. The longitudinally induced strain reaches up to 0.4%, which is much larger than that expected in normal piezoelectrics or electrostrictors. A rectangular-shaped hysteresis in Fig. 5 (left), referred to as a "digital displacement transducer" because of the two on/off

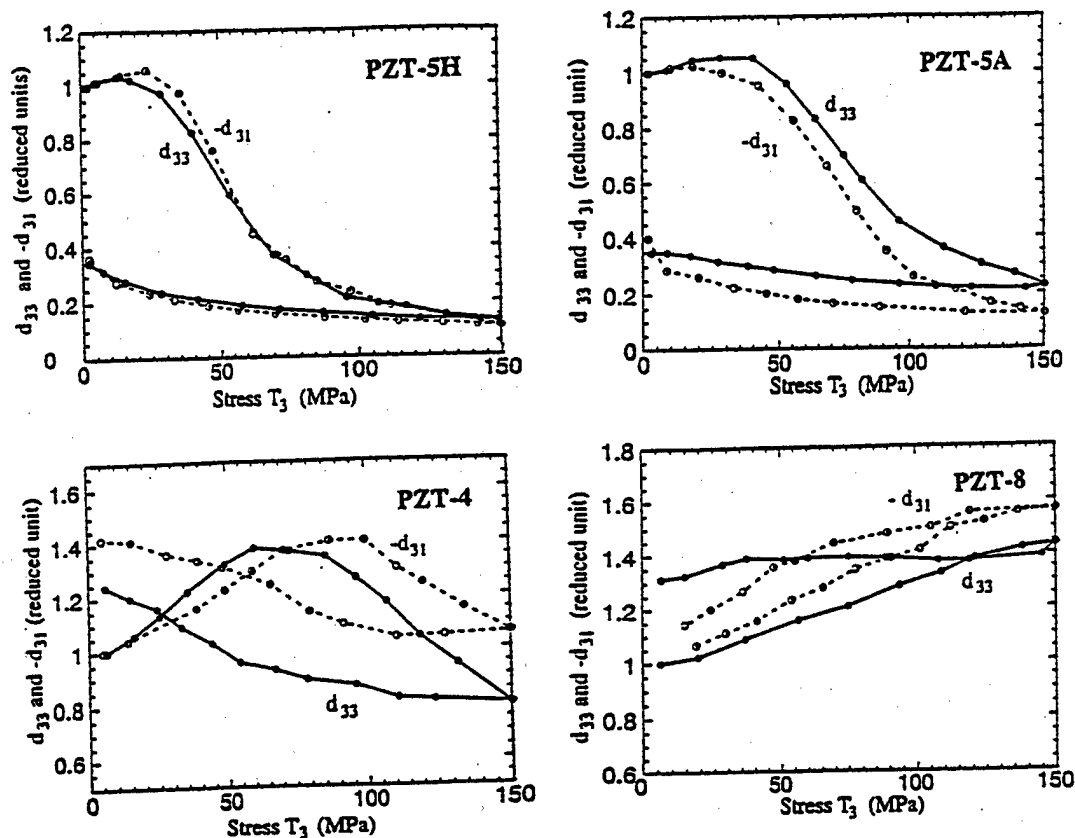


Fig. 4. Compressive uniaxial stress dependence of the weak-field piezoelectric constant d in PZT (from top to bottom, "soft" to "hard").

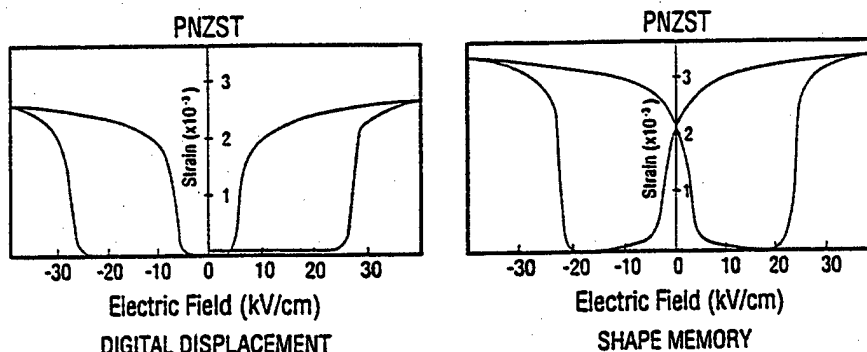


Fig. 5. Electric field-induced strains in phase-change materials $\text{Pb}(\text{Zr.Sn.Ti})\text{O}_3$.

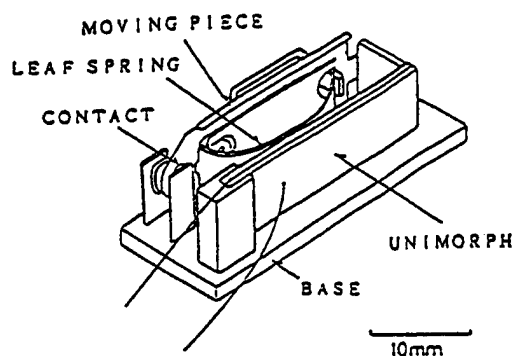


Fig. 6. Latching relay using a shape memory ceramic unimorph.

strain states, is interesting. Moreover, this field-induced transition exhibits a shape memory effect in appropriate compositions [Fig. 5 (right)]. Once the ferroelectric phase has been induced, the material will "memorize" its ferroelectric state even under a zero-field condition, although it can be erased with the application of a small reverse bias field. Recent research by other groups were focused on sample fabrication processes and composition variation for obtaining larger induced strains [13, 14].

This shape memory ceramic was used in energy saving actuators. A latching relay in Fig. 6 was composed of a shape memory ceramic unimorph and a mechanical snap action switch, which was driven by a pulse voltage of 4 ms [15]. Compared with the conventional electromagnetic relays, the new relay was much simpler and compact in structure with almost the same response time.

3.2. Monomorph actuators

A conventional bimorph-type actuator consists of two piezoelectric plates bonded together and electroded so that their piezoelectric expansion/contraction directions are opposing one another. This

actuator will execute a large bending motion of several hundred micrometers with the application of an electric field. The most serious problem associated with this type of actuator concerns the bonding of the ceramic plates and the elastic shim. Poor adhesion between these individual elements results in the rapid deterioration of the device after repeated use and displacement drift (creep). The monomorph actuator made from only one ceramic plate, which can achieve the bending displacement, will be a promising design in its simple construction. While avoiding the bonding problems of the bimorph structure, it also allows for significant cost reduction and production efficiency in manufacturing.

The operating principle is based on the coupling of a semiconductor contact phenomenon with the piezoelectric/electrostrictive effect [16]. When metal electrodes are applied to both surfaces of a semiconductor plate and a voltage is applied as shown in Fig. 7(a), the electric field is concentrated on one side (Schottky barrier), thereby generating a non-uniform field within the plate. By making the piezoelectric slightly semiconductive in this manner, contraction along the surface occurs through the piezoelectric effect only on the side at which the electric field is concentrated. The non-uniform field distribution generated in the ceramic causes an overall bending of the entire plate. Figure 7(b) is a modified structure, where a very thin insulative layer improves the breakdown voltage [17].

Research underway is focused on barium titanate based and lead zirconate titanate based piezoelectric ceramics to which dopants have been added to produce semiconductive properties. The PZT ceramics were made semiconductive by preparing solid solutions with a semiconductive perovskite compound ($K_{1/2}Bi_{1/2}$)ZrO₃. When 300 V was applied to a ceramic plate 20 mm in length and 0.4 mm thick, fixed

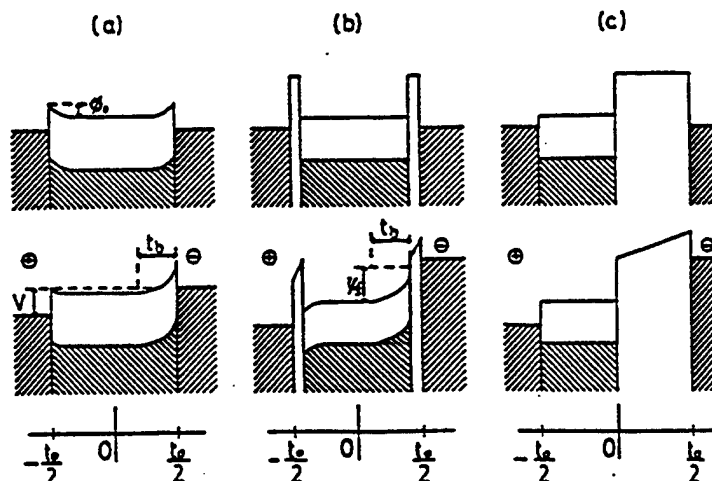


Fig. 7. Energy band models for the monomorph actuator: (a) Schottky type; (b) metal-insulator-semiconductor (MIS) structure with very thin insulative layer; (c) MIS structure with a very thick insulative layer.

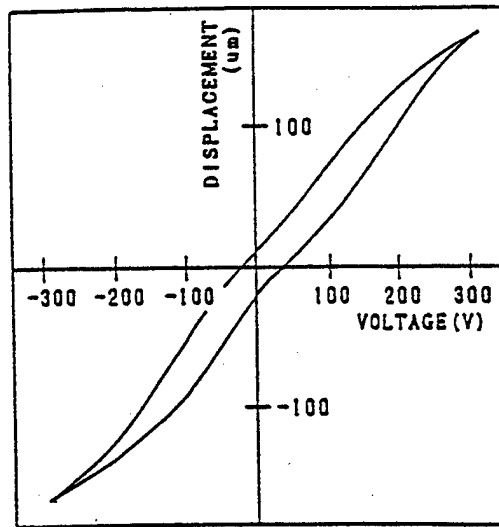


Fig. 8. Drive voltage vs tip displacement of a monomorph plate. The sample was made of $0.7\text{Pb}(\text{Zr}_{0.9}\text{Ti}_{0.1})\text{O}_3-0.3(\text{K}_{1/2}\text{Bi}_{1/2})\text{ZrO}_3$ (20 mm \times 10 mm \times 0.4 mm in size).

at one end, a tip deflection of as much as 200 μm could be obtained, equal in magnitude to that of bimorphs (Fig. 8) [18].

The "rainbow" actuator by Aura Ceramics [19] is a modification of the above-mentioned semiconductive piezoelectric monomorphs, where half of the piezoelectric plate is reduced so as to make a thick semiconductive electrode to cause bending. Figure 7(c) shows the electron energy band structure of the "rainbow". The monomorph was applied to a simple speaker. Though its acoustic characteristics were not satisfactory in comparison with the conventional piezoelectric unimorph types, the mono-

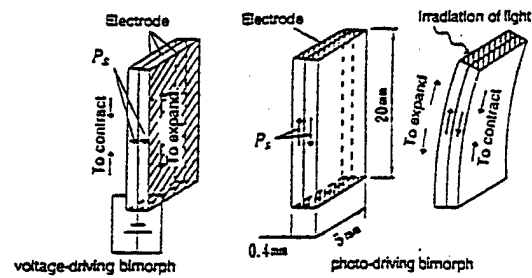


Fig. 9. Structures of voltage- and photo-driven bimorphs and their driving principles.

morph speaker has advantages in mass production and low cost.

3.3. Photostrictive actuators

The photostrictive effect is a phenomenon in which strain is induced in the sample when it is illuminated. This effect is focused especially in the field of micromechanism (or MEMS). On decreasing the size of miniaturized robots/actuators, the weight of the electric lead wire connecting the power supply becomes significant, and remote control will be definitely required for sub-millimeter devices. A photo-driven actuator is a very promising candidate for micro-robots [20].

In certain ferroelectrics, a constant electromotive force is generated with exposure to light, and a photostrictive strain results from the coupling of this bulk photovoltaic effect to inverse piezoelectricity. A bimorph unit has been made from a PLZT 3/52/48 ceramic doped with slight additions of niobium or tungsten [21]. The remanent polarization of one PLZT layer is parallel to the plate and in the

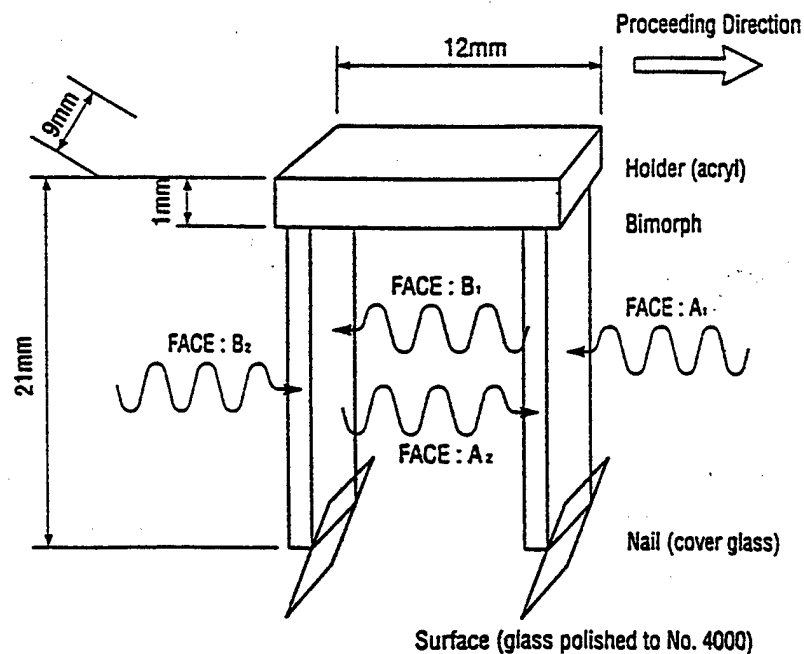


Fig. 10. Structure of the photo-driven micro walking machine and the illumination direction.

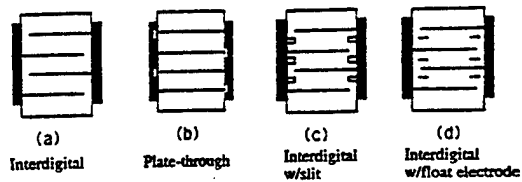


Fig. 11. Various electrode configurations for multilayer ceramic actuators.

direction opposite to that of the other plate. Figure 9 shows the structure of a photo-driven bimorph in contrast to a voltage-driven one. Note the large illumination area, small capacitance, and d_{33} mode, leading to large bending with quick response. When a violet light is irradiated onto one side of the PLZT bimorph, a photovoltaic voltage of 1 kV/mm is generated, causing a bending motion. The tip displacement of 150 μm was obtained within a couple of seconds for a 20 mm bimorph with a thickness of 0.4 mm.

A photo-driven micro walking device, designed to begin moving by light illumination, has been developed [22]. As shown in Fig. 10, it is simple in structure, having neither lead wires nor electric circuitry, with two bimorph legs fixed to a plastic board. When the legs are irradiated alternately with light, the device moves like an inchworm with a speed of 100 $\mu\text{m}/\text{min}$.

Very recently, the photo-mechanical resonance of a PLZT ceramic bimorph has been successfully induced using chopped near-ultraviolet irradiation, using neither electric lead wires nor electric circuits [23]. A dual beam method was used to irradiate the two sides of the bimorph alternately. The achievement of photo-induced mechanical res-

onance suggests the promise of photostrictors as vibration actuators such as "ultrasonic motors".

4. RELIABILITY OF DEVICES

Popular silver electrodes have a serious problem of migration under a high electric field and high humidity. This problem can be overcome with usage of a silver-palladium alloy (or more expensive Pt). To achieve inexpensive ceramic actuators, Cu or Ni electrodes need to be introduced, which require a sintering temperature as low as 900°C. Low temperature sinterable actuator ceramics will be the next target of research.

Delamination of the electrode layer is another problem in multilayer types as well as bimorphs. To enhance adhesion, composite electrode materials with metal and ceramic powder colloid, ceramic electrodes, and electrode configurations with via-holes are recommended [24]. To suppress the internal stress concentration which initiates the crack in the actuator device, several electrode configurations have been proposed, as shown in Fig. 11: plate-through type, slit-insert type, and float-electrode-insert type [25]. The reason why the lifetime is extended with decreasing layer thickness has not yet been clarified.

Lifetime prediction or "health" monitoring systems have been proposed using failure detection techniques [26]. Figure 12 shows such an "intelligent" actuator system with acoustic emission (AE) monitoring. The actuator is controlled by two feedback mechanisms: position feedback, which can compensate the position drift and the hysteresis, and breakdown detection feedback which can stop

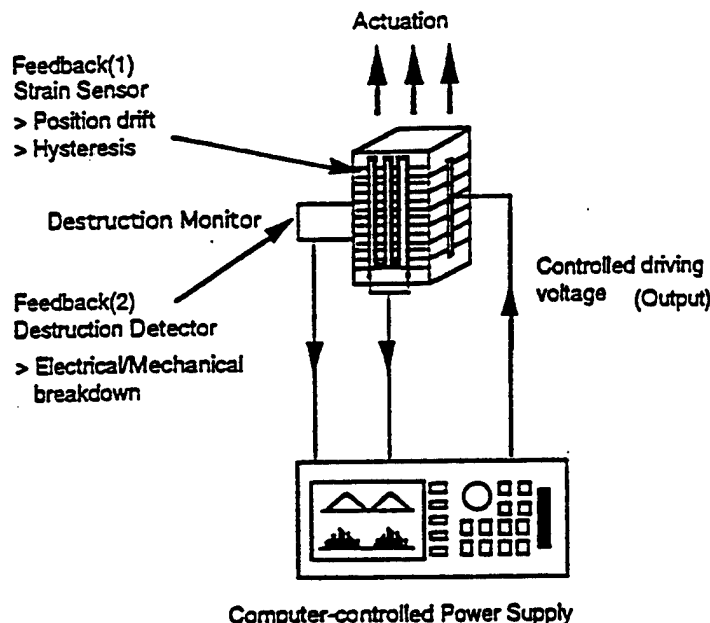


Fig. 12. Intelligent actuator system with both position feedback and breakdown detection feedback mechanisms.

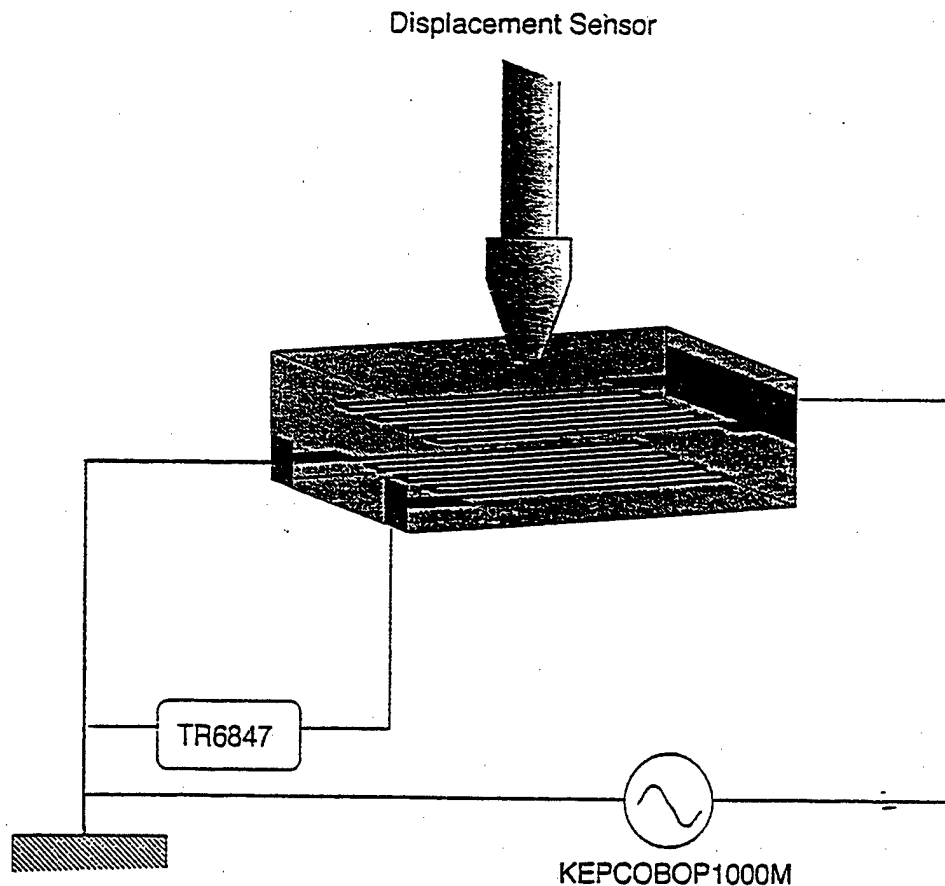


Fig. 13. Multilayer ceramic actuator with a strain-gauge type electrode.

the actuator system safely without causing any serious damage to the work, e.g. in a lathe machine. Acoustic emission measurements of a piezo-actuator under a cyclic electric field provides a good predictor for lifetime. Acoustic emission is detected largely when a crack propagates in the ceramic actuator at maximum speed. During normal drive of a 100-layer piezoelectric actuator, the number of AEs was counted and a drastic increase by three orders of magnitude was detected just before complete destruction. Note that part of the piezo-device can be utilized as an AE sensor.

A recent new electrode configuration with a strain gauge type (Fig. 13) is another intriguing alternative for health monitoring [27]. By measuring the resistance of the strain-gauge shaped electrode embedded in the ceramic actuator, both electric-field induced strain and the symptom of cracks in the ceramic can be monitored.

5. DRIVE TECHNIQUES

Pulse drive of the piezoelectric/electrostrictive actuator generates very large tensile stress in the device, sometimes large enough to initiate cracks. In such cases, compressive bias stress should be

employed on the device through clamping mechanisms such as a helical spring and a plate spring.

Temperature rise is occasionally observed, particularly when the actuator is driven cyclically, i.e. in pulse drive or ultrasonic motor applications. Temperature rise is due to the imbalance between heat generation, basically caused by dielectric hysteresis loss, and the heat dissipation determined by the device size (surface area!) [28]. Figure 14 shows

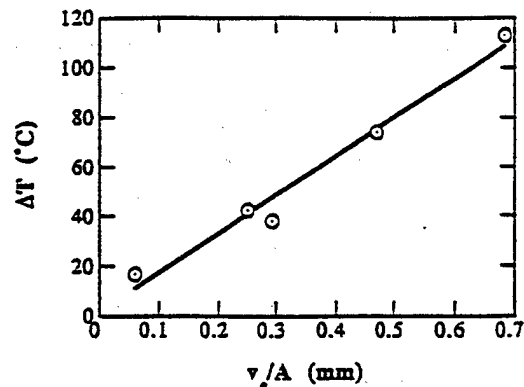


Fig. 14. Temperature rise vs v_e/A for various size multilayer ceramic actuators (applied field: 3 kV/mm at 300 Hz).

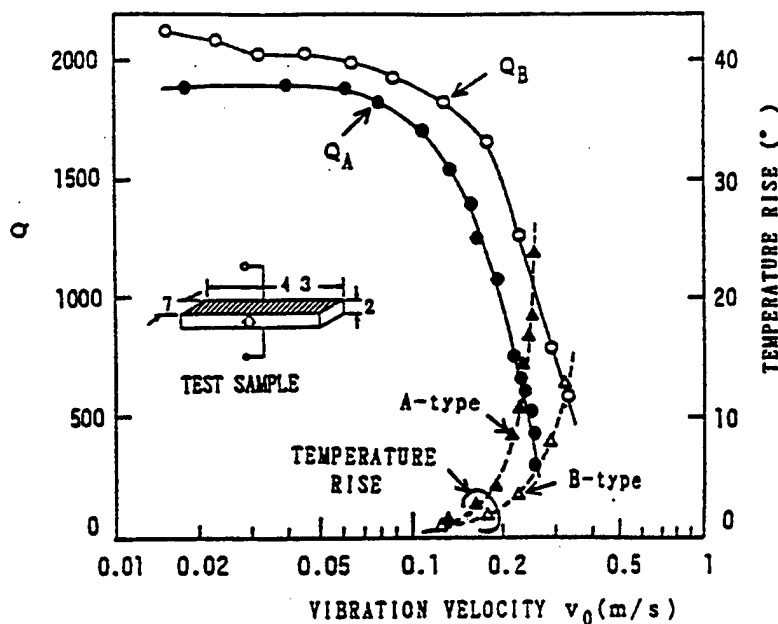


Fig. 15. Vibration velocity dependence of the quality factor and temperature rise for both A- and B-type resonances of a PZT resonator.

a linear relation between temperature rise and the v_e/A value, where v_e is the effective volume and A the surface area of a multilayer actuator, when driven at a fixed magnitude and frequency of the electric field. A suitable drive power or a driving duty ratio needs to be selected so as not to produce a temperature rise of more than 20°C, especially when used in a polymer-embedded state, which suppresses the heat dissipation drastically.

Regarding ultrasonic motors, the usage of the antiresonance mode has been proposed [29]. Quality factor Q and temperature rise have been investigated on a PZT ceramic rectangular bar, and the results for the fundamental resonance (A-type) and antiresonance (B-type) modes are illustrated in Fig. 15 as a function of vibration velocity. It is recognized that Q_B is higher than Q_A over the whole vibration velocity range. In other words, the antiresonance mode can provide the same mechanical vibration level without generating heat.

All the previous ultrasonic motors have utilized the mechanical resonance mode at the so-called "resonance" frequency. However, the mechanical resonant mode at the "antiresonance" frequency reveals higher Q and efficiency than the "resonance" state. Moreover, the usage of "antiresonance", whose admittance is very low, requires low current and high voltage for driving, in contrast to high current and low voltage for the "resonance". This means that a conventional inexpensive power supply may be utilized for driving the ultrasonic motor.

There are many possibilities to improve the durability and reliability of ceramic actuators. Future widespread commercialization appears to be likely.

Acknowledgements—This work was partly supported by U.S. Army Research Office and Office of Naval Research through Contract Nos. DAAL 03-92-G-0244, N00014-91-J-4145, and N00014-96-1-1173.

REFERENCES

1. Uchino, K., *Ceramic Actuators and Ultrasonic Motors*. Kluwer, Dordrecht, 1997.
2. Uchino, K., *MRS Bull.*, 1993, 18, 42.
3. Uchino, K. and Takasu, T., *Inspec.*, 1986, 10, 29.
4. Abe, K., Uchino, K. and Nomura, S., *Japan. J. appl. Phys.*, 1982, 21, L408.
5. Hagimura, A. and Uchino, K., *Ferroelectrics*, 1989, 93, 373.
6. Takahashi, S. and Hirose, S., *Japan. J. appl. Phys.*, 1993, 32, 2422.
7. Uchino, K., Kuwata, J., Nomura, S., Cross, L. E. and Newnham, R. E., *Japan. J. appl. Phys.*, 1981, 20(Suppl. 20-4), 171.
8. Zhang, Q. M., Zhao, J., Uchino, K. and Zheng, J., *J. Mater. Res.*, 1997, 12, 226.
9. Nagata, K., *Mater. Res. Soc. Bull.*, 1993, 18, 42.
10. Berlincourt, D., Krueger, H. H. A. and Jaffe, B., *J. Phys. Chem. Solids*, 1964, 25, 659.
11. Uchino, K. and Nomura, S., *Ferroelectrics*, 1983, 50, 191.
12. Oh, K. Y., Furuta, A. and Uchino, K., *J. Ceram. Soc. Jpn.*, 1990, 98, 905.
13. Pan, W. Y., Zhang, Q., Bhalla, A. and Cross, L. E., *J. Am. Ceram. Soc.*, 1989, 72, 571.
14. Xu, Z., Viehland, D. and Payne, D. A., *J. appl. Phys.*, 1993, 74, 3406.
15. Furuta, A., Oh, K. Y. and Uchino, K., *Sensors Mater.*, 1992, 3, 205.
16. Uchino, K., Yoshizaki, M., Kasai, K., Yamamura, H., Sakai, N. and Asakura, H., *Japan. J. appl. Phys.*, 1987, 26, 1046.
17. Uchino, K., Yoshizaki, M. and Nagao, A., *Japan. J. appl. Phys.*, 1987, 26(Suppl. 26-2), 201.
18. Uchino, K., Yoshizaki, M. and Nagao, A., *Ferroelectrics*, 1989, 95, 161.

19. Furman, F., Li, G. and Haertling, G. H., *Ferroelectrics*, 1994, 160, 357.
20. Uchino, K., *J. Innovations Mater. Res.*, 1995, 1, 11.
21. Tanimura, M. and Uchino, K., *Sensors Mater.*, 1988, 1, 47.
22. Uchino, K., *J. Rob. Mech.*, 1989, 1, 124.
23. Chu, S. Y., Ye, Z. and Uchino, K., *J. Adv. Performance Mater.*, 1994, 1, 129.
24. Abe, K., Uchino, K. and Nomura, S., *Ferroelectrics*, 1986, 68, 215.
25. Aburatani, H., Uchino, K., Furuta, A. and Fuda, Y., Destruction mechanism and destruction detection technique for multilayer ceramic actuators, in *Proc. 9th Int. Symp. Appl. Ferroelectrics*, 1995, p. 750.
26. Uchino, K. and Aburatani, H., Destruction detection techniques for safety piezoelectric actuator systems, in *Proc. 2nd Int. Conf. Intelligent Mater.*, 1994, p. 1248.
27. Uchino, K., Reliability of ceramic actuators, in *Proc. Int. Symp. Appl. Ferroelectrics*, Vol. 2, 1997, p. 763.
28. Zheng, J., Takahashi, S., Yoshikawa, S., Uchino, K. and de Vries, J. W. C., *J. Am. Ceram. Soc.*, 1996, 79, 3193.
29. Hirose, S., Aoyagi, M., Tomikawa, Y., Takahashi, S. and Uchino, K., High-power characteristics at anti-resonance frequency of piezoelectric transducers, in *Proc. Ultrasonic Int.*, 1995, p. 1.

APPENDIX 46

Design and fabrication of a high performance multilayer piezoelectric actuator with bending deformation

Kui Yao,^{1,2*} Weiguang Zhu,² Kenji Uchino³, Zhe Zhang,² and Leong Chew Lim¹

¹Institute of Materials Research and Engineering, Singapore 119260

²Microelectronics Center, School of Electrical and Electronic Engineering, Nanyang Technological University, Singapore 639798

³International Center for Actuators and Transducers, Materials Research Laboratory, The Pennsylvania State University, University Park, PA 16802, USA

Abstract

A new bending mode multimorph actuator was designed and fabricated successfully by a multiple screen-printing process. Unlike the conventional bimorph actuator, in which the bend occurs in the thickness direction, the bend in the multimorph actuator occurs in the widthwise direction due to synchronistical deformation of each single monolithic layer in the multilayer structure. The theoretical analysis and experimental measurements were conducted to study the performance of this type of actuator, and a comparison was made with the conventional bimorph actuator. Larger displacement, higher resonance frequency, and much larger blocking force could be achieved with the multimorph actuator than with a bimorph actuator of similar dimensions. The multimorph actuator presented in this paper provides a valuable alternative for actuator applications beyond those available with the popular bimorph and longitudinal multilayer actuators.

Key words: piezoelectric actuator, lead zirconate titanate, multilayer, multimorph structure, bimorph structure, screen-printing.

* Current address: A5 Materials Research Laboratory, The Pennsylvania State University, University Park, PA 16802, USA. E-mail: k-yao@imre.org.sg

I. INTRODUCTION

Multilayer and bimorph actuators are two popular piezoelectric ceramic designs currently in wide use [1]. The multilayer piezoelectric actuator has several advantages: quick response, large generative force, and high electromechanical coupling. Many applications such as a printer head [2] and an X-Y stage [3] have been attempted using the multilayer actuators. However, higher displacement/voltage sensitivity can only be achieved for this type of actuator by greatly increasing the number of piezoelectric layers and decreasing the thickness of each layer, hence resulting in higher cost, lower reliability, and larger dimensions. Compared with the multilayer stack structure, the bimorph actuator consists of a simple, low cost structure, that has been applied in tracking control systems [4], swing CCD mechanisms [5], etc. Unfortunately this kind of actuator can only provide a small generative force and has a low resonance frequency, thus limiting its responsivity.

In some specific cases such as the magnetic head tracking mechanism in hard disk drive of computer, high displacement/voltage sensitivity as well as high resonance frequency is essential for the successful application of an actuator in the servo control system. The applicability of the aforementioned two types of actuators for this case is restrained due to the low resonance frequency of the bimorph structure and the low displacement/voltage sensitivity of the multilayer structure. It was disclosed that a multilayer piezoelectric actuator could be built in the distal end portion of the head supporting arm of the hard disk drive so as to precisely position the head [6]. However, in order to achieve sufficient displacement, this required large numbers of piezoelectric layers coupled with increasing cost, and/or a required voltage that is too high for hard

disk drive applications. Moreover, the large mass and moment of inertia to be driven by the d_{33} based longitudinal actuator and the corresponding additional mechanical structure limit the feasibility of the entire dynamic mechanism.

A new design for a piezoelectric actuator compromising the merits of high displacement/voltage sensitivity, high resonance frequency, and low cost is presented in this paper. Such a multilayer piezoelectric actuator essentially consists of a multilayer bending mode actuator with displacement occurring in the transverse widthwise direction. The blocking force, resonance frequency and even the displacement/voltage sensitivity can be greatly improved over the conventional bimorph actuator. This new design is substantially different from the previously reported multimorph bending actuator [7], in which displacement occurs in the thickness direction, as is the case for the bimorph structure.

In the conventional fabrication process for bimorph actuators, two ceramic plates are bonded using cohesive coating such as resin. However, this method is not efficient to realize a multilayer structure capable of low driving voltage, miniaturization and hybridization. Therefore, a thick-film multiple screen printing process followed by co-firing of metal electrodes and ceramic layers has been applied to produce the newly designed bending mode actuators. Some studies about fabricating d_{33} based longitudinal piezoelectric multilayer actuators by the screen printing methods have been reported in previous literature [8], [9]. The preparation process is compatible with the industrial manufacturing process so as to keep high yield and productivity at low cost.

II. DESIGN OF THE ACTUATOR

Figure 1 shows an exploded view of the new multilayer piezoelectric device design comprising a plurality of piezoelectric layers alternately laminated with a plurality of electrode layers. Each of electrode layers includes a separate pair of electrodes with each separate electrode portion consisting of a finger at its terminal point. The two fingers of each odd numbered electrode layer are spaced by much smaller distance in the widthwise direction, i.e. the y direction in Figure 1, than that between the fingers of even numbered electrode layers. Therefore, the four groups of exposed terminals of the fingers can be connected to their separate external electrical collectors, as shown in Figure 2.

Thus, each piezoelectric layer is sandwiched between two pairs of electrode, and the two electrodes of each pair are opposed in the thickness direction, i.e. the z direction. From the view along the length direction, i.e. the x direction, the multilayer actuator seems to be divided into two symmetric portions, which are designated as A and B respectively in Figure 2. The poling electric field can be applied to each half of each piezoelectric ceramic layer separately through the external electrodes, as depicted in Figure 2. The resulted polarization vectors of all the piezoelectric ceramic layers in each portion of the actuator are parallel with each other in the z direction in the same portion. However, the polarization vector of the piezoelectric ceramic layers in portion A is anti-parallel with those in portion B.

The driving field is applied such that on each half of piezoelectric layer the electric field is parallel to the polarization vector in each layer of one portion of the actuator, but anti-parallel to the polarization vector in each layer of the other portion. Consequently, each piezoelectric ceramic layer in one portion of the multilayer body extends

synchronistically in the x direction, and each layer in another portion of the multilayer body contracts in the x direction. Thus, a transverse bending deformation is realized in the y direction. Clamping the end of the actuator to form a cantilever beam, a displacement of the free end is produced in the widthwise direction.

The poling mode shown in Figure 2 is not only for the designed structure. Another working mode is that in which the poling vector of all layers are kept parallel but the applied drive electric field in the two portions are anti-parallel with each other.

III. PREPARATION AND MORPHOLOGY OF THE ACTUATOR

The samples were prepared from lead zirconate titanate (PZT) by a multiple screen-printing process. PZT ceramic powders (Shanghai Ceramic Institute, China) with 4wt% lead oxide powders added, were dispersed in a commercial organic vehicle and then the mixture was ball-milled to prepare the thick-film paste. Excess PbO was added to the PZT powders to promote the sintering process and to compensate Pb loss due to vaporization at high firing temperature.

The prepared PZT paste and commercial Pd-Ag paste were printed on Al_2O_3 substrate alternatively to construct the multilayer structure. Each PZT layer is rectangular shaped, and each electrode layer includes a separate pair of electrodes such that the odd numbered electrode and even numbered electrode layers have the terminal fingers spaced by a different distance in the widthwise direction, as depicted in Figure 2. Figure 3 shows the photo of the PZT multilayer green bodies printed on 2 x 2 inches Al_2O_3 substrates. Multiple printings are required for each PZT layer to achieve the expected thickness.

After released from the substrate, the multilayer green bodies were co-fired at 1130°C in a furnace.

Each fired PZT layer is about 60-70 μm and each electrode layer is approximately 3-5 μm in thickness. Multilayer samples with 7-15 layers were fabricated. The Scanning Electron Microscopic (SEM, JEOL-JSM-5410LV) photo of the cross-section of the multilayer sample, as presented in Figure 4, shows a dense co-fired multilayer structure. Two adjacent groups of the edges of the electrode fingers, exposed in the side surface of the laminate body for electrode connection, are shown in Figure 5. The electrode terminal groups are clearly spaced from each other so as that they can be connected to separate electrical leads.

Four fine leads were bonded to the four groups of exposed edges of the electrode finger, respectively, as illustrated in Figure 2. The final multimorph sample consisted of an overall width of 3.5 mm, and a length of 11 mm. The total thickness of the sample depends on the number of the layers. For 7-layer to 15-layer samples, the thickness is about 0.44 to 0.95 mm, respectively.

Finally, the multilayer samples were poled as illustrated in Figure 2 with a voltage of 250 V for 30 min to obtain the multimorph actuators.

IV. EXPERIMENTAL MEASUREMENTS

The multimorph actuator was clamped in one end to form a cantilever structure, as shown in Figure 6, and the bend displacement δ in widthwise direction was measured by an HP 5529A due-frequency dynamic laser interferometer controlled by a host computer. The laser interferometer was set on an optical table and was well shielded to minimize

environmental disturbance. In terms of the Doppler-shift effect, the displacement of the actuator response was determined from variations in frequency of the reflected laser beam from a highly reflective mirror, which was adhered to the lateral surface of the free end of the actuator. The specified resolution of the system was 1 nm for static displacement measurement and 10 nm for the time based dynamic measurement, respectively.

Figure 7 shows the static displacement of a cantilevered multimorph actuator in response to a step voltage. The efficient length of the cantilevered sample, excluding the length of the clamped stub, was about 9.2 mm. The stepped voltage was increased from 0 to 12 V (corresponding to 0.19 kV/mm), and then decreased from 12 to -12 V and finally increased from -12 to 0 V to form one cycle, with an increment of 1 V of each step. The bending displacement was increased from 0 to 1.3 μm with the drive voltage increased from 0 to 12 V, and then changed from 1.3 μm to about -1.3 μm when the drive voltage decreased from 12 to -12 V step by step. Finally, with the voltage coming back to 0 from -12 V, the displacement returned to near 0 from -1.3 μm . Figure 7 also indicates that the displacement was approximately linear with the applied voltage.

Figure 8 presents the dynamic displacement behavior of the multimorph actuator sample under a square-wave driving signal. The input was 6 V at a frequency of 50 Hz. The measured displacement response is reasonably rapid, stable and repeatable. The displacement response to a step voltage in a short period is magnified in Figure 9. The roughness of the dynamic displacement response curve is attributed to the limited number of data points due to the measurement system. The frequency of the transient vibration of the actuator accompanying the displacement overshoot should be mathematically

equivalent to the resonance frequency of the actuator. From the measurement result in Figure 9, the resonance frequency of the actuator is determined to be about 20.5 kHz.

V. THEORETICAL ANALYSIS

The theoretical analysis in this section is aimed to clarify the performance of the cantilever structure comprising the piezoelectric multimorph actuator, as illustrated in Figure 6. The resonance frequency, displacement, and the blocking force of the actuator are analyzed below.

A. Resonance frequency

If the effect of the electrode layers can be ignored, the stiffness of the cantilevered structure in the widthwise direction can be expressed as:

$$E_p I = \frac{nrw^3}{12} E_p \quad (1)$$

where E_p is the Young's modulus of the PZT ceramic, I is the moment of inertial of the cantilevered structure. n and t is the number of the PZT layers and the thickness of each layer, respectively, and w is the width of the actuator.

By only considering the internal shear forces and moment in the y direction, and neglecting the other forces in the y direction and all the forces in other directions in Figure 6, the followed Euler's beam equation [10] can be used to describe the elastic vibration in the width direction,

$$\frac{E_p I}{m} \frac{\partial^4 y}{\partial x^4} + \frac{\partial^2 y}{\partial \tau^2} = 0 \quad (2)$$

where m is the mass of the beam per unit length along x axis, and τ stands for time.

The equation (2) can be solved under the boundary conditions of the one-end clamped cantilever beam, and the fundamental natural bending resonance frequency f_r in the widthwise direction can be obtained as:

$$f_r = \frac{\lambda_1^2}{2\pi^2} \sqrt{\frac{E_p I}{m}} = \frac{\lambda_1^2 w}{4\pi^2} \sqrt{\frac{E_p}{3\rho}} \quad (3)$$

where ρ is the density of the PZT ceramic, and $\lambda_1=1.875$. The resonance frequency is proportional to the width of the multilayer body but not related to the thickness.

B. Displacement

The multimorph actuator can be divided into three portions along the width direction, i.e., two symmetric active portions with electrode layers sandwiched, and the central inactive portion without electrodes. The strain and stress of the two active portions in the length direction, S_1 and T_1 , can be expressed according to their piezoelectric and elastic equations:

$$S_1 = s_{11}^E T_1 \pm d_{31} E_3 \quad (4)$$

$$T_1 = E_p S_1 \pm E_p d_{31} E_3 = E_p \kappa y \pm E_p d_{31} E_3 \quad (5)$$

where s_{11}^E is the compliance constant under constant electric field, d_{31} is the piezoelectric constant, E_3 is the electric field in z direction, κ is the curvature of the bending cantilever

[11]. The positive and negative signs in the equations are used when electrical field parallel and anti-parallel to the polarization vector.

The stress along the x direction in the inactive portion of the ceramic between the two active portions is:

$$T_1 = E_p \kappa y \quad (6)$$

Thus, the torque M due to the elastic force can be expressed as,

$$M = \int_{-\frac{w_0}{2}}^{\frac{w_0}{2}} (E_p \kappa y + E_p d_{31} E_3) n t y dy + \int_{-\frac{w_0}{2}}^{\frac{w_0}{2}} E_p \kappa y n t y dy + \int_{\frac{w_0}{2}}^{\frac{w}{2}} (E_p \kappa y - E_p d_{31} E_3) n t y dy \quad (7)$$

The curvature of the cantilever beam at zero loading can be determined by setting $M=0$ in equation (7), and the displacement δ of the free end of the cantilever beam can be hence determined by equation (8),

$$\delta = \frac{\kappa l^2}{2} = \frac{3l^2(w^2 - w_0^2)}{2w^3 t} d_{31} V \quad (8)$$

where V is the voltage applied to each PZT layer. Taking account of $w_0 \ll w$, equation (8) can be simplified as:

$$\delta = \frac{3l^2}{2wt} d_{31} V \quad (9)$$

When $w_0 < 0.1 w$, the error from ignoring the effects of w_0 is less than 1%.

According to equation (9), for an actuator with specific length and d_{31} , the displacement is inversely proportional to the total width and thickness of each PZT layer under constant voltage, but not related to the number of the layers. Under the condition of

constant electric field, the displacement becomes independent on the thickness of a single PZT layer.

C. Blocking force

Another important parameter for the bending mode actuator is the blocking force at the tip of the beam to characterize the strength of the actuator. The blocking force is an external equivalent force, F_b , which can be applied at the tip to counteract the electric field induced tip deflection, and hence to maintain the tip of the cantilever at a fixed original position. It is also termed the maximum generative force. For the cantilever beam, the force required to make the beam produce a displacement δ is [11]:

$$F_b = \frac{3E_p I \delta}{l^3} \quad (10)$$

Substituting equation (10) by equations (1) and (8), F_b can be expressed as,

$$F_b = \frac{3nt(w^2 - w_0^2)}{8l} E_p d_{31} E_3 \quad (11)$$

By ignoring the minor effect of w_0 , equation (11) can be further simplified as,

$$F_b = \frac{3nw^2}{8l} E_p d_{31} V \quad (12)$$

When the length and the material are fixed, the blocking force of the actuator is proportional to the number of the layers and the square of the width under the condition of constant voltage.

D. Calculated results for the measured sample

The performance of the PZT multimorph actuator can be calculated based on the above-obtained equations and the material's parameters. The density ρ , Young's modulus E_p and piezoelectric constant d_{31} for the PZT material used in this work are about $7.5 \times 10^3 \text{ kg/m}^3$, $6.5 \times 10^{10} \text{ N/m}^2$, and $175 \times 10^{-12} \text{ C/N}$, respectively. The resonance frequency calculated from equation (3) is 19.7 kHz for the multimorph actuator sample. When 12 V is applied, the displacement and the blocking force, calculated from equations (9) and (12), are 1.2 μm and 1.02 N, respectively. Therefore, the calculated displacement and resonance frequency are very close to the measured values.

It is useful to make a comparison with the well-known bimorph actuator for clarifying the outstanding features of the new multimorph design. Figure 10 shows the cantilever beam comprising a PZT bimorph. The fundamental resonance frequency f_r' , displacement δ' , and the blocking force F_b' are expressed as follows,

$$f_r' = \frac{3.52t'}{4\pi l'^2} \sqrt{\frac{E_p}{3\rho_p}} \quad (13)$$

$$\delta' = \frac{3l'^2}{t'^2} d_{31} V \quad (14)$$

$$F_b' = \frac{3w't'}{4l'} E_p d_{31} V \quad (15)$$

where V is the voltage applied to each PZT layer of the bimorph [12]. The theoretically calculated performance parameters of the conventional bimorph actuator and our multimorph actuator are listed in Table I. The dimensional data of the bimorph structure are supposed to be similar to those of the multimorph counterpart. The displacement of the multimorph actuator is 2 times that of the bimorph actuator and the blocking force is

more than 27 times. Moreover, the resonance frequency is about 3.7 times that of the bimorph actuator. It is obvious that the multimorph structure is superior to the bimorph structure with the similar dimension as a piezoelectric actuator.

VI. DISCUSSION

Comparing the structures shown in Figures 6 and 10, it can be found that the multimorph actuator is distinct from the bimorph actuator in the direction in which the transverse bend occurs. This distinction is one of the essential reasons for the subsequent difference in performance. Another feature is that the multilayer structure has been adopted into a multimorph actuator.

For the bimorph actuator, the bend of the cantilever structure occurs in the thickness direction in which the two plates are bonded i.e., the z direction in Figure 10. This direction is the same direction in which the drive electric field is applied. Increasing the dimension of the actuator in which bend occurs is advantageous to improve the resonance frequency and the blocking force, however is disadvantageous to increase the bend displacement. According to equations (13) - (15), the resonance frequency and the blocking force of the bimorph actuator is proportional to the thickness t' , but the displacement/voltage sensitivity is inversely proportional to t'^2 . The quadratically inverse proportion relation is attributed to the consistence of the electric field direction and the bending direction, which results in the decrease of the efficient electric field with increasing thickness under constant voltage and hence further aggravates the thickness-dependent decrease of the displacement accordingly. Therefore, the improvement of the resonance frequency and blocking force by improving the thickness can only be achieved

at a great sacrifice of the displacement/voltage sensitivity. The common improvement of the resonance frequency and the displacement/voltage sensibility at the same time is restrained to a great extent by the bimorph characteristics.

Unlike the bimorph structure, the transverse bend of the multimorph actuator occurs in the widthwise direction rather than in the thickness and the lamination direction, in which the drive voltage is applied. According to the equations (3) and (12), the resonance frequency increases linearly with the width w and the blocking force increases quadratically. Although the displacement decreases linearly with w according to the equation (9), this unfavorable effect is substantially smaller than that for the bimorph structure. The displacement/voltage sensitivity of the bimorph degrades quadratically with thickness but its blocking force only linearly increase with thickness.

Since the width of the multimorph structure is actually much larger than the thickness of the bimorph without the unfavorable effect of decreasing the efficient electric field, the multimorph structure can possess a higher resonance frequency and a much larger blocking force. Anyway, the unfavorable side-effect of the decreased displacement/voltage sensitivity due to the large dimension in width still exists for the multimorph actuator. even if this side-effect is not so strong as in the case of the bimorph actuator according to the above analyses. Thus, the multilayer structure is adopted into our actuator in order to improve the efficient driving electric field under constant voltage, and the displacement/voltage sensitivity, which inversely proportional to the thickness of each PZT single layer.

It should be noted that the resonance frequency and the displacement of the multimorph actuator are independent on the number of the PZT layers, as expressed in

equations (3) and (9). The number of the laminated layers can be reduced to fewer and even single layer for various applications without affecting the resonance frequency and displacement. This differs from longitudinal piezoelectric multilayer actuators [13], in which the great number of the laminated layers is a prerequisite to produce sufficient displacement under a very low drive voltage. Thus, the cost of the multimorph actuator can be reduced over that of the longitudinal multilayer actuator due to its small number of laminated piezoelectric layers. The displacement of a longitudinal multilayer with such a small number of active layers is much smaller than the displacement of the multimorph actuator. For example, a 7 layer multimorph actuator can produce a displacement of more than 30 times that of the longitudinal multilayer actuator under a specific drive voltage.

According to equation (12), the blocking force is proportional to the number of the laminated layers. The strength and generative force of the multimorph actuator can be improved by increasing the number of the laminated piezoelectric layers. In comparison with the bimorph structure of a similar size, the blocking force of the multimorph actuator is tens times that of the bimorph structure and on the order of Newtons. This is a very appreciable force for bend mode piezoelectric actuator with such a small size.

Since the displacement of the multimorph actuator is derived from the bending mode, the generative force and the resonance frequency are still lower than the longitudinal multilayer piezoelectric actuator. However, the new multimorph actuator presents a useful compromise amongst the displacement, resonance frequency, blocking force and cost. From a comprehensive evaluation on the performance and cost, the multimorph actuator overcomes or ameliorates one or more of the disadvantages of the conventional bimorph and longitudinal multilayer actuators, and hence provides a valuable alternative

for actuator applications. For example, such a multimorph actuator with a very low drive voltage, large servo bandwidth and high displacement/voltage sensitivity, are particularly suitable to be applied for the servo control system in the magnetic head tracking mechanism in the hard disc drive of computers [14], [15].

VII. CONCLUSIONS

A bending mode multimorph actuator has been designed and successfully fabricated by a multiple screen-printing process. The bend displacement occurs in the widthwise direction, not in the thickness direction as in the conventional bimorph actuator. By both theoretical analysis and actual measurements, it was found that larger displacement, higher resonance frequency, and much larger blocking force could be achieved with the multimorph actuator than with the bimorph actuator of similar size. It is believed that the presented multimorph actuator provides a valuable alternative for piezoelectric actuator applications in addition to existing conventional bimorph and longitudinal multilayer actuators.

ACKNOWLEDGMENTS

The authors gratefully acknowledge the support of Data Storage Institute of Singapore and discussions with Dr Qing-Ming Wang.

REFERENCES

- [1] K. Uchino, *Piezoelectric Actuators / Ultrasonic Motors*. Boston: Kluwer Academic Publishers, 1996.
- [2] T. Kitahara, "Ink jet head with multilayer piezoelectric actuator," in *Proc. IS&T's 11th International Congress on Advances in Non-Impact Printing Technologies*, 1995, pp. 346-349.
- [3] K. Mori, T. Kumagae, and H. Hirai, "Ultrasonic linear motor for a high precision X-Y stage," in *Proc. IEEE Ultrason. Symp.*, 1989, pp. 657-660.
- [4] Z. W. Jiang, S. Chonan, and J. Tani, "Tracking control of a miniature flexible arm using piezoelectric bimorph cell," *Int. J. Robotics Res.*, Vol. 11, No. 3, pp. 260-267, 1992.
- [5] P. Li, and Y. Wen. "Image resolution improvement by swing CCD array imager in two dimensions and its signal processing," in *Proc. SPIE*, 1994, Vol. 2308, Part 2, pp. 915-920.
- [6] K. Mori, H. Hirai, H. Otsuki, T. Takahashi, J. Naruse, Y. Nishimura, and M. Kawamoto, "Disk system with sub-actuators for fine head displacement," U.S. Patent 5189578, 1993.
- [7] Y. Zhao, and B. Jones. "Pulse width modulated reinforced piezo air jet actuators," *Mechatronics*, Vol. 7, No. 1, pp. 11-25, 1997.
- [8] H. Moilanen, J. Lappalainen, and S. Leppavuori, "Development of piezoelectric micromovement actuator fabrication using a thick-film double-paste printing method," *Sensors and Actuators A*, Vol. 43, pp. 357-365, 1994.

- [9] K. Yao, and W. Zhu, "Improved preparation procedure and properties for multilayer piezoelectric thick-film actuator," *Sensors and Actuators A*, Vol. 71, pp. 139-143, 1998.
- [10] M. L. James, G. M. Smith, J. C. WOLFORD, and P. W. Whaley, *Vibration of Mechanical and Structural Systems: With Microcomputer Applications*. New York: Harper & Row, Publishers, pp. 600-609, 1989.
- [11] S. P. Timoshenko, and J. M. Gere, *Mechanics of Materials*. New York: D. Van Nostrand Company, pp. 167-179, 1972.
- [12] J. G. Smits, S. I. Dalke, and T. K. Cooney, "The constituent equations of piezoelectric bimorphs," *Sensors and Actuators A*, Vol. 28, pp. 41-61, 1991.
- [13] S. Takahashi, "Longitudinal mode multilayer piezoelectric actuators," *Ceramic Bulletin*, Vol. 65, No. 8, pp. 1156-1157, 1986.
- [14] L. S. Fan, H. H. Ottesen, T. C. Reiley, and R. W. Wood, "Magnetic recording head positioning at very high track densities using a microactuator-based, two-stage servo system," *IEEE Tans. on Ind. Elect.*, Vol. 42, No. 3, pp. 222 - 233, 1995.
- [15] K. Takaishi, T. Imamura, Y. Mizoshita, S. Hasegawa, T. Ueno, and T. Yamada, "Micromotor control for disk drive," *IEEE Trans. on Mag.*, Vol. 32, No. 3, pp. 1863-1866, 1996.

FIGURE CAPTIONS

- Figure 1 An exploded view for the assembly of the multiple electrode and piezoelectric layers in the multilayer bending mode actuator, 1 – electrode layers, 2 – piezoelectric layers, and 3 – the electrode fingers.
- Figure 2 The structure and working principle for the multilayer bending mode actuator, 1 – electrode layers, 2 – piezoelectric layers, 3 – the terminals of the electrode fingers, 4 – the four external electrical leads, A and B stand for the two symmetric portions of the actuator.
- Figure 3 The photo of the PZT multilayer green bodies printed on the 2 x 2 inches Al_2O_3 substrate.
- Figure 4 The cross-sectional morphologies of the PZT multilayer co-fired with Pd-Ag electrode.
- Figure 5 Two adjacent groups of the terminals of the electrode fingers, which are exposed in the side surface of the laminate body for electrical connection, 1 – exposed terminals of the electrode fingers, and 2 – PZT.
- Figure 6 The schematically illustrated structure of the cantilevered PZT multimorph actuator.
- Figure 7 The static displacement of a multimorph actuator sample in widthwise direction in response to step voltage ($l = 9.2$ mm, $w = 3.5$ mm, $w_0 = 0.3$ mm, $n = 15$, and $nt = 0.945$ mm. The designations as specified in Figure 6).
- Figure 8 The dynamic displacement behavior of a multimorph actuator sample under a square-wave driving signal ($f = 50$ Hz, $V = 6$ V, $l = 9.2$ mm, $w = 3.5$ mm,

$w_0 = 0.3$ mm, $n = 15$, and $nt = 0.945$ mm. The designations as specified in Figure 6).

Figure 9 The real time transient vibration of a multimorph actuator sample in response to a step voltage ($l = 9.2$ mm, $w = 3.5$ mm, $w_0 = 0.3$ mm, $n = 15$, $nt = 0.945$ mm, and $V = 6$ V. The designations as specified in Figure 6).

Figure 10 The schematically illustrated structure of the cantilevered bimorph actuator.

Table I Comparison between the calculated performance parameters of the cantilevered bimorph actuator and the new multimorph actuator with similar dimensions.*

Actuators	Conventional bimorph	New multimorph
Resonance frequency f_r	5.3 kHz	19.7 kHz
Displacement δ ($V = 12$ V)	0.6 μm	1.2 μm
Blocking force ($V = 12$ V)	0.037 N	1.02 N

*For the multimorph actuator, $l = 9.2$ mm, $w = 3.5$ mm, $w_0 = 0.3$ mm, $n = 15$, $n_t = 0.945$ mm; for the bimorph actuator, $l' = 9.2$ mm, $w' = 3.5$ mm, $t' = 0.945$ mm. The designations of the dimensions for the two actuators are specified in Figures 6 and 10, respectively. The voltage given in this table is applied to each layer of the multimorph actuator and each layer of the bimorph actuator.

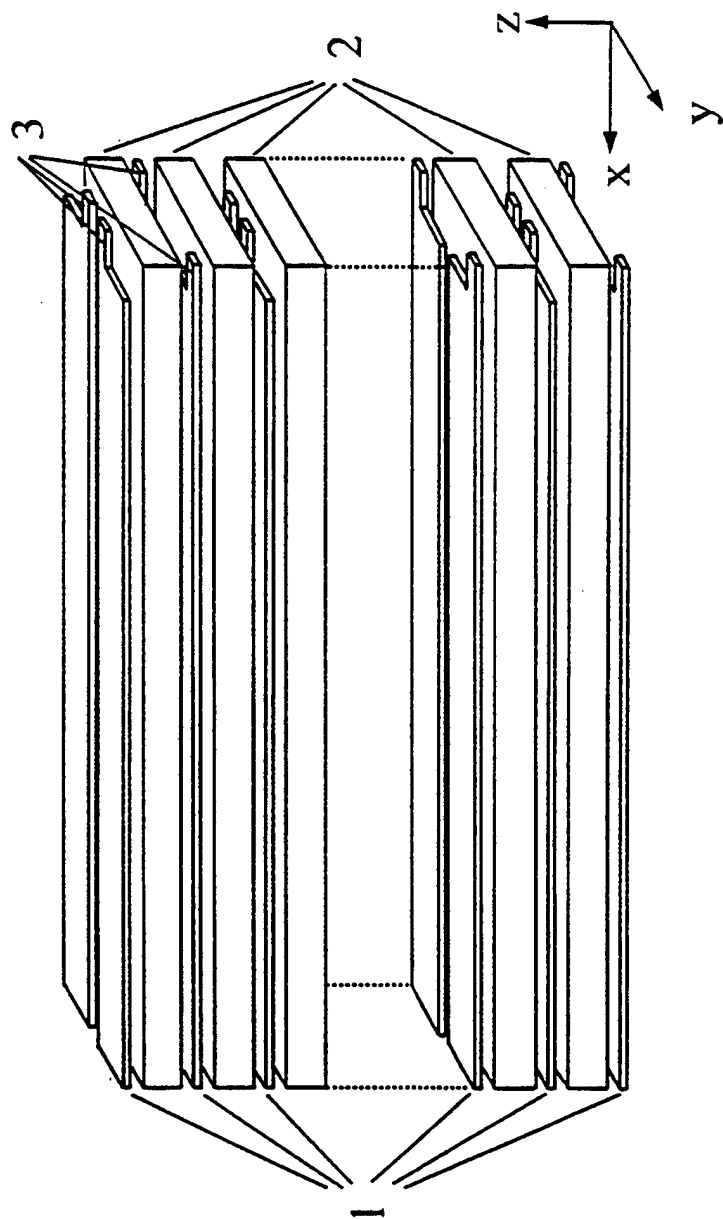


Fig. 1

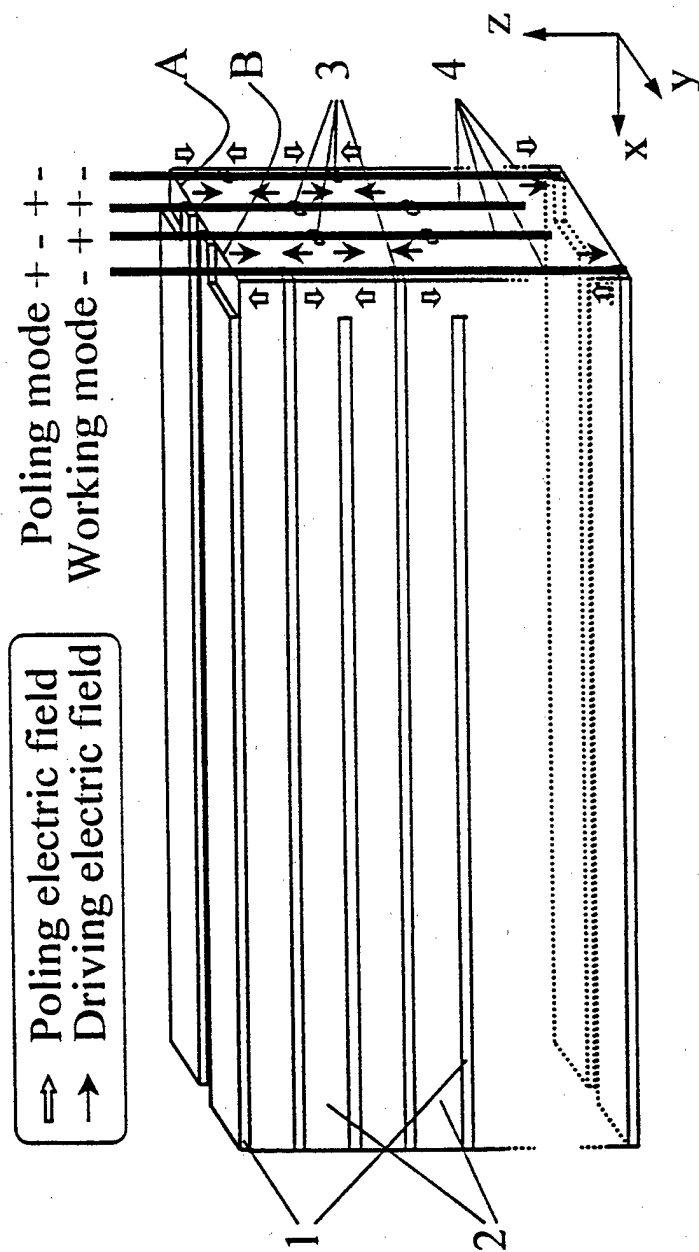


Fig. 2

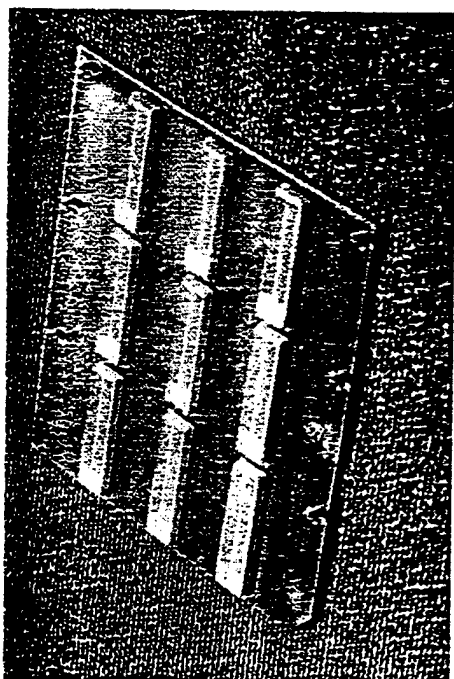


Fig. 3

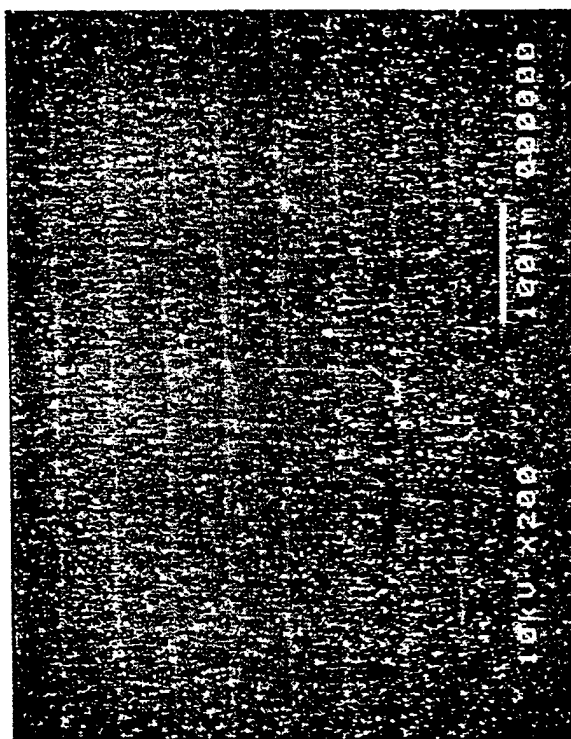


Fig. 4

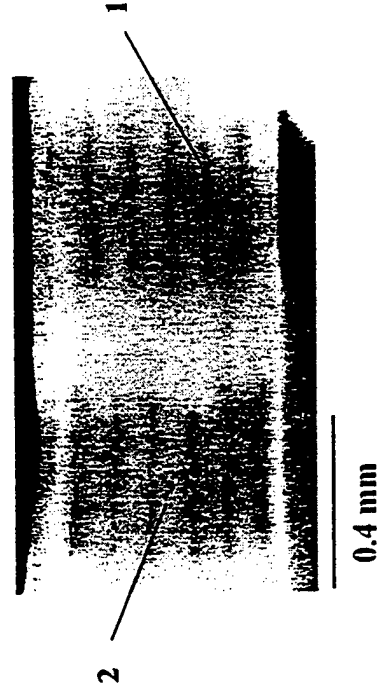


Fig. 5

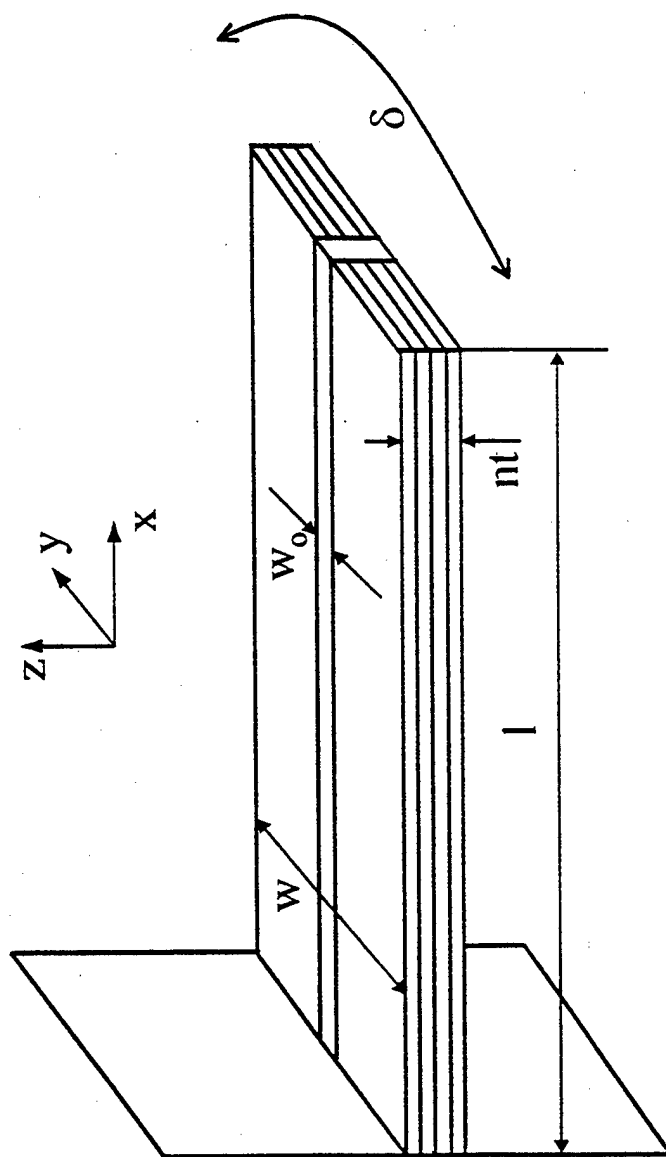


Fig. 6

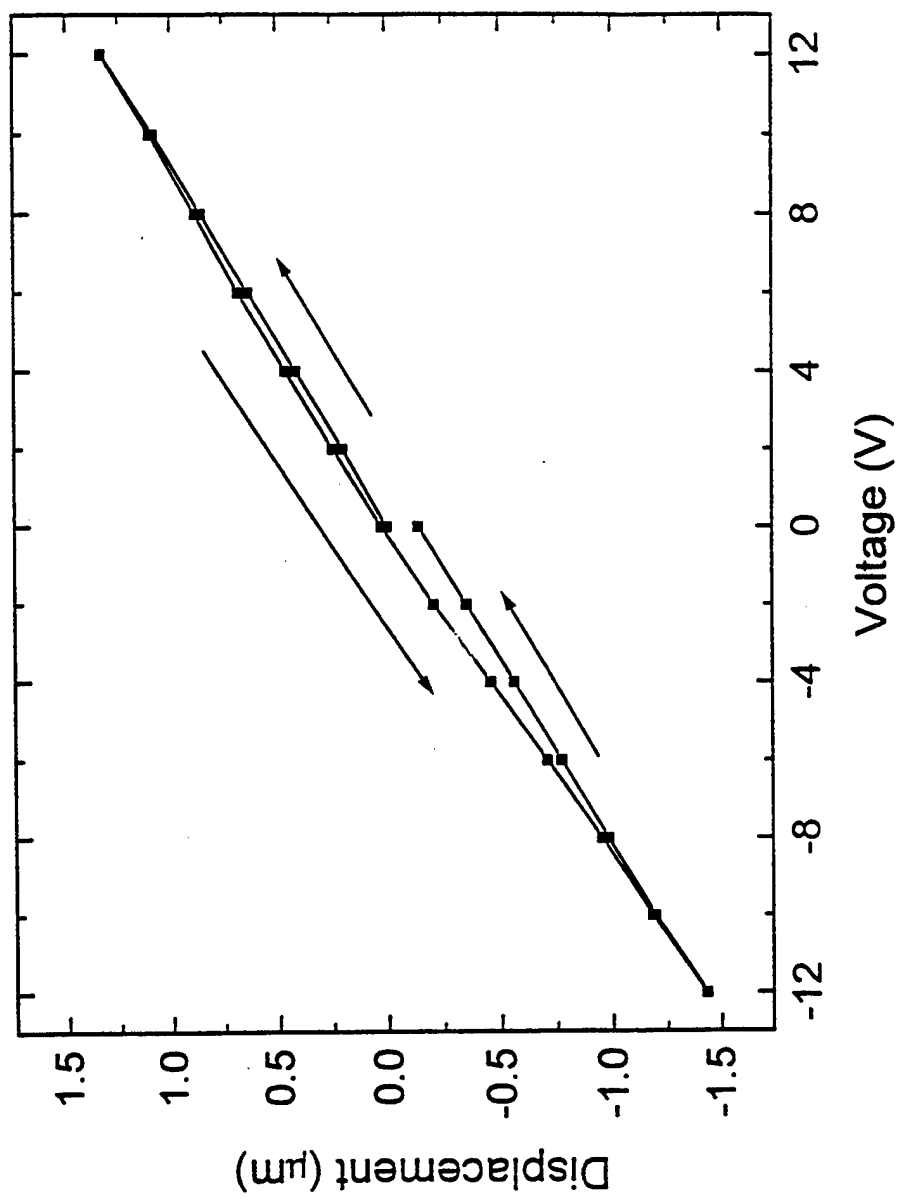


Fig. 7

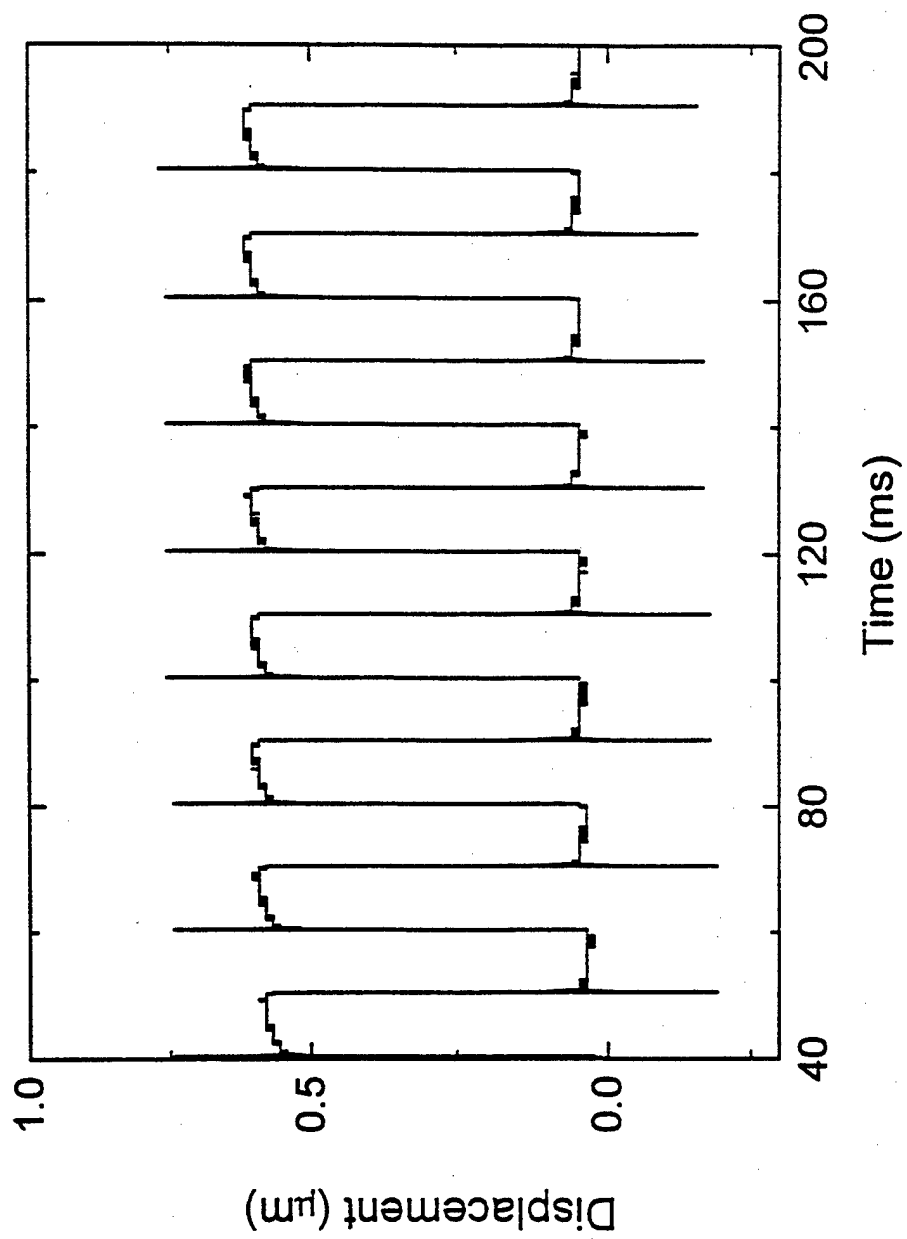


Fig. 8

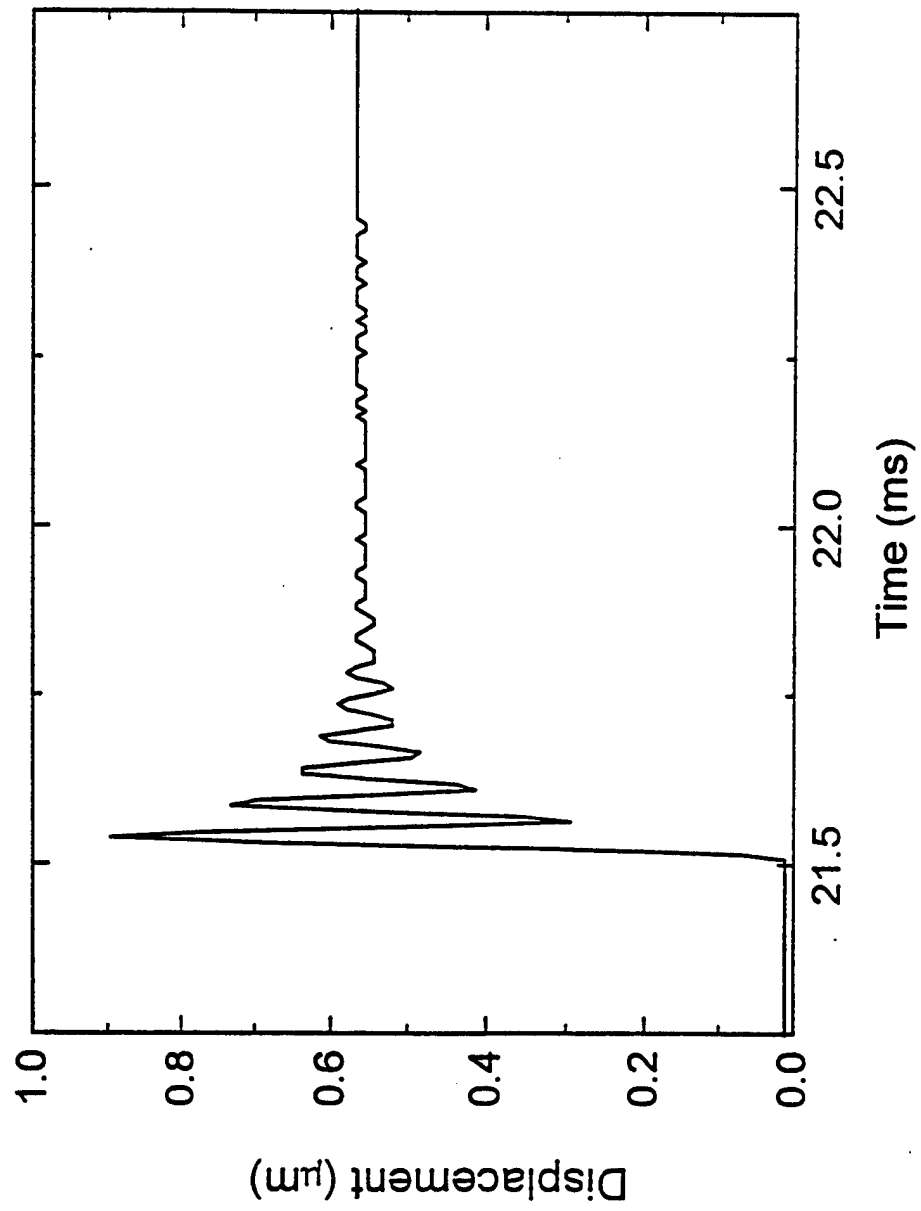


Fig. 9

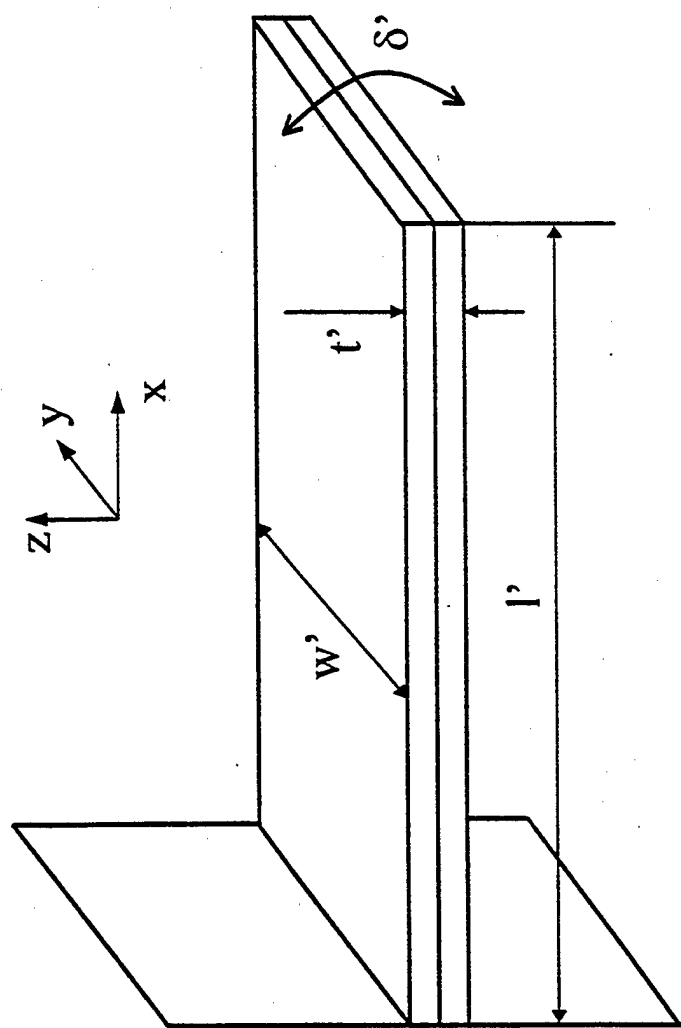


Fig. 10

APPENDIX 47

Acoustic Emission in Damaged Ferroelectric Lead Zirconate Titanate Ceramics

Hideaki ABURATANI and Kenji UCHINO

International Center for Actuators and Transducers (ICAT), Materials Research Laboratory, The Pennsylvania State University,
 University Park, PA 16802, USA

(Received January 19, 1998; accepted for publication March 23, 1998)

Field induced acoustic emissions (AE) in damaged ferroelectric ceramics have been studied. The field induced AE was not observed after the poling was completed at given electric fields. However, new AE was generated when the samples were damaged. It has been demonstrated that the AE method can be used to detect the damage of piezoelectric/ferroelectric materials and to determine safe driving electric fields.

KEYWORDS: acoustic emission (AE), crack, lead zirconate titanate (PZT), reliability, thermal shock

1. Introduction

The contributions of domain structures for the field induced strain in the ferroelectrics have been studied using AE method. By eliminating extrinsic AE signals caused by an electromechanical coupling between sample's piezoelectricity and feedback from power supply, it was confirmed that the field induced AE originated at the initiation of induced displacement and ended when the applied field was decreased during poling.¹⁾ The AE was not observed after domain reorientation was completed at given electric fields except under bipolar field in which butterfly shape induced displacement takes place. Since new AE generation required larger electric fields than that applied during poling, the Kaiser effect²⁾ in terms of the electric field was observed in the ferroelectric ceramics.¹⁾ The damage of ferroelectric material at high electric field levels during the poling process was also examined by AE method.^{3,4)} However, the intrinsic AE signals generated by domain reorientation processes and cracking were not separated from the extrinsic AE signals caused by the coupling between the piezoelectricity of the sample and the feedback from the power supply. The AE generations in the damaged ferroelectric ceramics after poling have not been studied yet. In cracked ferroelectric ceramics, the electric field induced displacement may cause a friction, which can generate the AE, at the crack surface. This type of AE which is independent of domain processes is expected at lower electric fields than the poling electric field.

This paper deals with the AE generations in the damaged ferroelectric ceramics. The damage of the thermally shocked single plate lead zirconate titanate $\text{Pb}(\text{Zr}, \text{Ti})\text{O}_3$ (PZT) ceramics was evaluated and compared to electrically damaged and non-damaged samples. A feasibility of using the non-destructive AE method for the damage evaluation in ferroelectric ceramics is demonstrated.

2. Experimental Procedures

For this experiments, commercialized PZT ceramics (Morgan Motroc: PZT 5A) with dimensions of 12.7 mm in diameter and 0.4 mm in thickness was used. The ceramics had silver fired electrodes which means that any damage to the interface between the electrode and ceramics also contributed to the final results.

A thermal shock was employed to introduce the crack into the samples in this study. The samples were placed in an oil bath at 200 °C for 30 s, then in an oil bath at room temperature for 30 s under the short circuit condition. This process was

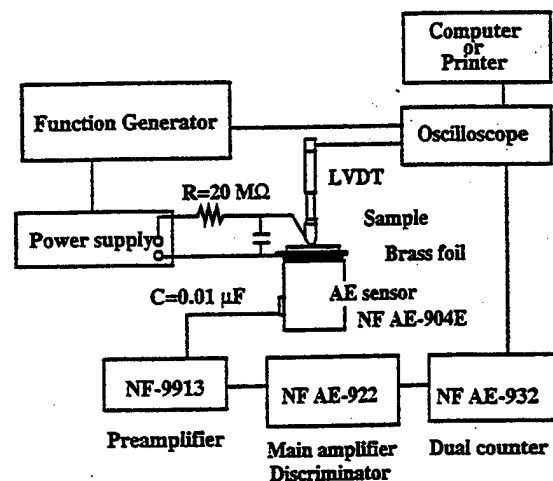


Fig. 1. AE measurement system.

repeated for 10 cycles.

The induced displacement, frequency response and AE were measured to evaluate the damage of the samples. Figure 1 shows the AE measurement system. In order to eliminate the coupling which caused the sample vibration, a capacitor of 0.01 μF and a resistor of 20 MΩ were connected in parallel and series to the sample, respectively. The total amplification of the AE signal was set to be 90 dB with a signal threshold level of 400 mV. The natural background level was about 10 dB lower than the threshold level. Thus, it was ensured that the measured AE results did not contain any noises from the environment.

3. Results and Discussions

3.1 Induced displacement and frequency response measurements

The field induced displacement of both non-shocked and thermally shocked samples as a function of the applied field is shown in Fig. 2. The applied field had a triangular wave form with a peak value of 37.5 kV/cm at a frequency of 0.01 Hz. The results were obtained after 10 cycles of the electric field application. There was no apparent differences in the induced displacement between non-shocked and thermally shocked samples. The obtained piezoelectric constants d_{33} were almost identical. It seemed that even if the damage such as microcrack existed in the sample, it was too small to affect the macroscopic displacement. The coupling factor k_p of 0.65 was obtained for both thermally shocked and non-shocked

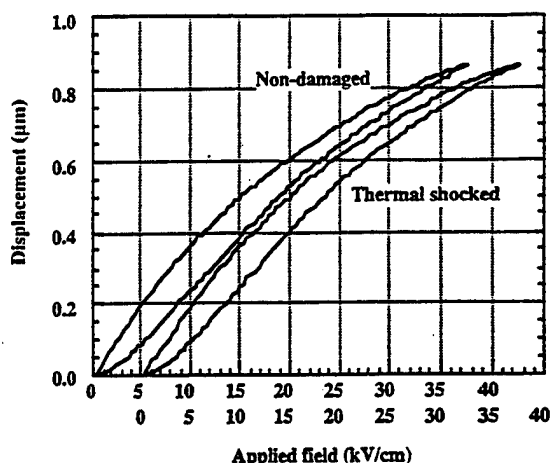


Fig. 2. Field induced displacement of non-shocked and thermally shocked PZT ceramics as a function of applied field.

samples. The mechanical quality factor Q_m of the thermally shocked and non-shocked samples were also observed to be around $Q_m = 75$.

3.2 AE measurements

The normalized total AE event count per cycle as a function of the number of field application cycle is shown in Fig. 3. The AE event rate per cycle decreased markedly after poling with an electric field of 25 kV/cm. No AE was observed after the domain reorientation was completed at this electric field level. When an electric field of 37.5 kV/cm was applied to the non-shocked sample poled at 25 kV/cm, the AE event count simply decreased with the number of field application cycle. Yet, the AE event was observed even after 10 cycles at which the AE event was not observed in the sample exposed to the electric field of $E = 25$ kV/cm. It seemed that the domain reorientation process was not completed due to high internal stresses present at higher fields, resulting in AE generations.

In the thermally shocked samples, the AE event count per cycle decreased first, then started to fluctuate. It was supposed that AE events in the thermally shocked samples originated from two sources: domain reorientation process and damage caused by the thermal shock. The domain reorientation process related AE was supposed to decrease with the number of field application cycle. However, the AE caused by the damage (i.e. microcrack) could be present throughout the field application cycles and started to dominate in the measurement after the level of the domain reorientation process related AE tapered off.

The AE event rate and induced displacement of the non-shocked sample as a function of time are shown in Fig. 4(a). The AE generations of the non-shocked sample falls into two categories. A small number for the AE events was observed at first (Type I). The AE event rate then reached a maximum at the maximum field (Type II). The AE onset field and the AE event count rate at the maximum field as a function of field application cycle are shown in Fig. 4(b). The AE event count rate at the maximum field decreased with the number of field application cycle. On the contrary, the AE onset field did not change through the cycle. Thus, the AE at the maximum field (Type II) was identified as the domain reorientation process related AE, because of the decrease in AE event rate with

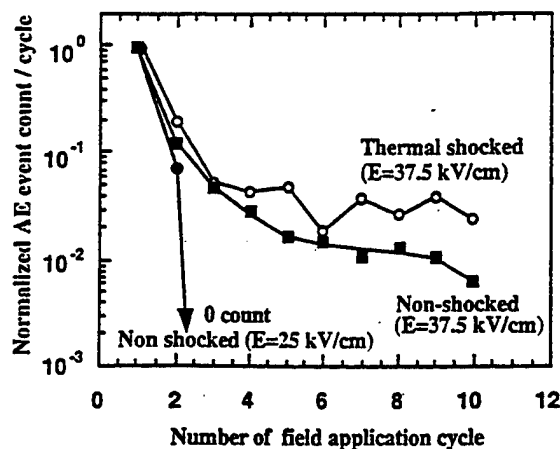


Fig. 3. Normalized AE event count per cycle as a function of field application cycle.

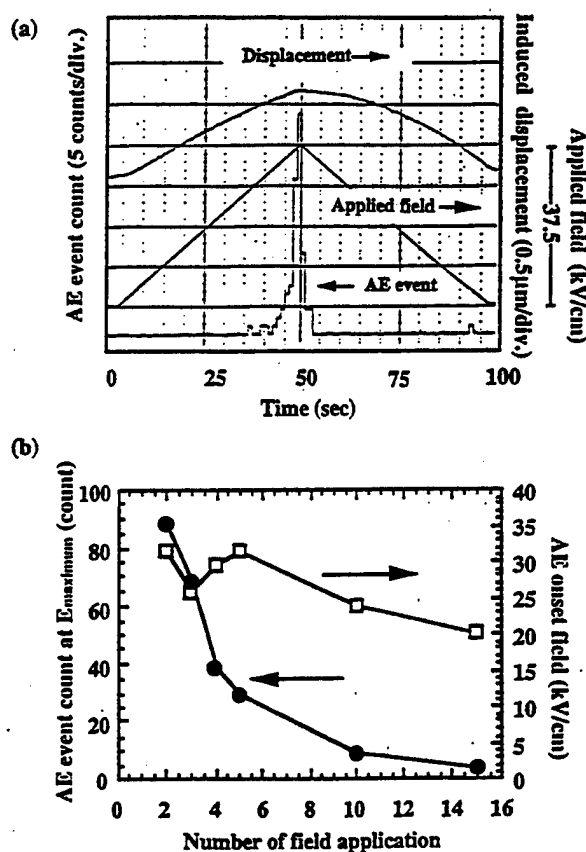


Fig. 4. (a) AE event count rate and induced displacement of non-shocked sample as a function of time, and (b) AE onset field and AE event count at the maximum field as a function of field application cycle.

the number of cycle. If the AE observed at lower field (Type I) was related to the domain reorientation process, it should decrease similarly with the number of cycle. Thus it was concluded that the AE observed at lower fields (Type I) was due to electrically induced damages. It was also supposed that the AE event count near 0 kV/cm was caused by the electrically induced damage.

For the thermally shocked samples, the AE was observed at lower fields than the AE onset field of the non-shocked sam-

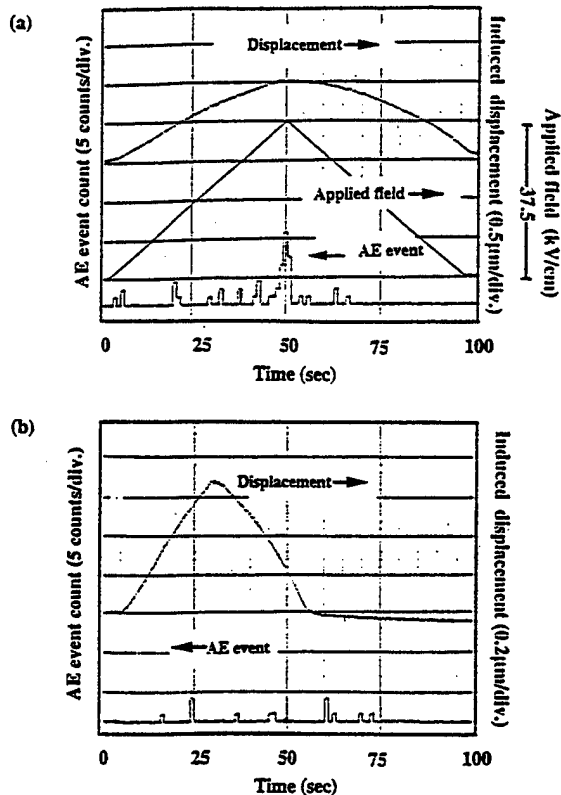


Fig. 5. AE event count rate and induced displacement of thermally shocked sample as a function of time (a) applied field $E = 37.5$ kV/cm, and (b) applied field $E = 25$ kV/cm.

ple as shown in Fig. 5(a). The samples became "noisy" in terms of the AE generation. These AE were most probably caused by the friction at the crack surfaces through internal motions. The AE generation was observed even when the applied electric field was decreased to 25 kV/cm (Fig. 5(b)). After the displacement was induced, the AE events were also observed even after the applied field reached $E = 0$ kV/cm. This was probably due to the time dependent motion (stress relaxation near cracks) in the samples. Since this type of AE was not observed in the non-shocked samples exposed to the electric field of 25 kV/cm after poling, these AE events were obviously caused by the induced damage.

The damage related AE event count was observed to be

much less than that associated with domain reorientation. This could be due to that during the poling the entire sample contributed to the AE generation (domain reorientation process related AE), and the damage related AE was originated by the individual cracking regions and friction at the crack surfaces. Therefore, the damaged volume was much less than that generating AE during the poling, resulting in a small number of AE events.

4. Summary

The induced displacement, frequency response measurements and AE method were used for the damage evaluation of the thermally shocked ferroelectric PZT ceramics under the unipolar fields. The thermally shocked and non-shocked samples were exposed to an electric field of 37.5 kV/cm. Non-shocked samples were also examined at an electric field of 25 kV/cm. Neither the induced displacement nor frequency response measurements obviously indicated damage among the samples. On the contrary, the damages of the sample was clearly observed using the AE method as an AE generation at low electric fields. The friction caused by induced internal motions and its relaxation at crack surfaces might be the sources of these AE. Moreover, it seemed that the electric field of 37.5 kV/cm was large enough to damage non-shocked samples.

It was shown that the thermally and the electrically induced damages in the samples were observed in the AE measurements. These experiments show that the AE method can be extended to determine safe poling and driving fields for piezoelectric/ferroelectric. Using the obtained result that AE generations were observed at low electric fields, damage detection in materials can be carried out.

Acknowledgment

This work was supported by the Office of Naval Research through Contract No. N00014-92-J-1510.

- 1) H. Aburatani and K. Uchino: *Proc. 10th IEEE Int. Symp. Appl. Ferroelectrics* (1996) p. 871.
- 2) H. Aburatani and K. Uchino: *Jpn. J. Appl. Phys.* 35 (1996) L516.
- 3) R. Halmshaw: *Non-Destructive Testing* (Edward Arnold, London, 1991) 2nd ed., Chap. 2, p. 273.
- 4) E. C. Subbarao, V. Srikanth, W. Cao and L. E. Cross: *Ferroelectrics* 145 (1993) 271.
- 5) D. G. Choi and S. K. Choi: *J. Mater. Sci.* 32 (1997) 421.

APPENDIX 48

NEW DEVELOPMENTS IN PIEZO MOTORS AND MECHANISMS

P.D.Atherton
Queensgate Instruments Ltd, Bracknell, UK

K. Uchino
International Center for Actuators and Transducers, Materials Research Laboratory,
The Pennsylvania State University, University Park, PA, USA

Abstract:

In this review article we seek to outline recent progress in the areas of pzt development, mechanisms and motors, and to point out areas where further work is required.

Introduction

The use of piezo-electric materials in actuator applications continues to grow strongly, driven by the unique properties of the material:- its quick response, high stiffness, low power consumption and high electro-mechanical conversion efficiency.

The principal challenge to the design engineer is to find ways to overcome the major disadvantage of pzt-type materials - the small stroke. A variety of techniques have been established for this purpose, which can be divided into mechanisms (which use some kind of lever to amplify the motion), and motors (which use a walking or sliding action).

PZTs are used widely in instrumentation such as a scanning probe microscopy, where tube or tripod type scanners raster a probe across a surface and precision stages move samples about to enable measurements of linewidths and depths in the process of semiconductor manufacture.

Consumer applications are driven by the virtuous circle of higher volumes and increased reliability, which drives costs down further. Lower voltage designs of actuator (produced using thinner layers) decrease the implementation costs. PZTs are now widely used in cameras (autofocus mechanisms) and CD players (tracking mechanisms) and are beginning to penetrate the automotive market where the demands on price and performance are the highest.

Piezoceramics are also used for both passive and active mechanical vibration suppression in military vehicles and space structures.

In these situations the issue of lifetime and reliability are of extreme importance. Even though this reliability issue has been systematically investigated and a textbook has been published [1], there still remains many studies required to predict the actuator performance in each given application.

It has long been the case that the microscopic material properties are poor predictors of actual device performance.

In this article, we review recent progress in the areas of PZT development, mechanisms and motors, and to point out areas where further work is required.

MECHANISMS

Hysteresis and creep

Some examples are reviewed here on the hysteresis and creep. Figure 1 shows the characteristic hysteresis curve for a piezo translator as the amplitude of the stroke is gradually reduced. It can be seen that the amplitude of the hysteresis is a fairly constant fraction of the stroke, and also that the loop rotates slightly as the amplitude is reduced (in other words the 'scale factor' changes).

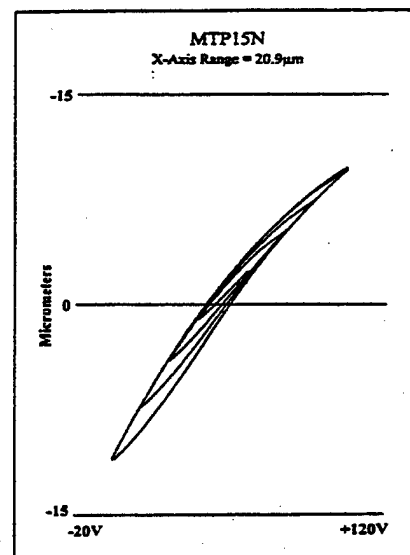


Fig 1: Piezo Hysteresis

Figure 2 shows the behaviour when the piezo is scanned from the same start position to various different end positions.

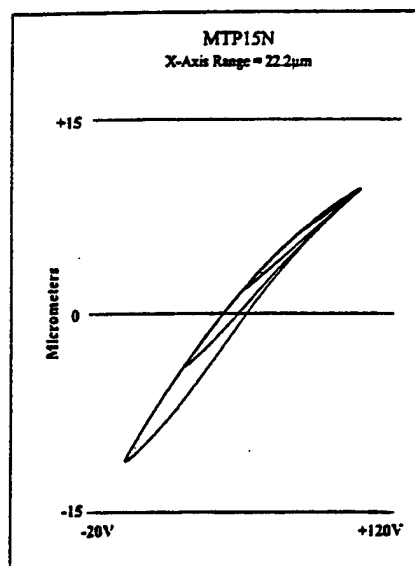


Fig 2: Piezo Hysteresis

Clearly the exact position of the actuator is not well determined, and depends to an extent on its history.

Figure 3 shows the phenomenon known as creep. Following a voltage step, although the voltage applied to the device remains constant, the pzt continues to move in the same direction, decaying exponentially towards a stable position.

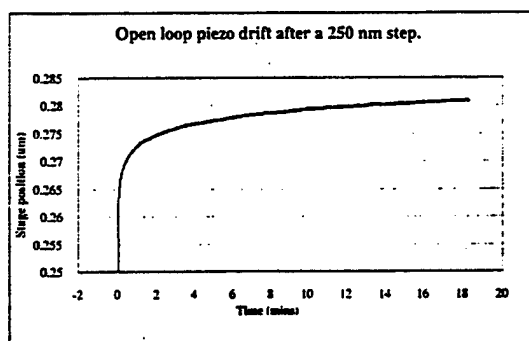


Fig 3: Piezo Creep

Open loop piezo tube scanners are widely used in Scanning Probe Microscopes, and the images produced are distorted by the hysteresis and creep. Various workers have attempted to correct for these hysteresis effects. Ge and Jouaneh [2] used a modified Preisach model to improve the ability of the pzt to follow sine waves in tracking control applications, reducing the errors from about 12% of the stroke to about 2.3%. However their model only

works for dynamic errors, and proved unable to predict or cope with the effects of creep.

Heider and Weiss [3] used LiNbO_3 material as a tube scanner, which has much lower hysteresis, but also much lower stroke, than the soft PZT materials. Hues et al [4] showed that hysteresis and creep affected their Nano-Indentation measurements significantly, and that PMN devices with lower hysteresis, performed significantly better. While PMN seems to have important benefits in terms of hysteresis over PZT materials, it is not widely available, and seems to offer these benefits over a fairly narrow temperature range. [5]

Such strategies for compensating for the hysteresis seem to be able to reduce it to about 3% of the stroke. To reduce it further requires both a sensor and a control loop.

Sensors for PZT control

LVDTs can measure over several mm, and are inexpensive, but because they are fundamentally a contact technique it is hard to measure to better than 40nm. Strain gauges can do better, but are thermally sensitive in their simple cheap form. They can get to about 10nm. Laser interferometers are very expensive, but usually longer range, and traceable. Step sizes of 2nm are normal. Heterodyne laser interferometers can measure to 0.01nm over short ranges, but are complex and expensive. Capacitance sensors have a range of only about 1mm but can measure to 0.01nm and are cheaper and smaller than laser interferometers.

Optical fiber types have become less expensive very recently. See Ref. [1] for further information.

Control strategies

General control strategies for piezoelectric actuators can be found in Ref. [6]. Campos Rubio [7] has reviewed the general control strategies for actuator control, and these are dealt with further by Hicks et al [8]. Simple strategies using just an integrator term are now giving way to PID loops and fuzzy logic techniques.

The availability of low cost Digital Signal Processing chips makes possible highly sophisticated control strategies, which embrace fuzzy logic and even neural networks.

Ringling and Overshoot : New techniques have evolved over the past few years for controlling resonant systems, by shaping the input signal so as not to excite any underlying resonances. At its most simple this involves not putting sharp steps on the input. More sophisticated techniques involve Finite

Impulse Response Filtering, where the input function is processed to remove any of the Fourier components which might excite system resonances. In this manner the overshoot and ringing of a system, which can increase the settle time dramatically, can be minimised. Algorithms developed and patented at MIT and marketed by Convolve [9], take an even more sophisticated approach to this problem, which they call Input Shaping. This technique is capable of optimizing systems with multiple resonances.

Flexure Mechanisms

When a piezo actuator expands in one direction it also contracts in other directions, and twists and tilts in a complicated way. For example not only does the tilt of the end of the piezo also show hysteresis, but the axis of tilt also rotates. Thus in order to use a piezo to produce precision motions it is necessary to de-couple these 'parasitic' motions. This is usually achieved by getting the pzt to drive some form of mechanism. Most precision slides that are available commercially use roller bearings of some form, and are incapable of the resolution that the pzt can achieve. Furthermore the small stroke of the pzt usually needs to be amplified in some way. Flexure mechanisms are used both to produce amplification, by means of levers, and also to de-couple the parasitic motions. Such mechanisms are either produced from individual parts, using parallel spring strips, and/or flex pivots, or produced by machining away a solid block of metal.

Scire and Teague [10] described one of the first X-Y flexure stages made by drilling holes to form notch hinges in a solid block of Aluminium. They used amplifications of more than 10 to get a 50 μ m by 50 μ m range stage.

Since then much work has been done on understanding how best to form the flexure hinges. Smith et al [11] have produced design calculations for elliptical hinges and compared the results with experimental data, while Ryu and Gweon [12] have analysed the effects of manufacturing errors on the parasitic motions.

While Xu and King [13] provide a brief review of pzt amplifiers and flexures a more comprehensive treatment is given by Smith [14]

Ryu et al [15] published a design of an XY θ mechanism for use in inspection of silicon wafers, while Yang and Jouneh [16] have published a design for a 200 μ m range X stage.

In order to produce a high quality flexure mechanism it is necessary to use Finite Element

Analysis to understand how the stage distorts as the piezo expands, and to understand the effects of manufacturing errors in the hinges on the stage performance. Electric Discharge Machining (sometimes called spark-erosion) is used to produce hinges in solid blocks of Aluminium, stainless steel, or SuperInvar. However the EDM process is not well understood, and there are many interacting variables. For example, to achieve the accuracy necessary to reduce parasitic errors, and the surface finish necessary to maximize hinge lifetime requires many slow passes, which is very expensive. Furthermore the surface finish achieved varies greatly from one type of EDM machine to another.

Performance

State-of-the-art mechanisms [17] are fabricated from a solid block of SuperInvar, and can move over 100 μ m with sub-nanometer repeatability, and parasitic motions of less than 2nm or 10 microradians, settling in a few milliseconds. They use DSP based controllers, with FIR filtering, and have resolutions of 21 bits. PID loop parameters can be changed dynamically under software control, according to the requirements, introducing the possibility of using Fuzzy Logic type control.

MOTORS

Ultrasonic motors have been an attractive research topic for the last two decades and some of the designs already found and continue to find applications in electrical and electronic equipment as compact, high efficiency, silent motors. However, this area of research is still open to new ideas, designs and improvement of the designs that are already in use. This section briefly reviews some of the recent developments (1994-98) and new designs in ultrasonic motors. Refer to Ref. [18] for general review.

Contact Motors

Compact, small motors with large torque output are required in the area of robotics. A hybrid transducer type ultrasonic motor is developed by Satonobu et al. [19] by combining torsional and longitudinal vibrations from two piezoelectric rings in the stator section of the motor. A schematic of this design is shown in Fig. 4.

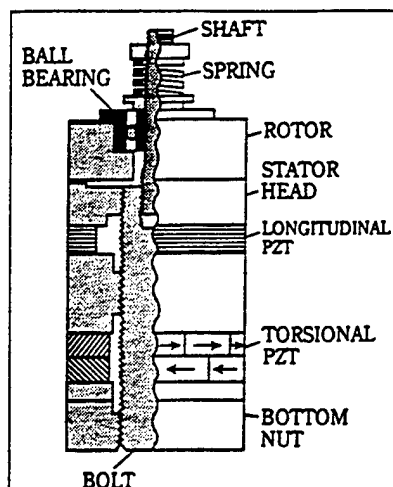


Fig. 4

In this design one of the ceramic ring is polarized in the circumferential direction for the excitation of torsional vibration that provides the driving torque to the motor. Whereas the second ring is polarized in the axial direction to obtain the longitudinal vibration that controls the normal force between the rotor and the stator periodically to transmit only half a cycle of the torsional vibration. Theoretically, it is possible to obtain a megatorque (i.e. 1000 kgf.cm) with a motor diameter of 140 mm. and a 400 kgf.cm orque is obtained experimentally from a 120 mm diameter motor with 15 % maximum efficiency.

In the basic operation principle of piezoelectric motors, multi-mode motors use a combination of different vibration modes to produce elliptic motion of the contact surface to drive the rotor by friction. However, most of these designs use flexural modes of the piezoelectric element and therefore are strongly stress-limited. A new motor developed by Claeysen et al. [20] suggests a solution to this limitation. This design, shown in Fig. 5, is composed of two longitudinal pre-stressed actuators and a mechanical coupler that amplifies the vibration in the normal direction. It has two modes of vibration: a translation mode of the coupler when the actuators are excited in opposition and alternatively, a flexural vibration when both of the actuators are excited in 90° phase difference, the tip of the coupler moves elliptically. The results indicate a 56 mNm torque, 300 rpm revolution speed and 10 % efficiency for this motor design.

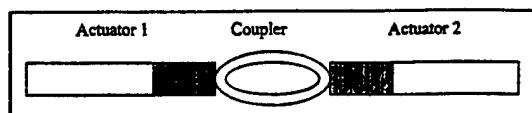


Fig.5

Continuing the advances in robots and mechatronics requires small, highly accurate actuators with high torque density and multi-degree of freedom in motion. A spherical ultrasonic motor is developed by Toyama et al. [21] to obtain multi-degree of freedom. As it is shown in Fig. 6, this USM has a very simple structure with a spherical rotor made-out of an engineering plastic, four stators which consist of an elastic body (brass) and piezoelectric ceramic. Stators facing each other are driven simultaneously in pairs to drive the rotor at the top of the travelling waves by friction. A position detector measures the direction of the output shaft. Results of this work demonstrated that a 0.7 kgf.cm torque with 40 rpm rotation speed and two degrees of freedom can be obtained from this spherical USM design.

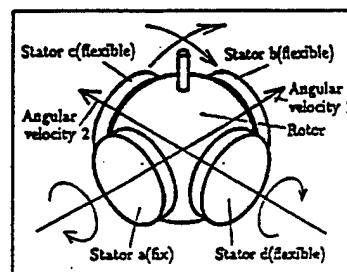


Fig.6:

Aiming at the micro-surgery application at the tip of an intravascular catheter, Penn State has been developing a compact ultrasonic motor as tiny as 3 mm diameter. As shown in Fig. 7, the stator consists of a piezoelectric ring and two concave/convex metal endcaps with "windmill" shaped slots bonded together, so as to generate a coupled vibration of up-down and torsional type [22]. Since the component number and the fabrication process were minimized, the fabrication price would be decreased remarkably, and it would be adaptive to the disposable usage. When driven at 160 kHz, the maximum revolution 600 rpm and the aximum torque 1 mNm were obtained for a 11 mmØ motor.

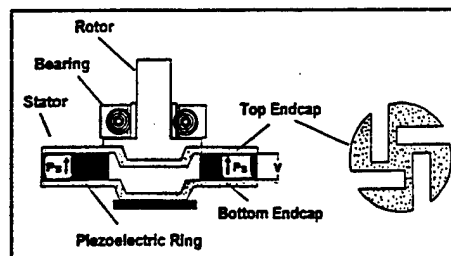


Fig.7:

Non-contact motors

Up to this point all the USM designs discussed were conventional designs where the rotor is in direct contact with the stator. However, this direct contact restricts the operation range of the motor. The rotation speed of the motor is limited and the wear and abrasion on the contact surface limits the life span of the motor as well. Another problem, namely the surface roughness of the rotor and stator, also arises when the size of the motor decreases or the operation frequency increases. The amplitude of the ultrasonic vibration is inversely proportional to the velocity and increasing drive frequency requires smoother surfaces, and small roughness disturbs operation of the motor. In order to solve these problems ultrasonic motors which operate without direct contact, or with no contact at all between the stator and the rotor are proposed. One such design by Nakamura et al. [23] suggests the use of a liquid medium between the stator and the rotor to cut the direct contact. Figure 8 shows the configuration of this motor where a piezoelectric ring is bonded on to the metallic stator.

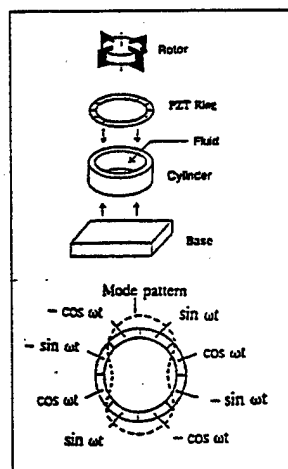


Fig.8:

The piezoelectric ring is divided into 8 sections and each section is electroded separately. The bottom of the cylinder is sealed with soft rubber and inside is filled with a liquid and the rotor is floating on that liquid. The travelling wave excited on the circumference of the cylinder creates an acoustic wave in the fluid and at a certain specific angle to the tangential direction of the inside surface of the cylinder. This acoustic wave drives the fluid and the rotor in the same direction. The rotor can be rotated with a 50 rpm rotation speed with this design.

Although the idea to use a fluid to drive the motor is demonstrated to work, the fluid flow velocity saturates due to the acoustic nonlinearity as the vibration velocity of the stator increases. Therefore, there appears a certain upper limit for the velocity of

a USM coupled with a fluid. The best way to eliminate problems such as abrasion and heat generation that arise from the contact between the stator and the rotor, and at the same time to obtain high rotation velocities, is to have no contact and no intermediate medium between them. It was reported by S. Ueha [24] that masses weighing up to several kilograms can be levitated up to 10 – 100μm by ultrasonic vibration. Based on this development, Yamazaki et al. [25] proposed a noncontact ultrasonic motor where the rotor is ultrasonically levitated. The design of this motor, which is shown in Fig. 9, includes a hollow cylinder rotor inserted into the hollow cylinder stator.

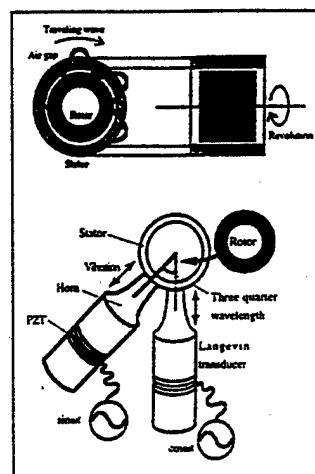


Fig. 9:

The travelling wave on the stator is excited by superposition of two standing waves created by two Langevin transducers. This travelling sound field creates two unidirectional forces on the rotor: one is in the radial direction and levitates the rotor, and the other one is a near-boundary streaming in the circumferential direction which drives the rotor. Rotation velocity of up to 3000 rpm can be obtained through this design.

MARKET OF CERAMIC ACTUATORS

More than 20 years have passed since the intensive development of piezoelectric actuators began in Japan, then spread worldwide. Now the focus has shifted from the development of materials and manufacturing technology to practical device applications.

The markets in the USA are not in consumer applications, but in military and defense, and in test equipment and analytical instrumentation for semiconductor and disk drive manufacturing. The current needs from the Navy are smart submarine skins, hydrophone actuators, prop noise cancellation etc., and smart aircraft skins from Air Force, while

the Army requires helicopter rotor twisting, aeroservoelastic control and cabin noise/seat vibration cancellation. High precision PZT stages are used to test M-R heads for Disk Drives, measure linewidths on wafers and control autofocus mechanisms for high powered inspection microscopes.

On the contrary in Japan, piezoelectric shutters (Minolta Camera) and automatic focusing mechanisms in cameras (Canon), dot-matrix printers (NEC) and part-feeders (Sanki) are now commercialized and mass-produced by tens of thousands of pieces per month. During the commercialization, new designs and drive-control techniques of the ceramic actuators have been mainly developed in the past few years. A number of patent disclosures have been found particularly in NEC, TOTO Corporation, Matsushita Electric, Brother Industry, Toyota Motors, Tokin, Hitachi Metal, Toshiba etc.

Several years ago Mr. T. Sekimoto, Former President of NEC, forecast in his New Year's speech that the market-share of piezoelectric actuators and their employed devices would reach up to \$10 billion (\$10¹⁰) in the future. If we estimate the annual sales in 2000 (without considering the current serious economic recession in Japan), ceramic actuator units, camera-related devices and ultrasonic motors will be expected to reach \$500 million, \$300 million and \$150 million, respectively. Regarding the final actuator-related products, \$10 billion will not be very different from the realistic amount.

References

- [1] Uchino, K., "Piezoelectric Actuators and Ultrasonic Motors," Kluwer Academic Publishers, MA (1997).
- [2] Ge, P., Joauneh, M., Precision Engineering, 20, 99 (1997)
- [3] Heider and Weiss, Rev. Sci. Instrum. 64, 3534, (1993)
- [4] Hues, S.M., et al Rev. Sci. Instrum. 65, 1561, (1994)
- [5] Uchino, K., Ceramic Databook '88, Chap. Ceramic Actuators, Inst. Industrial Manufacturing Tech., Tokyo (1988)
- [6] Uchino, K., "Piezoelectric/Electrostrictive Actuators," Morikita Publ., Tokyo (1986)
- [7] Rubio, C., et al., ASPE 14, 294 (1996)
- [8] Hicks, T.R., Atherton, P.D., The Nano-Positioning Book. Queensgate Instruments (1997)
- [9] Convolv, Inc, 132, Nassau St, Suite 619, NY10038
- [10] Scire, F.E., Teague, E.C., Rev. Sci. (1987)
- [11] Smith, S.T., et al, Rev. Sci. Instrum. 68 1474 (1997)
- [12] Ryu, J.U., Gweon, D., Precision Engineering 21, 83 (1997)
- [13] Xu, Y., King, T., Precision Engineering 19, 4, (1996)
- [14] Smith, S.T., Chetwynd, D.G., Foundations of Ultra Precision Mechanism Design, Gordon and Breach (1994)
- [15] Ryu, J.U., Gweon, D., Moon, K.S., Precision Engineering 21, 18 (1997)
- [16] Yang, R., et al Precision Engineering, 18, 20, (1996)
- [17] Queensgate Instruments Ltd, Waterside Park, Bracknell, RG12 1RB, UK
- [18] Uchino, K., "Piezoelectric Ultrasonic Motors: Overview," J. Smart Mater. & Structures - Special Issue (1998)
- [19] Satonobe, J., N. Torii, K. Nakamura and S. Ueha, Jpn. J. Appl. Phys. Part I, Vol.35, 9B, 5038 (1996)
- [20] Claeysen, F., R. LeLety, L. Chouteau, N. Lherhem, L. Petit, R. Briot and P. Gonnard, Int'l Soc. Optical Eng. 3rd. Int'l Conf. Intelligent Mater., Lyon, France, Proc. SPIE, Vol.2779, p.634 (1996)
- [21] Toyama, S., Manufacturing Technology, Vol.45, 27 (1996)
- [22] Koc, B., A. Dogan, Y. Xu and K. Uchino, Jpn. J. Appl. Phys. (1998) [submitted]
- [23] Nakamura, K., T. Ito, M. Kurosawa and S. Ueha, Jpn. J. Appl. Phys. Vol.29, L160 (1990)
- [24] Hashimoto, Y., Y. Koike and S. Ueha, J. Acoust. Soc. Jpn. (E), Vol. 16, p.189 (1995)
- [25] Yamazaki, T., J. Hu, K. Nakamura and S. Ueha, Jpn. J. Appl. Phys. Part I, Vol.35, 5B, 3286, (1996)

APPENDIX 49

COMPACT PIEZOELECTRIC ULTRASONIC MOTORS

Kenji Uchino and Burhanettin Koc
International Center for Actuators and Transducers
Materials Research Laboratory, The Pennsylvania State University
University Park, PA 16802, USA

This paper reviews recent developments of compact ultrasonic motors using piezoelectric resonant vibrations. Following the historical background, ultrasonic motors using the standing and traveling waves are introduced. Driving principles and motor characteristics are explained in comparison with the conventional electromagnetic motors.

Keywords: ultrasonic motor, piezoelectric actuator, standing wave motor

INTRODUCTION

In office equipment such as printers and floppy disk drives, market research indicates that tiny motors smaller than 1 cm^3 would be in large demand over the next ten years. However, using the conventional electromagnetic motor structure, it is rather difficult to produce a motor with sufficient energy efficiency. Piezoelectric ultrasonic motors, whose efficiency is insensitive to size, are superior in the mm-size motor area.

In general, piezoelectric and electrostrictive actuators are classified into two categories, based on the type of driving voltage applied to the device and the nature of the strain induced by the voltage: (1) rigid displacement devices for which the strain is induced unidirectionally along an applied dc field (servo displacement transducers and pulse drive motors), and (2) resonating displacement devices for which the alternating strain is excited by an ac field at the mechanical resonance frequency (ultrasonic motors). The AC resonant displacement is not directly proportional to the applied voltage, but is, instead, dependent on adjustment of the drive frequency. Although the positioning

accuracy is not as high as that of the rigid displacement devices, very high speed motion due to the high frequency is an attractive feature of the ultrasonic motors.

The materials requirements for these classes of devices are somewhat different, and certain compounds will be better suited for particular applications. The servo-displacement transducer suffers most from strain hysteresis and, therefore, a PMN electrostrictor is preferred for this application. The pulse-drive motor requires a low permittivity material aiming at quick response with a limited power supply rather than a small hysteresis, so that soft PZT piezoelectrics are preferred to the high-permittivity PMN for this application. On the contrary, the ultrasonic motor requires a very hard piezoelectric with a high mechanical quality factor Q_m , in order to minimize heat generation and maximize displacement. Note that the resonance displacement is equal to $\alpha \cdot dEL$, where d is a piezoelectric constant, E , applied electric field, L , sample length and α is an amplification factor proportional to the mechanical Q .

This paper deals with ultrasonic motors using resonant vibrations, putting a particular focus on miniaturized motors. Following the historical background, various ultrasonic motors are introduced. Driving principles and motor characteristics are explained in comparison with the conventional electromagnetic motors.

CLASSIFICATION OF ULTRASONIC MOTORS

Historical Background

Electromagnetic motors were invented more than a hundred years ago. While these motors still dominate the industry, a drastic improvement cannot be expected except through new discoveries in magnetic or superconducting materials. Regarding conventional electromagnetic motors, tiny motors smaller than 1cm long are rather difficult to produce with sufficient energy efficiency. Therefore, a new class of motors using high power ultrasonic energy -- ultrasonic motor, is gaining wide spread attention. Ultrasonic motors made with piezoceramics whose efficiency is insensitive to size are superior in the mini-motor area. Figure 1 shows the basic construction of an ultrasonic motor,

which consists of a high-frequency power supply, a vibrator and a slider. Further, the vibrator is composed of a piezoelectric driving component and an elastic vibratory part, and the slider is composed of an elastic moving part and a friction coat.

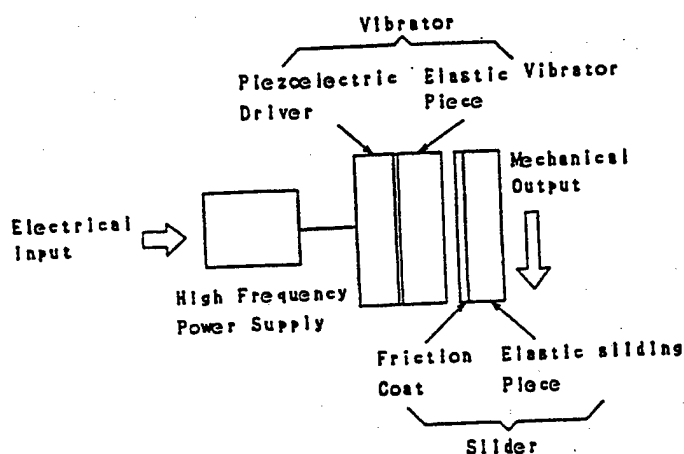


Fig. 1 Fundamental construction of ultrasonic motors.

Though there had been some earlier attempts, the practical ultrasonic motor was proposed firstly by H. V. Barth of IBM in 1973.¹⁾ A rotor was pressed against two horns placed at different locations. By exciting one of the horns, the rotor was driven in one direction, and by exciting the other horn, the rotation direction was reversed. Various mechanisms based on virtually the same principle were proposed by V. V. Lavrinenko²⁾ and P. E. Vasiliev³⁾ in the former USSR. Because of difficulty in maintaining a constant vibration amplitude with temperature rise, wear and tear, the motors were not of much practical use at that time.

In 1980's, with increasing chip pattern density, the semiconductor industry began to request much more precise and sophisticated positioners which do not generate magnetic field noise. This urgent request has accelerated the developments in ultrasonic motors. Another advantage of ultrasonic motors over the conventional electromagnetic motors with expensive copper coils, is the improved availability of piezoelectric ceramics at reasonable cost. Japanese manufacturers are producing piezoelectric buzzers around 30 - 40 cent price range at the moment.

Let us summarize the merits and demerits of the ultrasonic motors:

Merits

1. Low speed and high torque -- Direct drive
2. Quick response, wide velocity range, hard brake and no backlash
 - Excellent controllability
 - Fine position resolution
3. High power / weight ratio and high efficiency
4. Quiet drive
5. Compact size and light weight
6. Simple structure and easy production process
7. Negligible effect from external magnetic or radioactive fields, and also no generation of these fields

Demerits

8. Necessity for a high frequency power supply
 9. Less durability due to frictional drive
 10. Drooping torque vs. speed characteristics
-

Classification and Principles of Ultrasonic Motors

From a customer's point of view, there are rotary and linear type motors. If we categorize them from the vibrator shape, there are rod type, π -shaped, ring (square) and cylinder types. Two categories are being investigated for ultrasonic motors from a vibration characteristic viewpoint: a standing-wave type and a propagating-wave type. The standing wave is expressed by

$$u_s(x,t) = A \cos kx \cdot \cos \omega t, \quad (1)$$

while the propagating wave is expressed as

$$u_p(x,t) = A \cos (kx - \omega t). \quad (2)$$

Using a trigonometric relation, Eq. (2) can be transformed as

$$u_p(x,t) = A \cos kx \cdot \cos \omega t + A \cos (kx - \pi/2) \cdot \cos (\omega t - \pi/2). \quad (3)$$

This leads to an important result, i. e. a propagating wave can be generated by superimposing two standing waves whose phases differ by 90 degree to each other both in time and in space. This principle is necessary to generate a propagating wave on a limited volume/size substance, because only standing waves can be excited stably in a finite size.

The standing-wave type is sometimes referred to as a vibratory-coupler type or a "woodpecker" type, where a vibratory piece is connected to a piezoelectric driver and the tip portion generates flat-elliptical movement. Figure 2 shows a simple model proposed by T. Sashida.⁴⁾ A vibratory piece is connected to a piezoelectric driver and the tip portion generates flat-elliptical movement. Attached to a rotor or a slider, the vibratory piece provides intermittent rotational torque or thrust. The standing-wave type has, in general, high efficiency, but lack of control in both clockwise and counterclockwise directions is a problem.

By comparison, the propagating-wave type (a surface-wave or "surfing" type) combines two standing waves with a 90 degree phase difference both in time and in space. The principle is shown in Fig. 3. A surface particle of the elastic body draws an elliptical locus due to the coupling of longitudinal and transverse waves. This type requires, in general, two vibration sources to generate one propagating wave, leading to low efficiency (not more than 50 %), but it is controllable in both the rotational directions.

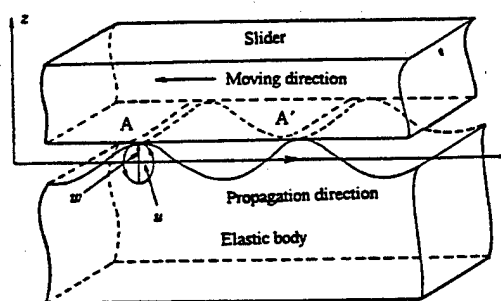
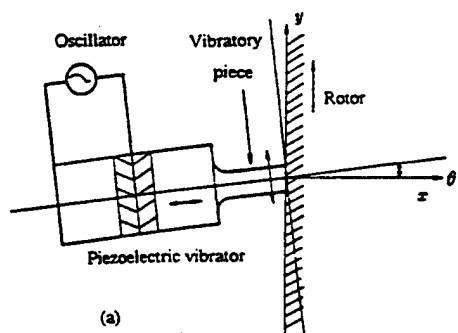


Fig. 2 Vibratory coupler type motor. Fig. 3 Principle of the propagating wave type motor.

CONVENTIONAL MOTOR DESIGNS

Sashida Motor

Figure 4 shows the famous Sashida motor.⁵⁾ By means of the traveling elastic wave induced by a thin piezoelectric ring, a ring-type slider in contact with the "rippled" surface of the elastic body bonded onto the piezoelectric is driven in both directions by exchanging the sine and cosine voltage inputs. Another advantage is its thin design, which makes it suitable for installation in cameras as an automatic focusing device. Eighty percent of the exchange lenses in Canon's "EOS" camera series have already been replaced by the ultrasonic motor mechanism. Most of the studies on ultrasonic motors done in the US and Japan have been modifications of Sashida's type.

The PZT piezoelectric ring is divided into 16 positively and negatively poled regions and two asymmetric electrode gap regions so as to generate a 9th mode propagating wave at 44 kHz. A proto-type was composed of a brass ring of 60 mm in outer diameter, 45 mm in inner diameter and 2.5 mm in thickness, bonded onto a PZT ceramic ring of 0.5 mm in thickness with divided electrodes on the back-side. The rotor was made of polymer coated with hard rubber or polyurethane. Figure 5 shows Sashida's motor characteristics.

Canon utilized the "surfing" motor for a camera automatic focusing mechanism, installing the ring motor compactly in the lens frame. It is noteworthy that the stator elastic ring has many teeth, which can magnify the transverse elliptical displacement and improve the speed. The lens position can be shifted back and forth through a screw mechanism. The advantages of this motor over the conventional electromagnetic motor are:

1. Silent drive due to the ultrasonic frequency drive and no gear mechanism (i. e. more suitable to video cameras with microphones).
2. Thin motor design and no speed reduction mechanism such as gears, leading to space saving.
3. Energy saving.

A general problem encountered in these traveling wave type motors is the support of the stator. In the case of a standing wave motor, the nodal points or lines are generally supported; this causes minimum effects on the resonance vibration. To the contrary, a traveling wave does not have such steady nodal

points or lines. Thus, special considerations are necessary. In Fig. 4, the stator is basically fixed very gently along the axial direction through felt so as not to suppress the bending vibration. It is important to note that the stop pins which latch onto the stator teeth only provide high rigidity against the rotation.

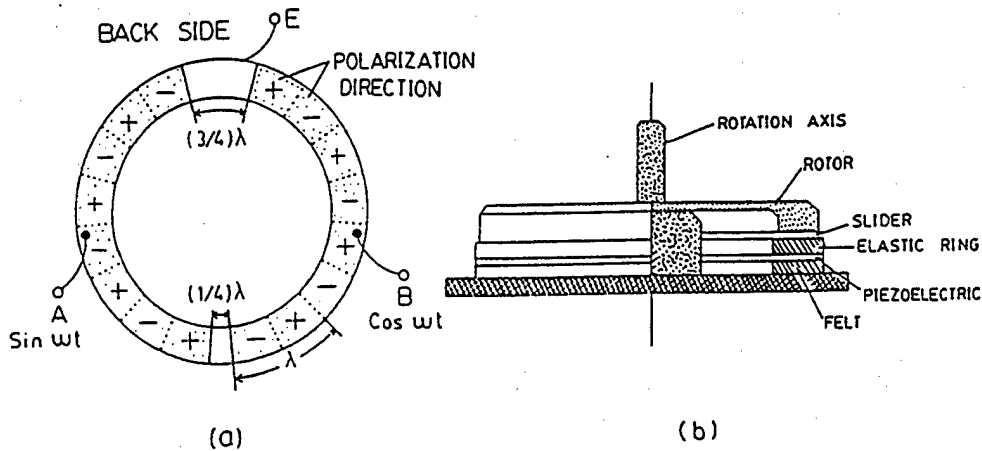


Fig. 4 Stator structure of Sashida's motor.

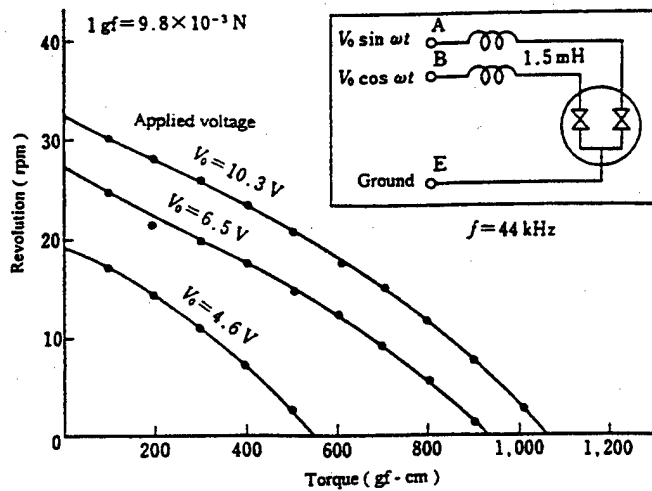


Fig. 5 Motor characteristics of Sashida's motor.

Inchworm Devices

Although the motion principle is different, inchworm devices move fast in apparent similarity to ultrasonic motors. The inchworm is driven by a rectangular wave below the resonance frequency, and moves intermittently and discretely.

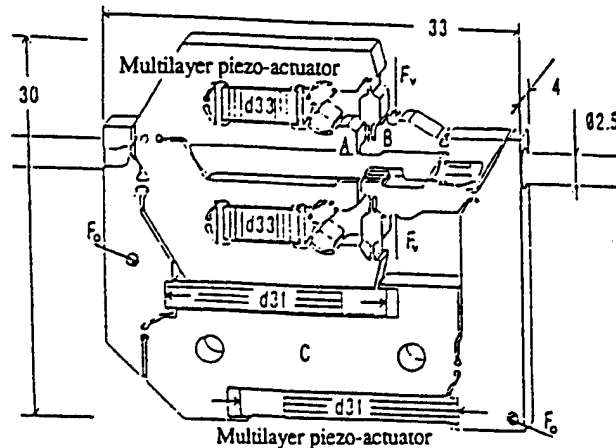


Fig. 6 Philips' inchworm.

Sophisticated linear walking machines have been developed by two German companies. Philips fabricated a linear drive inchworm using two d_{33} (longitudinal mode) and two d_{31} (transverse mode) multilayer actuators (Fig. 6).⁶⁾ Very precise positioning of less than 1 nm was reported. The problems with this type of device are: (1) audible noise, and (2) heat generation, when driven at high frequency. Physik Instrumente manufactured a two-leg inchworm.⁷⁾ A pair of inchworm units consisting of two multilayer actuators, are coupled with 90° phase difference in time so as to produce a smooth motion instead of a discrete step motion.

COMPACT MOTOR DESIGNS

Traveling Wave Types

Using basically the same principle as Sashida's, Seiko Instruments miniaturized the ultrasonic motor to as tiny as 10 mm in diameter.⁸⁾ Figure 7 shows the construction of this small motor with 10 mm diameter and 4.5 mm thickness. A driving voltage of 3 V and a current 60 mA provides 6000 rev/min (no-load) with torque of 0.1 mN·m. Seiko installed this tiny motor into a wrist watch as a silent alarm. Rotating an imbalanced mass provides enough hand shake to a human without generating audible noise. AlliedSignal developed ultrasonic

motors similar to Shinsei's, which would be utilized as mechanical switches for launching missiles.⁹⁾

A significant problem in miniaturizing this sort of traveling wave motor can be found in the ceramic manufacturing process; without providing a sufficient buffer gap between the adjacent electrodes, the electrical poling process (upward and downward) easily initiates the crack on the electrode gap due to the residual stress concentration. This may restrict the further miniaturization of the traveling wave type motors. To the contrary, standing wave type motors, the structure of which is less complicated, are more suitable for miniaturization as we discuss in the following. They require only one uniformly poled piezo-element, less electric lead wires and one power supply.

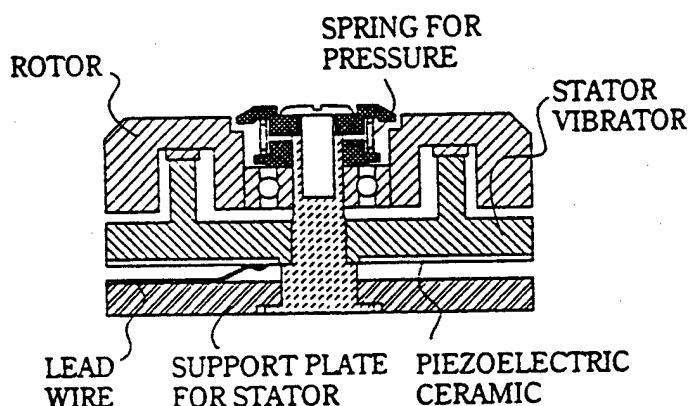


Fig. 7 Construction of Seiko's motor.

Standing Wave Types

Linear motors

Uchino et al. invented a π -shaped linear motor.¹⁰⁾ This linear motor is equipped with a multilayer piezoelectric actuator and fork-shaped metallic legs as shown in Fig. 8. Since there is a slight difference in the mechanical resonance frequency between the two legs, the phase difference between the bending vibrations of both legs can be controlled by changing the drive frequency. The walking slider moves in a way similar to a horse using its fore and hind legs when trotting. A test motor $20 \times 20 \times 5 \text{ mm}^3$ in dimension exhibited a maximum speed of 30 cm/s and a maximum thrust of 0.9 kgf with a maximum

efficiency of 20%, when driven at 98kHz at 6V (actual power = 0.7 W). This motor has been employed in a precision X-Y stage.

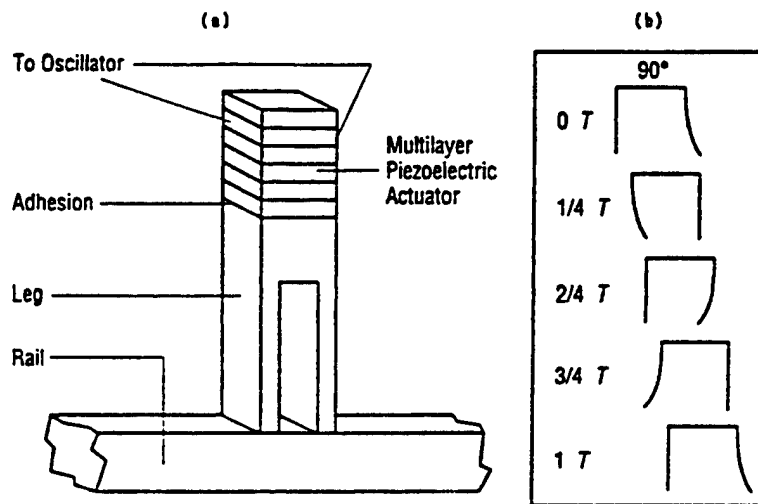


Fig. 8 π -shaped linear ultrasonic motor. (a) construction and (b) walking principle. Note the 90 degree phase difference like human walk.

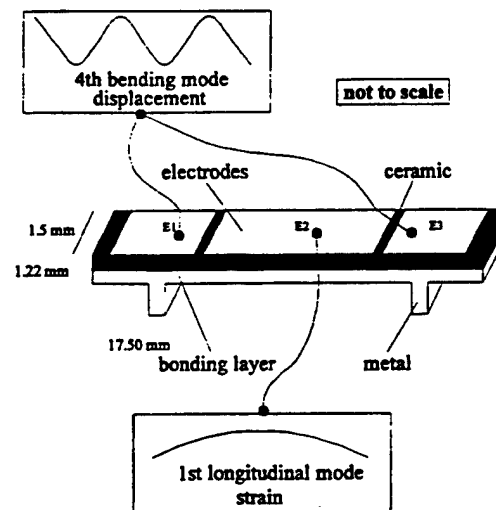


Fig. 9 Miniature ultrasonic linear motor.

We further miniaturized this "Shepherd" shape by 1/10 into a "Dachshund" shape by reducing the leg length (Fig. 9).¹¹⁾ According to this miniaturization, we utilized a unimorph type drive mechanism in conjunction with a coupling mode between 1st longitudinal and 4th bending modes. Under

100 V_{p-p} applied (0.6 W), this linear motor exhibited the maximum speed of 160 mm/sec and the thrust of 0.25 - 1.00 N.

One ceramic multilayer component actuator was proposed by Mitsui Chemical.¹²⁾ Figure 10 shows the electrode pattern. Only by the external connection, a combined vibration of the longitudinal L₁ and bending B₂ modes could be excited.

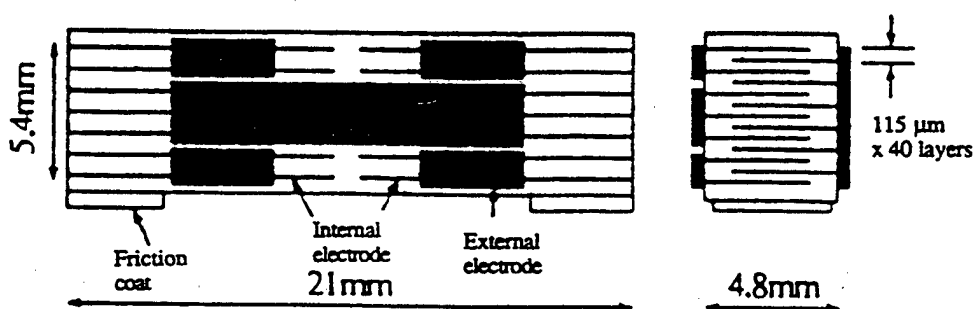


Fig. 10 Multilayer ceramic simple linear motor (Mitsui Chemical).

Rotary motors

Hitachi Maxel significantly improved the torque and efficiency by using a torsional coupler, and by the increasing pressing force with a bolt.¹³⁾ The torsional coupler looks like an old fashioned TV channel knob, consisting of two legs which transform longitudinal vibration generated by the Langevin vibrator to a bending mode of the knob disk, and a vibratory extruder. Notice that this extruder is aligned with a certain cant angle to the legs, which transforms the bending to a torsion vibration. This transverse moment coupled with the bending up-down motion leads to an elliptical rotation on the tip portion. A motor with 30mm x 60mm in size and 20 - 30° in cant angle between a leg and a vibratory piece provided the torque as high as 1.3 N·m and the efficiency of 80%. However, this type provides only unidirectional rotation.

The Penn State University has developed a compact ultrasonic rotary motor as tiny as 3 mm in diameter. As shown in Fig. 11, the stator consists basically of a piezoelectric ring and two concave/convex metal endcaps with "windmill" shaped slots bonded together, so as to generate a coupled vibration

of up-down and torsional type.¹⁴⁾ Since the component number and the fabrication process were minimized, the fabrication price would be decreased remarkably, and it would be adaptive to the disposable usage. When driven at 160 kHz, the maximum revolution 2000rpm and the maximum torque 0.8mN·m were obtained for a 5 mm ϕ motor. Notice that even the drive of the motor is intermittent, the output rotation becomes very smooth because of the inertia of the rotor. Figure 12 shows motor characteristics plotted as a function of motor size for modified "windmill" motors.¹⁵⁾

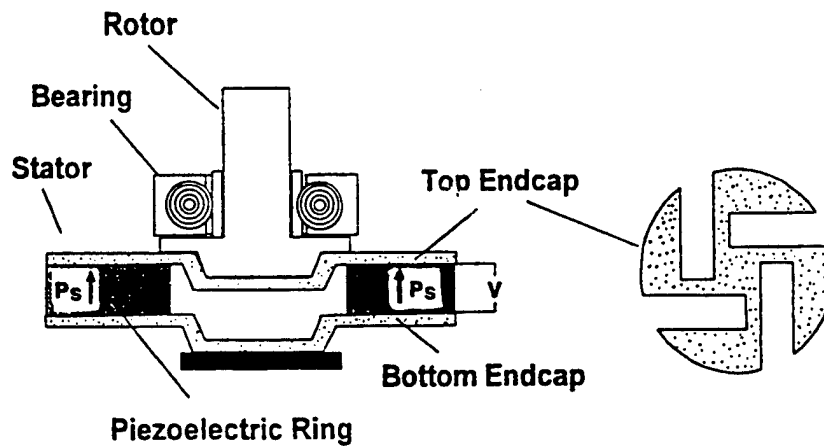


Fig. 11 "Windmill" motor with a disk-shaped torsional coupler.

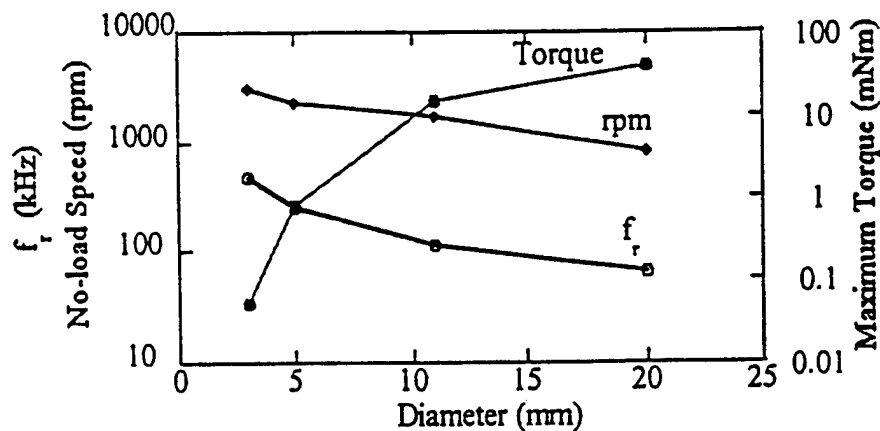


Fig. 12 Radial mode resonance frequency, no-load speed and starting torque vs. diameter of the stator. Speed and torque were measured at 15.7 V.

INTEGRATED MOTOR DESIGNS

We will introduce an ultrasonic motor fabricated on a Si substrate, jointly developed by MIT and Penn State.¹⁶⁾ After coating a PZT thin film on a Si membrane (2.2mm x 2.2mm), an 8-pole stator (1.2mm and 2.0mm inner and outer diameters) was patterned on the surface electrode. The 8 segmented electrode pads were driven in a four phase sequence repeated twice. A small contact glass lens was used as a rotor. This simple structure provided already 10^3 time higher torque than the conventional electrostatic MEMS motors.

Another intriguing surface acoustic wave motor has been proposed by Kurosawa and Higuchi.¹⁷⁾ Rayleigh waves were excited in two crossed directions on a 127.8°-rotation Y-LiNbO₃ plate with two pairs of interdigital electrode patterns. A slider was composed of three balls as legs. The driving vibration amplitude and the wave velocity of the Rayleigh waves were adjusted to 6.1 nm and 22 cm/sec for both x and y directions. It is important to note that even though the up-down vibrational amplitude is much smaller ($< 1/10$) than the surface roughness of the LiNbO₃, the slider was transferred smoothly. The mechanism has not been clarified yet, it might be due to the locally enhanced friction force through a ball-point contact.

SUMMARY

Ultrasonic motors are characterized by "low speed and high torque," which are contrasted with "high speed and low torque" of the conventional electromagnetic motors. Thus, the ultrasonic motors do not require gear mechanisms, leading to very quiet operation and space saving. Negligible effects from external magnetic or radioactive fields, and no generation of these fields are suitable for the application to electron beam lithography etc. relevant to the semiconductor technology. Moreover, high power / weight ratio, high efficiency, compact size and light weight are very promising for the future micro actuators adopted to catheter or tele-surgery.

For the further applications of the ultrasonic motors, systematic investigations on the following issues will be required:

- (1) development of low loss & high vibration velocity piezo-ceramics,
- (2) piezo-actuator component designs with high resistance to fracture and good heat dissipation,
- (3) ultrasonic motor designs;
 - a. motor types (standing-wave type, traveling-wave type, hybrid type, integrated type),
 - b. simple displacement magnification mechanisms of vibratory piece (horn, hinge-lever),
 - c. frictional contact part,
- (4) inexpensive and efficient high frequency/high power supplies.

Acknowledgement

This work was partially supported by the Office of Naval Research through Contract No. N00014-96-1-1173.

References

- 1) H. V. Barth: IBM Technical Disclosure Bull. 16, 2263 (1973).
- 2) V. V. Lavrinenko, S. S. Vishnevski and I. K. Kartashev: Izvestiya Vysshikh Uchebnykh Zavedenii, Radioelektronika 13, 57 (1976).
- 3) P. E. Vasiliev et al.: UK Patent Application GB 2020857 A (1979).
- 4) T. Sashida: Oyo Butsuri 51, 713 (1982).
- 5) T. Sashida: Mech. Automation of Jpn., 15 (2), 31 (1983).
- 6) M.P.Coster: Proc.4th Int'l Conf.on New Actuators, 2.6,p.144, Germany (1994).
- 7) R.Gloess: Proc. 4th Int'l Conf. on New Actuators, P26, p.190, Germany (1994).
- 8) M. Kasuga, T. Satoh, N. Tsukada, T. Yamazaki, F. Ogawa, M. Suzuki, I. Horikoshi and T. Itoh: J. Soc. Precision Eng., 57, 63 (1991).
- 9) J. Cummings and D. Stutts: Amer. Ceram. Soc. Trans. "Design for Manufacturability of Ceramic Components", p.147 (1994).
- 10) K. Uchino, K. Kato and M. Tohda: Ferroelectrics 87, 331 (1988).
- 11) T. Bein, E. J. Breitbach and K. Uchino: Smart Mater. Struct. 6, 619 (1997).
- 12) H. Saigo: 15th Symp. Ultrasonic Electronics (USE 94), No. PB-46, p.253 (Nov. 1994).
- 13) A. Kumada: Jpn. J. Appl. Phys., 24, Suppl. 24-2, 739 (1985).
- 14) B. Koc, A. Dogan, Y. Xu, R. E. Newnham and K. Uchino: Jpn. J. Appl. Phys. 37, 5659 (1998).
- 15) B. Koc, Y. Xu and K. Uchino: Proc. IEEE Int'l Ultrasonic Symp., Sendai, Japan (1998) [in press].
- 16) A. M. Flynn, L. S. Tavrow, S. F. Bart, R.A.Brooks, D.J.Ehrlich, K.R.Udayakumar and L. E. Cross: J. Microelectro-mechanical Systems, 1, 44 (1992).
- 17) M. Takahashi, M. Kurosawa and T. Higuchi: Proc. 6th Symp. Electro-Magnetic Dynamics '94, No. 940-26 II, D718, p.349 (July, 1994).

For further reading:

- 18) K. Uchino: "Piezoelectric ultrasonic motors: overview" Smart Mater. Struct. 7, 273 (1998).
- 19) K. Uchino: "Piezoelectric Actuators and Ultrasonic Motors," Kluwer Academic Publishers, MA (1996).

APPENDIX 50

Ceramic/Metal Composite Piezoelectric Motors

Burhanettin Koc, Yuan Xu and Kenji Uchino

International Center For Actuators and Transducers

Materials Research Laboratory

The Pennsylvania State University,

University Park, Pa, 16802

Abstract - This paper deals with design and fabrication of a newly developed metal/ceramic composite ultrasonic motor. Inwardly directed arms at the inner circumference of metal ring, sandwiched between two uniformly poled piezoelectric ceramic rings, transfer radial vibration into torsional vibration. The stator vibrators, using different diameters (3.0, 5.0, 11.0 and 20.0 mm) and thickness of 0.5 mm piezoelectric ring, were fabricated and the characteristics of the motors were measured.

Introduction

Piezoelectric ultrasonic motors are generally categorized as travelling wave and standing wave types. Currently, most of advanced miniaturized motors are utilizing travelling wave type. The piezoelectric element in travelling wave type, generally annular ring, needs to be sectorized and the neighboring sectors are poled alternately opposite direction which makes the poling process difficult and causes sample damage. In order to produce a travelling wave on a vibrating piezoelectric element at least two ac power sources with 90 degree phase difference both in time and space are required. Furthermore, the maximum admissible mechanical stress for material working in flexion is also relatively low. These drawbacks limit the miniaturization of travelling wave type piezoelectric motors to a size of less than 7.0 mm range with a reasonable price[1,2].

However, standing wave type piezoelectric ultrasonic motors, the structure of which is less complicated, are more suitable for miniaturization. Recently we can find several examples of one phase driven motors using composite structures. In order to obtain twisting motion some non-piezoelectric materials such as carbon fiber reinforced plastic were used with piezoelectric material [3,4].

We proposed an ultrasonic motor design "windmill" using a metal/ceramic composite vibrator as the stator

element [5-7]. The stator in that motor consists of a piezoelectric ring poled uniformly in thickness direction, and bonded with windmill-like slotted and reshaped two metal endcaps. The radial vibration of the piezoelectric ring is transferred into torsional and longitudinal vibrations by the four legs on the metal endcaps (Fig. 1).

The "windmill" motor has some exceptional properties such as simple structure, no excessive temperature rise, and single source driving. However, torque generation from a motor of 11.0 mm in diameter was not high (1.3 mNm). One way to improve the motor torque is increasing the thickness of the metal. Since the metal endcap in windmill structure is not thick (0.2mm), the force in radial direction was not transferred into tangential direction efficiently; instead the thin legs deform. The other drawback of the windmill motor is difficulty of downsizing the stator structure.

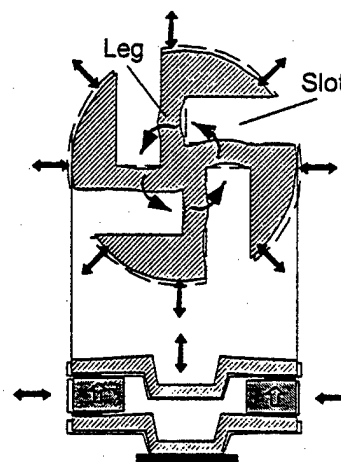


Fig. 1 Structure of the "windmill" motor's stator vibrator.

In this study, the original "windmill" design was modified to obtain larger torque and also to miniaturize the stator vibrator to a few millimeter range. The stator vibrator, in this motor is a thicker metal ring with eight inwardly directed arms, sandwiched with two uniformly poled piezoelectric ceramic rings from both sides. The

inwardly directed arms of the metal ring, oriented with an angle to the center, transfer the radial displacement into tangential displacement when the whole structure is excited at a radial mode resonance frequency. The frictional force at the tips of the arms causes the cylindrical rod to rotate. Detailed description of the operational principle and the fabrication process of different size ultrasonic motors are given in the following sections.

Structure and Operating Principle of the Motor

The basic configuration of the motor's stator is shown in Fig. 2. It has a metal ring with eight inwardly directed arms sandwiched between two uniformly poled piezoelectric ceramic rings. The metal arms are angled from the radial direction, and their tips are tapered to an angle of 17° . The rotor we used in our experiments is a cylindrical rod of which one end, touching to the eight tips of the stator's metal arms, has a truncated cone shape.

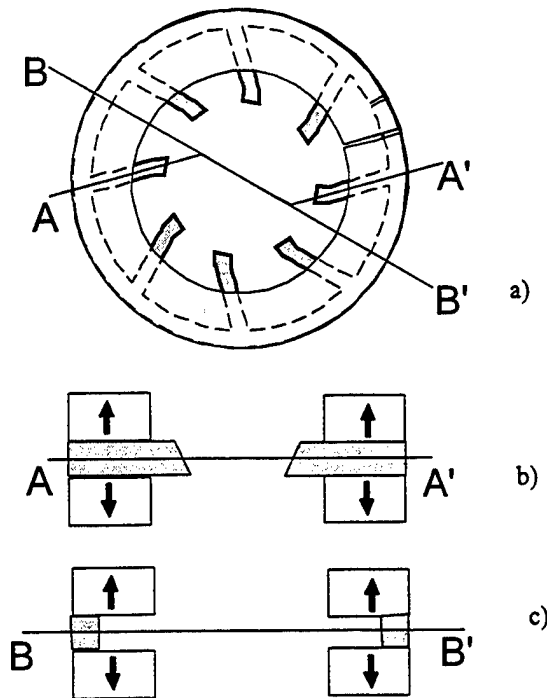


Fig. 2 Structure of the metal ceramic composite vibrator
a) Top view, b) cross-sectional view (A-A') c) cross-sectional view (B-B')

When the stator vibrator is electrically excited at its radial resonance mode, the piezoelectric and metal rings expand and contract in the radial direction. The radial component of the force that is generated by the ring vibration is transferred to the rotor via the metal arms. Since these arms are angled from the radial direction by θ_1 , normal and tangential force components are generated at the periphery of the rotor (Fig.3).

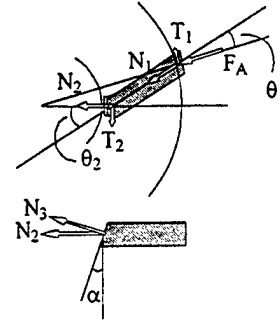


Fig. 3 Scheme of the force transformation. Normal N_3 and tangential T_2 forces were generated from piezoelectric ring's force F_A through the arms.

The displacement transformation was visualized by modeling one eighth of the stator using ATILA software.

The vibration mode of the free stator is shown in Fig.4. As can be seen in Fig.4, there is a small tangential displacement at the tip of the arm for the free stator vibrator. When the tip of the arm is constrained in the radial direction, which is equivalent to a loaded condition (rotor at the center), vibration transformation in tangential direction can be seen in Fig.5.

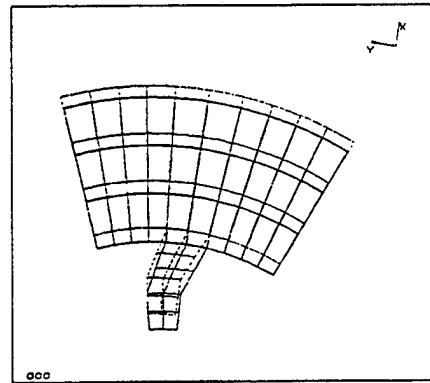


Fig. 4 Vibration mode of the free stator (dashed line shows the stator at rest).

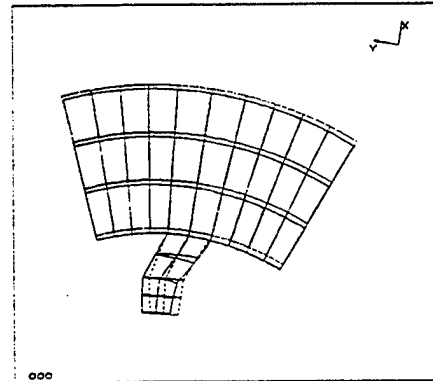


Fig. 5 Vibration transformation from radial to tangential direction at the tip of the arm (dashed line shows the stator at rest).

Fabrication of the Stator

The stator vibrators were constructed by using piezoceramic and metal rings with diameter ranging from 3.0 to 20.0 mm (3.0, 5.0, 11.0 and 20.0 mm). The thickness of piezoelectric rings (P841 from American Piezo Ceramic) were kept constant at 0.5 mm. The metal rings, the dimensions of which are given in Table 1, were cut by electrical discharge machining (EDM) and sandwiched between two piezoelectric rings using adhesive epoxy (Fig.6).



Fig. 6 Copper beryllium rings with inwardly directed arms oriented with an angle (θ_i) to the radius.

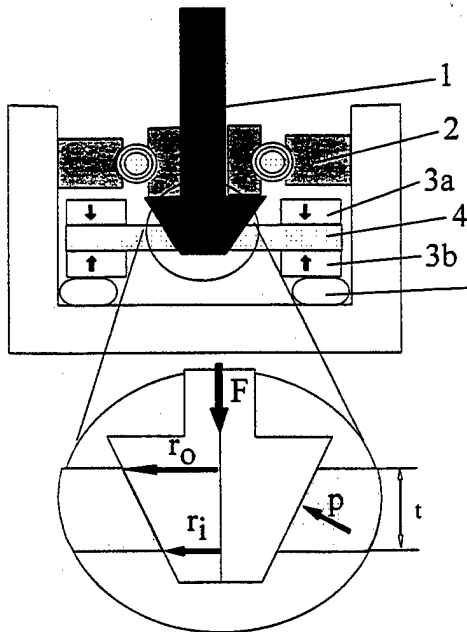


Fig. 7 Structure of the motor. 1)rotor, 2) ball bearing, 3a, b) Piezoelectric rings, 4)metal ring, 5) rubber ring as spring.

Using fabricated stators, different size ultrasonic motors were assembled as shown in Fig.7. The performance of the motors of 3.0 to 20.0 mm in diameter was measured under the same condition, that the normal

stress between stator and arms' tips p was kept constant according to the following equation.

$$p = 2F / \pi r_i (r_o - r_i) \quad (1)$$

where, F is the normal pressing force, r_i and r_o are the radius of the conical touching surface of the rotor.

Table 1 Pre-load condition and dimensions of metal rings

Diameter (mm)	3.0	5.0	11.0	20.0
r_i (mm)	1.0	2.0	4.74	8.6
r_o (mm)	1.12	2.2	5.0	9.2
t (mm)	0.2	0.35	0.45	0.86
F (N)	0.35	1.16	3.6	15.0

The driving frequency of this motor is close to the first radial mode resonance frequency of the stator. In order to decide driving frequency of each motor, the low field admittance spectrum of all motors were measured. Quality factor Q_m and effective electromechanical constant k_{eff} were also calculated using the admittance spectrum data. Q_m and k_{eff} vs. diameter of the stator curves are shown in Fig.8. As the size of the motor decreases, (diameter of piezoelectric stator vibrator), the piezoelectric and electromechanical characteristics does not change significantly, the mechanical loss, however, decreases gradually. This decrease of quality factor may be due to the effect of bonding layer and metal thickness. Even solder used for cable connection on a small motor's stator causes additional mass which increases the electrical and mechanical losses. In conclusion, small ultrasonic motor fabrication process requires high precision positioning and thinner bonding layer thickness. Moreover, the structure of the motor should be simple and number of the components should be minimized.

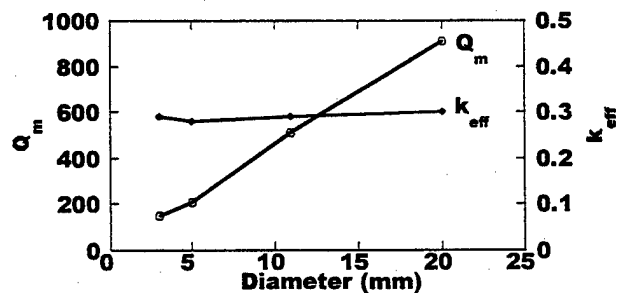


Fig. 8 Electromechanical constant and quality factor vs. diameter of the stator.

The starting torque and no-load speed of the trial motors were also measured using a torque watch gauge (Data Instruments, USA) and Digital Tachometer (Shimpo Industries Co.). The applied voltage was kept constant at 15.7 V for all the motors. The results are shown in Fig.9 together with the radial mode resonance frequency.

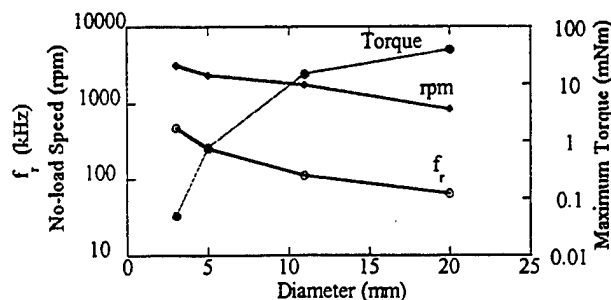


Fig. 9 Radial mode resonance frequency, no-load speed and starting torque vs. diameter of the stator. Speed and Torque were measured at 15.7 V.

Conclusion

A new piezoelectric ultrasonic motor design is proposed. The structure of the motor is simple, therefore, the motor can be fabricated easily as small as few millimeters (3.0 mm) or as large as several tens of millimeter with low cost.

The design of the motor could be optimized by tailoring length, number and orientation angle of the inwardly directed arms at the inner circumference of the metal ring. Performance of the motor can be improved by adjusting a bending frequency of arms to the radial resonance frequency of the stator. Further improvement can be expected by poling piezoelectric ring in radial direction which leads to the usage of thickness mode piezoelectric constant d_{33} instead of transverse mode piezoelectric constant d_{31} .

Acknowledgment

The authors would like to thank the Office of Naval Research for supporting this work through contract: N00014-96-1-1173

References

- [1] M. Kasuga, T. Satoh, N. Tsukada, T. Yamazaki, F. Ogawa, M. Suzuki, I. Horikoshi and T. Itoh, *Journal of the Society of Precision Engineers*, Vol. 57 (1991) 63.
- [2] D. Stutts and J. Cummings, *Smart Actuator Symposium*, University Park, PA, October 22 (1994).
- [3] K. Ohnishi, Y. Tomikawa, C. Kusakabe, M. Aoyagi. "Ultrasonic Actuator using orthotopic composite Materials", *Ultrasonic* 34, 283-285, (1996).
- [4] S-W R. Lee, and H. L. Li, "Anisotropic Piezoelectric Laminate for Rotary Actuators", *SPIE Vol. 3321*, 484-491, (1998).
- [5] K. Uchino and B. Koc, U.S. Patent Application, PSU Invention Disclosure no:96-1633
- [6] B. Koc, A. Dogan, Y. Xu, R.E. Newnham and K. Uchino, "An Ultrasonic motor using Metal Ceramic Composite Stator Generating Torsional Displacement", *Jpn. J. Appl. Phys.* (1998) (in press).
- [7] B. Koc, Y. Xu, and K. Uchino, "Roto-Linear Ultrasonic Motor", *Actuator 98*, 6th International Conference on New Actuators, Bremen, Germany, 156-159, (1998)

APPENDIX 51

ROTO-LINEAR ULTRASONIC MOTORS

B. Koc, Y. Xu and K. Uchino
International Center for Actuator and Transducers
Materials Research Laboratory
The Pennsylvania State University
University Park, Pa, 16802, USA

Abstract:

In this study, a new single phase driven piezoelectric motor design is presented for both rotary and linear motions on horizontal plane. Two metal-ceramic composite actuators, a piezoelectric ring poled in thickness direction and bonded to a metal endcap from one side, were used as the active elements of this motor. Using ATILA Finite element analysis software, mode shapes of a free actuator were obtained to clarify the working principle of this motor. Only the rotary characteristics of the motor were measured. Maximum starting torque of 1.20 mNm in clockwise and 1.25 mNm in counterclockwise direction were obtained from a prototype motor at 20 Vrms.

Introduction

It is difficult to miniaturize electromagnetic motors less than 1 cm^3 with high efficiency. On the other hand Ultrasonic motors, the energy efficiency of which is insensitive to the size, have a great potential for miniaturization. Current miniaturized ultrasonic motors are traveling wave types [1-3]. In order to produce a traveling wave on a vibrating piezoelectric element at least two ac power sources with 90 degree phase difference both in time and space are required. Furthermore, the stator, a piezoelectric ring, needs to be divided into sectors and these sectors on the piezoelectric ring need to be poled in alternately opposite directions, which makes a poling process difficult and causes the sample damage.

A new single phase driven ultrasonic motor "windmill" was designed using a metal ceramic composite component as the stator element [4,5]. The stator in that motor consists of a piezoelectric ring poled uniformly in thickness direction, and bonded with uniquely slotted and reshaped two metal endcaps. The radial vibration of the piezoelectric ring is transferred into torsional and longitudinal vibrations by the four legs on the metal endcaps.

In this study, the original "windmill" design was

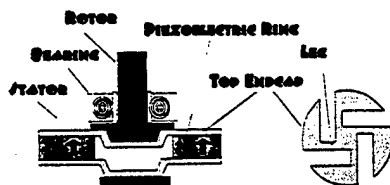


Fig.1: Structure of the "windmill" ultrasonic motor.

modified to obtain linear motion in addition to rotary motion by cutting the center part of the metal endcap and putting the rotor at the center.

Structure of the Motor

The basic configuration of the free stator structure and proposed ultrasonic motor are shown in Figures 2 and 3, respectively. A cylindrical rod was utilized as the rotor. The stators are metal ceramic composites, piezoelectric rings poled in thickness direction and bonded with metal (copper beryllium) rings which has eight inwardly directed arms. The inner diameters of the piezoelectric rings are different so that the actuators exhibit different resonance frequencies. The two stators were oriented in a way that one actuator expand and the other actuator shrink in radial direction under an AC voltage driving. If one actuator is driven at its radial resonance frequency the piezoelectric ring and metal endcap expand and compress in radial direction. In the compressing cycle of one particular stator the eight arms at the center of the metal endcap clamp the shaft (rotor) and push it in tangential direction. In the expansion cycle the arms release the shaft. Since the other stator, which is working at off resonance, compresses and clamps the shaft with a smaller force, therefore, the shaft does not come back to its original position.

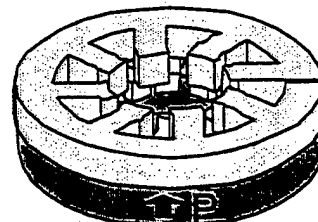


Fig.2: Metal-Ceramic Stator Element.

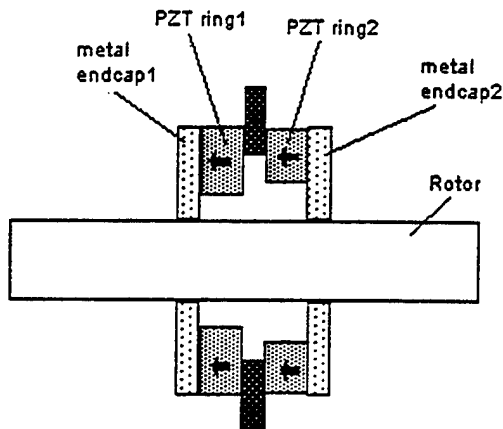


Fig. 3: Basic configuration of the motor

A linear motion can also be obtained by exciting a stator at first flexure (umbrella) mode resonance frequency which is usually less than half of the radial mode resonance frequency.

Figure 4 shows the 3D mesh of a free stator element for mode shape analysis using ATILA code [6]. The first flexure mode shape is shown in Figure 5. Perspective view of the first radial mode is shown in Fig. 6a. Top views when stator shrink and expand in radial direction are shown in Fig. 6b and c.

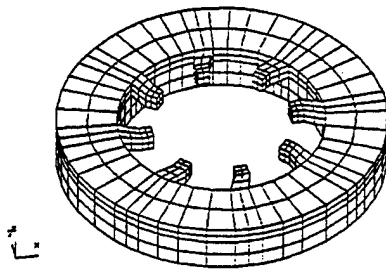


Fig. 4. ATILA 3D mesh of the stator.

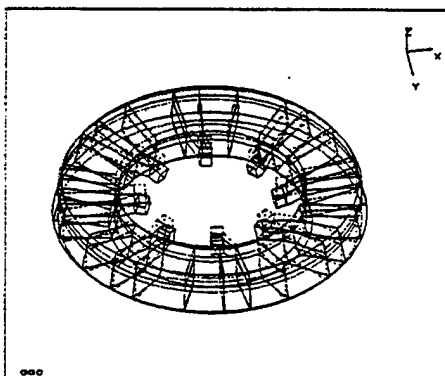


Fig. 5. Flexure mode shape.

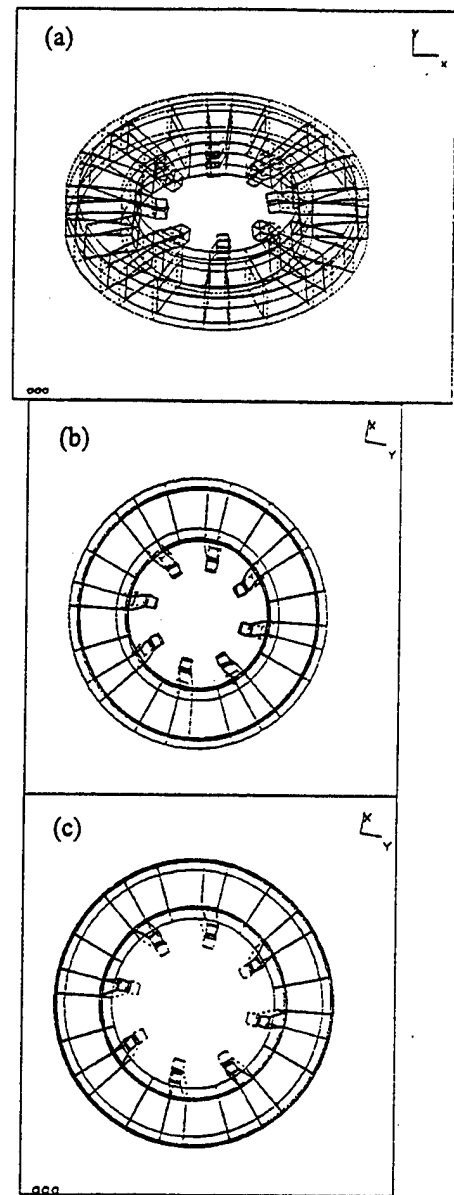


Fig. 6. a) Mode shape at radial resonance frequency b) top view when stator shrink in radial direction. c) top view when stator expand in radial direction.

Rotary Motor Characteristics.

The proposed motor is a standing wave type and the torsional force is produced by transferring the radial displacement of piezoelectric element through the inwardly directed arms of the metal endcaps. Then the frictional force between tips of the arms and the surface of the cylindrical rotor generates rotation.

The rotary motor structure shown in Fig. 7 was constructed having the following stator dimensions:

Outer diameter of piezoelectric ring: 11.0 mm
Thickness of the piezoelectric ring : 0.5 mm

Inner diameters of the piezoelectric rings:
7.0 mm (for stator1 3b 4b in Fig. 7) and 6.5 mm (for
stator2 3a 4a in Fig.7). Diameter of cylindrical rod :
4.5 mm
thickness of the metal endcaps (copper beryllium): 0.45
mm.

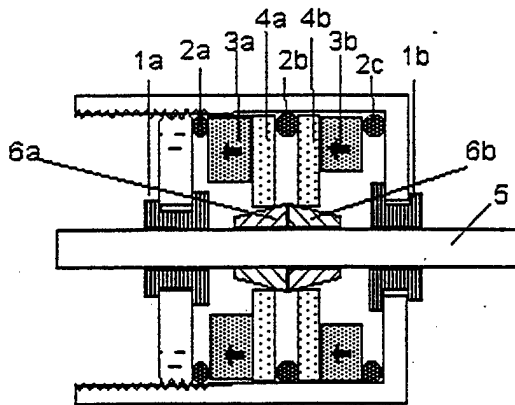


Fig. 7: Structure of the proposed rotary ultrasonic motor. (1a, b) plastic bearing, (2a, b, c) rubber ring, (3a, b) piezoelectric ring poled in thickness direction, (4a, b) metal endcaps bonded onto piezoelectric ring from one side, (5) rotor, (6a, b) ferrule.

The piezoelectric ceramic material utilized was P841 (American Piezo Ceramic). The metal endcaps were cut by electrically discharge machining (EDM) and bonded on one side of the piezoelectric ring using adhesive epoxy. The first flexure and radial mode resonance frequencies were measured as 36.1 kHz and 114.8 kHz for stator1 (44.2 kHz and 122.5 kHz for stator2), respectively. Free stators admittance curves are shown in Fig. 8.

Pair of stainless steel ferrules were mounted on a thinner cylindrical rod to increase the matching between the tip of the endcap and the rotor in order to increase the pressing force, thus, the torque of the motor. The experimental motor was driven only at resonance frequencies of the stators at 118.2 kHz and 125.7 kHz to obtain clockwise and counterclockwise rotations, respectively. The speed of the motor in clockwise or counterclockwise direction as a function of input rms voltage is shown in Fig. 9. The clockwise and counterclockwise speeds of the motor were increased at almost same rate as the input voltage increased from 10 to 20 Vrms.

Starting torque in clockwise and counterclockwise directions as a function of input rms voltage were measured using a torque Watch Gauge (Data Instruments) (Fig. 10). The starting clockwise and

counterclockwise torque of the motor is increasing amount linearly with input voltage from 10 to 20 Vrms.

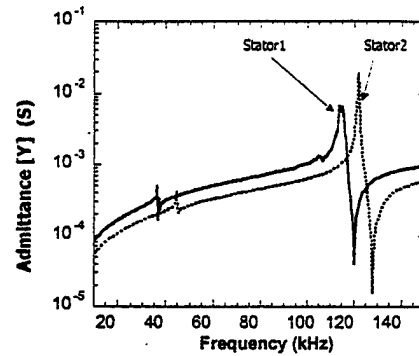


Fig. 8. Admittance spectrum of the free stators

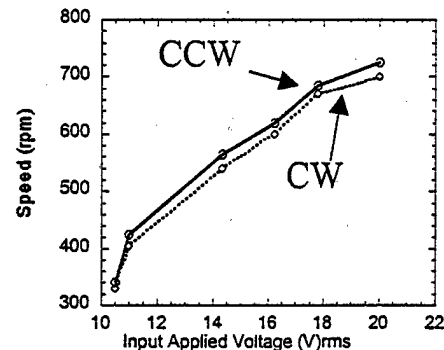


Fig. 9. CW and CCW Speeds as a function of input voltage.

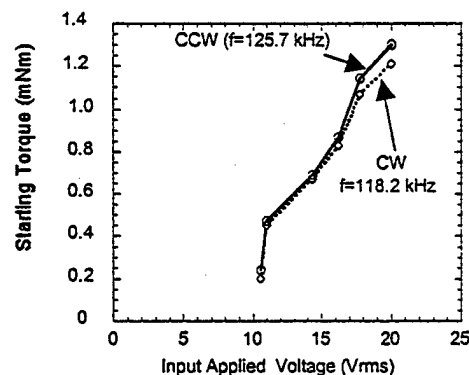


Fig. 10 Starting torque of the motor as a function of input voltage

Conclusion

A new multi functional ultrasonic motor design was proposed using a pair of metal ceramic composite actuators as the active stator elements. Finite element

Analysis of Mode shapes of the free stator element were carried out to clarify the working principle of the proposed motor using ATILA code.

A trial motor was constructed and driven at radial mode resonance frequencies of the stator elements and similar clockwise and counterclockwise starting torque and speed values were obtained for the same input voltage.

Important features of this motor are its simple structure and the capability of miniaturization down to 3 mm Φ .

Acknowledgement

The authors acknowledge Turkish Higher Educational Council.

References

- [1] M. Kasuga, T. Satoh, N. Tsukada, T. Yamazaki, F. Ogawa, M. Suzuki, I. Horikoshi and T. Itoh, Journal of the Society of Precision Engineers, 57 (1991) 63-75.
- [2] D. Stutts and J. Cummings, Smart Actuator Symposium, State College, USA (1994)
- [3] S. Kumada, Jpn. J. Appl. Phys. Suppl. 24 2 (1985) 719-723.
- [4] K. Uchino and B. Koc, U.S. Patent Application, PSU Invention Disclosure no:96-1633
- [5] B. Koc, A. Dogan, Y. Xu, R.E. Newnham and K. Uchino, Jpn. J. Appl. Phys. (1998) Submitted.
- [6] ATILA, a 3D FEM software for piezoelectric & magnetostrictive structures, Magsoft (US).

APPENDIX 52

An Ultrasonic Motor Using a Metal-Ceramic Composite Actuator Generating Torsional Displacement

Burhanettin KOC, Aydin DOĞAN¹, Yuan XU, Robert E. NEWNHAM and Kenji UCHINO

International Center for Actuators and Transducers, Materials Research Laboratory, The Pennsylvania State University, University Park, PA 16802, USA

¹*Ceramic Engineering Department, Anadolu University, Eskişehir, Turkey*

(Received April 15, 1998; accepted for publication July 13, 1998)

An ultrasonic motor composed of three components; a stator, a rotor and a ball bearing is proposed. The stator is made of an active piezoelectric ring, poled in the thickness direction and bonded with two windmill-like slotted metal endcaps. The stator is excited through its two electrodes, generating ultrasonic vibration in the radial direction at a radial mode resonance frequency. The two identical metal endcaps on both sides of the ring, bonded after shifting 45° with each others, transfers the radial vibration into longitudinal and tangential vibrations. The combination of these vibrations (longitudinal and tangential) generates rotation due to frictional interaction between the center part of the top endcap and the periphery of the rotor. A prototype motor with 11.0 mm diameter was fabricated and its transient characteristics were measured. The maximum torque of 1.36 mNm was obtained at a speed of 480 rpm.

KEYWORDS: ultrasonic motor, piezoelectric ring, metal endcap, windmill-like slot, radial, longitudinal, torsional vibration, transient response

1. Introduction

Miniaturization of conventional electromagnetic motors to sizes smaller than 1 cm with high energy efficiency is rather difficult. On the other hand, ultrasonic motors, the energy efficiency of which is insensitive to the size, have a great potential for miniaturization. Currently, most of miniaturized ultrasonic motors such as the products by Seiko¹⁾ and AlliedSignal,²⁾ are utilizing a travelling wave type. In order to produce a traveling wave on a piezoelectric element, at least two driving ac power sources with 90° phase difference both in time and space are required. Besides, the stator, a ring shape piezoelectric active element needs to be divided into sectors. Since the sectors on the piezoelectric ring are usually poled in alternately opposite directions, a high stress concentration is generated at the unelectroded slit between two electroded sectors. This makes the poling process difficult and even causes sample damage. Thus, for miniaturizing the ultrasonic motor, we are taking the following two strategies: 1) utilizing a standing wave, 2) minimizing the number of the components. One idea has been proposed by Hitachi Maxcell using a Langevin-type piezo-transducer coupled with a torsional vibration coupler.³⁾ This motor exhibited very high torque up to 1.3 Nm.

We reported metal-ceramic composite structures called "Moonie" and "Cymbal" for sensor and actuator applications.⁴⁻⁶⁾ The idea behind these transducers is transferring the radial displacement of the piezoelectric ceramics into the longitudinal displacement through the endcap, or the longitudinal stress into the radial stress so as to make the conventionally ineffective planer mode piezoelectric coefficient effective, increasing the sensitivity of the actuators or sensors.

In this paper we propose a new ultrasonic motor in which a metal-ceramic composite component was used as the stator element to generate ultrasonic vibrations. The stator consists of a piezoelectric ring poled uniformly in the thickness direction, and bonded with uniquely slotted and reshaped two metal endcaps. The radial vibration of the piezoelectric ring is transferred into torsional and longitudinal vibrations by the legs of the metal endcaps. These vibrations, torsional and longitudinal, drive the rotor to rotate through the frictional

coupling.

2. Structure and Operational Principle

The basic configuration of the proposed ultrasonic motor is shown in Fig. 1. The principle of the motor can be understood through analysis of the metal endcap motion. When the piezoelectric ring vibrates in the radial direction, the metal endcaps, bonded to the outside circumference of the ring, will also move together with the piezoelectric ring. The legs connecting the outer to the center part of the endcaps make the latter deformed not only in the tangential but also in the longitudinal direction [Fig. 2(a)].

Referring to Fig. 2(b), the top and cross-sectional views of the stator displacement, a poled and electroded piezoelectric single ring was bonded with two metal endcaps. The metal endcaps were cut by electrically discharge machining (EDM). Before the metal endcaps were bonded using adhesive epoxy to the piezoelectric ring, the center part of the endcaps were indented from the rest of the body. The purposes of the indent were; a) to hold the rotor at the center of the stator and b) to provide a contact surface between the periphery of rotor and the indented surface of the top endcap. The last step before

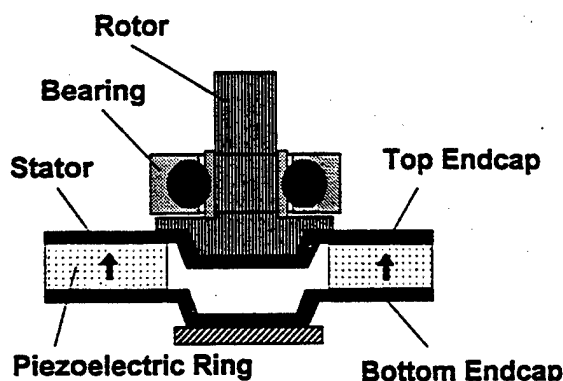


Fig. 1. Structure of the ultrasonic motor (arrows indicate the poling direction of piezoelectric ring). Metal endcaps were bonded to piezoelectric ring using adhesive epoxy.

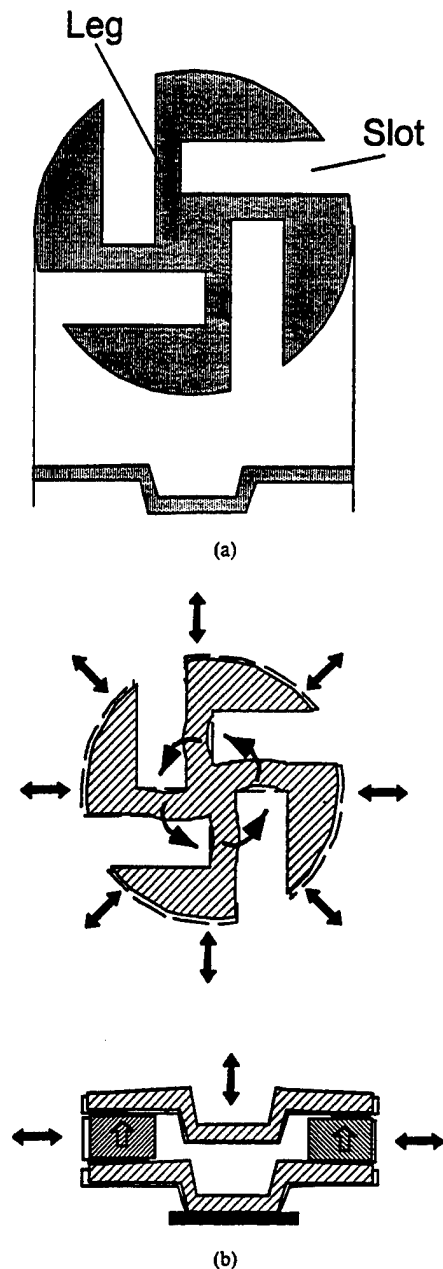


Fig. 2. (a) Top and cross-sectional views of the metal endcap. (b) Top and cross-sectional view of the stator displacement. Windmill-like slits were cut by EDM.

mounting the motor was to join the stator to a metal base or to the bottom of the housing unit that had acoustic impedance different from the endcap material. Table I summarizes the size of the stator.

The vibration transformation from the radial direction to the longitudinal direction was verified by measuring the displacement of the stator element at the center of the top endcap by using a Fotonic Sensor (MTI 2000). The displacement at 110 kHz which is close to the first radial mode resonance frequency of the particular stator element was about $2\text{ }\mu\text{m}$ peak-to-peak. Before mounting the rotor on the top of the stator, the admittance magnitude of the stator was measured with an HP4194A Impedance/Gain-Phase analyzer and the result is shown in Fig. 3. This measurement gives an idea about the

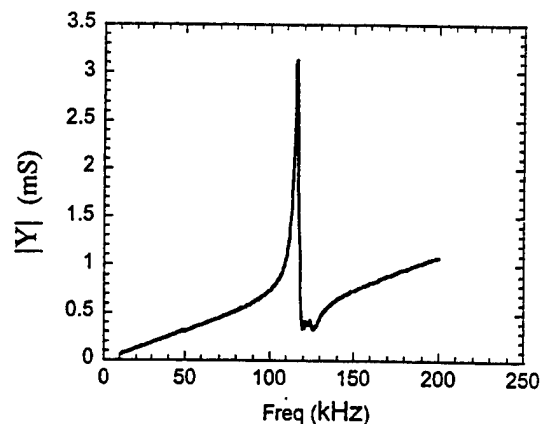


Fig. 3. The admittance spectrum of the free stator.

Table I. Dimensions of the stator.

Outer diameter of the piezoelectric ring	=11.0 mm
Inner diameter of the piezoelectric ring	=6.0 mm
Thickness of the piezoelectric ring	=0.5 mm
Thickness of the metal endcap	=0.2 mm
Weight of the stator	=0.8 g

stator bonding layer quality and the driving frequency of the motor. Insufficient bonding decreased the mechanical quality factor significantly. When a rotor was mounted on the top endcap, the tangential and longitudinal motion made the rotor rotate due to the frictional interaction between the top endcap and the rotor surface whose periphery fitted to the center part of the metal endcap.

3. Transient Response Characteristics of the Motor

The experimental system to obtain the motor characteristics by measuring the transient response is shown in Fig. 4. In this system, the position of the rotor, which was matched closely to the bore diameter of the ball bearings, was fixed through a bar. The outer diameter of the ball bearings were also matched closely to the hole at the center of the bar. Therefore, mounting a load (metal disk) does not apply an extra pressure to the stator. The stator position was adjusted with XYZ stage. Since the space was limited we could not measure the pressure on the stator surface.

The metal disk (50 g) with a high moment of inertia ($1.33 \times 10^{-5} \text{ kg m}^2$) compared to the rotor was mounted as a load (see Table II). Thus the motor was driven under various applied voltages at 110.80 kHz. A stator with an outer diameter of 11.0 mm (Table I) was used. The position of the rotor was recorded using a digital oscilloscope. In order to record the position of the rotor, a thin aluminum foil was attached to the rotor and its position was detected through an electronic circuitry that utilized a photocell pair. The position data were recorded as a function of time till the motor reach the steady state speed after starting from zero speed. The derivative of the recorded position data with respect to time gives the motor transient speed. Second derivative of the recorded data gives the angular acceleration (α). Finally, the product of the angular acceleration and the moment of inertia of the rotating disk (I) give the motor transient torque (Γ).

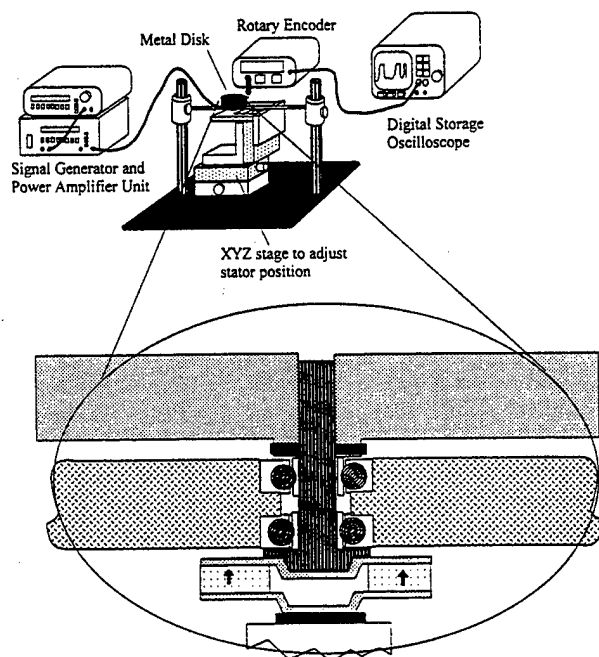


Fig. 4. Experimental setup for the transient response measurement. The rotor is fixed into the bore of ball bearings. The outer diameter of the bearing is also fixed into the hole on bar. The stator was mounted on a XYZ stage to adjust the position of the stator was adjusted by using the micrometer on the stage.

Table II. Load conditions.

Weight of the rotating load (disk)	=50 g
Diameter of the rotating load	=46.0 mm
Thickness of the rotating load	=6.75 mm
Inertia of the rotating load	= 1.33×10^{-5} kgm ²

The transient output speed and torque as a function of time were measured at input 46 Vrms and plotted in Fig. 5. The steady state speed reached 870 rpm in 2 s at this voltage, while the maximum torque read around 1.36 mNm at a speed of 480 rpm. Similar curves were further obtained for different input voltages.

Instantaneous output mechanical power (P_o) was also calculated by multiplying torque (Γ) with angular speed (ω). Input electrical power (P_i) was calculated from measured input voltage, current and phase angle between them. From input and output powers the efficiency was calculated by dividing output mechanical power to input electrical power. The efficiency curve calculated from measured speed, torque and input electrical power is also shown in Fig. 6. The maximum efficiency of 21% was obtained at 42 V and it starts to decrease when the input voltage was further increased beyond 43 V. Plots of the maximum values of torque and efficiency attained for applied rms voltages from 0 V to 46 V are shown in Fig. 6. It is concluded that in a range of applied voltage from 25 to 46 V, the maximum motor torque increases in proportion to the input voltage.

Steady state speed with applied voltage from 0 to 46 V was measured under loaded and unloaded conditions (Fig. 7). Under the unloaded condition (when the rotating disk was not mounted to rotor), the motor started to rotate at 3 V. The start-

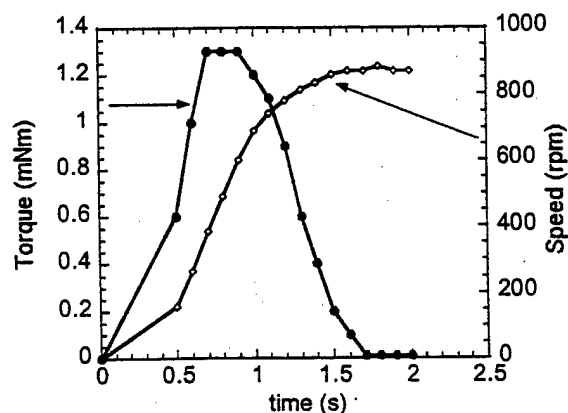


Fig. 5. The transient responses of motor torque and speed as a function of time at an input voltage of 46 Vrms. The speed was obtained from measured position data.

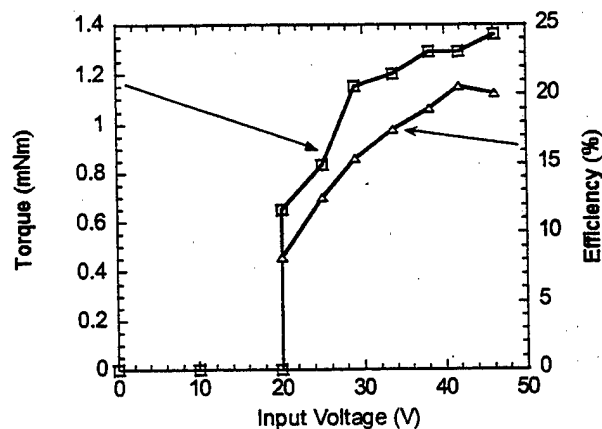


Fig. 6. Maximum torque and efficiency vs. input voltage.

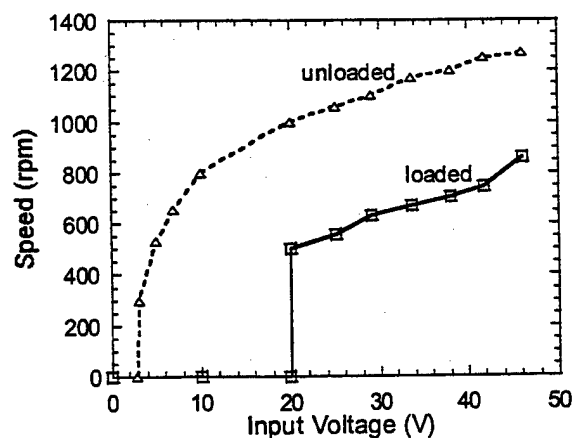


Fig. 7. Steady state speed vs. input voltage under loaded and unloaded condition.

ing voltage for the loaded condition was 20 V. The loaded and unloaded speeds were increased same amount between 20 to 46 V.

The motor load characteristics; speed and efficiency-torque curves at 42 and 46 V are shown in Fig. 8. These data were

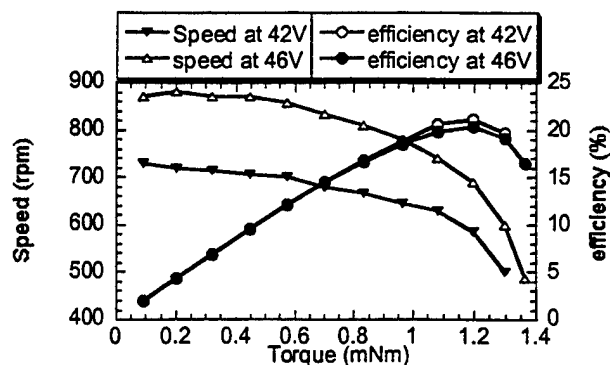


Fig. 8. Loaded characteristics of the motor. Speed-torque and efficiency-torque curves at 42 and 46 V.

obtained from transient torque and speed measurements. The output torque tends to saturate beyond 1.2 mNm and the motor speed decreases sharply. However, the efficiency of the motor at 42 and 46 V increase steadily until 1.2 mNm torque value. When the output torque starts to saturate the efficiency of the motor starts to decrease. The output torque of this motor depends on the force that the four legs on the endcap can produce. Once the force generated by the endcap legs reach the maximum value, the legs will no longer push the rotor tangentially but they will buckle. The output maximum torque may be tailored by changing the metal endcap thickness.

4. Conclusion

A new type of ultrasonic motor "windmill" design was proposed. The preliminary characteristics of the prototype motor are:

- i. A maximum torque of about 1.36 mNm was obtained at 46 Vrms. This torque was obtained before the motor speed reached the steady state.
- ii. Maximum efficiency of 21% was obtained at 42 V.
- iii. The motor torque steadily increases with applied input voltage, in the range of 25 and 46 V.

The proposed motor has the following advantages over commercial motors:

1. The size of the motor can be reduced easily without changing the design procedure.
2. The unique multifunctional metal-ceramic composite stator element of the motor can generate longitudinal and torsional vibration at the same time.
3. Since the metal endcaps also act as a spring element, no extra spring is necessary during stacking the stator with rotor which reduces the number of the components used in the motor.
4. The piezoelectric ring element is electroded uniformly and there is only one poling direction on the ring element, which makes the poling process easier.
5. The motor is basically consists of only 4 components, stator, rotor, ball bearing and housing unit and it is driven with one ac power supply.

By exciting two natural modes,⁷⁾ such as radial and flexensional modes of the stator element, an elliptical motion would be generated at the center part of the top endcap. This would make the clockwise and counterclockwise rotation possible with one ac source.

Acknowledgement

This work was partly supported by the Office of Naval Research through Contract No. N00014-96-1-1173.

The authors also gratefully acknowledge the support of the Turkish Higher Educational Council and Singapore, Institute of Materials Research and Engineering.

- 1) M. Kasuga, T. Satoh, N. Tsukada, T. Yamazaki, F. Ogawa, M. Suzuki, I. Horikoshi and T. Itoh: *J. Soc. Precis. Eng.* **57** (1991) 63.
- 2) D. Stutts and J. Cummings: *Smart Actuator Symp.* 1994.
- 3) S. Kumada: *Proc. 6th Int. Meet. Ferroelectricity*, Jpn. J. Appl. Phys. **24** (1985) Suppl. 24-2, p. 719.
- 4) A. Dogan, K. Uchino and R. E. Newnham: *IEEE Ultrason. Ferroelectr. Freq. Control* **44** (1997) 597.
- 5) B. Koc, A. Dogan, J. F. Fernandez, R. E. Newnham and K. Uchino: *Jpn. J. Appl. Phys.* **35** (1996) 4547.
- 6) Q. C. Xu, S. Yoshikawa, J. R. Belsick and R. E. Newnham: *IEEE Ultrason. Ferroelectr. Freq. Control* **38** (1991) 634.
- 7) M. Fleisher, D. Stain and H. Meixner: *IEEE Ultrason. Ferroelectr. Freq. Control* **36** (1989) 614.

ACTUATOR STUDIES

Photostrictive Actuators

APPENDIX 53

Photostrictive Effect in Lanthanum-Modified Lead Zirconate Titanate Ceramics Near The Morphotropic Phase Boundary

Patcharin Poosanaas and Kenji Uchino

International Center for Actuators and Transducers, Materials Research Laboratory,
The Pennsylvania State University, University Park, PA 16802

Abstract

Photostrictive effect in lanthanum-modified lead zirconate titanate (PLZT) ceramics, one of the promising candidates for photostrictive materials, has been investigated with different content of La and the ratio of Zr/Ti, near the morphotropic phase boundary compositions. The maximum photocurrent and photovoltage were obtained at different compositions of PLZT ceramics: maximum photocurrent at 4/48/52, maximum photovoltage at 5/54/46. New figures of merit for evaluating these materials, which includes both the magnitude of strain and response speed were proposed.

Keywords: Photovoltaic effect; Photostriction; PLZT ceramics; Compositional variation; Morphotropic phase boundary; Photostrictive actuators

1. Introduction

Lanthanum-modified lead zirconate titanate (PLZT) ceramics are known to exhibit a range of interesting electro-optical properties [1, 2]. Recently, the application of PLZT in photostrictive actuators has drawn considerable attention [3-7]. The idea of photo-driven

actuator arises from the photostrictive effect, which is the combination of the photovoltaic and converse-piezoelectric effects in ferroelectric materials. Such a direct conversion of photonic to mechanical energy by the photostrictive effect can lead to a broad range of applications. One of the promising applications is the tailored films of photostrictive PLZT on a flexible substrate for bio-morphic explorers in future space missions [8]. Moreover, they can be used for photostrictive motors, transducers, advanced mobiles, shape controllers, and microvalves [8, 9].

The photostrictive materials were evaluated on the basis of the product of photovoltage (E_{ph}) and the piezoelectric coefficient (d_{33}). Figure 1 shows the room temperature phase diagram of the PLZT system by Haertling and Land [1]. The largest product of E_{ph} and d_{33} has been reported for the PLZT 3/52/48, which is around the morphotropic phase boundary (MPB) separating the rhombohedral and tetragonal ferroelectric phases in Fig. 1 [5, 7]. However, a rigorous comprehensive investigation on the compositional dependence, varying both La concentration and Zr/Ti ratio especially close to the MPB, has not yet been carried out. Since the material characteristics, i.e. dielectric, piezoelectric, and photovoltaic properties of PLZT are sensitive to compositional variation, investigation of compositional dependence near MPB is very important for the material optimization.

In pursuit of an enhanced photostrictive material, this paper examines the optimum composition range for obtaining the maximum photovoltaic effect in the PLZT ceramics.

2. Experimental procedure

PLZT compositions are given in the form of $\text{Pb}_{1-x}\text{La}_x(\text{Zr}_y\text{Ti}_{1-y})_{1-x/4}\text{O}_3$ (abbreviated as PLZT $X/Y/Z$, $X=100x$; $Y=100y$; and $Z=100(1-y)$). PLZT ceramics with concentration of La varying from 2-5 at% , Zr/Ti ratio varying from 48/52 to 54/46 were prepared by the conventional oxide mixing process (see Fig. 1). These series of compositions are located in the area of morphotropic phase boundary, including the particular composition 3/52/48 which was reported to exhibit the maximum photovoltaic effect. Figure 2 illustrates a flow chart for the sample preparation by the conventional oxide mixing process. The details of this technique was reported in an earlier publication [10].

Phase identification was performed using X-ray diffraction (Scintag diffractometer, Vax 3100 System). All samples exhibited perovskite structures. Microstructure and grain size of the samples were observed by scanning electron microscopy (ISI-DS 130). Dielectric properties of PLZT samples were measured with an impedance analyzer (HP-4284A). Samples for dielectric measurements were polished to about 10 mm in diameter and 1 mm in thickness, then electroded with platinum (Pt) by sputtering. Piezoelectric properties of all the samples were measured by using a Berlincourt d33 meter (Channel Products, Inc.) at 100 Hz. Samples for piezoelectric measurement were of the same configuration as for dielectric measurements, except that they were poled in silicone oil at 120 °C under a 2 kV/mm electric field for 10 min.

The samples of $5 \times 5 \times 1 \text{ mm}^3$ were cut and polished for photovoltaic measurements. The $5 \times 1 \text{ mm}^2$ surfaces were Pt electroded. Photovoltaic measurements were done by using a high-input-impedance electrometer (Keithley 617). The photovoltage and photocurrent were

determined from the current-voltage relation by applying voltage in the range of -100 and +100 V along with the radiating light to the samples. The photovoltage was determined in an open circuit state from the intercept of the horizontal applied voltage axis, while the photocurrent was obtained from the short circuit state from the intercept of the vertical current axis. A high pressure mercury lamp (Ushio Electric USH-500D) was used as a light source. The white radiation was passed through an Infrared (IR) blocking filter and an Ultraviolet (UV) bandpass filter to obtain a monochromatic beam with a maximum strength around 366 nm wavelength and an intensity of 3.25 mW/cm^2 , before illuminating the samples ($5 \times 5 \text{ mm}^2$ polished surface). The light beam with this wavelength has been reported to yield the maximum photovoltaic properties for PLZT [7]. The details of this experimental set-up was reported in an earlier paper [10].

3. Results

Grain size

Since the photovoltaic and piezoelectric effects are strongly dependent on the grain size [5], the grain size data are shown firstly. Average grain sizes of the PLZT ceramics were obtained from the polished sample surface by SEM observations using the intercept method. Grain sizes of the samples ranged from 1 to $5 \mu\text{m}$. Figure 3 shows the average grain size as a function of Zr/Ti ratio and La content. The average grain size were observed to decrease with La addition. As Zr/Ti ratio increased, the average grain size increased and approaches to the MPB region. This agrees with the previous report [11, 12].

Dielectric and Piezoelectric properties

Figure 4 and 5 show the dielectric constant (ϵ) and piezoelectric constant (d_{33}) contour maps at room temperature for the PLZT system. The dielectric constant showed the maximum at the MPB for all the La content and decreased with increasing Ti content (decrease in Zr/Ti ratio). The d_{33} increased with increasing Zr/Ti ratio and the maximum d_{33} has been found at the MPB.

Photovoltaic properties

The maximum photovoltaic properties has been reported earlier at PLZT 3/52/48 for a coarse composition change. The compositional variation especially around the MPB plays an important role. The contour map of the photocurrent at room temperature in the PLZT phase diagram is shown in Fig. 6, while Fig. 7 illustrates the photovoltage contour map. In these two figures, the solid circles indicate the location of PLZT 3/52/48 which has been reported earlier to exhibit the maximum photocurrent and photovoltage. In this new fine measurement, the maximum photocurrent and photovoltage have been found at different compositions of PLZT ceramics. The maximum photocurrent was found at PLZT 4/48/52 which corresponds to the tetragonal phase, while the maximum photovoltage was found at PLZT 5/54/46 which is along the MPB. The photocurrent and photovoltage were found to get enhanced by more than twice for these new compositions.

It is noteworthy that the maximum photocurrent and photovoltage are obtained at different compositions. In order to explain this, the current source model, which has been

proposed by one of the authors is used here [13]. The electron energy band of PLZT is basically generated by the hybridized orbit of p-orbital of oxygen and d-orbital of Ti/Zr. The donor impurity levels induced in accordance with La doping (or other dopants) are present slightly above the valence band. Transition from these levels with an asymmetric potential due to the crystallographic anisotropy may provide the preferred momentum to electron. Electromotive force is generated when electrons are excited by illumination and move in a certain direction of the ferroelectric materials, which may arise along the spontaneous polarization direction, resulting in photocurrent. PLZT 4/48/52 exhibits the maximum photocurrent, suggesting the product of the number of impurity level and the asymmetry of materials is maximized. As La content and Zr/Ti ratio increase, the system transforms to more symmetry form of cubic system resulting in decreasing of photocurrent even though addition of La content will increase the impurity level. Photocurrent at rhombohedral phases are lower than tetragonal phases can also be attributed to this reason as well.

Considering the contour map of photoconductance in the PLZT phase diagram in Fig. 8, which shows the minimum along the MPB especially for PLZT 5/54/46, photovoltage at this composition is observed as the maximum. The minimum of conductivity near the MPB of Lead Zirconate Titanate (PZT) ceramics was also reported in the previous study [14].

4. Discussion

Since the maxima in photocurrent which governs the response speed and in photovoltage which governs the magnitude of strain are located at different compositions of PLZT ceramics, new figures of merit for photostriction should be proposed by considering

both the terms for response speed and magnitude of strain. The new figures of merit for photostriction were derived as follows:

Since the strain is induced as a function of time, t , as

$$x_{ph} = d_{33}E_{ph}(1 - \exp(\frac{-t}{RC})), \quad (1)$$

where x_{ph} is the photo-induced strain, d_{33} , the piezoelectric constant of the materials, E_{ph} , photovoltage, I_{ph} , photocurrent, t , time, R and C are resistance and capacitance of the material, respectively.

For $t \ll 1$, we obtain

$$x_{ph} = d_{33}E_{ph}(\frac{t}{RC}). \quad (2)$$

Thus, the figure of merit for response speed should be provided by $d_{33}E_{ph}(\frac{1}{RC})$.

Taking account of the relation $I_{ph} = \frac{E_{ph}}{R}$, this figure of merit is transformed to $\frac{d_{33}I_{ph}}{C}$.

Or, it can be given by $\frac{d_{33}I_{ph}}{\epsilon}$ (ϵ : permittivity). On the other hand, for $t \gg 1$, the

saturated strain is provided by:

For $t \gg 1$, we obtain

$$x_{ph} = d_{33}E_{ph}. \quad (3)$$

which is similar to the previous paper [6]. Thus, the figure of merit for the magnitude of strain is defined by $d_{33}E_{ph}$.

In order to obtain a high photo-induced strain, materials with high d_{33} and E_{ph} are needed. On the contrary, for high response speed, materials with high d_{33} , I_{ph} and low dielectric constant are required. Figure 9 and 10 show the contour maps of $\frac{d_{33}I_{ph}}{C}$ (sec^{-1}) and $d_{33}E_{ph}$ (unitless) on the PLZT composition diagram, respectively.

4. Conclusion

A rigorous investigation of the composition dependence, especially near the morphotropic boundary, on photovoltaic properties in PLZT ceramics was carried out in order to examine compositions for the maximum photovoltaic properties. It has been found that the maximum photocurrent and photovoltage exist at different compositions of PLZT ceramics. Maximum photocurrent was found at PLZT 4/48/52 which is in tetragonal phase while maximum photovoltage was found at PLZT 5/54/46 which is around the MPB of the PLZT phase diagram. The photocurrent and photovoltage were improved more than twice higher for the new compositions of PLZT. The new figures of merit for photostriction for the magnitude of strain or the response speed term have been proposed. The high performance photostrictive materials can be tailored using these new compositions.

Acknowledgments

One of the authors (P. Poosanaas) would like to acknowledge the Royal Thai Government and Dr. Harit Sutabutr from the National Metal and Materials Technology Center (Thailand) for granting MOSTE fellowship.

References

- [1] G. Haertling and C. Land, *J. Am. Ceram. Soc.*, 54 (1971) 1.
- [2] Y. Xu, *Ferroelectric Materials and Their Application*, Elsevier Science Pub. Co., New York, 1991.
- [3] S. Y. Chu and K. Uchino, *Ferroelectrics*, 174 (1995) 185.
- [4] S. Y. Chu, Z. Ye, and K. Uchino, *Smart Mater. Struct. Mater.*, 3 (1994) 114.
- [5] T. Sada, M. Inoue, and K. Uchino, *J. Ceram. Soc. Jpn. Inter. Ed.*, 95, 499 (1987).
- [6] K. Uchino, M. Aizawa, and Late S. Nomura, *Ferroelectrics*, 64, 199 (1985).
- [7] K. Uchino and M. Aizawa, *Jpn. J. Appl. Phys. Suppl.*, 24 (1985) 139.
- [8] S. Thakoor, J. M. Morookian, and J. A. Cutts, *Proceedings of the Tenth IEEE International Symposium on Applications of Ferroelectrics Transactions*, 1 (1996) 205.
- [9] M. Sayer, M. Lukacs, and T. Olding, *Integrated Ferroelectrics*, 17 (1997) 1.
- [10] P. Poosanaas, A. Dogan, A. V. Prasadaraao, S. Komarneni, and K. Uchino, *J. Electroceramics*, 1 (1997) 111.
- [11] G. Haertling, *Proceedings of the Ninth IEEE International Symposium on Applications of Ferroelectrics Transactions*, (1994) 313.
- [12] M. A. Akbas, I. M. Reaney and W. E. Lee, *J. Mater. Res.*, 11 (1996) 2293.
- [13] K. Uchino, *Innovations Mater. Res.*, 1 (1996) 11.
- [14] K. Uchino, M. Yoshizaki, and A. Nagao, *Ferroelectrics*, 95 (1989) 161.

Figure captions

Fig. 1. Room temperature phase diagram of PLZT system showing the morphotropic phase boundary separating the rhombohedral and tetragonal ferroelectric phases [1] and the compositions that have been investigated in this study.

Fig. 2. Flow diagram of sample preparation by the conventional oxide mixing process.

Fig. 3. The contour map of the average grain size in PLZT ceramics. Larger grain sizes were found along the MPB of PLZT system.

Fig. 4. Variation of room temperature dielectric constant as a function of compositional variation along the MPB of PLZT system. Dielectric constants show the maxima along the MPB.

Fig. 5. Variation of piezoelectric constant (d_{33}) in the PLZT system. The maxima of d_{33} have been found along the MPB.

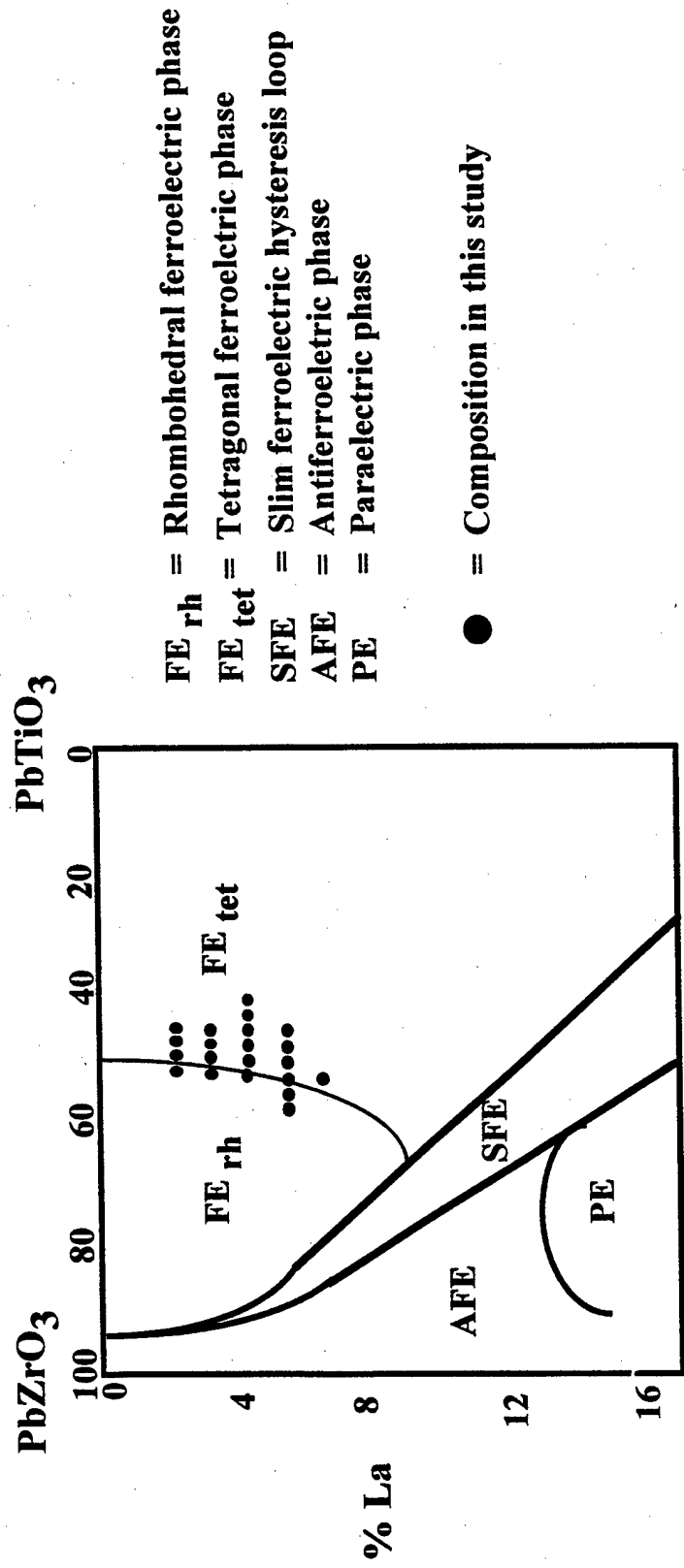
Fig. 6. The contour map of photocurrent in PLZT ceramics. The maximum photocurrent was found at PLZT 4/48/52 having tetragonal phase. • represented the maximum photocurrent composition reported earlier.

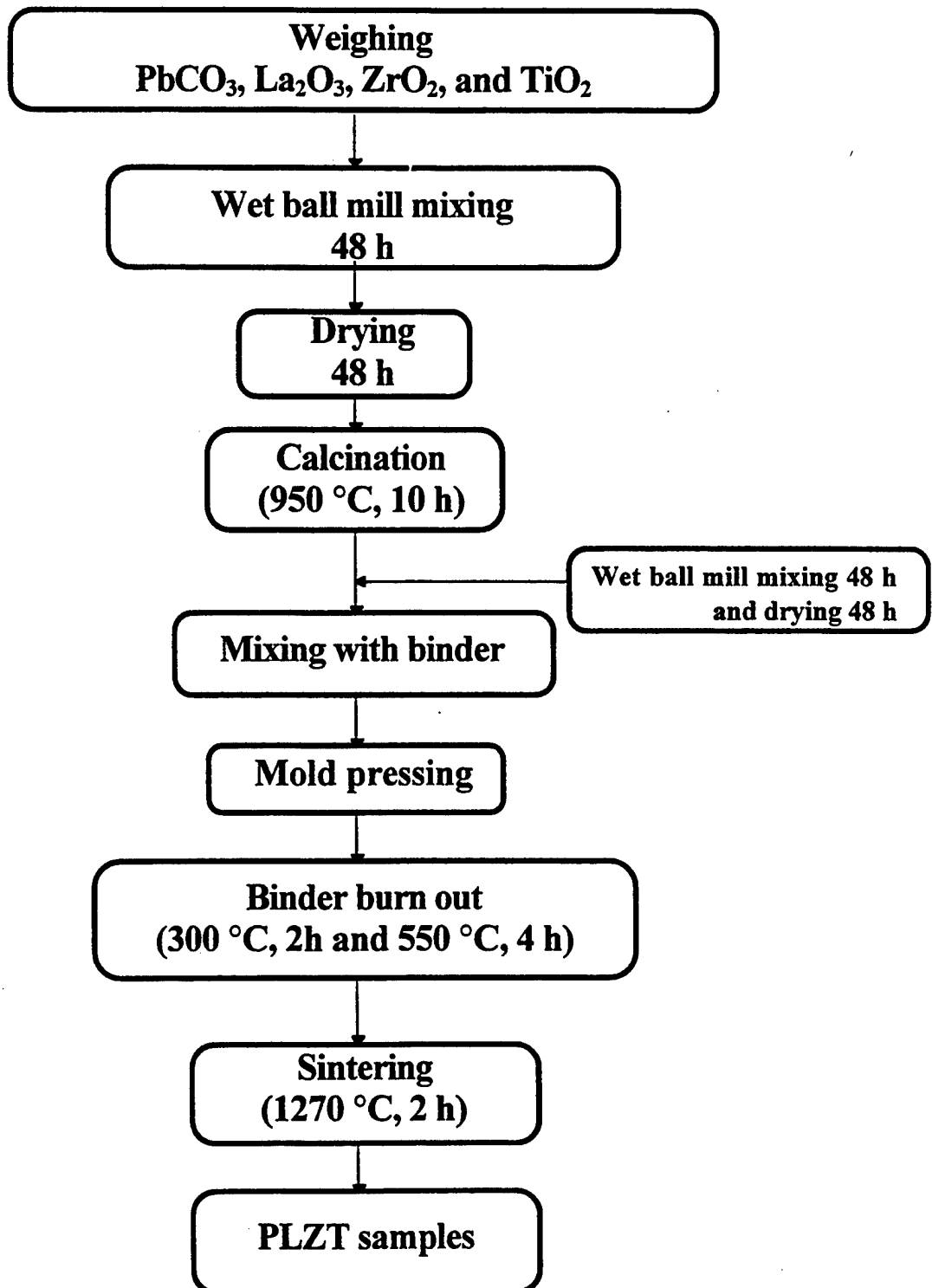
Fig. 7. The contour map of photovoltage in PLZT ceramics. Photovoltage was found to be maximum at PLZT 5/54/46 and along the MPB of PLZT system. • represented the composition with maximum photovoltage reported earlier.

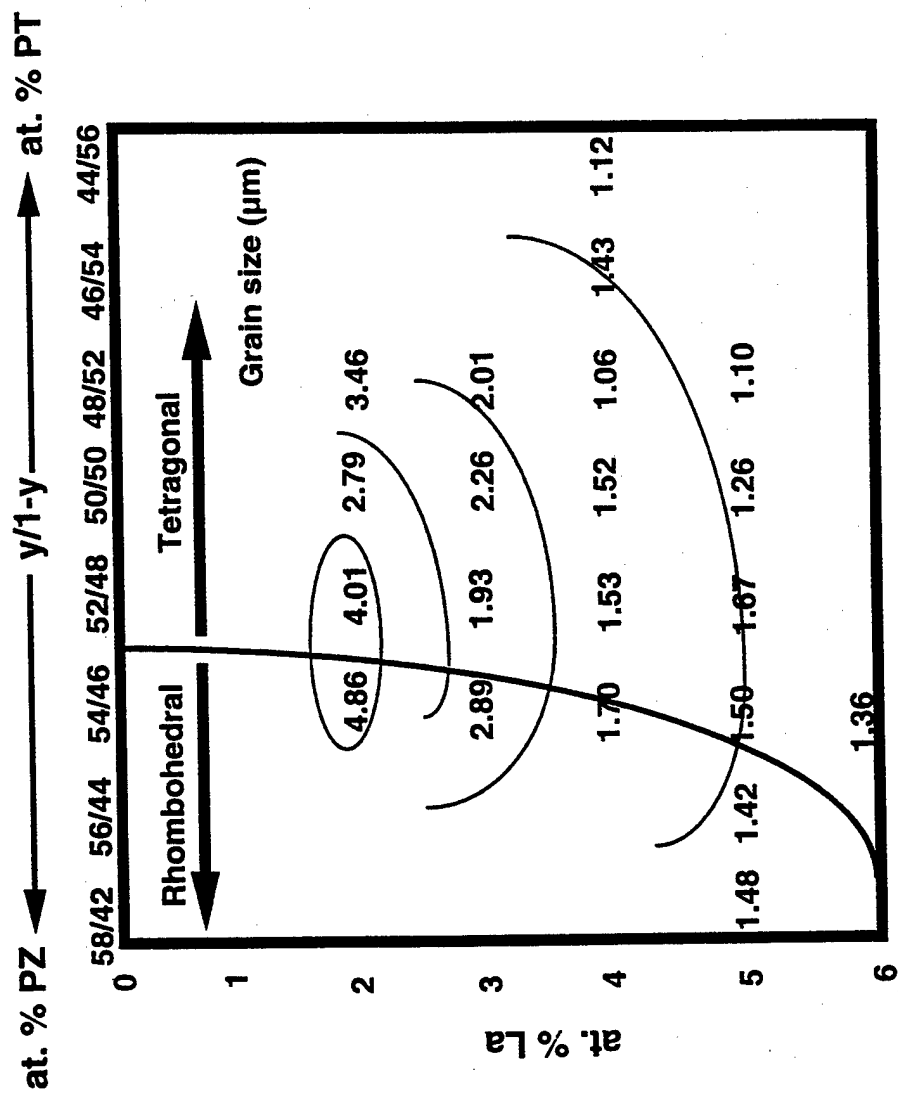
Fig. 8. The contour map of photoconductance in PLZT system. Photoconductance is minimum along the MPB. The minimum photoconductance was found at PLZT 5/54/46 where it also exhibits the maximum photovoltage.

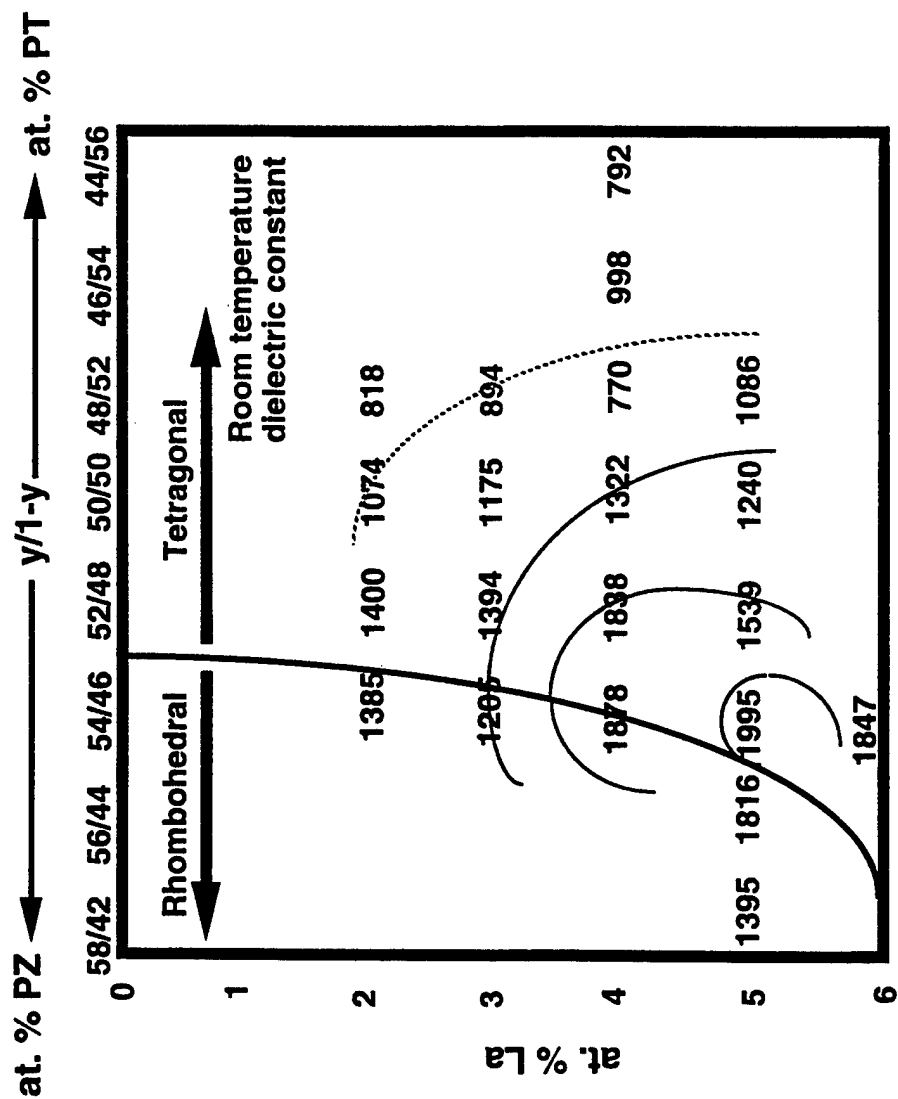
Fig. 9. The contour map of $\frac{d_{33}I_{ph}}{C}$, figure of merit for response speed. PLZT 4/48/52 is best suited for high response speed material in PLZT system.

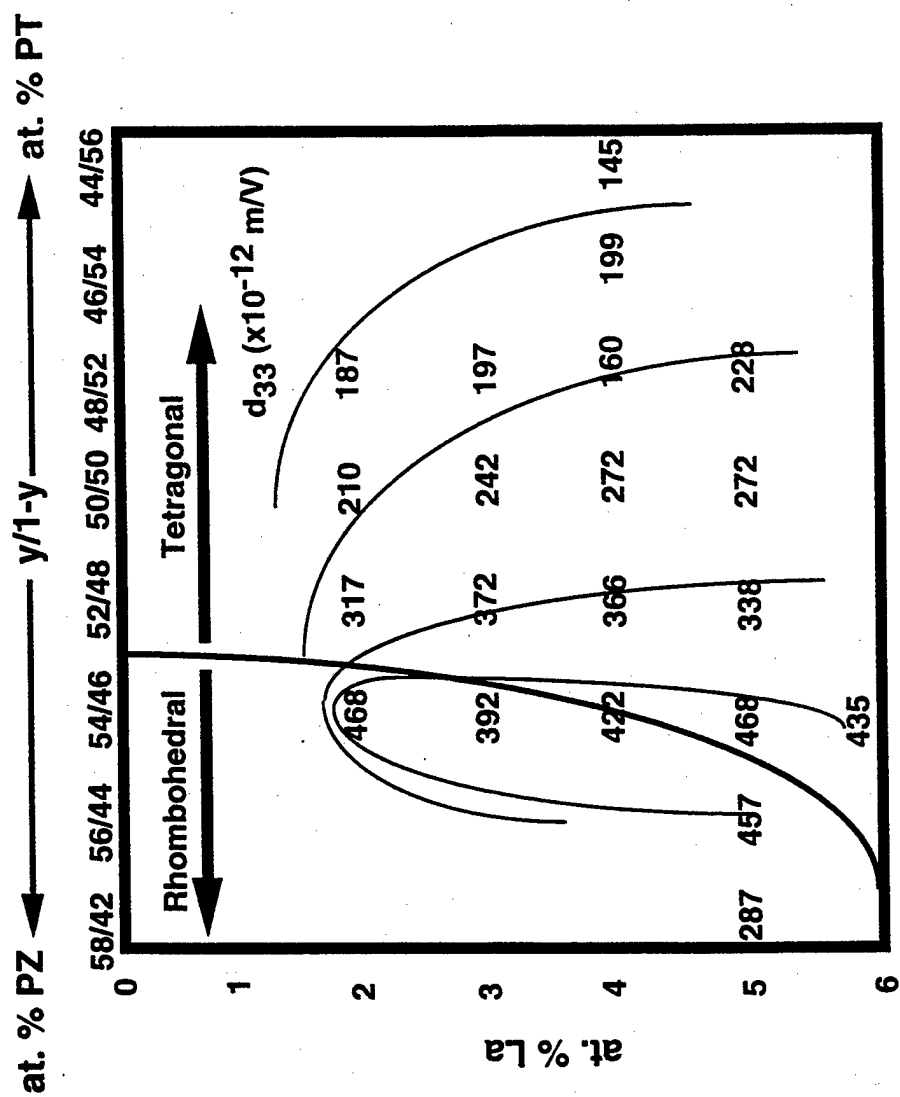
Fig. 10. The contour map of $d_{33}E_{ph}$, figure of merit for magnitude of strain. PLZT 5/54/46 is best suited for the maximum strain in PLZT system.

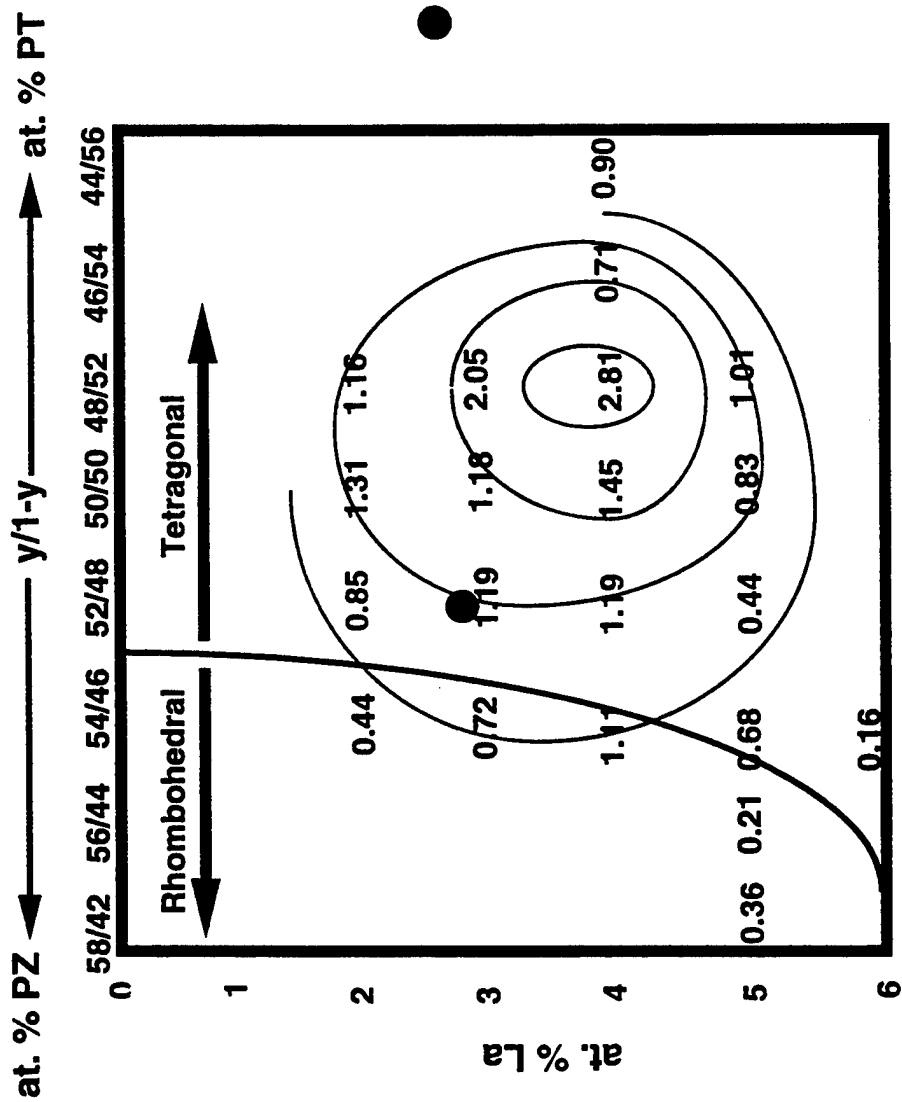






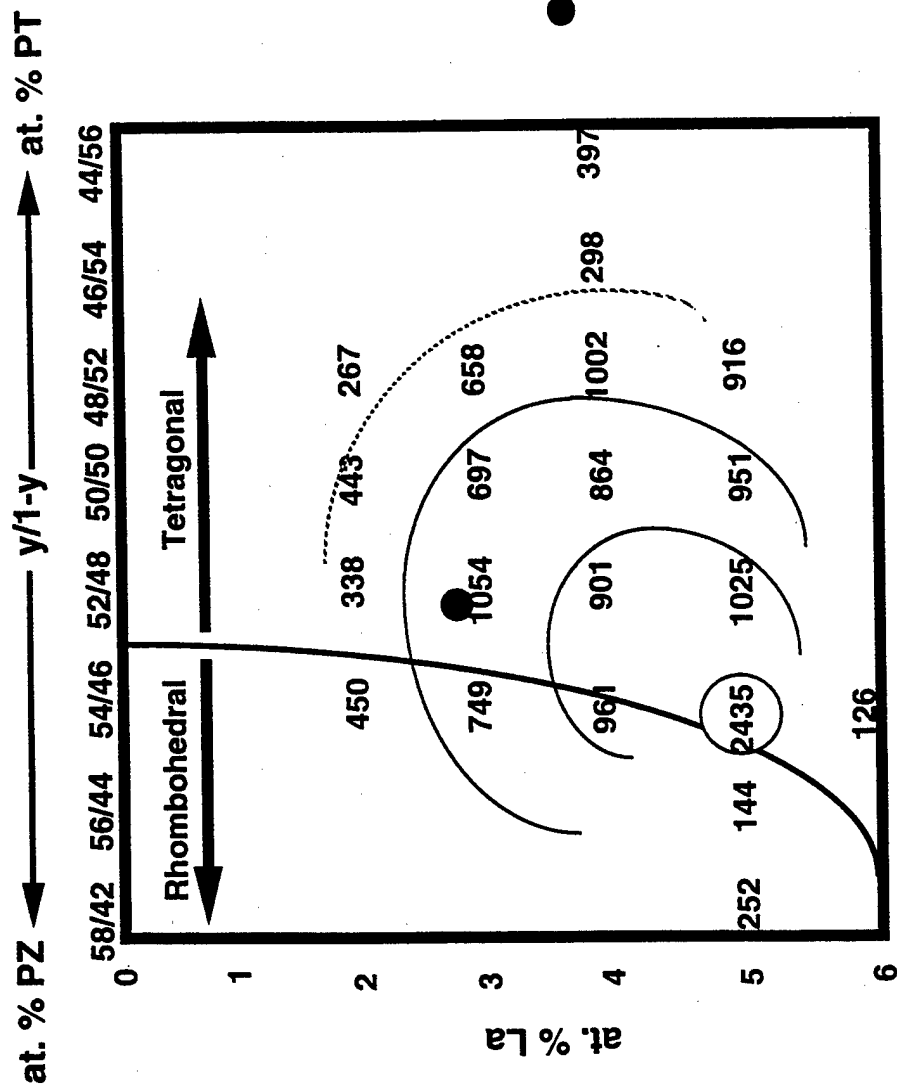






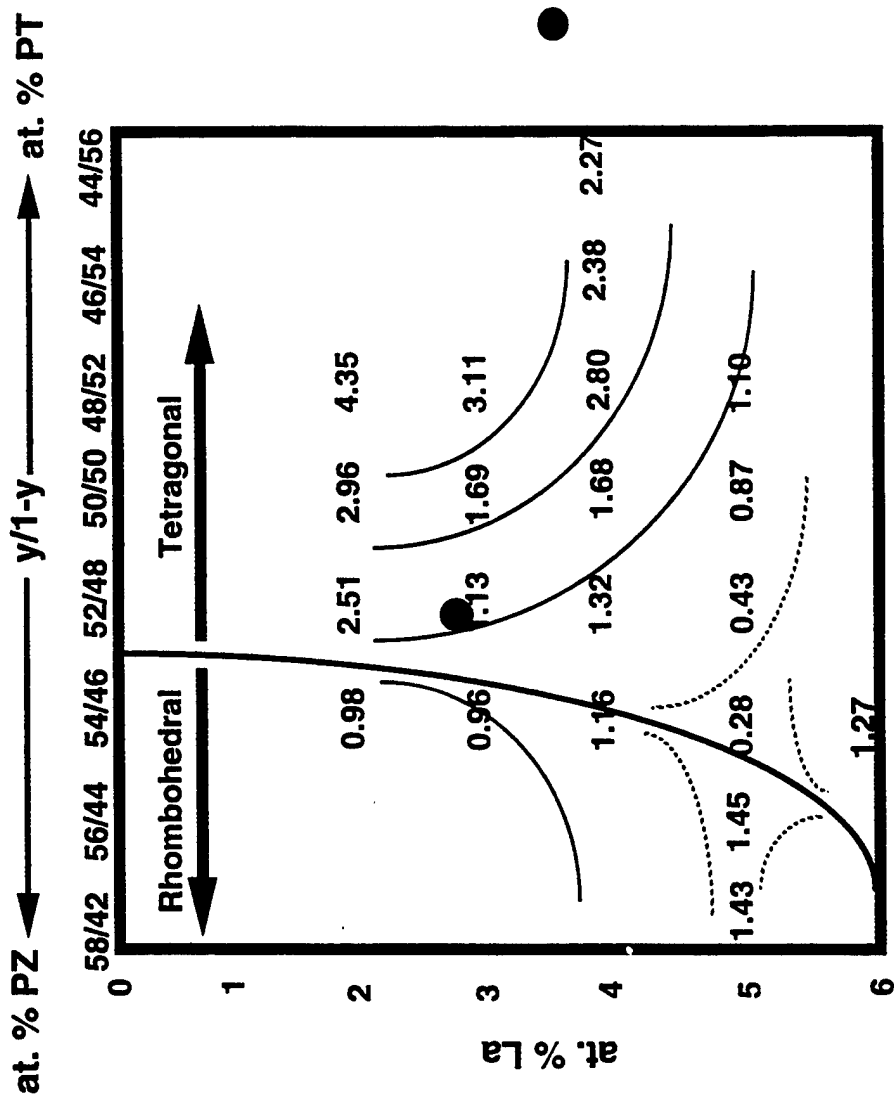
I_{ph} = photocurrent (nA/cm)

- Composition with maximum photocurrent/photovoltage in the previous study



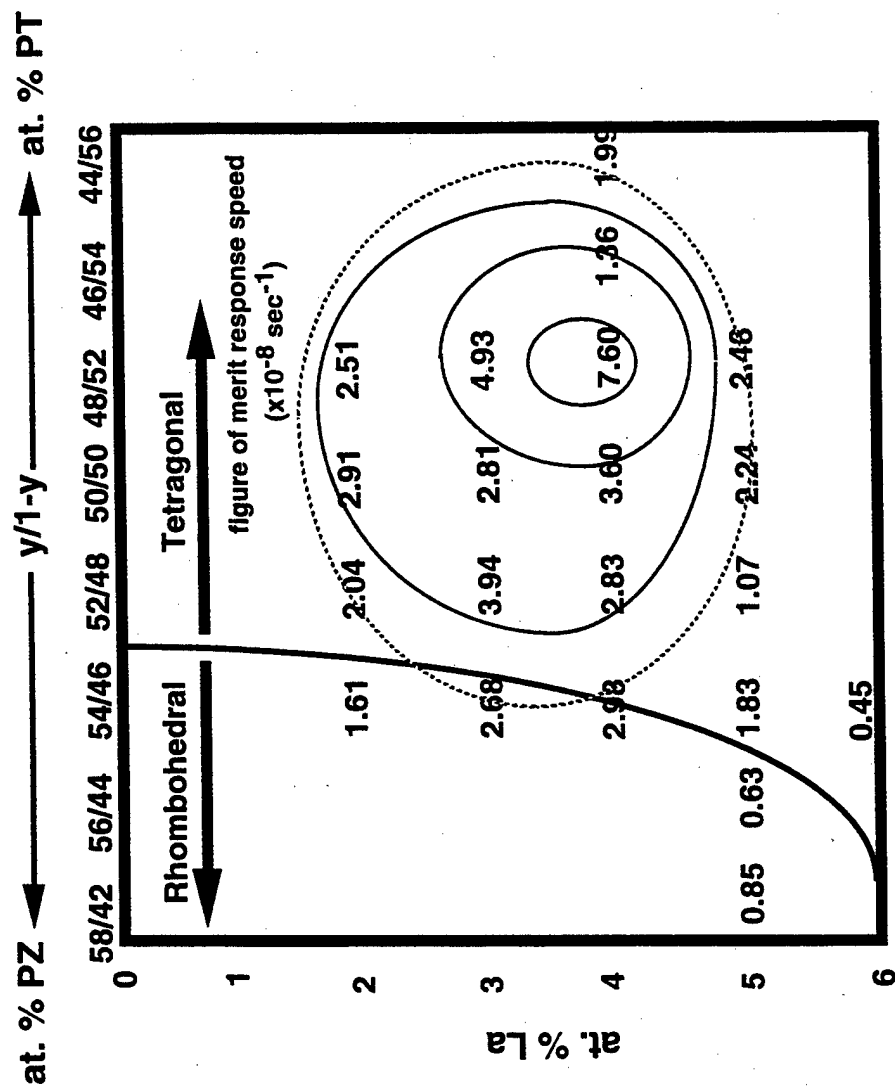
E_{ph} = photovoltage (V/cm)

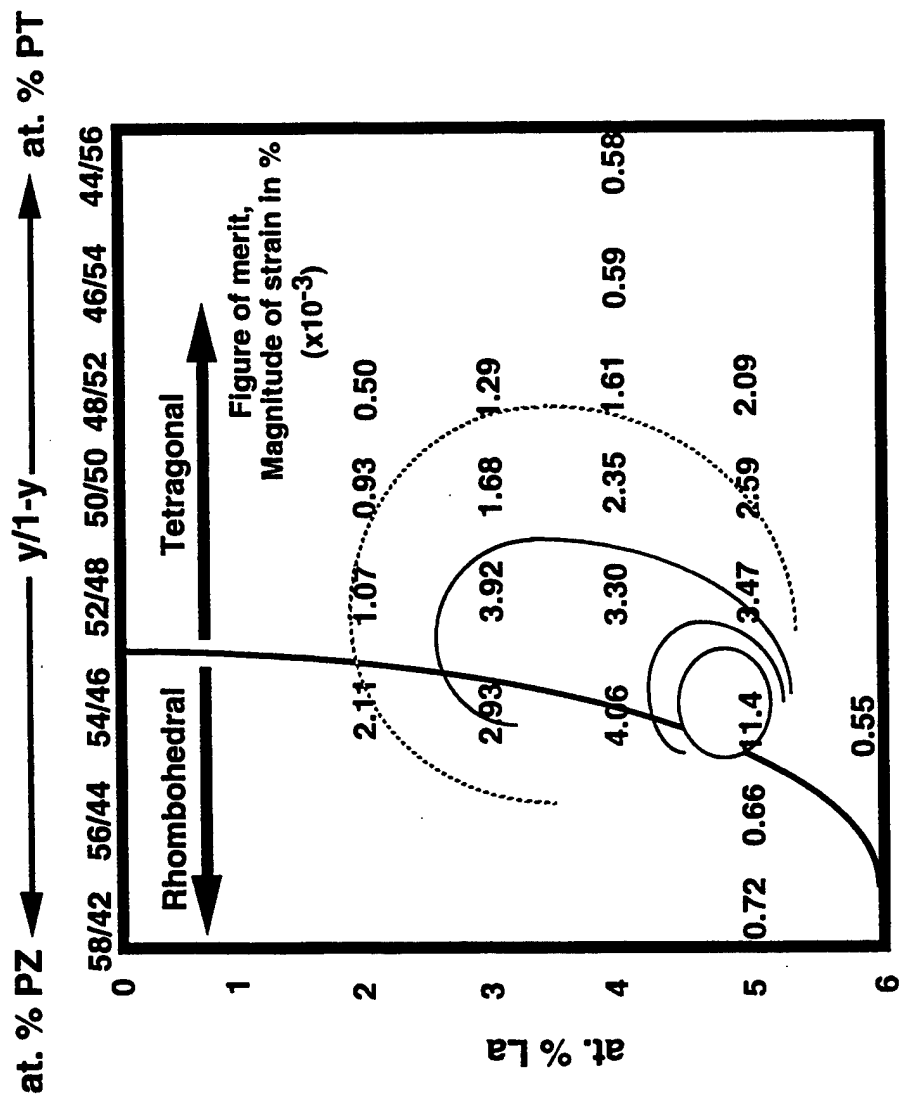
- Composition with maximum photocurrent/photovoltage in the previous study



G_{ph} = photoconductance
($\times 10^{-12}$ A/V)

- Composition with maximum photocurrent/photovoltage in the previous study





APPENDIX 54

PHOTOSTRICTION IN PLZT AND ITS APPLICATIONS

Kenji UCHINO and Patcharin POOSANAAS

International Center for Actuators and Transducers, Materials Research Laboratory
The Pennsylvania State University, University Park, PA 16802, USA

Keywords: photostriction, PLZT, actuator, piezoelectricity, photovoltaic effect

Photostriction in ferroelectrics arises from a superposition of photovoltaic and inverse piezoelectric effects. $(\text{Pb},\text{La})(\text{Zr},\text{Ti})\text{O}_3$ ceramics doped with WO_3 exhibit large photostriction under irradiation of near-ultraviolet light, and are applicable to remote control actuators and photoacoustic devices. Using a bimorph configuration, a photo-driven relay and a micro walking device have been developed, which are designed to start moving as a result from the irradiation, having neither electric lead wires nor electric circuits.

1. INTRODUCTION

Photostrictive effect is a phenomenon in which strain is induced in the sample when it is illuminated. In principle, the photostrictive effect arises from a superposition of a photovoltaic effect, where a large voltage is generated in a ferroelectric through the irradiation of light [1], and a piezoelectric effect, where the material expands or contracts under the voltage applied. It is noteworthy that this photostriction is neither the thermal dilatation nor the pyroelectrically-produced strain associated with a temperature rise due to the light illumination. Also the photovoltaic effect mentioned here generates a greater-than-band-gap voltage (several kV/cm), and is quite different from that based on the p-n junction of semiconductors (i. e. solar battery).

This paper describes the fundamental photostrictive effect in $(\text{Pb},\text{La})(\text{Zr},\text{Ti})\text{O}_3$ ceramics and sample geometry dependence of this effect first, then introduces its applications to a photo-driven relay, a micro walking machine and a photophone, which are designed to function as a result of irradiation, having neither lead wires nor electric circuits.

2. PHOTOSTRICTIVE PROPERTIES

2.1. Principle

Although the origin of this photovoltaic effect has not been clarified yet, the key point to understand it is the necessity of both *impurity doping* and *crystal asymmetry* [2,3]. The donor impurity levels induced in accordance with La doping (or other dopants) are present slightly above the valence band. The transition from these levels with an asymmetric

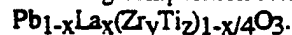
potential due to the crystallographic anisotropy may provide the "preferred" momentum to the electron. Electromotive force is generated when electrons excited by light move in a certain direction of the ferroelectric crystal, which may arise along the spontaneous polarization direction.

The asymmetric crystal exhibiting a photovoltaic response is also piezoelectric in principle, and therefore, a photostriction effect is expected as a coupling of the bulk photovoltaic voltage (E^{ph}) with the piezoelectric strain constant (d).

2.2. Materials Research

The figure of merit of the photostriction is evaluated by the product of the photovoltaic voltage (E^{ph}) and the piezoelectric coefficient (d) for a static response. PZT based ceramics are currently focused because of their excellent piezoelectric properties, i.e. high d values. PLZT is one of such materials, which is also famous as a transparent (good sintered without pores) ceramic applicable to electrooptic devices.

PLZT ($x/y/z$) samples were prepared in accordance with the following composition formula:



The contour maps of the photovoltaic response and the piezoelectric strain constant d_{33} on the PLZT phase diagram indicated that the largest product $d_{33} \cdot E^{\text{ph}}$ was obtained with the composition (3/52/48) [4,5]. Impurity doping on PLZT also affects the photovoltaic response significantly [3]. The photovoltaic response is enhanced by donor doping onto the B-site (Nb^{5+} , Ti^{5+} , W^{6+}). On the other hand, impurity ions substituting at the A-site and/or acceptor ions substituting at the B-site, whose ionic valences are small (1 to 4), have no significant effect on the response.

Even when the composition is fixed, the photostriction still depends on the sintering condition or the grain size [5]. The smaller grain sample is preferable, if it is sintered to a high density.

2.3. Influence of Sample Thickness

Since the photostrictive/photovoltaic effect requires efficient light energy absorption, we cannot expect a large response from either too-thin or too-thick materials. Photocurrent was measured as a function of sample thickness, with the radiation of light (14 mW/cm^2) to the PLZT samples poled at 2 kV/mm

electric field [6]. As is expected, photocurrent increases with decreasing in the sample thickness. An incident radiation is absorbed in the surface region as it penetrates into the crystal lattice of a sample.

The relationship between sample thickness and photovoltaic response was explained by a model, in which the absorption coefficient α is assumed to be independent of light intensity and the photocurrent density is taken to be proportional to light intensity. The optimum thickness (for the present set of samples) which yields maximum photocurrent was found at $33 \mu\text{m}$ (nearly equal to $1/\alpha$). It should be noted that the samples used in this study were thicker than this optimum thickness, and the thick film designs will be suitable for practical applications.

3. DISPLACEMENT AMPLIFICATION

Since the maximum strain level of the photostriction is only 0.01 %, we need to consider a sophisticated magnification mechanism of the displacement. We employed a bimorph structure, in which two PLZT plates were pasted back to back, but were placed in opposite polarization, then connected on the edges electrically [3]. A purple light (366 nm) was shined to one side, which generated a photovoltaic voltage of 7 kV across the length. This caused the PLZT plate on that side to expand by nearly 0.01 % of its length, while the plate on the other (unlit) side contracted due to the piezoelectric effect through the photovoltage. Since the two plates were bonded together, the whole device bent away from the light. For this 20 mm long and 0.35 mm thick bi-plate, the displacement at the edge was $150 \mu\text{m}$, and the response speed was a couple of seconds.

4. DEVICE APPLICATIONS

4.1. Photo-Driven Relay

A photo-driven relay was constructed using a PLZT photostrictive bimorph as a driver [3]. A dummy PLZT plate was positioned adjacent to the bimorph to cancel the photovoltaic voltage generated on the bimorph. Utilizing a dual beam method, switching was controlled by alternately irradiating the bimorph and the dummy. The time delay of the bimorph that ordinarily occurs in the off process due to a low dark conductivity could be avoided, making use of this dual beam method. The amount of displacement observed at a tip of the bimorph was $\pm 150 \mu\text{m}$. A snap action switch was used for the relay. Switching by a displacement of several tens of micron was possible with this device. The typical delay time for the on/off response of the photo-driven relay was 1 - 2 seconds.

4.2. Micro Walking Device

A photo-driven micro walking machine has also been developed using the photostrictive bimorphs [7].

It was simple in structure, having only two ceramic legs fixed to a plastic board. When the two legs were irradiated with purple light alternately, the device moved like an inchworm. The photostrictive bimorph as a whole was caused to bend by $\pm 150 \mu\text{m}$. The inchworm built on a trial basis exhibited rather slow walking speed (several tens $\mu\text{m}/\text{min}$), since slip occurred between the contacting surface of its leg and the floor.

4.3. Photophone

Photo-mechanical resonance of a PLZT ceramic bimorph has been successfully induced using chopped near-ultraviolet irradiation, having neither electric lead wires nor electric circuits. A thin cover glass was attached on the photostrictive bimorph structure to decrease the resonance frequency so as to easily observe the photo-induced resonance. A dual beam method was used to irradiate the two sides of the bimorph alternately; intermittently with a 180 deg phase difference. The mechanical resonance was then determined by changing the chopper frequency.

Photo-induced mechanical resonance was successfully observed at 75 Hz with the mechanical quality factor Q of about 30. The maximum tip displacement of this photostrictive sample was $5 \mu\text{m}$ at the resonance point, smaller than the level required for audible sound. However, the achievement of photo-induced mechanical resonance in the audible frequency range suggests the promise of photostrictive PLZT bimorph-type devices as photo-acoustic components, or "photophones", for the next optical communication age.

5. REFERENCES

- [1] V. M. Fridkin, *Photoferroelectrics*, Ed. by M. Cardona, P. Fulde, H. -J. , Queisser, Solid State Sciences 9, Springer-Verlag, New York (1979).
- [2] A. M. Glass, D. von der Linde, D. H. Austin and T. J. Negran, *J. Elec. Mater.*, 4 [5], 915 (1975).
- [3] M. Tanimura and K. Uchino, *Sensors and Materials*, 1, 47 (1988).
- [4] K. Uchino, M. Aizawa and Late S. Nomura, *Ferroelectrics*, 64,199 (1985).
- [5] T. Sada, M. Inoue and K. Uchino, *J. Ceram. Soc. Jpn.*, 5, 545 (1987).
- [6] P. Poosanaas, A. Dogan , S. Thakoor and K. Uchino, *J. Appl. Phys.*, (1998) [accepted].
- [7] K. Uchino, *J. Rob. Mech.*, 1, 124 (1989).

Corresponding author: Kenji Uchino, 134 Materials Research Laboratory, The Pennsylvania State University, University Park, PA 16802, USA
Fax: 814-863-8035, E-mail: kenjiuchino@psu.edu